ASME
SETTING THE STANDARD

Transactions of the ASME, Journal of Fluids Engineering (ISSN 0098-2202) is published monthly by The American Society of Mechanical Engineers, Three Park Avenue, New York, NY 10016. Periodicals postage paid at New York, NY and additional mailing offices.
POSTMASTER: Send address changes to Transactions of the ASME, Journal of Fluids Engineering, c/o THE AMERICAN SOCIETY OF MECHANICAL ENGINEERS, 22 Law Drive, Box 2300, Fairfield, NJ 07007-2300.
CHANGES OF ADDRESS must be received at Society headquarters seven weeks before they are to be effective. Please send old label and new address.
STATEMENT from By-Laws. The Society shall not be responsible for statements or opinions advanced in papers or ... printed in its publications (B7.1, Par. 3).

Journal of Fluids Engineering

Published Monthly by ASME

VOLUME 130 • NUMBER 7 • JULY 2008

RESEARCH PAPERS

Flows in Complex Systems

Fundamental Issues and Canonical Flows

Multiphase Flows

TECHNICAL BRIEFS

(Contents continued on inside back cover)

This journal is printed on acid-free paper, which exceeds the ANSI Z39.48-1992 specification for permanence of paper and library materials. ♾™
♻ 85% recycled content, including 10% post-consumer fibers.

(**Contents continued**)

ANNOUNCEMENTS

The ASME Journal of Fluids Engineering is abstracted and indexed in the following:

Applied Science & Technology Index, Chemical Abstracts, Chemical Engineering and Biotechnology Abstracts (Electronic equivalent of Process and Chemical Engineering), Civil Engineering Abstracts, Computer & Information Systems Abstracts, Corrosion Abstracts, Current Contents, Ei EncompassLit, Electronics & Communications Abstracts, Engineered Materials Abstracts, Engineering Index, Environmental Engineering Abstracts, Environmental Science and Pollution Management, Excerpta Medica, Fluidex, Index to Scientific Reviews, INSPEC, International Building Services Abstracts, Mechanical & Transportation Engineering Abstracts, Mechanical Engineering Abstracts, METADEX (The electronic equivalent of Metals Abstracts and Alloys Index), Petroleum Abstracts, Process and Chemical Engineering, Referativnyi Zhurnal, Science Citation Index, SciSearch (The electronic equivalent of Science Citation Index), Shock and Vibration Digest, Solid State and Superconductivity Abstracts, Theoretical Chemical Engineering

Aerodynamics of Large-Scale Vortex Generator in Ground Effect

Joseph Katz
Professor
Chair
Department of Aerospace Engineering,
San Diego State University,
San Diego, CA 92119

Frederic Morey[1]
San Diego State University,
San Diego, CA 92119

The aerodynamic performance of several vortex generators (VGs) of the type used on the lower surface of race cars was tested in a low-speed wind tunnel. In this particular application, the vortices emanating from the VGs create a suction force between the vehicle and the ground, thereby improving tire adhesion and the vehicle's cornering/traction performance. Since the size of these devices is much larger than the local boundary layer thickness, they are termed "large scale" in this study. Results of the wind tunnel tests indicate that the aerodynamic adhesion forces increase with reduced ground clearance while the corresponding drag increase is much smaller. The parameters investigated in this study are the VG length, shape, and the effect of incidence angle. Amongst the various shapes tested, the traditional rectangular VG created the largest forces while the simple triangular design was the most efficient in terms of the incremental lift to drag ratio. [DOI: 10.1115/1.2948361]

Introduction

Vortex generators (VGs), labeled here as "small-scale VGs," are widely used for boundary layer transition and flow separation control. Some of the most common applications are on the suction side of aircraft wings [1] or in the diffuser section of wind tunnels where (due to their presence) a reduction in drag and surface resistance is observed. Another form of vortex generating devices are the leading-edge strakes used for lift augmentation on high speed airplanes. These highly swept surfaces are effective at the higher angles of attack, when a strong vortex is formed along the leading edge. The suction induced by the swirling vortex not only creates lift on the strake but significantly augments the lift of the main wing behind it. A survey depicting the shapes of several frequently used leading-edge devices with focus on unsteady flow effects is presented in Ref. [2]. A quite different utilization of vortex flow was investigated by Rossow [3] where a trapped vortex was used to augment the lift of airfoils. The basic idea is that if a strong vortex can be stabilized above an airfoil, its circulation and resulting lift could be considerably augmented. The main hurdle for a practical application of this concept remains the stabilization of the (trapped) vortex above the airfoil. In Ref. [4] several fences, placed normal to the airfoil's upper surface, were used but a practical utilization was not demonstrated. Further efforts to stabilize the vortex above the wing were experimented with by Riddle et al. [5]. In addition to the vertical fences they used suction (through the end plates of a two dimensional wing) and showed that the vortex can be stabilized above the wing. In spite of this successful experiment, the practical use of this principle remains unclear. The above mentioned vortex stabilization problem can be resolved by high leading-edge sweep, as discussed in Ref. [6]; but again, no large benefits were demonstrated.

The combination of the traditional boundary layer control VGs and the lift augmentation oriented trapped vortex concepts led to a third application, widely used in the race-car industry. These devices rely on creating a strong trailing vortex behind the VG, capable of altering the local flow directions around cooling inlets, wheels, and lifting surfaces. Another less publicized application is aimed at increasing the vehicle's downforce [7,8] in order to improve high-speed cornering, braking, and acceleration. The present study is focused on the aerodynamics of this latter category, and the primary function of these VGs may be clarified by the diagram in Fig. 1. Here, a flat plate is immersed in the freestream with a velocity of V_∞. A "small-scale" VG is shown at the left hand side and its height is on the order of the local boundary layer thickness.

If placed ahead of the transition point, it can reduce the likelihood of laminar separation and will force transition from a laminar to a turbulent boundary layer. In some cases such VGs are placed in the turbulent region in order to energize the boundary layer and delay flow separation. On the other hand, a "large-scale" VG, shown at the right hand side of Fig. 1, is much larger and its function is to interact with the outer flow and not with the much thinner boundary layer. Race-car designers occasionally incorporate similar VGs into the lower surface of the car in an effort to create low pressure there. A typical application of a single VG (per side) is shown in Fig. 2 where it is attached to the lower side of the vehicle. In most cases, the vehicle's lower surface is almost flat and more than one (per side) VGs are used. Because of the relative incidence (yaw) of this plate (e.g., the VG) a strong tip vortex is formed, extending along the underside of the car. The suction force created in the vicinity of the VG and by its wake behind the VG can significantly enhance the downforce of the vehicle (and downforce improves performance).

Previous studies of such VGs [7,8] focused on rectangular VGs (as shown in Fig. 2 and their angle of attack and spacing effects. Note that the heights of these VGs cannot change much because of the available ground clearance under the vehicle. The present study, therefore, will investigate additional geometrical aspects of these VGs, such as length and shape.

Experimental Apparatus

The experimental setup used in the present study is similar to the one used in Refs. [7,8] and is shown schematically in Fig. 3. A closed circuit wind tunnel with a 4 ft wide and 3 ft high (1.22 $\times$ 0.91 m) test section was used and maximum freestream speed could be as high as 170 mph (76 m/s). The lower surface of the car (sometimes called the underwing) was represented by a flat rectangular plate, onto which the VGs were mounted. This plate was set at zero incidence at the center of the test section and was mounted onto the six-component balance (located under the test section) by three struts, as shown in the figure. Ground clearance variation was obtained by moving a larger rectangular thin plate up or down relative to the model (see ground plane in Fig. 3). The advantage of this inverted setup (e.g., the ground is above the model) was that the flat-plate model was mounted directly to the balance and only the nonmetric ground plane was moving.

[1]Visiting Student from Institut Français de Mécanique Avancée (IFMA).

Contributed by the Fluids Engineering Division of ASME for publication in the JOURNAL OF FLUIDS ENGINEERING. Manuscript received February 26, 2007; final manuscript received January 15, 2008; published online June 25, 2008. Assoc. Editor: Hamid Johari.

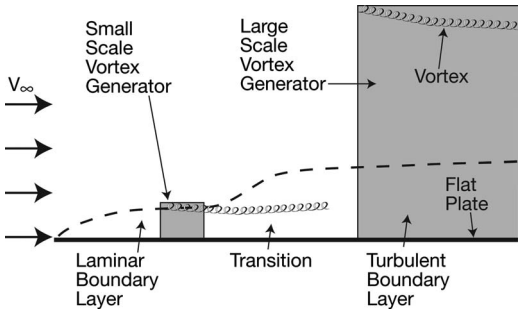

Fig. 1 Schematic description of "large-" and "small-scale" VGs

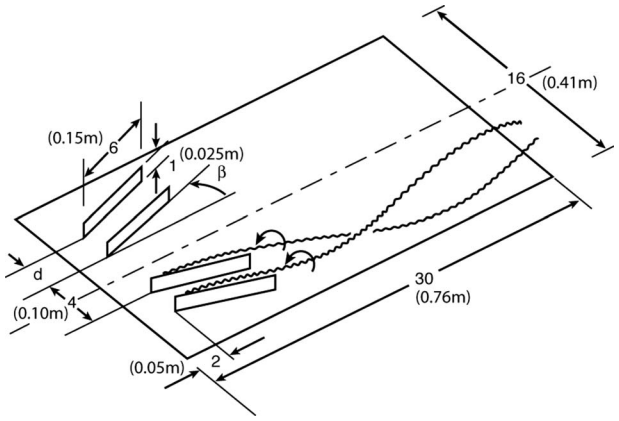

Fig. 4 The wind tunnel model consists of a horizontally placed flat plate with four VGs. Dimensions are in inches (meters) and the spacing *d* was kept constant at *d*=2 in. (0.05 m) throughout the whole test. Note the schematic description of the vortices emanating from the left side.

Since both the model and ground plane were made of thin flat plates, wind tunnel blockage was small (less than 1%) and the effect of the ground plane installation (on the blockage ratio) was negligible too. Two rectangular VGs per side were used (see Fig. 4), following Rossow's [3,4] observation that at least two fences are required to stabilize the vortex. The spanwise and chordwise position and the yaw angle of the VGs were adjustable, but their vertical orientation was fixed (e.g., at 90 deg to the flat plate). For the data presented here the separation distance between the leading edges of the inner VGs was kept constant (at a total of 4 in. =0.10 m) and each VG was yawed about this point (positive β defined in the outward direction, see Fig. 4). Other parameters such as the angles β and the distance d between adjacent VGs were selected based on the findings reported in Ref. [7] (e.g., β =20 deg and d=2 in.=0.05 m). Therefore, the leading edges of all VGs tested here remained at the same point, as shown in Fig. 4. Also, the geometrical parameters of this study were dictated by the Indycar geometry shown in Fig. 2. Thus, the flat-plate size, and the relative size, location, and orientation of the VGs were all set by this open-wheel race-car application.

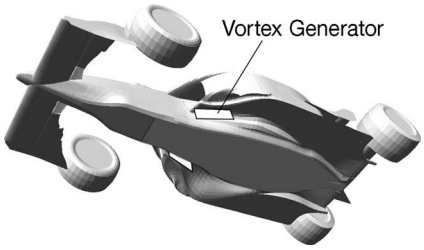

Fig. 2 Typical application of large-scale VGs on the lower surface of an open-wheel race car

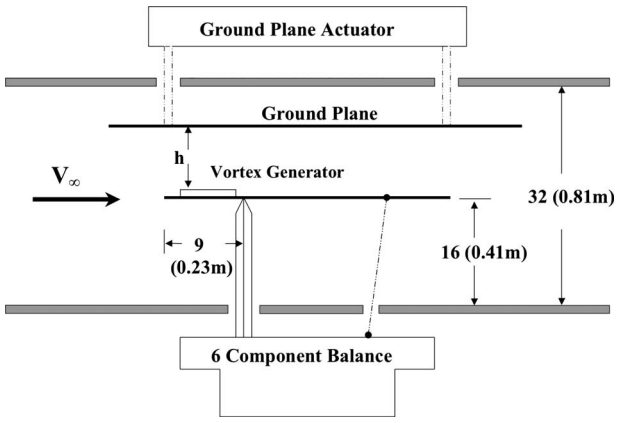

Fig. 3 The flat-plate model with the VGs mounted upside down at the center of the test section. Ground clearance variations were simulated by moving the thin ground plane down, toward the stationary model. Dimensions are in inches (meters).

Additional dimensions of the model and test section are depicted in Figs. 3 and 4. The freestream speed was set at V_∞ =120 mph (53.6 m/s) and turbulence levels were below 2%. Although previous studies (with wings [9]) reported noticeable effects when freestream turbulence levels were about 9%, those results do not directly relate to the present experimental setup. Also, because of the sharp edges of the VGs it is assumed that Reynolds number and freestream turbulence effects are less pronounced and results of this vortex flow experiment are scalable. Based on the flat-plate length the test Reynolds number was 2.7 $\times 10^6$. Boundary layer thickness on the flat plate and near the VGs was about 2–4% of the VG height, which is much smaller than the schematic description in Fig. 1. It was assumed that the boundary layer is laminar ahead of the VGs, and due to the vortex flow, transitions to turbulent behind it. Accuracy of the six-component balance was about ± 0.004 for C_L, ± 0.002 for C_D. Note that in this setup positive lift is upward and the ground clearance was measured between the upper tip of the VG and the ground plane above it (Fig. 3).

Results

Earlier aerodynamic studies of such large-scale VGs [7,8] focused mainly on the effect of the spacing, d, between adjacent VGs and on their incidence, β. Based on the "best results" from Refs. [7,8] the spacing d in the present study was set at 2 in. (0.05 m), and the side slip of the inner VGs was set at β =20 deg while the outer VG was set either to β=20 or β =30 deg. As noted, the parameters investigated in the present study are the VG shape and length.

Since the experimental apparatus of Refs. [7,8] was slightly modified (from the structural point of view), a comparison with the earlier data is presented first. The results for this comparison, in terms of the measured lift and drag coefficients, are presented in Figs. 5 and 6, respectively. The magnitudes of the nondimensional coefficients are small since the plate's planview area was used for the data reduction (e.g., S=480 in.^{2}=0.31 m^2). In order to visualize the magnitude of data uncertainty, error bars were added to these two figures (only). The VGs were set at β =20 deg and the comparison also included the results for the flat-plate model without any VGs on it (from Ref. [8]). This was necessary because of the difference in the definition of "tares" between the two experiments.

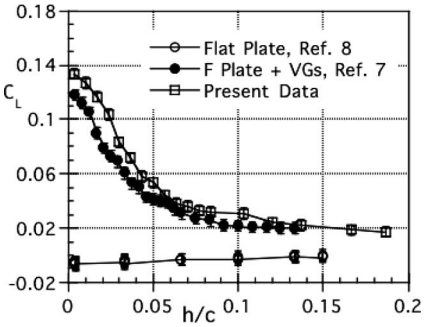

Fig. 5 Variation of the lift coefficient versus ground clearance h/c and comparison with previously published data (rectangular VGs at $\beta=20$ deg). Note that uncertainty in C_L is represented by the vertical error bars (which are hardly visible)!

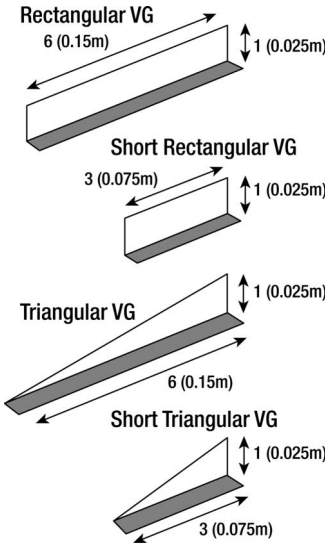

Fig. 7 Dimensions of the rectangular/triangular long/short VGs. Dimensions in inches (meters).

It is expected that a flat plate at zero incidence will not produce lift. However the data from Ref. [8] indicate that the model may have had a small negative incidence, which created negative lift that increased with reduced ground clearance (Fig. 5). This small negative incidence was corrected in the present test and the lift (with the VGs) is therefore slightly higher than the lift reported in Ref. [7]. (Note that the data reported in Refs. [7,8] were taken at the same time.) The increase in lift when ground clearance is reduced is attributed to the vortex being closer to the flat plate and perhaps also being stronger due to faster air speeds around its edge (with reduced ground clearance). Of course, at close to zero ground clearance, no flow passes above the VG and therefore no vortex is created, so lift must be reduced. This extreme condition was not measured in order not to damage the model (by mistakenly running the ground plane too close to the VGs). However, this data clearly show that the lift increases, even for very small ground clearance values.

The drag coefficient data in Fig. 6 show the difference between the methods of accounting for tares. The earlier drag data include the drag of the flat plate and its supporting brackets, while the present data show the added effect of the VGs only (so in the later data the tares included the flat-plate loads as well). Consequently, the present drag data should be compared with the difference between the previous data minus the drag of the flat plate. Based on these data, the drag of the flat plate, including the installation hardware, was about $C_D \sim 0.035$, and the increment due to the VGs was on the order of $C_D \sim 0.01$. This is close to the order of magnitude drag estimates for a flat plate given by Winter [10] (e.g., the drag of the individual VG was calculated assuming an isolated flat plate at an angle of attack β). Also, the error bars shown in Fig. 6 depict the maximum errors in the drag force, which are much larger than the error bars in Fig. 5, mainly due to the smaller magnitude of the drag force.

Highly swept triangular surfaces such as delta wings [11] can also function as VGs in ground proximity. One advantage they may have is when ground clearance momentarily reaches zero (due to suspension oscillations), then a triangular VG will still produce a sizable trailing vortex. The first set of experiments, therefore, focused on comparing the performance of rectangular versus triangular VGs. At the same time the effect of VGs length was also studied by simply reducing their length by one-half. The geometry of this set of VGs is depicted in Fig. 7.

A comparison between the rectangular and triangular VGs (having the same length and height) in terms of lift and drag coefficients is presented in Figs. 8 and 9. These two figures present the data for the long VGs (e.g., 6 in. long=0.15 m) and the data for the shorter VGs are presented later. At the larger values of ground clearance the effect is quite small; however, with reduced h/c the rectangular design creates consistently more lift, compared to the triangular ones. When the angle of the outer VGs was increased to $\beta=30$ deg, the lift increased for both rectangular and triangular VGs, as seen in Fig. 8. At the lower h/c values, the rectangular VGs show signs of a halt in the lift increase, possibly due to blocking the flow between the VG and the ground (or vortex burst, as suggested in Ref. [7]). On the other hand, the triangular design does not have this deficiency, and its lift increases, even for very low h/c values. It was also suggested that the vortices ema-

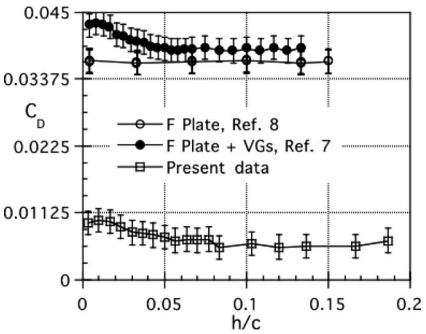

Fig. 6 Variation of the drag coefficient versus ground clearance h/c and comparison with previously published data (rectangular VGs at $\beta=20$ deg). Note that uncertainty in C_D is represented by the vertical error bars!

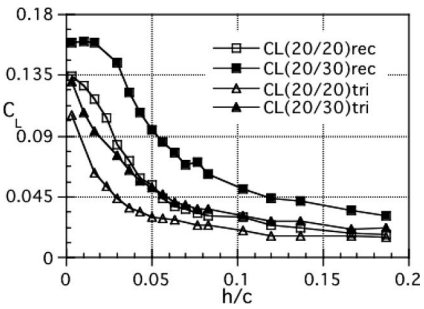

Fig. 8 Variation of the lift coefficient versus ground clearance h/c for rectangular and triangular VGs, and the effect of larger incidence, β ($\beta=20/20$ means all VGs are at 20 deg, and $\beta=20/30$ stands for outer VGs at $\beta=30$ deg)

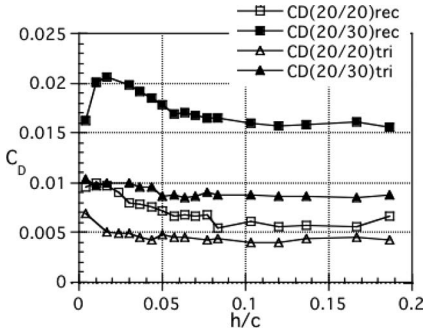

Fig. 9 Variation of the drag coefficient versus ground clearance h/c for rectangular and triangular VGs, and the effect of larger incidence, β (β=20/20 means all VGs are at 20 deg, and β=20/30 stands for outer VGs at β=30 deg)

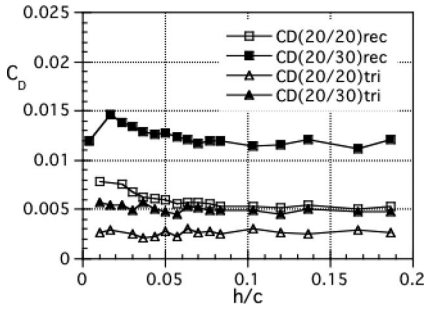

Fig. 11 Variation of the drag coefficient versus ground clearance h/c for short rectangular and triangular VGs, and the effect of larger incidence, β (β=20/20 means all VGs are at 20 deg, and β=20/30 stands for outer VGs at β=30 deg)

nating from the VGs create a "local blockage" for the flow between the two large flat plates. This blockage will increase the local velocity (and C_L) as ground clearance is reduced. However, data for larger VG angles (e.g., β=30/40 deg), reported in Ref. [7], showed an earlier lift loss when ground clearance was reduced. This observation and the fact that the lift of the triangular VGs is not half of the rectangular VGs suggest that the local blockage effect is not dominant.

The frontal area of the triangular VG is one-half of the rectangular VG, and therefore less drag is expected. This is verified in Fig. 9. Again, increasing the incidence of the outer VGs to β =30 increases the drag for both shapes, but in the case of the rectangular VGs the increase is the largest. As expected, the drag data follow the trends of the lift data presented in Fig. 8. For example, the drag of the rectangular VGs reaches a maximum before approaching minimum ground clearance and then shows a clear drop (for both β=20/20 and β=20/30).

The lift and drag coefficient variation versus ground clearance for the shorter VGs (both rectangular and triangular) is presented in Figs. 10 and 11. Note that the "short" VGs had one-half the length of the "long" or base line VGs. Basically, the same trends remain as seen with the long VGs, but as expected, with less lift and less drag. Although the surface area of the VGs was reduced by 50%, the reduction in both lift and drag was far less. This demonstrates again that the trailing vortex effect is not local and its induced suction affects areas behind the VG. The lift coefficient data in Fig. 10 indicate that the triangular VG generates less lift than the rectangular one, while increasing the incidence of the outer VGs to β=30 deg was as effective as for the longer VGs. Also note that some of the drag coefficient data fall close to the previously mentioned uncertainty of $\pm$0.002 for C_D.

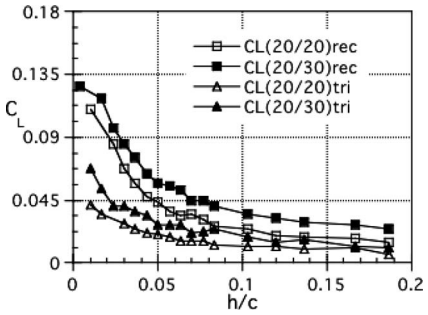

Fig. 10 Variation of the lift coefficient versus ground clearance h/c for short rectangular and triangular VGs, and the effect of larger incidence, β (β=20/20 means all VGs are at 20 deg, and β=20/30 stands for outer VGs at β=30 deg)

A direct comparison between the long and the short VGs is presented in Fig. 12. Basically all the data presented in Figs. 8–11 could have been crossplotted, but for brevity only the lift with β=20/20 deg is presented (but results for the β=20/30 are basically the same). Clearly, the rectangular VGs generate more lift than the triangular ones, and the lift of the longer VG is also higher. A close examination of the lift to drag ratio (not plotted here) shows a small advantage for the triangular design.

A VG may be viewed as one-half of a small aspect-ratio wing at an angle of attack. With this analogy in mind, many other shapes may be considered, and the most common are summarized in Fig. 13. In terms of area, the gothic shape is larger than the triangle and smaller than the rectangular design. This shape was created by simply blending a 40 deg initial leading-edge sweep into an otherwise rectangular VG. The ogive shape on the other hand has the same area as the triangular VG but the leading edge was smoothed by a sinusoidal curve. The parabolic shape had the smallest area, and started at a much larger sweep at the apex (compared to the triangular design). Thus, from the visual aspect, the area is the main parameter. However, from the aerodynamic point of view, vortex stability (delay of vortex burst in this case) is a more important parameter influencing the lift coefficient of the VG.

A comparison of the lift coefficient versus ground clearance, generated by the five short VGs, is shown in Fig. 14. In this case the incidence is moderate (all VGs at β=20/20 deg) so vortex breakdown is not immediately behind the VG trailing edge. This way the differences between the five designs are more representative. The data in Fig. 14 clearly show that the lift is almost directly related to the VG area. Clearly the rectangular design has the highest lift while the parabolic shape has the lowest. In the case of the triangular and ogive shapes (having the same area), the ogive VG demonstrates a slight advantage, and indeed most small aspect-ratio airplane wings (e.g., Concorde) have similar planform shapes. The drag data in Fig. 15 follow similar trends, but in this case the triangular design has the lowest drag.

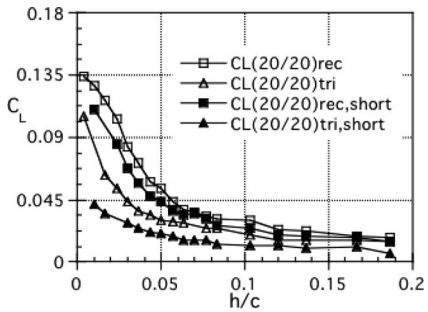

Fig. 12 Lift coefficient comparison for short/long and rectangular/triangular VGs at β=20/20

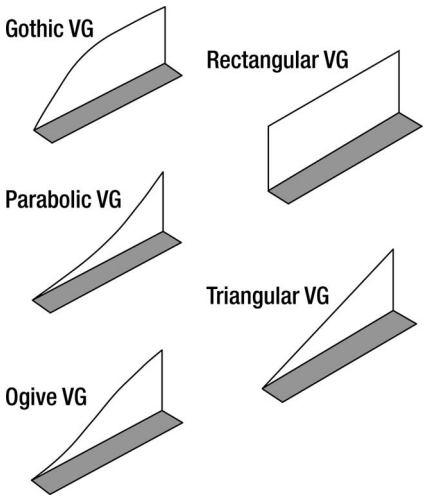

Fig. 13 Additional VG shapes evaluated during this test. Note that only the "short" versions were tested (e.g., length=3 in. and height is 1 in. or 0.08×0.026 m^2)

When increasing the incidence of the outer VGs to $\beta=30$ deg, as shown in Fig. 16, the lift data follow similar trends shown earlier in Fig. 14. The lift increase in the rectangular VGs, however, seems to slow down at the lower ground clearances, possibly due to the outer VGs vortex breakdown (near the VG trailing edge, as discussed in Ref. [7]). This loss of lift results in a dip in the drag, as shown by Fig. 17. Otherwise the drag data repeat the conclusions drawn from Fig. 15, clearly showing the drag advantage of the triangular design. This brief study of the VG's shape indicates that the simple geometries of the triangle or rectangle are the most effective for this type of application.

The data presented so far indicate that the $\beta=20/20$ deg configuration is more efficient than the $\beta=20/30$ deg case. However,

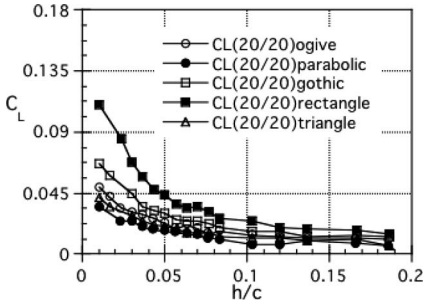

Fig. 14 Variation of the lift coefficient versus ground clearance h/c for several short VGs ($\beta=20/20$ means all VGs are at 20 deg)

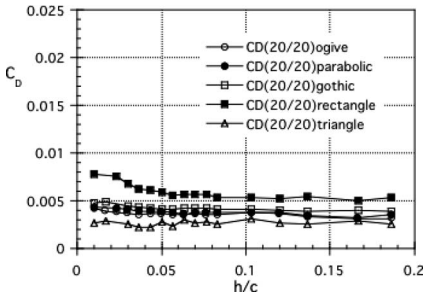

Fig. 15 Variation of the drag coefficient versus ground clearance h/c for several short VGs ($\beta=20/20$ means all VGs are at 20 deg)

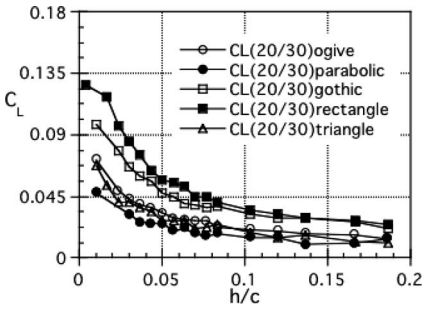

Fig. 16 Variation of the lift coefficient versus ground clearance h/c for several short VGs ($\beta=20/30$ stands for inner VGs at $\beta=20$ deg, and outer VGs at $\beta=30$ deg)

it is not yet clear which configuration has the best L/D. Also for the sake of brevity, the L/D information was not plotted for all the cases presented here. Therefore the incremental lift to drag ratio of the four most efficient VG configurations is summarized in Fig. 18 (basically the long versus short triangular/rectangular shapes). The results for all four VG shapes are very close but the triangular VGs reach a slightly higher L/D. Note that the L/D curves increase almost like the previously presented C_L versus h/c data, demonstrating the effectiveness of this device for race-car applications. Also, as noted in the discussion in Fig. 6, the drag of the large flat plate was not included in the present data. Therefore, the L/D numbers in Fig. 18 are much higher than in Ref. [7]. Furthermore, since the flat plate's drag (which was included in the tares) was almost three times larger than the drag of the VGs alone, the L/D data of Fig. 18 must be viewed in terms of "general trend" only.

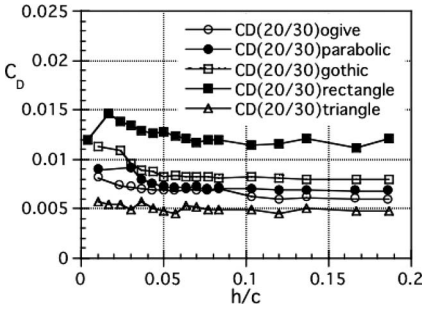

Fig. 17 Variation of the drag coefficient versus ground clearance h/c for several short VGs ($\beta=20/30$ stands for inner VGs at $\beta=20$ deg, and outer VGs at $\beta=30$ deg)

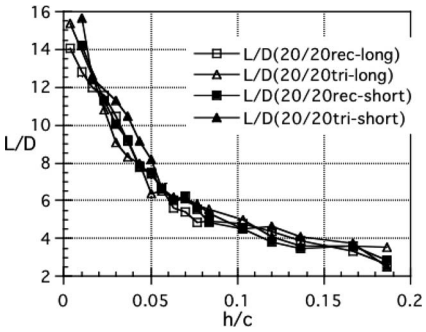

Fig. 18 Variation of incremental lift to drag ratio versus ground clearance h/c for the four most efficient VGs ($\beta=20/20$ deg)

Concluding Remarks

Results of this study demonstrate the potential of such VGs to generate sizable levels of downforce in race-car applications. For most shapes of the VGs tested, the lift (or downforce for a race car) increases with reduced ground clearance. Near the zero ground clearance level, the triangular VGs were found to be less likely to lose lift, an important feature for race-car applications. The data presented here consist of the integral lift and drag. However, many aspects of the flow, such as the vortex rollup or breakdown behind the VGs and the mechanism of skin friction on the flat plate, remain unclear. Therefore, further studies must focus on additional flow visualizations, measurement of pressure distributions, and numerical simulations to better explain the data presented here.

Nomenclature

a = VG height (1 in.)
c = plate chord (30 in.)
C_D = coefficient=$D/(0.5\ \rho\ V_\infty{}^2\ \mathrm{S})$
C_L = lift coefficient=$L/(0.5\ \rho\ V_\infty{}^2\ \mathrm{S})$
d = lateral spacing between VGs (2 in.)
D = drag
h = ground clearance
l = VG length (6 in.)
L = lift
L/D = lift/drag ratio
S = reference area ($30\times 16=480$ in.^{2})
V_∞ = freestream speed
w = plate width (16 in.)
β = VG yaw angle

References

[1] Bragg, M. B., 1987, "Experimental Study of Airfoil Performance With Vortex Generators," J. Aircr., **24**(5), pp. 305–309.
[2] Katz, J., 1999, "Wing/Vortex Interactions and Wing Rock Review," Prog. Aerosp. Sci., **35**(7), pp. 727–750.
[3] Rossow, V. J., 1978, "Lift Enhancement by an Externally Trapped Vortex," J. Aircr., **15**(9), pp. 618–625.
[4] Rossow, V. J., 1994, "Aerodynamics of Airfoils With Vortex Trapped by Two Spanwise Fences," J. Aircr., **31**(1), pp. 146–153.
[5] Riddle, T. W., Wadcock, A. J., Tso, J., and Cummins, R. M., 1999, "An Experimental Analysis of Vortex Trapping Techniques," ASME J. Fluids Eng., **121**(3), pp. 555–559.
[6] Buchholz, M. D., and Tso, J., 2000, "Lift Augmentation on Delta Wing With Leading-Edge Fences and Gurney Flap," J. Aircr., **37**(6), pp. 1050–1057.
[7] Garcia, D., and Katz, J., 2003, "Trapped Vortex in Ground Effect," presented at the *32nd AIAA Fluid Dynamics Conference*, St. Louis, MO, June 26, 2002, AIAA Paper No. 2002-3307, also AIAA J., **41**(4), pp. 674–678.
[8] Katz, J., and Garcia, D., 2002, "Aerodynamic Effects of Indy Car Components," SAE Journal of Passenger Cars: Mechanical Systems, SAE 2002-01-3311.
[9] Hoffmann, J. A., 1991, "Effects of Freestream Turbulence on the Performance Characteristics of an Airfoil," AIAA J., **29**(9), pp. 1353–1354.
[10] Winter, H., 1937, "Flow Phenomena on Plates and Airfoils of Short Span," NACA, TM 798.
[11] Katz, J., and Levin, D., 1984, "Measurement of Ground Effect for Delta Wings," J. Aircr., **21**(6), 442–443.

Evaluation of the Mixing Performance of the Micromixers With Grooved or Obstructed Channels

Yeng-Yung Tsui[1]
e-mail: yytsui@mail.nctu.edu.tw

Ching-Shiang Yang

Chung-Ming Hsieh

Department of Mechanical Engineering,
National Chiao Tung University,
Hsinchu 300,
Taiwan R.O.C.

The mixing flows in microchannels were examined using numerical methods. To speed up fluid mixing, it is essential to generate lateral transport of mass. In this study, the mixing flow is disrupted by either placing grooves or block obstacles on the walls of the channels. Since the grooves or the blocks appear in a periodic configuration, the velocity is solved only in a section of the channel. With the repeating cycle of flow velocity field, the fluid concentration can be calculated throughout the entire length of the channel. Good agreement with experiments in the mixing performance justifies the present methodology. Two different channel configurations are under consideration: grooved channels and obstructed channels. The results reveal that with straight grooves, a well organized vortex flow is formed in the vertical plane along the groove, which leads to a helical flow in the channel. The mixing performance can be enhanced by having grooves on both the top and the bottom walls arranged in a staggered manner, by which the transversal velocity is largely increased. It is seen that the strength of the secondary flow and, thus, the mixing can be improved by suitably choosing geometric parameters of the groove, such as the depth, the width, and the oblique angle. It is also shown that the efficient mixing for the staggered herringbone type groove is due to the fluid stratification caused by the exchange of position of the resulted counter-rotating vortices. As for the obstructed channels, the flows are in essence two dimensional. Very strong transversal velocity can be produced by narrowing down the flow passage in the channel. However, the efficient mixing is obtained at the cost of large pressure head loss. [DOI: 10.1115/1.2948364]

1 Introduction

Rapid mixing is crucial to the microfluid systems, which are now widely used in biochemistry analysis, chemical synthesis, drug delivery, high-throughput screening, among others. In microsystems, the small size prohibits turbulent mixing. The Reynolds number is generally less than 100 and can be as low as 0.01, which lies in the creeping regime. Hence, the mixing in microchannels is predominantly governed by molecular diffusion. If the thickness of the lamella structure of the fluid is much larger than the characteristic diffusion length, it is difficult to obtain rapid mixing.

To enhance fluid mixing, either active or passive methods can be employed. Active mixing is usually achieved by periodically perturbing the flow field. A number of fluid actuation methods have been introduced, including electrokinetic force [1,2], ultrasonic actuation [3,4], thermal power [5,6], periodic pressure perturbation [7–9], etc. Active mixers have obvious disadvantages over passive mixers in the requirement of external power sources and the complexity in terms of fabrication, operation, maintenance, and package. On the other hand, passive mixers utilize no extra forcing mechanism other than the basic pressure head used to drive the fluid flow.

In smooth and regular flow fields, efficient mixing can be obtained by creating chaotic advection, which stretches and folds fluid elements [10,11]. According to chaotic advection theory, the chaos can arise in a nonlinear dynamic system provided that three degrees of freedom are present [12]. For two-dimensional flows, a time-dependent perturbation is usually imposed to provide the third degree of freedom to generate chaotic mixing. Under the condition of steady state, a three-dimensional flow is required. The active micromixers are of the former type, while the passive ones usually belong to the latter. Therefore, it is essential for the passive micromixers to generate strong enough lateral flows such that the fluid interface can be greatly stretched and folded.

Mengeaud et al. [13] examined a zigzag microchannel. Below a critical Reynolds number of about 80, the flow remains parabolic and the mixing is ensured by molecular diffusion. At high Reynolds numbers, a transversal velocity is induced due to the flow recirculation behind the sharp turning corners, which improves the mixing process. Similar results were observed in the study of Liu et al. [14] for square-wave channels. The flow field in these two types of micromixer is essentially two dimensional because the channels make sharp turns only on a plane. To create fully three-dimensional flow, Liu et al. [14] proposed a serpentine design by which the channel periodically makes sharp turning in a three-dimensional manner. It was shown that with this kind of microchannel the mixing ability is much improved over the square-wave channel for Reynolds numbers between 6 and 70. As an example, at a Reynolds of 70, the former produces 1.6 times more reacted phenolphthalein than the latter. However, the complex three-dimensional structure of the serpentine channel has posed a challenge to fabrication.

Another way to induce lateral transport is the use of patterned grooves on the wall surface of the channel [15]. It was schematically shown in the experimental study of Stroock et al. [16] that by placing straight grooves on the floor, a secondary flow is formed in transversal planes and the flow streamlines in the channel become helical. Similar transversal flows were also observed by Johnson et al. [17]. Instead of straight grooves, patterned grooves with herringbone structure result in a pair of counter-rotating helical flows. Chaotic advection can be generated by ar-

[1]Corresponding author.

Contributed by the Fluids Engineering Division of ASME for publication in the JOURNAL OF FLUIDS ENGINEERING. Manuscript received May 17, 2007; final manuscript received April 23, 2008; published online June 25, 2008. Assoc. Editor: Rajat Mittal.

ranging the herringbone grooves in a staggered manner: The direction of asymmetry of the herringbones switches with respect to the centerline of the channel from half a cycle to the other half. The results obtained by Stroock et al. [16] revealed that efficient mixing can be achieved for Reynolds numbers from 10^{-2} to 10.

To create corotating transversal flows, Kim et al. [18] placed barriers along the top surface of a channel while the floor was formed from ablated walls. The periodic insertion of the barriers leads to continuous exchange of flow pattern between the single vortex type and the double vortex type.

In the study of Howell et al. [19], two sets of straight grooves and two sets of chevron-shaped grooves appeared on both the top and bottom of the channel. The chevrons on the two walls direct in opposite directions. It was shown that due to the strengthened lateral velocities by the double grooves and the resulted complex vortex flows, the mixing is greatly enhanced.

To look into detailed flow behaviors and evaluate the mixing performance, it is required to visualize the flow field in the microchannel. Computational fluid dynamics is a good approach to fulfill this task and has been employed to examine different channel designs. For quantification of the mixing performance, either the particle tracking method or the transport equation method has been adopted. In the former, a number of particles are introduced into the channel and the positions of all particles are traced by using the Lagrangian approach. Because of the periodic configuration of the microchannel, the recording of the particle tracking can be used to generate the Poincare map to check if chaos occurs [9,20,21]. In the above studies, the particles are released at the inlet plane. By this means, the distribution of particles cannot be controlled; some regions in the outflow plane, especially near the walls, are often poorly covered by the particles seeded at the inflow plane. Mott et al. [22] developed a backtracking method in which the trace particles are introduced from the outlet plane. In this way, a uniform distribution of information across the entire outflow plane is obtained. A drawback of the Lagrangian approach is that the molecular diffusion is not taken into account. As for the other method, the distribution of the mass concentration for the mixed fluids is obtained by solving a transport equation [13,23,24]. This method requires that the grids used for calculation have sufficient resolution and the difference scheme must be of high order accuracy to avoid numerical diffusion. Comparing with the transverse dimension, the length of the channel is so long that most studies restrict their calculations to a short length due to enormous computational cost.

The present work aims at evaluating the mixing performance of different micromixers in full length of the channel. To take advantage of the periodic arrangement of the channel geometry, it is not necessary to solve for the velocity in the entire channel; only a section covering several periodic units is required to represent the velocity field. The transport equation for mass concentration is then solved throughout the full length of the channel by repeatedly making use of the periodic velocity field. This approach is applied to two types of micromixers (see Fig. 1). One is that with patterned grooves, including straight grooves and herringbone grooves, and in the other type the channel is partially obstructed by block obstacles. The use of block to disturb flow field is common in large-scale mixers and heat exchangers, but hardly found in micromixers.

2 Numerical Method

The flow field in the microchannels can be considered as steady and incompressible. The fluid density ρ, viscosity μ, and mass diffusivity D are assumed to be uniformly distributed, regardless of the different fluids used for mixing. The governing equations for mass, momentum, and concentration can be expressed as

$$\nabla \cdot \mathbf{V} = 0 \tag{1}$$

$$\nabla \cdot (\mathbf{V} \otimes \mathbf{V}) = -\nabla P + \frac{1}{\mathrm{Re}}\nabla^2 \mathbf{V} \tag{2}$$

$$\nabla \cdot (\mathbf{V}C) = \frac{1}{\mathrm{Pe}}\nabla^2 C \tag{3}$$

where $\mathbf{V}$ is the velocity vector and C the mass concentration. The above equations have been nondimensionalized using the mean velocity $\bar{U}$ and the channel height h as reference scales. The Reynolds number is defined by $\rho\bar{U}h/\mu$ and the Peclet number by $\bar{U}h/D$. The Peclet number and the Reynolds number are related by Pe=ReSc. Here, Sc is the Schmidt number defined by Sc $=\nu/D$, where ν is the kinematic viscosity.

To cope with the irregular geometry of the considered micromixers, a fully conservative finite volume method suitable for unstructured grid computation is utilized. The equations, being of divergence form as given in the above, are integrated over a control volume, which, in general, can be a polyhedron with arbitrary topology. With the use of the divergence theorem, the volume integrals of the convective and diffusive transports are transformed into surface integrals. The convective flux through the surface of the control volume is approximated by the second-order, nondiffusive central difference scheme. The use of central differencing is essential to the mixing computation because a scheme such as the upwind differencing possesses an inherent character of numerical diffusion. The numerical diffusion may overshadow physical diffusion during flow mixing. However, it is known that the central difference may result in oscillations in the solution. This causes serious problems in concentration calculation because it may exceed the limiting values of 0 and 1. Therefore, in the approximation of the convective flux for the concentration, we employ a blending strategy by which a weighting of 0.9 is assigned to the central difference and a weighting of 0.1 to the upwind difference. The diffusive flux is approximated by an over-relaxed approach [25,26]. This approach is applicable to a mesh with arbitrary shape and degenerates into the central difference form when the mesh is rectangular.

The governing equations are solved in a segregated manner. The nonlinearity of the equations and the coupling between them are treated in an iterative way. The momentum equation is solved first. The resulting velocities require adjustment and the pressure must be upgraded such that the mass is conserved. The enforcement of the continuity constraint brings about a pressure-correction equation. The pressure correction obtained by solving this equation is then used to correct the prevailing velocity and pressure fields. The same procedure is carried out repeatedly until convergence is achieved. After the velocity field is finalized, the distribution of fluid concentration is then sought by solving the corresponding transport equation. More details about the discretization and the solution method can be found in the studies of Tsui and Pan [25] and Tsui and Jung [26].

The heights of the microchannels are usually characterized by a dimension in the order of 100 μm, while the lengths are in the range of 3–5 cm. As a three-dimensional grid is constructed to cover these relatively long channels, millions of control volumes are required. This is an enormous burden to the computer resource.

As seen form Fig. 1, the grooves or obstacles appear periodically in the channel. To take advantage of the periodically varying geometry, the flow only in a periodic module is needed as the flow becomes fully developed. For periodic calculations, the same velocities must be imposed at the corresponding periodic boundaries. Particularly, a special treatment of the pressure field must be undertaken. It was first proposed by Patankar et al. [27] to decompose the pressure gradient into a periodic part and a linearly varying part. For a duct flow with a given mass flow rate, the linearly varying part of pressure gradient must be determined in an iterative manner [27–29]. Therefore, this procedure is time consuming

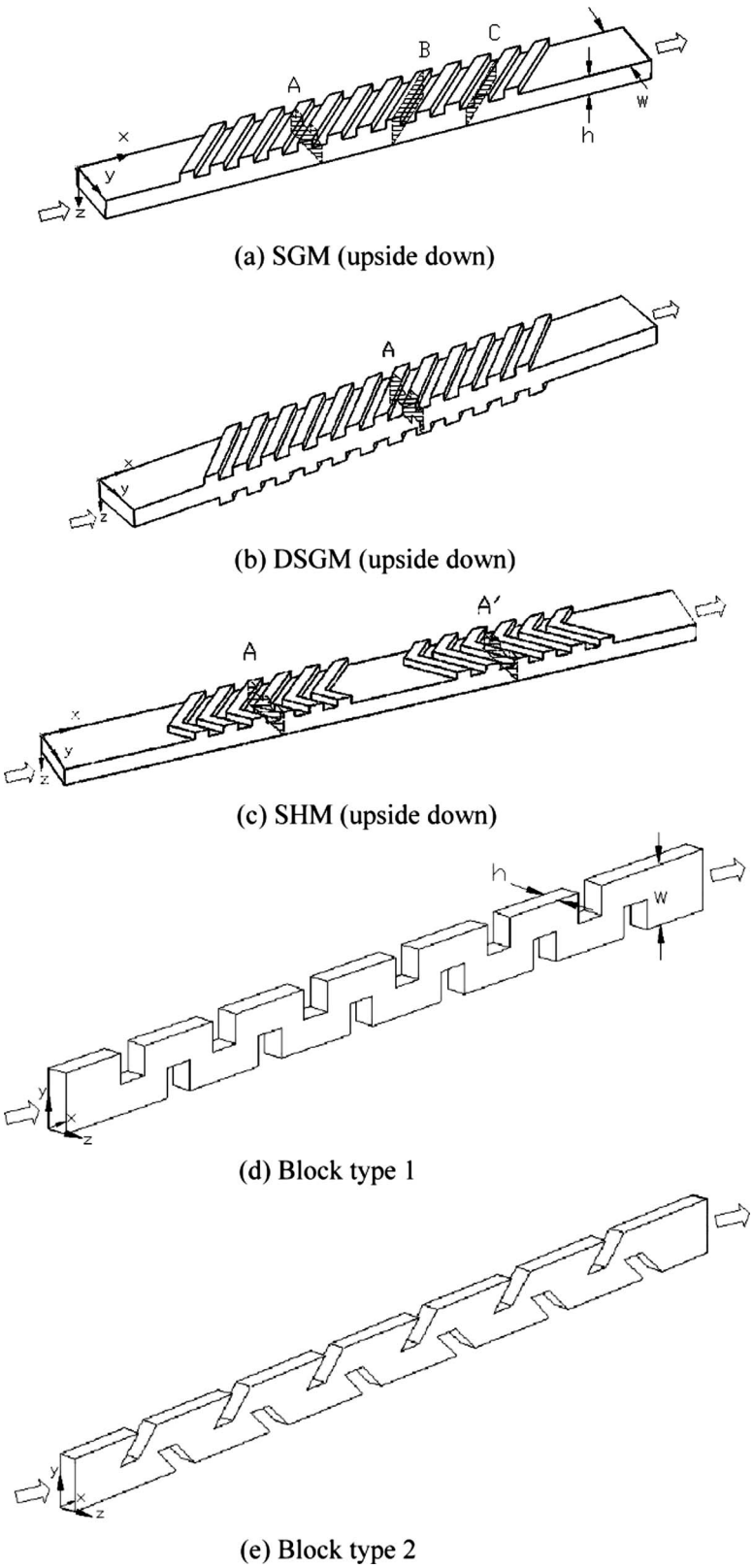

Fig. 1 Schematic drawings of the considered micromixers: (*a*) SGM, (*b*) DSGM, (*c*) SHM, (*d*) Block Type 1, and (*e*) Block Type 2

and modification on the existing computer code is required. In the present study, a simple procedure is used without bother of periodicity conditions. As an illustration, in calculating the velocity field for the straight groove micromixer (SGM), the computational domain comprises 12 grooves together with an entrance section at the beginning and an outflow section at the end (see Fig. 1(*a*)). In the simulation, a uniform velocity profile is prescribed at the inlet and the zero-gradient condition is imposed at the outlet. The re-

Table 1 Grid sizes for the meshes considered in the refinement tests for the SGM

	Cell number	Main passage	Groove
Mesh A	42,000	$\Delta x=\Delta y=\Delta z=0.1$	$\Delta x=\Delta y=\Delta z=0.1$
Mesh B	147,840	$\Delta x=\Delta y=\Delta z=0.07$	$\Delta x=\Delta y=0.07$ $\Delta z=0.03$
Mesh C	235,008	$\Delta x=\Delta y=\Delta z=0.06$	$\Delta x=\Delta y=0.06$ $\Delta z=0.026$
Mesh D	303,264	$\Delta x=\Delta y=\Delta z=0.055$	$\Delta x=\Delta y=0.055$ $\Delta z=0.024$

Table 2 Grid sizes for the meshes considered in the refinement tests for the SHM

	Cell number	Main passage	Groove
Mesh A	101,700	$\Delta x=\Delta y=\Delta z=0.1$	$\Delta x=\Delta y=\Delta z=0.1$
Mesh B	219,528	$\Delta x=\Delta y=\Delta z=0.08$	$\Delta x=\Delta y=0.08$ $\Delta z=0.04$
Mesh C	283,842	$\Delta x=\Delta y=\Delta z=0.07$	$\Delta x=\Delta y=0.07$ $\Delta z=0.036$
Mesh D	340,830	$\Delta x=\Delta y=\Delta z=0.06$	$\Delta x=\Delta y=0.06$ $\Delta z=0.03$

sulting velocity field in the grooved section becomes periodic and fully developed quickly. In order to get rid of the effects of the inlet and outlet, a section of seven grooves in the middle region is taken as a periodically repeating mixing cycle. The concentration field is then solved for by using the cyclic velocity field repeatedly until the required channel length is reached. As for the herringbone micromixer, 3 cycles of groove (each cycle comprises 12 grooves, as seen in Fig. 1(*b*)) are included in the velocity calculation and the velocity field in the second cycle is then used to compute mass mixing.

3 Results and Discussion

The simulated channels have a cross section with a height $h=70$ μm and a width $w=200$ μm ($w/h=2.86$). The total length of the channels is 3 cm ($l/h=428.6$). The width is the length scale in the y-direction and the height that in the z-direction. The x-, y- and z-axes are in the streamwise, spanwise, and cross stream (vertical) directions, respectively, which are defined in Fig. 1 for each type of microchannel considered. The Schmidt number used in the simulations is fixed at a value of 2×10^5. Thus, for a case with $\mathrm{Pe}=2\times10^5$, the Reynolds number is 1, while for $\mathrm{Pe}=2\times10^3$, the corresponding Reynolds number is 0.01.

The mixing performance is represented by the mixing index defined as

$$\sigma=\sqrt{\frac{1}{A}\sum_i (C_i-\bar{C})^2 A_i} \tag{4}$$

where C_i is the concentration at a computational cell with a cross-sectional area A_i, $\bar{C}$ an average of the concentration over the two fluids (=0.5 for the present study), and A the cross-sectional area of the channel. The summation is taken over all the cells in the cross section. The mixing index is 0.5 for completely segregated fluids and 0 for fully mixed fluids.

Grooved Micromixers. In order to validate the methodology described above, computations have been conducted to simulate the flows in a SGM and a staggered herringbone micromixer (SHM). The geometric configurations of the channels are taken from the study of Stroock et al. [16] Grid refinement tests were carried out to ensure the obtained solution being grid independent. Four different meshes, ranging from 96,900 cells to 621,108 cells for the SGM and from 319,200 cells to 1,053,360 cells for the SHM, were adopted in the tests. It is noteworthy that, as described previously, only a section in the middle is considered as a periodic cycle for concentration calculation. The numbers of cells for the meshes in 1 cycle are in the range of 42,000–303,264 for the SGM and in the range 101,700–340,830 for the SHM. The corresponding grid size is 0.1 h for the coarsest grid and about 0.024–0.06 h for the finest grid. The grid sizes for the different levels of mesh are given in Tables 1 and 2 for the SGM and SHM, respectively. Typical grid layouts used for the two types of mixer are shown in Fig. 2. Comparison with the experimental data of Stroock et al. for the flow with $\mathrm{Pe}=2\times10^5$, as shown in Fig. 3, indicates close resemblance between the two results. It can be seen that with the use of coarse meshes, the mixing rate is faster than that for the finer meshes and deviates more from the measurements. This result is not unexpected, based on the understanding that numerical diffusion is proportional to the grid size.

The groove-induced secondary velocity is usually weak, but is important to the mixing performance. Figure 4 presents the secondary flows in a cross section for the SGM and SHM. Also included is that for a double straight groove micromixer (DSGM) in which the grooves appear on both the bottom wall and the top wall in a staggered way to each other (see Fig. 1(*b*)). In the grooves, the flow field is characterized by a lateral flow from the right to the left in Fig. 4(*a*) for the SGM. More important is that there exists a transversal velocity flowing in the opposite direction

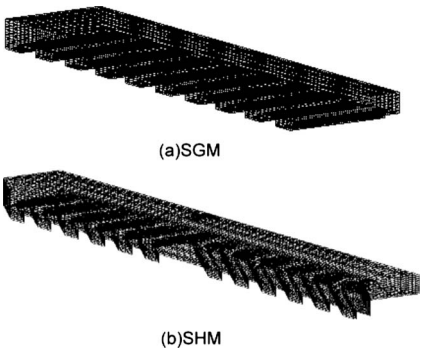

Fig. 2 Typical grid layouts used for (*a*) SGM and (*b*) SHM

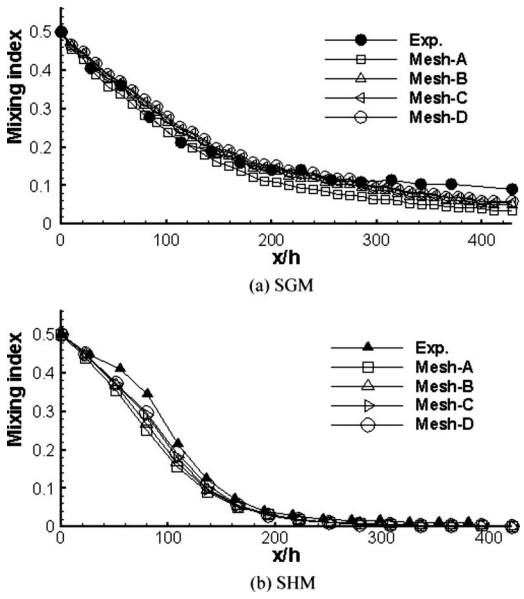

Fig. 3 Comparison of the predicted mixing indices with experiments using different meshes for (*a*) SGM and (*b*) SHM

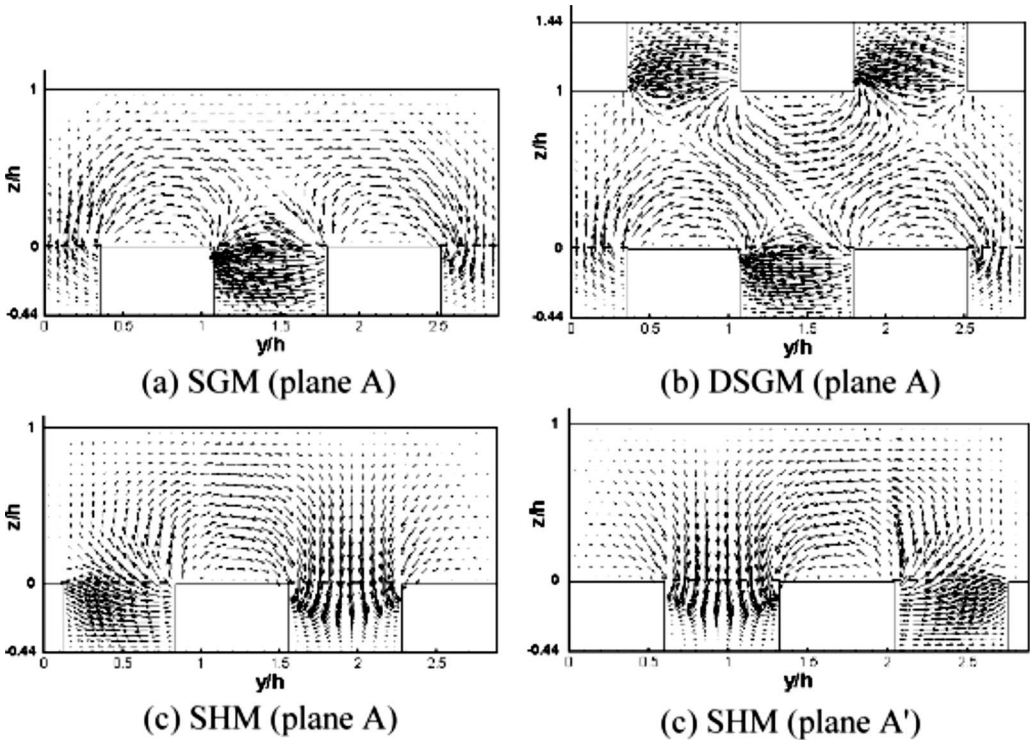

Fig. 4 Secondary velocity fields in cross sections for (*a*) SGM, (*b*) DSGM, and (*c*) SHM. The Planes A and A′ are referred to Fig. 1.

above the ridges. It is this secondary velocity resulting in helical streamlines in the channel [16]. It is evidenced from Fig. 5(*a*) that the two fluids, represented by two colors in blue and red, rotate in a clockwise sense during mixing evolution due to the transport by the helical flow. While the interface between the two fluids is twisted and, thus, elongated by the rotating flow, the sharp gradient in the interface is gradually smeared out by the molecular diffusion. To look into the mechanism causing the secondary flow, the projection of the velocity field onto the midplanes of a groove and a ridge (Planes B and C in Fig. 1) is given in Fig. 6. It appears that the flow in the floor region in Plane B is directed by the groove, followed by a returning flow along the top wall to form a perfect vortex flow rotating in the clockwise direction. The returning flow prevails in Plane C, which is located in the main passage of the channel.

For the DSGM, the staggered arrangement of the grooves on both walls induces a stronger secondary velocity in the channel core than that for the SGM, as shown in Fig. 4(*b*). The flow

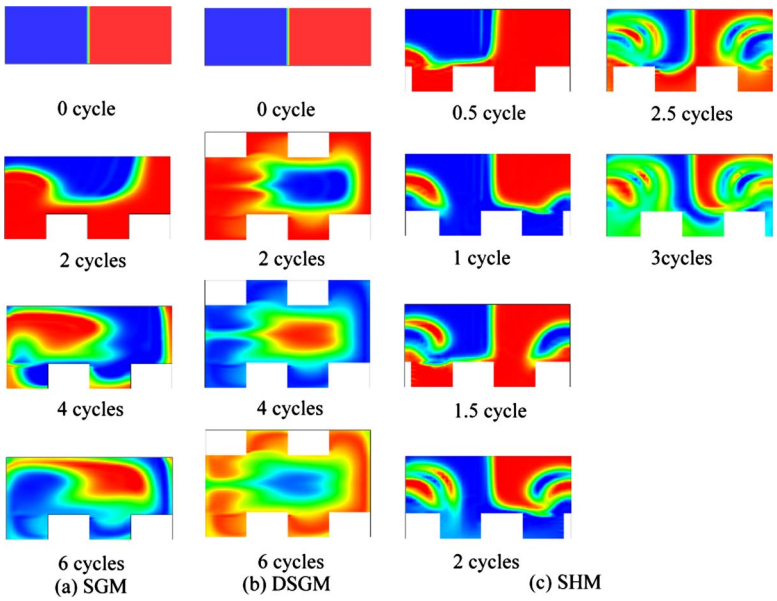

Fig. 5 Visualization of the concentration distribution in the *y-z* plane at different cycles for (*a*) SGM, (*b*) DSGM, and (*c*) SHM. Note that the length of a cycle for a SHM is longer than that for the SGM and DSGM.

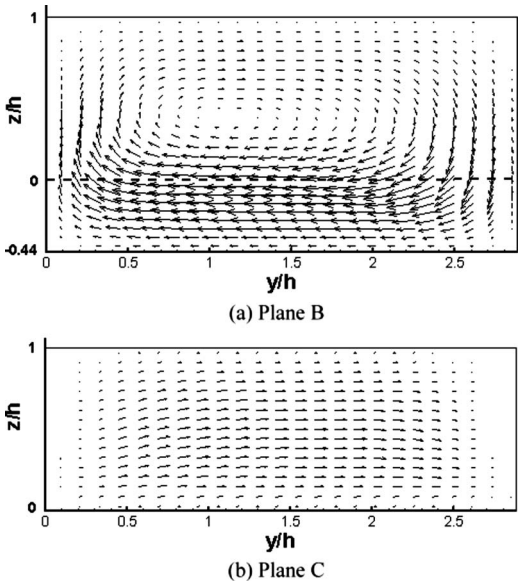

Fig. 6 Secondary velocity vectors in Planes B and C for the SGM. Plane B is a transversal plane in the middle of a groove and Plane C is located in the middle of a ridge. The locations of the planes are referred to Fig. 1. These planes are projected onto the *y-z* plane

rotates around both the upper and the lower ridges. The concentration plots given in Fig. 5(*b*) illustrate that in the beginning the fluid in blue is transported from the left to the right in the core region, while that in red fills up the grooves. It is followed by quick exchanges of the relative positions of the two fluids in the latter stage due to the secondary flow transportation. As a result, the mixing performance is enhanced when comparing with the SGM.

In the SHM, the asymmetry of the herringbone grooves with respect to the centerline brings about two circulating flows in different sizes, rotating in opposite directions. It is evident in Fig. 4(*c*) (Plane A) that the two flows merge at about $y/h=1.92$, which is the bending location of the herringbone grooves. In the second half of the cycle, the bending location together with the merging line shifts to $y/h=0.96$ (Plane A′) and the velocity field in the corresponding cross section changes accordingly to mirror the flow in the first half cycle. The mixing process is illustrated in Fig. 5(*c*) by presenting the concentration field every half a cycle until 3 cycles are completed. It is worthwhile to note that the mixing patterns shown have a strong resemblance to the fluorescent confocal micrographs of Stroock et al. [16]. The exchange of the two circulation patterns in each cycle causes the position change of the two fluids from one side of the cross section to the other side. After each exchange, part of one fluid is left to form an island being surrounded by the other fluid. The effects of this process can be more clearly identified by viewing the transversal plane at mid height of the channel. As seen in Fig. 7, the SHM functions like a lamination mixer [30,31], which constantly separates the flow into partial streams to form more and more laminae. Different from lamination mixers, the stratification of fluid is generated by the exchange of the circulation patterns in the SHM.

The mixing index shown in Fig. 8 implies that the SGM is a rather poor mixer. It could be seen from the Poincare map [20,21] that the flow behavior in the SGM is not really chaotic. The performance of this type of micromixer can be improved by using double grooves, as shown in the figure for the DSGM. Chaotic advection occurs in the SHM and its superiority is reflected in the plot.

The flow in the grooved microchannel and its performance depend strongly on the geometry of the groove. In the following, the

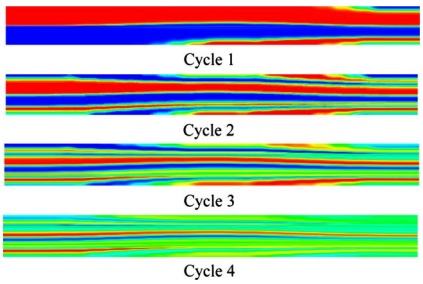

Fig. 7 Concentration filed in the *x-y* plane at mid height of the channel for the SHM

effects of the parameters such as the groove depth G_d, the groove width G_w, and the oblique angle of the groove α are examined for the SGM. The reference case has a groove depth of $0.44h$, a groove width of $0.72h$, and a groove angle of 45 deg. Totally, there are three kinds of depth ($G_d=0.2h$, $0.44h$, and $0.86h$) and three kinds of width ($G_w=0.36h$, $0.72h$, and $1.44h$) under consideration. Figures 9(*a*) and 9(*b*) reveal that the performance is enhanced with increasing values of groove depth and groove width. However, it does not mean that both can be enlarged without limits. There exist optimum values to maximize the mixing rate. This point can be demonstrated in Fig. 9(*c*). The mixing is enhanced by increasing the oblique angle from 30 deg through 45–60 deg. It is followed by a quick decline in performance when the angle is further increased to 75 deg. The improvement of the mixing is ascribed to the strengthening of the secondary flow. For demonstration, the transversal velocity along the channel height in the center of Planes B and C is presented in Fig. 10. It can be identified that a much stronger vortex flow is seen in the Groove Plane B for the oblique angles 45 deg and 60 deg. In the Ridge Plane C, the case with $\alpha=60$ deg has the greatest transversal velocity, which, in turn, leads to the fastest mixing.

Obstructed Micromixers. Another means to induce transversal flow is the use of obstacles to partly obstruct the microchannel. In grooved mixers, the grooves are carved on the bottom and/or top walls of the channel. Thus, the height of the channel is enlarged in the groove region. For obstructed mixers, block obstacles are inserted into the channel such that the width of the channel passage is reduced. Wang et al. [32] used a 2D numerical method to investigate the micromixer with cylindrical blocks placed in the channel. It was found that the asymmetric layouts of the obstacle are favored rather than the symmetric arrangements. The calculations of Wang et al. [33] showed that the mixing in a straight channel can be greatly enhanced by incorporating rectangular blocks within the micromixer. Bhagat et al. [34] examined the design of diamond-shaped blocks within a micromixer experimentally. They also reported simulated results for the flows with circular-shaped, triangular-shaped, diamond-shaped, and stepped-diamond-shaped blocks. Among them, the stepped-diamond-

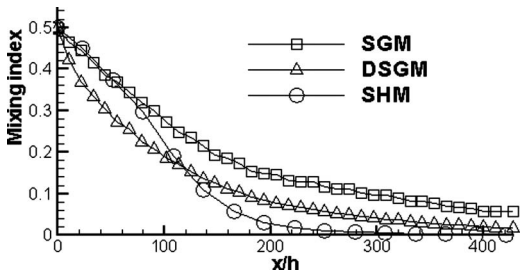

Fig. 8 Comparison of mixing performance for the SGM, DSGM, and SHM

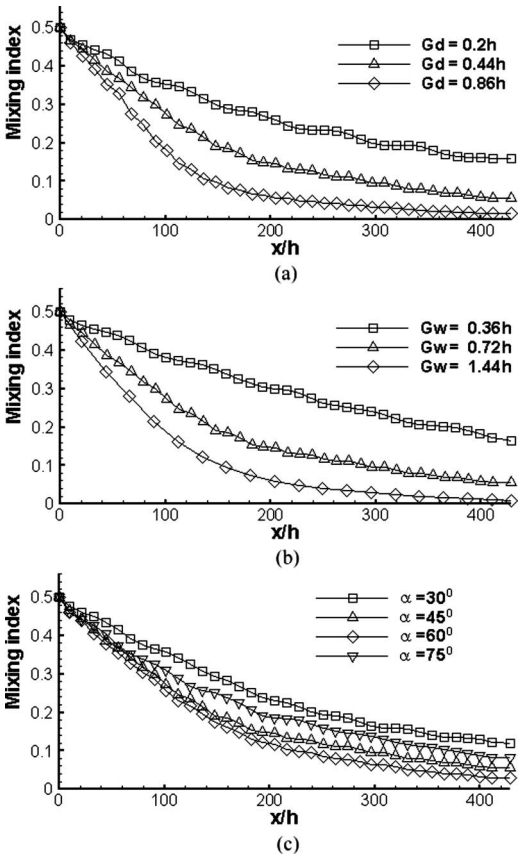

Fig. 9 Comparison of mixing performance for (*a*) different groove depths, (*b*) different groove widths, and (*c*) different oblique angles for the SGM

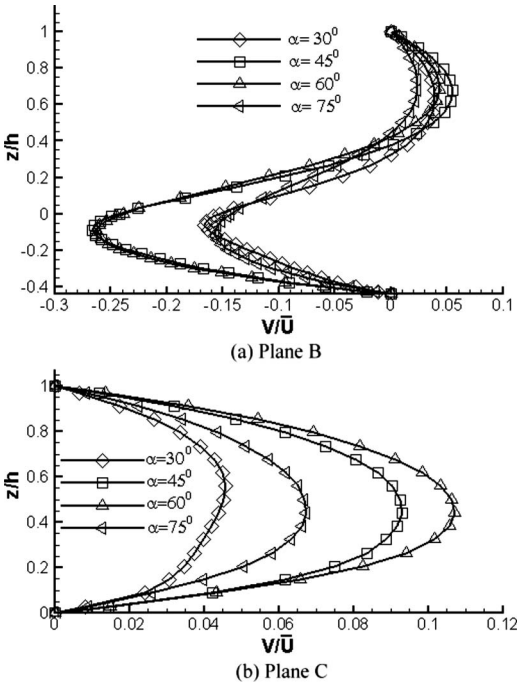

Fig. 10 Comparison of the transversal velocity along the vertical line in the center of Plane B and Plane C for different oblique angles. This transversal velocity is the component in the groove direction and is normalized by the inlet velocity $\bar{U}$.

shaped obstructions yield the best mixing.

In the above studies, the obstacles are placed in the core of the channel, away from the walls. An alternative way is to have obstacles intruding from the walls. In the following, we consider the micromixers with blocks being placed on the two side walls, arranged in a staggered manner, as shown in Figs. 1(*d*) and 1(*e*). The channel geometry of Fig. 1(*d*) is similar to the square-wave channel considered by Liu et al. [14]. The difference lies in the entrance and the outlet sections, which are of the same dimension as the wavy passage in the square-wave channel. In Fig. 1(*e*), the blocks are skew to the sidewalls, similar to the sawtooth structure investigated by Nichols et al. [35]. However, the sawtooth structure appeared only on one sidewall in their study. There are four types of arrangement in the present study (see Fig. 11). Types 1 and 3 are of rectangular type and the blocks of Types 2 and 4 are skew type with an oblique angle 45 deg to the walls. The block widths for Types 3 and 4 are half of those for Types 1 and 2 and the spaces between blocks are also reduced. The resulted mixing indices for Peclet numbers 2×10^5 and 2×10^3 are presented in Fig. 12. The results for the SGM and SHM are also included in the plots for comparison. For $\mathrm{Pe}=2\times10^5$, the performance of the block Type 1 is rather poor, being even worse than the SGM. The situation is much more improved in Type 2. The mixing performance is further enhanced by Types 3 and 4. Comparing with Type 3, Type 4 mixes the fluids a little faster in the initial stage. However, its mixing efficiency becomes slower for $x>0.5$ cm. As the Peclet number is reduced to 2×10^3 by decreasing the Reynolds number from 1 to 10^{-2}, the mixing rates for Types 1 and 3 are very similar to those for Types 2 and 4, respectively. It is of interest to note that at this extremely low Reynolds number even Types 1 and 2 perform better than the SHM.

The flow structure is illustrated in Fig. 13 for Types 1 and 2. Owing to the low velocity, flow separations are not detected at the sharp turnings and the corners formed by the blocks and the walls. It is noted that the two transversal passages in one period are not of the same width in the Type 2 channel. The narrower one has a width $w/2$, which is identical to that of the Type 1. However, the 45 deg oblique angle of Type 2 block results in higher flow velocity than Type 1. This explains the observation of higher mixing performance for the Type 2 at $\mathrm{Pe}=2\times10^5$. This advantage is lost when the importance of diffusion transport in the mixing process becomes more apparent as the Peclet number is reduced to 2×10^3. The evolution of the fluid mixing is illustrated in Fig. 14 for the four channel types. These obstructed channel flows are in essence two dimensional and, thus, nonchaotic because the vertical velocity component in the direction of the height is negligible. However, the great transversal velocity induced by the narrow passages in Types 3 and 4 leads to fast flow mixing. It may be claimed that the elongated passage length plays a more important role than the increased transversal velocity in the improvement of the mixing. In fact, the residence time of the fluid in these channels is not increased because the flow velocity is also greatly enlarged.

In the following, we compare the head losses for the considered micromixers. The variation of the mean pressure averaged over the cross section along the channel is shown in Fig. 15. The pressure shown is nondimensionalized by $\rho\bar{U}^2$. It is evident that in the macroscopic view, the pressure drops in a linear fashion along the channel. Note that there is a short intake duct at the inlet and an outlet duct at the exit, resulting in a piecewise linear variation of the curves. The grooved channels have almost the same pressure loss. The pressure gradients for SGM, SHM, and DSHM are −14.48, −14.35, and −13.65, respectively, for $\mathrm{Re}=1$ ($\mathrm{Pe}=2\times10^5$). The head loss is smaller for the DSHM because of the enlarged space by the double grooves. When the Reynolds number is reduced to 0.01 ($\mathrm{Pe}=2\times10^3$), the corresponding pressure gradients are increased by almost two orders. This result simply reflects the fact that the dimensionless head loss is inversely pro-

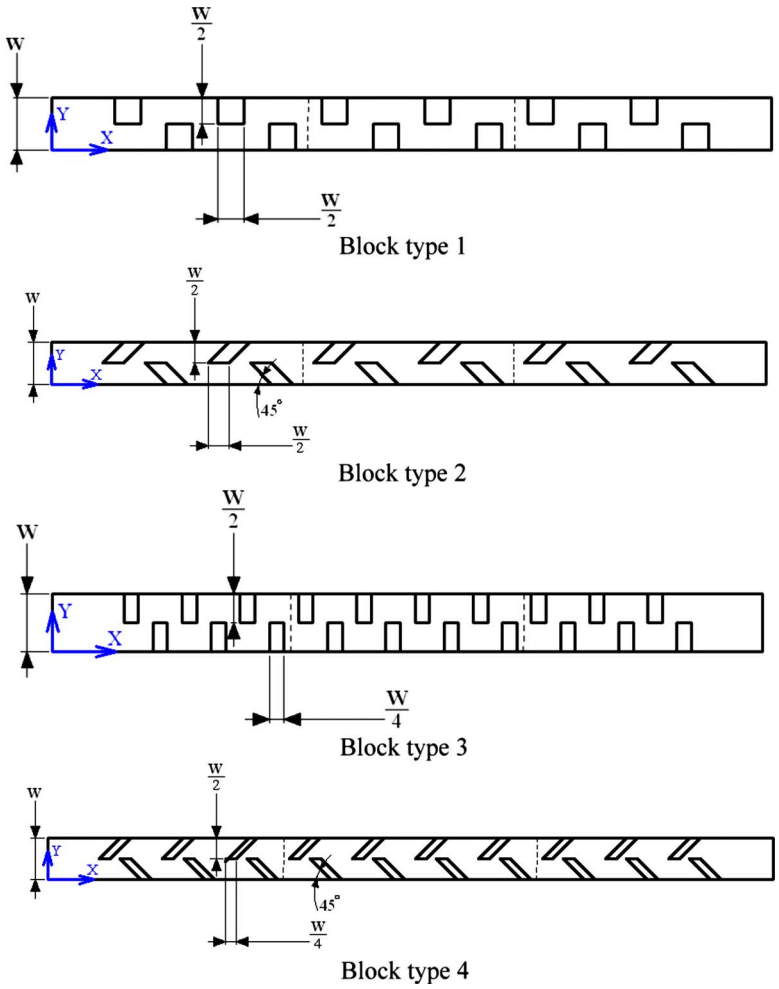

Fig. 11 Four types of block obstacles used in the obstructed microchannels

portional to the Reynolds number ($\Delta P/\rho \bar{U}^2 \sim 1/\mathrm{Re}$), which is expected in fully developed laminar flow. It can be identified from the figure that the blockage of the channel causes a large head loss. The slopes of the curves for Types 1–4 are −43.5, −41.1, −98.6, −90.5, respectively, which are about three to seven times as large as those for the grooved channels. It is interesting to note that the losses for Types 2 and 4 are slightly less than those for Types 1 and 3, respectively. This is attributed to that in a repeating period the second transversal passage between the blocks is much wider than the first one, which brings about a lower flow velocity and, thus, makes a pressure recovery.

4 Conclusions

A computational methodology has been developed to investigate the fluid mixing in microchannels. To make use of the periodic flow behavior, the calculation of velocity field is undertaken only in a part of the channel. With this cyclic velocity field, the evolution of the flow mixing throughout the channel can be monitored. Several mircomixers with either grooved channels or partially obstructed channels have been examined. Main findings are summarized in the following.

(1) For the microchannel with straight grooves (SGM), a well organized secondary vortex is induced in the groove plane. As a result, the flow in the channel features helical streamlines. Due to the helical flow, the interface between the fluids is distorted.
(2) By having grooves on both the top and the bottom walls,

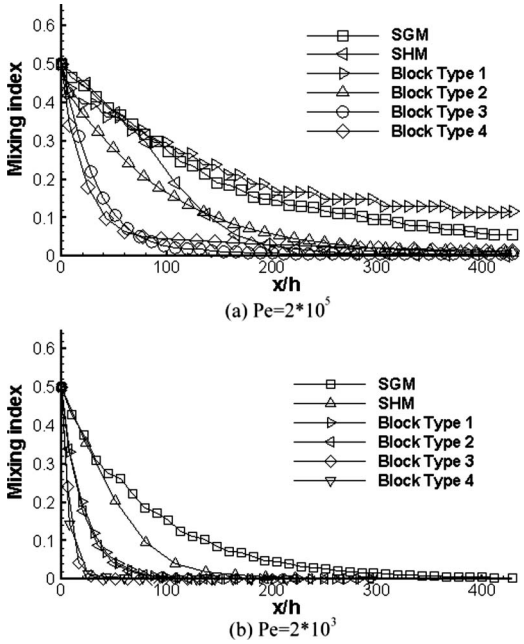

Fig. 12 Comparison of mixing performance for different block types: (*a*) Pe=2×10^5 and (*b*) Pe=2×10^3

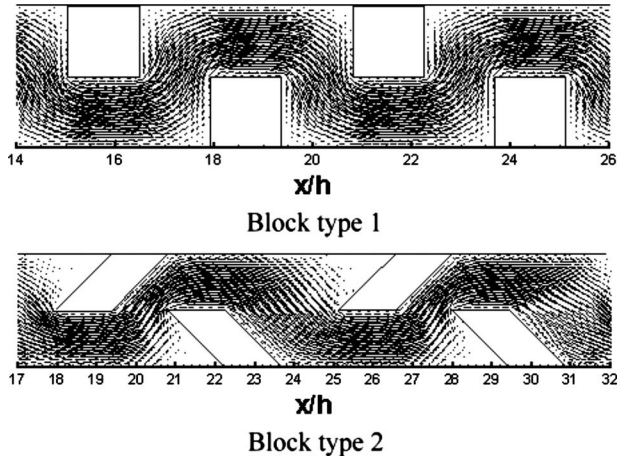

Fig. 13 Velocity field in the *x-y* plane at mid height of the channel for Block Types 1 and 2 at Pe=2×10^5

arranged in a staggered manner, the helical flow is greatly strengthened, leading to enhancement of the flow mixing.

(3) For the staggered herringbone microchannel, a pair of countervortices is created. The position exchange of the vortices results in stratification of the fluids. Consequently, a number of laminae are formed in the channel.

(4) The performance of the grooved micromixers can be improved by optimizing the geometric configuration of the groove. It was demonstrated for the SGM that with larger groove depths, groove widths, or oblique angles, the mixing is enhanced.

(5) The channel flows obstructed by blocks are indeed two dimensional. However, very strong transversal velocities can be produced via controlling the passage between the blocks to yield high mixing performance. However, this achievement is accompanied with a large pressure head loss.

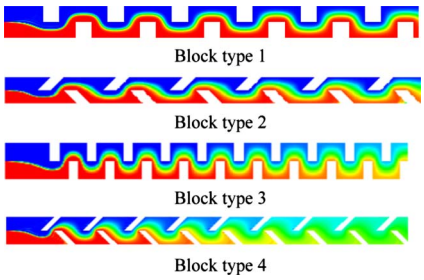

Fig. 14 Concentration field in the *x-y* plane at mid height of the channel for the four block types

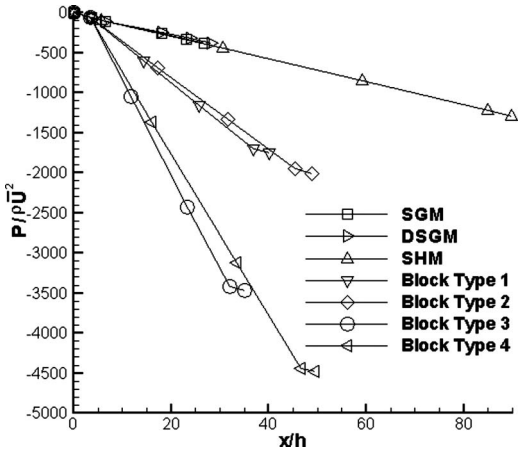

Fig. 15 Dimensionless pressure loss along the channel for all considered micromixers at Re=1 (Pe=2×10^5)

References

[1] Jacobson, S. C., McKnight, T. E., and Ramsey, J. M., 1999, "Microfluidic Devices for Electrokinetically Driven Parallel and Serial Mixing," Anal. Chem., **71**, pp. 4455–4459.

[2] Oddy, M. H., Santiago, J. G., and Mikkelsen, J. C., 2001, "Electrokinetic Instability Micromixing," Anal. Chem., **73**, pp. 5822–5832.

[3] Zhu, X., and Kim, E. S., 1998, "Microfluidic Motion Generation With Acoustic Waves," Sens. Actuators, A, **66**, pp. 355–360.

[4] Yang, Z., Matsumoto, S., Goto, H., Matsumoto, M., and Maeda, R., 2001, "Ultrasonic Micromixer for Microfluidic Systems," Sens. Actuators, A, **93**, pp. 266–272.

[5] Mao, H., Yang, T., and Cremer, P. S., 2002, "A Microfluidic Device with a Linear Temperature Gradient for Parallel and Combinatorial Measurements," J. Am. Chem. Soc., **124**(16), pp. 4432–4435.

[6] Tsai, J.-H., and Lin, L., 2002, "Active Microfluidic Mixer and Gas Bubble Filter Driven by Thermal Bubble Micropump," Sens. Actuators, A, **97–98**, pp. 665–671.

[7] Fujii, T., Sando, Y., Higashino, K., and Fujii, Y., 2003, "A Plug and Play Microfluidic Device," Lab Chip, **3**, pp. 193–197.

[8] Glasgow, I., and Aubry, N., 2003, "Enhancement of Microfluidic Mixing Using Time Pulsing," Lab Chip, **3**, pp. 114–120.

[9] Niu, X., and Lee, Y.-K., 2003, "Efficient Spatial-Temporal Chaotic Mixing in Microchannels," J. Micromech. Microeng., **13**, pp. 454–462.

[10] Ottino, J. M., 1989, *The Kinematics of Mixing: Stretching, Chaos, and Transport*, Cambridge University Press, Cambridge.

[11] Aref, H., 1984, "Stirring by Chaotic Advection," J. Fluid Mech., **143**, pp. 1–21.

[12] Aref, H., 2002, "The Development of Chaotic Advection," Phys. Fluids, **14**, pp. 1315–1325.

[13] Mengeaud, V., Josserand, J., and Girault, H. H., 2002, "Mixing Processes in a Zigzag Microchannel: Finite Element Simulation and Optical Study," Anal. Chem., **74**, pp. 4279–4286.

[14] Liu, R. H., Stremler, M. A., Sharp, K. V., Olsen, M. G., Santiago, J. G., Adrian, R. J., Aref, H., and Beebe, D. J., 2000, "Passive Mixing in a Three-Dimensional Serpentine Microchannel," J. Microelectromech. Syst., **9**, pp. 190–197.

[15] Stroock, A. D., Dertinger, S. K., Whitesides, G. M., and Ajdari, A., 2002, "Patterning Flows Using Grooved Surfaces," Anal. Chem., **74**, pp. 5306–5312.

[16] Stroock, A. D., Dertinger, S. K. W., Ajdarim, A., Mezic, I., Stone, H. A., and Whitesides, G. M., 2002, "Chaotic Mixer for Microchannels," Science, **295**, pp. 647–651.

[17] Johnson, T. J., Ross, D., and Locascio, L. E., 2002, "Rapid Microfluidic Mixing," Anal. Chem., **74**, pp. 45–51.

[18] Kim, D. S., Lee, S. W., Kwon, T. H., and Lee, S. S., 2004, "A Barrier Embedded Chaotic Micromixer," J. Micromech. Microeng., **14**, pp. 798–805.

[19] Howell, Jr., P. B., Mott, D. R., Fertig, S., Kaplan, C. R., Golden, J. P., Oran, E. S., and Ligler, F. S., 2005, "A Microfluidic Mixer with Grooves Placed on the Top and Bottom of the Channel," Lab Chip, **5**, pp. 524–530.

[20] Wang, H., Iovenitti, P., Harvey, E., and Masood, S., 2003, "Numerical Investigation of Mixing in Microchannels with Patterned Grooves," J. Micromech. Microeng., **13**, pp. 801–808.

[21] Kang, T. G., and Kwon, T. H., 2004, "Colored Particle Tracking Method for Mixing Analysis of Chaotic Micromixers," J. Micromech. Microeng., **14**, pp. 891–899.

[22] Mott, D. R., Howell, Jr., P. B., Golden, J. P., Kaplan, C. R., Ligler, F. S., and Oran, E. S., 2006, "A Lagrangian Advection Routine Applied to Microfluidic Component Design," *44th AIAA Aerospace Sciences Meeting and Exhibit*, AIAA Paper No. 2006-1086.

[23] Schonfeld, F., and Hardt, S., 2004, "Simulation of Helical Flows in Microchannels," AIChE J., **50**(4), pp. 771–778.

[24] Liu, Y. Z., Kim, B. J., and Sung, H. J., 2004, "Two-Fluid Mixing in a Microchannel," Int. J. Heat Fluid Flow, **25**, pp. 986–995.

[25] Tsui, Y.-Y., and Pan, Y.-F., 2006, "A Pressure-Correction Method for Incompressible Flows Using Unstructured Meshes," Numer. Heat Transfer, Part B, **49**, pp. 43–65.

[26] Tsui, Y.-Y., and Jung, S.-P., 2006, "Analysis of the Flow in Grooved Pumps with Specified Pressure Boundary Conditions," Vacuum, **81**, pp. 401–410.

[27] Patankar, S. V., Liu, C. H., and Sparrow, E. M., 1977, "Fully Developed Flow and Heat Transfer in Ducts Having Streamwise-Periodic Variations of Cross-Sectional Area," ASME J. Heat Transfer, **99**, pp. 180–186.

[28] Kelkar, K. M., and Patankar, S. V., 1987, "Numerical Prediction of Flow and Heat Transfer in a Parallel Plate Channel with Staggered Fins," ASME J. Heat Transfer, **109**, pp. 25–30.

[29] Murthy, J. Y., and Mathur, S., 1997, "Periodic Flow and Heat Transfer Using Unstructured Meshes," Int. J. Numer. Methods Fluids, **25**, pp. 659–677.

[30] Branebjerg, J., Gravesen, P., Krog, J. P., and Nielsen, C. R., 1996, "Fast Mixing by Lamination," *Proceedings of Ninth IEEE Int. Workshop on Micro Electro Mechanical Systems (MEMS'96)*, San Diego, CA, pp 441–446.

[31] Schonfeld, F., Hessel, V., and Hofmann, C., 2004, "An Optimized Split-and-

Recombine Micro-Mixer with Uniform 'Chaotic' Mixing," Lab Chip, **4**, pp. 65–69.
[32] Wang, H., Iovenitti, P., Harvey, E., and Masood, S., 2002, "Optimizing Layout of Obstacles for Enhanced Mixing in Microchannels," Smart Mater. Struct., **11**, pp. 662–667.
[33] Wang, R., Lin, J., and Li, H., 2007, "Chaotic Mixing on a Micromixer with Barriers Embedded," Chaos, Solitons Fractals, **33**, pp. 1362–1366.
[34] Bhagat, A. A. S., Peterson, E. T. K., and Papautsky, I., 2007, "A Passive Planar Micromixer with Obstructions for Mixing at Low Reynolds Numbers," J. Micromech. Microeng., **17**, pp. 1017–1024.
[35] Nichols, K. P., Ferullo, J. R., and Baeumner, A. J., 2006, "Recirculating, Passive Micromixer with a Novel Sawtooth Structure," Lab Chip, **6**, pp. 242–246.

Analytic and Experimental Investigation of Dihedral Configurations of Three-Winglet Planforms

David S. Miklosovic
MS
Assistant Professor
Mem. AIAA
Aerospace Engineering Department,
United States Naval Academy,
590 Holloway Road,
MS 11-B,
Annapolis, MD 21402-5042

An analytic and experimental effort was undertaken to assess the effectiveness and efficiency of three winglets mounted chordwise to the tip of a rectangular wing. The winglets, with an aspect ratio of 4.6, were mounted on a half-span wing having an effective aspect ratio of 6.29. 13 configurations of varying dihedral arrangements were analyzed with a vortex lattice method and tested in a low-speed wind tunnel at a Reynolds number of 600,000. While the analytic method provided fair agreement with the experimental results, the predicted trends in lift, drag, and (to a lesser degree) pitching moment were in good agreement. The analytic distributions of wake velocity, circulation, and downwash angle verified that highly nonplanar configurations tended to reduce and diffuse the regions of highest circulation and to create more moderate downwash angles in the wake. This was manifest as an overall drag reduction. More specifically, the results showed that the winglets could be placed in various optimum orientations to increase the lift coefficient as much as 65% at the same angle of attack, decrease the drag coefficient as much as 54% at the same lift coefficient, or improve the maximum L/D by up to 57%. The most dramatic findings from this study show that positioning the winglet dihedral angles had the result of adjusting the magnitude and slope of the pitching moment coefficient. These observations suggest that multiple winglet dihedral variations may be feasible for use as actively controlled surfaces to improve the performance of aircraft at various flight conditions and to "tune" the longitudinal stability characteristics of the configuration.
[DOI: 10.1115/1.2948372]

Keywords: multiple winglets, wind tunnel, vortex lattice, drag reduction

1 Introduction

Winglets have long been recognized for marked reductions in induced drag, which yields improved L/D, extended range, and reduced fuel burn [1–5]. These devices improve performance by altering the spanwise loading of the planform, thus altering the downwash distribution behind the wing and reducing the induced drag. The drag reduction that results from winglets is most commonly attributed to the increase in the effective aspect ratio (AR) of the planform. As such, this effect makes the most impact at high-lift conditions for an aircraft, namely, takeoff, landing, and maneuvering flight.

Winglets have proven effective at other flight conditions as well. Design has typically focused on the so-called "crossover point" on the drag polar, or the point at which the drag benefits overcome the drag penalties of the winglet configuration. While the added length of the winglet contributes to increasing the effective span of the wing (thus reducing lift-induced contributions to drag), the additional area and junction with the wing increase parasite drag through additional friction and interference drag. Thus, a wing will demonstrate an overall drag reduction if it operates below the crossover velocity. Maughmer [6] used two variations of this analysis to specify winglet height and the toe, twist, and cant angles that increased overall sailplane wing performance over much of its operating range. In other tests, the improvement was as much as 10% in glide ratio and sink rate. Some believe that higher performance is possible [7]. Whitcomb's wind tunnel work with winglets on a narrow-body jet transport [5] showed an improvement in lift-to-drag ratio of 9%, which was more than twice the improvement from using equivalent planar wingtip extensions. He asserts that optimized designs must consider a winglet that efficiently produces side forces to reduce the lift-induced inflow above the wing. Winglet configurations optimized to include viscous effects were shown by Chattot [8] to vary little from inviscid design methods, which suggests that potential-flow lifting line and vortex lattice analyses can yield useful, if not comprehensive, results for multiple lifting-surface planforms in the linear aerodynamic regime.

The concept of using multiple winglets is inspired by the study of bird flight, especially large soaring eagles with large wingtip pinions. If examined during soaring and maneuvering flight, these feathers can be seen to change orientation, in incidence and dihedral, with respect to the main wing. Hoey [9] discussed the impact of these active control surfaces on the stability and performance of the bird. The fact that these pinions separate, creating slots, has been recognized as a mechanism that reduces the overall drag at a finite lifting condition. Tucker's study of a Harris' hawk in a wind tunnel [10] showed that clipping the pinions increased the drag by as much as 42% over the unclipped wing. It was further proposed that the mechanism for drag reduction was the winglets' effect of making the wing nonplanar, thus "spreading" vorticity in the horizontal and vertical planes to reduce downwash.

Multiple lifting-surface planforms have demonstrated this diffusion in vorticity and downwash [4,11,12]. For Reynolds numbers from 160,000 to 300,000, an increase in L/D of 15–30% was measured by adding five flat-plate winglets to a rectangular baseline wing [11]. A substantial increase in lift curve slope was noted

Contributed by the Fluids Engineering Division of ASME for publication in the JOURNAL OF FLUIDS ENGINEERING. Manuscript received September 12, 2007; final manuscript received March 16, 2008; published online July 2, 2008. Assoc. Editor: Chunill Hah. Paper presented at the 2005 ASME Fluids Engineering Division Summer Meeting and Exhibition (FEDSM2005), Houston, TX, June 19–23, 2005.

and it was attributed to the dihedral spread of winglets at a zero local incidence. Furthermore, the percent increase exceeded the planform area added by the winglets. Work done by Kroo et al. [13] on nonplanar lifting systems has shown that the shape of the wake, rather than the shape of the wing, has the largest impact on induced drag for a given lifting condition. A split-tip configuration they studied computationally and experimentally showed a 13–15% increase in span efficiency ($e=1.11$) compared to an elliptic planar wing. The optimized "C" wing configuration produced a highly nonplanar wake and $e=1.46$, agreeing with Cone's [14] findings on spanwise "cambering," and suggesting that nonplanar distributions in the circulation can lead to practical drag reduction approaches. These are performance enhancements not predicted by classical linear aerodynamic methods, such as Prandtl [15] and Munk [16].

The present study was undertaken to study three independent, articulated winglets on a symmetrical half-span wing model to gain a better understanding of the aerodynamic effects of manipulating multiple winglets in flight. This work focused on the effect of dihedral configurations, and analytic results supported wind tunnel force measurements.

2 Experimental and Analytic Details

Facility and Models. The wind tunnel tests were performed in the former closed-circuit wind tunnel (CCWT) at the United States Naval Academy. The CCWT was a low speed, subsonic wind tunnel with a 137×97 cm^2 test section. Testing was conducted at near-atmospheric pressures, at effective Reynolds numbers of 579,000–603,000.

The baseline semispan wing had a constant NACA 0018 airfoil section [17] with a 55.9 cm halfspan and a 17.8 cm chord. Thus, the effective AR was 6.29 for a projected fullspan wing model. The baseline wing, with the winglets removed, had a rounded tip with a NACA 0018 profile. This geometry, along with the comparatively large leading-edge (LE) radius of the section, promoted effective side- and LE suction to affect the induced drag. Added to the tip of the baseline wing were three individual winglets, which approximate a NACA 0015 section [17]. Each winglet had a span of 20.3 cm and a chord of 5.0 cm with an AR of 4.6. The winglets were each capable of adjustment through ±90 deg local dihedral angle as well as ±180 deg local pitch angle (rotating about the winglet quarter chord). The winglets are numbered fore to aft for the purpose of codifying the dihedral configuration in the format of $\gamma_1/\gamma_2/\gamma_3$, as shown in Fig. 1(*a*), with γ in the units of degrees. Figure 1(*b*) shows the "0/30/60" configuration.

Force Measurements and Procedure. The semispan wing model was offset 1.8 mm above a splitter plate mounted 5.72 cm above the tunnel floor, with a carry-through structure to the balance installed beneath the test section. Aerodynamic loads were measured with a six-component compact platform balance. The measurement uncertainty of these force measurements was established by repetitive testing at a fixed flow condition. This was done at 11 deg angle of attack (AOA) over the acquisition of 20 consecutive datasets at Reynolds numbers of 200,000–700,000. The mean and uncertainty in the measurements were calculated using standard error analyses [18,19] and are shown in Table 1. In particular, the wing coefficients have shown a maximum 1 σ uncertainty of 0.0024 in C_L (0.3%), 0.0011 in C_D (2.3%), and 0.0017 in $C_{M_{c/4}}$ (11.8%) at the targeted Reynolds number.

The targeted Reynolds number was (nominally) 600,000. For each winglet configuration, the model was pitched through an alpha sweep of -2 to $+24$ deg in 1 deg increments using the pitch-pause technique. During data acquisition, nine channels were scanned (six balance outputs, the balance excitation voltage, the test section dynamic pressure, and the freestream air temperature) at 6.5-digit precision over an integration aperture of 20 power line cycles, as prescribed for high common mode rejection on low-level signals [20]. Reynolds number stability was maintained at $\pm50{,}000$ of the target condition. This procedure generally limited the freestream temperature to no more than 46°C. At the end of each test, the configuration was checked using a digital inclinometer to ensure that the winglets had not shifted in dihedral or local pitch angles.

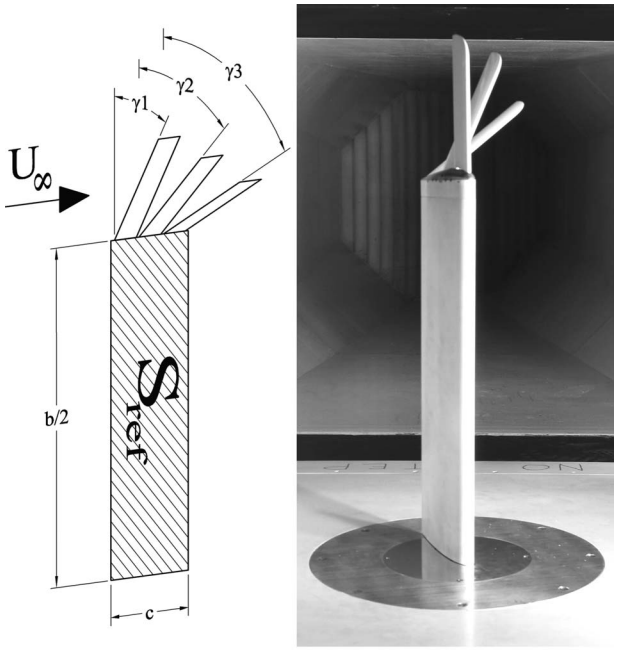

a) Geometry definition b) The 0/30/60 configuration

Fig. 1 Multiple winglet geometry

To affect equivalencies in comparison to the nondimensional coefficients, the reference area of the baseline wing was used in calculations of C_L, C_D, and C_M for all winglet configurations. Additionally, the baseline chord length was used for all Reynolds number calculations.

All force and moment measurements were corrected for wind tunnel wall interference effects. These included buoyancy, solid and wake blockage (single-pass Maskell method for separated flow), streamline curvature corrections, and downwash corrections as prescribed by common practice [21]. The semispan models had a low frontal-area blockage of 4% (and a planform-to-tunnel-cross-section ratio of $S/C=0.077$) and a span ratio of 54%. Thus, the prestall corrections created at most a 0.46 deg increase in AOA, a decrease in C_L of 0.016 or less, an increase in C_D of 0.0069 or less, and a change in C_M of less than 0.0006. The effective velocity through the test section was increased by 3% at 25 deg AOA as a result of solid and wake blockage effects.

Analytic Approaches. Analytic results were generated using two well-documented codes. The low Reynolds number airfoil performance was benchmarked using the XFOIL code. XFOIL is used for design and analysis for low Reynolds number airfoils and employs a high-order panel method with a fully coupled viscous/

Table 1 Measurement uncertainty: Baseline model at 11.3 deg

Mean value/1σ error			
Re_c	C_L	C_D	$C_{M_{c/4}}$
195,300/171	0.8190/0.0025	0.0584/0.0013	0.0047/0.0011
398,100/450	0.8123/0.0019	0.0505/0.0009	0.0100/0.0014
581,400/1386	0.8060/0.0024	0.0485/0.0011	0.0144/0.0017
722,500/3423	0.8049/0.0031	0.0478/0.0013	0.0161/0.0013

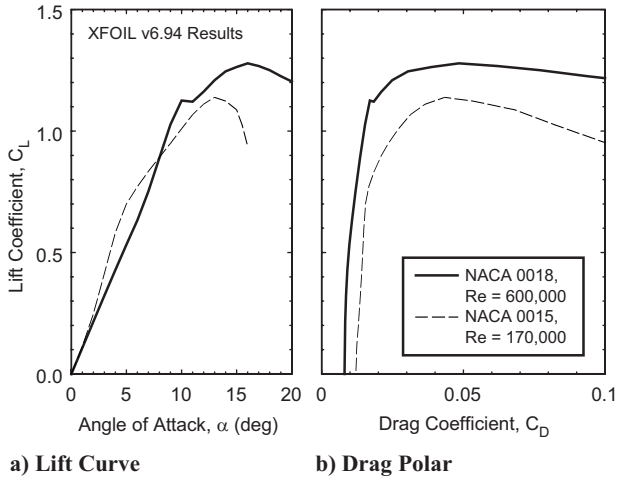

Fig. 2 XFOIL analysis of 2D airfoil sections used

inviscid interaction method. The free transition criterion (specifically, the $e^{n_{crit}}$ criterion) was used for the viscous calculations, where n_{crit} is the log of the amplification factor of the most amplified frequency that triggers transition. The present study used $n_{crit}=7$ (corresponding to a 0.161% turbulence level). This approximates the turbulence intensity of the CCWT. It should be noted that the assumptions for this transition criterion (no cross flow instabilities, attachment-line transition, or bypass transition) are met for the present 2D analysis [22]. Most computed cases for $\alpha < \alpha_{stall}$ converged within about a dozen iterations.

For 3D planform characteristics, the vortex lattice method (VLM) of Margason, Lamar, and Herbert [23,24] was applied. VLM is an extension of the finite step lifting-line theory, which assumes steady, irrotational, inviscid, attached flow. These calculations were performed assuming full LE suction and side-edge attached flow. The multiple-winglet configurations were modeled using three combined planforms and 270 horseshoe vortices: a 15×11 array (chordwise $\times$ spanwise) on the main wing and a 5×7 array on each winglet. VLM trade studies were performed to ascertain trends that were validated through wind tunnel testing. Furthermore, the VLM analysis enabled a detailed examination of span loading and flowfield distributions (wake velocity, circulation, and downwash) that were not available at the time of the experimentation.

3 Results

Results are presented for the semispan wing with and without three independent, articulated winglets. The primary value of these results lies in the comparisons at varying local dihedral angle configurations to wings without winglets to gain a perspective on the advantages and disadvantages of utilizing these types of configurations. In light of this comparison, all coefficients are based on the reference area of the baseline wing. This enables direct comparison of the aerodynamic forces produced by diverse configurations. The presented results focus on the analysis of the airfoil performance, the baseline wing performance, trade studies of specific families of winglet configurations, and a wake analysis of a few configurations.

Airfoil Section Analysis. The 2D analytic results for the NACA airfoils benchmarked the sectional characteristics, and were used to ascertain the magnitude of the Reynolds number effects. With the baseline wing section (18% thick) operating at a Reynolds number of 600,000, the winglet sections (15% thick) operate at a Reynolds number of 170,000. Therefore, differences in the airfoil performance were manifested as thickness and Reynolds effects. From the lift curves in Fig. 2(*a*), the baseline section encountered a laminar separation bubble, which affected the lift

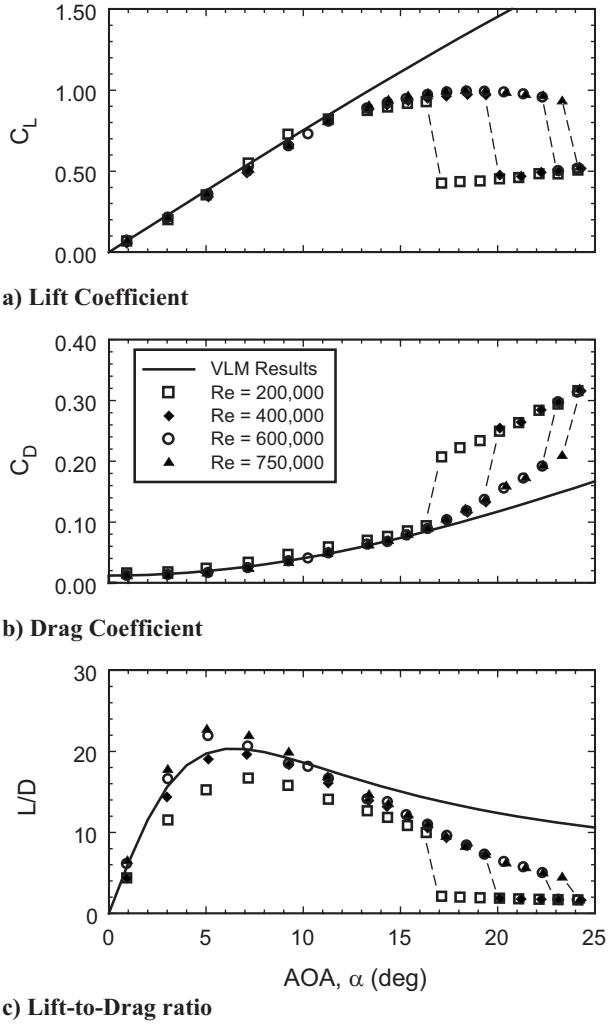

Fig. 3 Reynolds number sensitivity of baseline wing results

slope at around 10 deg AOA. However, the winglet section exhibited the classic LE stall characteristic at about 13 deg AOA. The main conclusion of this analysis is that the winglet airfoils stalled 3 deg sooner than the baseline airfoil at an 11% lower $C_{\ell,max}$. More significantly, Fig. 2(*b*) shows that the value of $C_{d,0}$ was 50% higher for the winglet airfoil sections, which had 82% laminar flow on the upper surface compared to 60% for the baseline wing section. Primarily due to increased pressure drag, this impacted the total contribution to parasite drag on a finite wing or a flight vehicle. This comparison emphasizes the trade-off involved at the crossover point: the reduction in induced drag at the cost of a higher overall parasite drag.

Baseline Wing Performance. The rectangular baseline wing was used as the reference configuration when comparing the winglet configurations and was benchmarked against the VLM analysis. Full alpha sweeps were run at four different Reynolds numbers (200,000, 400,000, 600,000, and 750,000) to determine the sensitivity to the flow regime. The results in the linear regime show a good comparison with the VLM analysis, including the lift curves of Fig. 3(*a*) and the drag polars of Fig. 3(*b*). For the drag coefficient comparison, the $C_{D,i}$ values from the VLM code were offset by the experimental $C_{D,0}$ as obtained in the wind tunnel (0.0120). While this method is imprecise at the theoretical level, it is a common practice in benchmarking analytic and experimental results [25], and has been validated in other comparative studies by the author [26]. In practice, the amount of LE suction would not be 100%, but around 97% for the present wings, thereby cre-

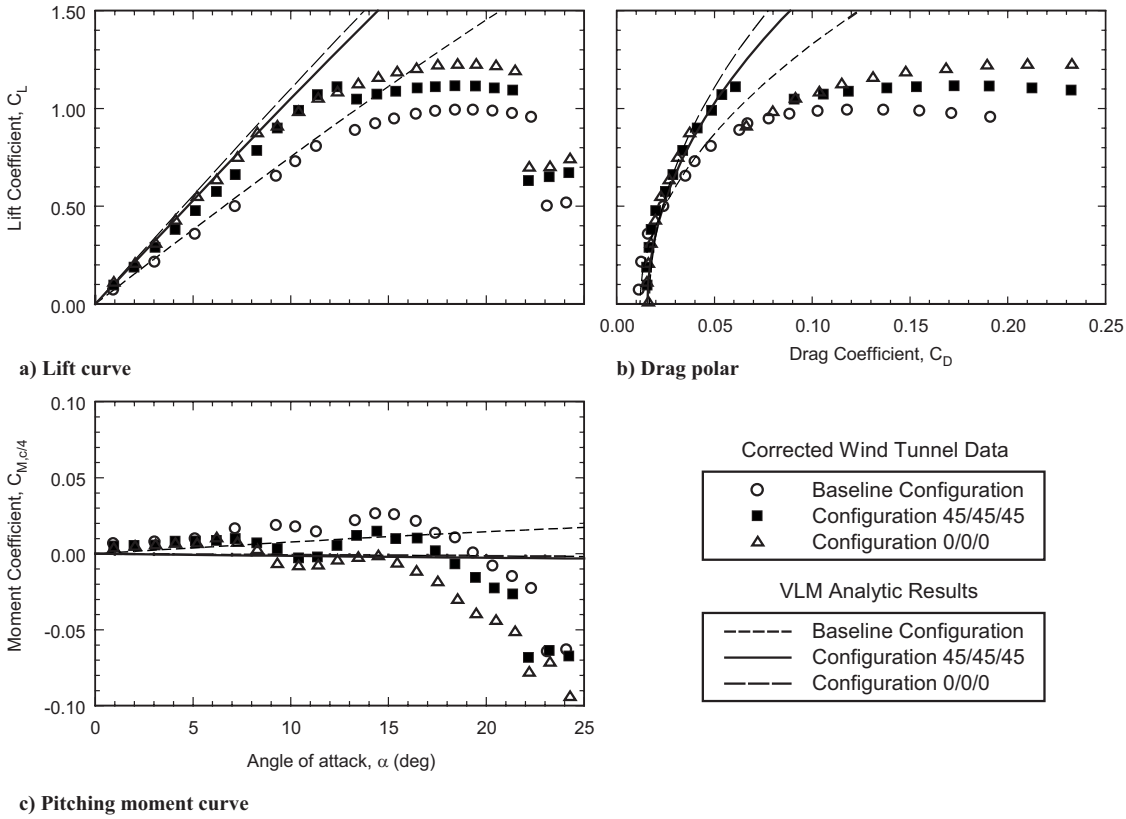

Fig. 4 Louvered-wing experimental and analytic results

ating a slightly steeper theoretical induced drag shape factor [27]. At a Reynolds number of 600,000, the baseline wing achieved a lift curve slope of 0.0704/deg, $C_{L,\max}=0.991$, $C_{D,\min}=0.0116$, and $(L/D)_{\max}=21.9$ at 5 deg AOA (refer to Fig. 3(*c*)).

The Reynolds number had a measurable effect on the lift and drag of the baseline wing. As the Reynolds number increased from 200,000 to 600,000, the insipient stall AOA progressively increased from 16.4 deg to 23.3 deg and the drag decreased progressively from $C_{D,\min}=0.0153-0.0113$. Therefore, this observed sensitivity due to Reynolds number resulted in limiting the test data Reynolds number variability to $\pm 50{,}000$.

"Louvered" Wing Configurations. The so-called "louvered" configurations indicated that all three winglets were adjusted to the same local dihedral angle, or $\gamma_1=\gamma_2=\gamma_3=k$, where k corresponded to 0 deg and 45 deg. These configurations were derivatives of the "wing grid" in literature [12]. In the practical application of multiple winglets, the winglets would always be present, so the 0/0/0 configuration also served as a "winglet-on" reference geometry. In this case, the addition of the winglets added 30% to the true planform area and 43% to the true AR of the base wing.

The experimental lift results (Fig. 4(*a*)) showed that the 45/45/45 configuration was limited to a 34% increase in the lift slope over 0–10 deg AOA, while the 0/0/0 configuration showed a 41% increase. The VLM analysis predicted these increases to be 40% and 46%, respectively, in the linear regime. Prandtl's work [15] originally predicted that the change in the lift slope over the linear region can be expressed as an AR effect. This is evident in the 0/0/0 configuration, which had the largest physical span, the highest effective AR (9.01), and yielded the highest lift slope of 0.100/deg. Despite the varying slopes, the stall point remained relatively unchanged (21–22 deg AOA). It should be noted here that the lift increments at the same geometric AOA for the 0/0/0 configuration in the linear regime were in excess of those expected by the addition of the winglet planform area (which would increase C_L 30%), and the increase in the AR (which would increase C_L another 8% for an elliptic span loading). The experimental results also showed a 17–25% increase in C_L from 10 deg to the stall AOA, increasing $C_{L,\max}$ 12–24% for the louvered configurations.

Figure 4(*b*) shows that $C_{D,0}$ increased by 32% with the addition of either louvered configuration, the result of added parasite drag due to Reynolds effects on the winglets plus the added interference between the four lifting surfaces. This also resulted in similar drag increases at the same geometric AOA as the baseline model. However, in terms of C_D for a given C_L, there was a noteworthy crossover point at around $C_L=0.45$. Above this point, the reductions in induced drag overcame the parasitic penalties. At $C_L=0.8$, the overall drag reduction was 27–31% for the louvered configurations, decrements which were far beyond those expected by a pure AR effect (which would act to decrease C_D 17–22% for the louvered configurations, assuming an elliptic span loading).

A notable feature of these drag polars was that C_D abruptly increased at $C_L=1.1$ for the 45/45/45 configuration and at $C_L=0.9$ for the 0/0/0 configuration. This was caused by Winglet 1 stalling due to its higher loading condition and the low Reynolds effects present (this has been confirmed by a decrease in the $C_{M,c/4}$ in Fig. 4(*c*)). The flow on the aft winglets remained attached due to the downwash from the upstream winglets. The peak lift-to-drag ratio increased by 7–11%, (24.2–23.4), the result of the disproportionate drag reduction compared to the lift increase. The improved L/D, which promotes better gliding characteristics, confirms increments of earlier studies [5,6,11]. In general, the analytic calculations at low AOA provided fair representations of lift, drag, and moment coefficients, but the predicted trends were in very good agreement.

To determine the relative loading of the winglets, the span load distributions were plotted for the louvered configurations at $C_L=0.8$ (see Fig. 5). This value of the lift coefficient was chosen

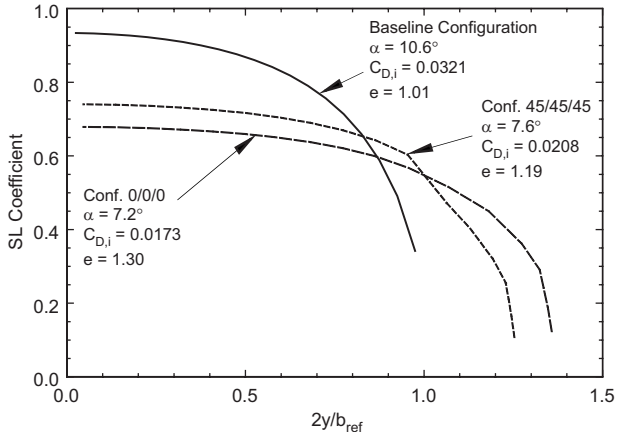

Fig. 5 Louvered-wing span load distributions for a lift coefficient of 0.8

because it represents a substantive lift load while remaining in the linear regime for all configurations (refer to Figs. 3(*a*) and 4(*a*)). The span load coefficient is defined in Eq. (1).

$$\text{SL coef} = \frac{C_\ell c}{C_L \bar{c}} \tag{1}$$

In an idealized wing as proposed by Prandtl [15], the span load coefficient would have an elliptical distribution over the span. For the configurations plotted, the baseline actually showed that $e = 1.01$, which corresponded to the VLM result for full LE suction (for 97% LE suction, e would be about 0.90 [27]). The VLM result predicted that $e = 1.19-1.30$ for the louvered configurations. These span efficiencies in excess of 1, which have been validated in literature [6,12–14], indicated that a more efficient distribution of the span loading is possible such that $C_{D,i}$ can be greatly reduced for the same C_L. For individual winglets, this means that the leading winglet was much more highly loaded than the successive ones, and it was found that Winglet 1 carried 67% of the loading outboard of the baseline wing tip. Winglets 2 and 3 carried 22% and 11% of the load, respectively.

High-Lift Winglet Configurations. The family of $2k/k/0$ winglet configurations consistently produced the largest increments in lift. These configurations were defined by setting $\gamma_3 = 0$, $\gamma_2 = k$, and $\gamma_1 = 2k$, where k corresponded to 10 deg, 20 deg, and 30 deg. The increments in lift coefficient compared to the baseline wing (Fig. 6(*a*)) showed that all configurations in this series essentially had the same high-lift characteristic up to around 10 deg AOA. The rate of change of ΔC_L with AOA averaged 0.03–0.04/deg higher than the baseline wing for the same AOA. Furthermore, the lift was also 7–12% higher than for configuration 0/0/0, which had a higher AR. This supports the assertion that the performance enhancements of the winglets exceed the benefits brought on by additional planform area and increased AR. Beyond 10 deg AOA, the ΔC_L characteristics were differentiated by the aerodynamic state of the leading winglet. The higher the value of γ_1, the lower the local winglet AOA, thereby suppressing stall on the leading winglet. As can be seen in the figure, the interruption of the linear portion of the lift curve occurred at around 9.5 deg for configuration 20/10/0, 10.5 deg for configuration 40/20/0, and 12 deg for configuration 60/30/0. The magnitude of $\Delta(C_{L,\max})$ was 0.21–0.23 higher compared to the baseline wing but 0.01–0.03 lower compared to the 0/0/0 configuration.

The pitching moment showed a consistent trend of decreasing slope with increasing γ_1. As a point of comparison, the baseline wing was characterized by $dC_M/d\alpha = +0.0016$/deg for AOA < 10 deg, which represented a slight destabilizing characteristic on the longitudinal static stability for a straight, rectangular wing.

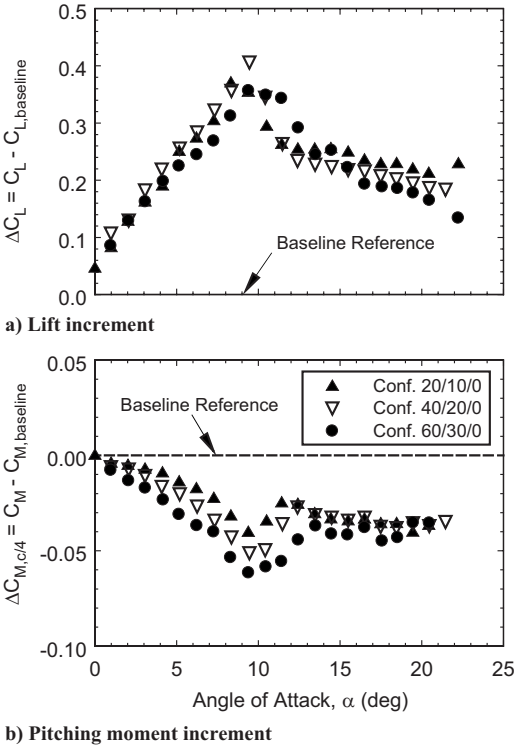

Fig. 6 High-lift winglet configurations

As shown in Fig. 6(*b*), the 20/10/0 configuration reverses this slope to −0.0019/deg and the 60/30/0 configuration, to as low as −0.0042/deg. The reduction in slope is a consequence of the winglets shifting the aerodynamic center of the entire planform to a more forward position, by as much as 6.5% of c_{ref}. For this to occur, a stronger circulation had to be present on the leading winglet than on the aft, supporting the VLM analysis. This shift resulted in a stabilizing effect on the wing at prestall conditions. Because the specific value of $dC_M/d\alpha$ was differentiated by the value of γ_1, the leading winglet had a significant impact on the planform stability characteristics. Therefore, the configuration in this family with the highest lift and the greatest stability was the 60/30/0 configuration.

High-L/D Winglet Configurations. The family of $i/45/j$ winglet configurations produced the highest increments in L/D measured in this study. These configurations were defined by setting $\gamma_2 = 45$ deg, $\gamma_1 = i = 45 + k$, and $\gamma_3 = j = 45 - k$, where k corresponded to 5 deg, 10 deg, and 15 deg. Although the lift curve slopes for these configurations were 38–39% higher than the baseline wing, the initial stall point on Winglet 1 established the maximum lift condition, as seen previously. This point is evident in the drag polars of Fig. 7(*a*). The drag polars followed a common trend up to $C_L = 1.2$, and the stall of Winglet 1 was demarked by a sharp rise in C_D thereafter. Although this figure does not show the deep stall regime, deep stall occurred at 21.5 deg AOA for all configurations in this family. The drag reduction for these configurations was a substantial 47–48% at $C_L = 0.9$, when compared to the baseline wing. $C_{D,0}$ was the same for all configurations, within the bounds of experimental uncertainty.

Figure 7(*b*) shows the dramatic increases in L/D that are possible with these configurations at equivalent lift coefficients. The highest increments in L/D were 11–14, increments which were maintained over a relatively broad plateau of $0.45 < C_L < 0.95$. At $C_L = 0.9$, these increments translated into L/D increases as high as 89–91%. At this same lift coefficient, the 0/0/0 configuration resulted in a mere 25% increase in L/D, once again demonstrating

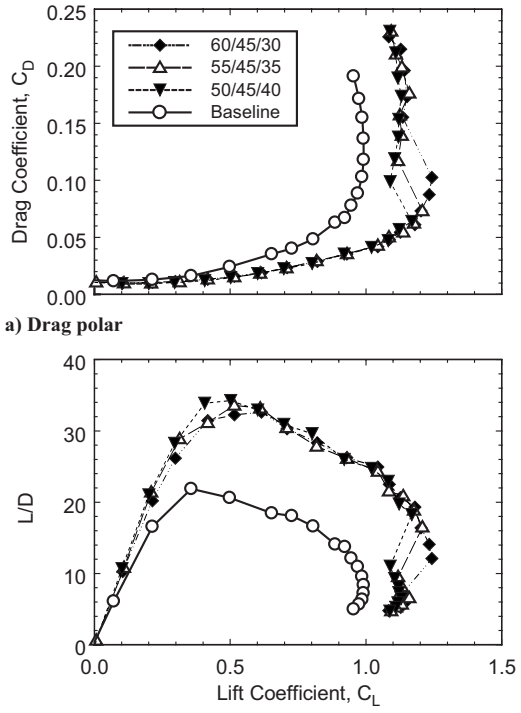

a) Drag polar

b) Lift-to-drag ratio

Fig. 7 High-L/D winglet configurations

that there was a much greater effect than planform area and AR. These increases were due to the nonplanar nature of the wake and its effect on the distribution of circulation and downwash. The trends in peak L/D (33–34 at 5–6 deg AOA) were fairly well predicted by the VLM analysis (28–30 at 5 deg AOA), considering that method's limitations. The large enhancements were due to the increased lift (39–43%) at a given AOA plus the reduced drag (31–34%) at a given C_L when compared to the baseline wing. The applicability of these configurations is that they maintained $L/D > 20$ over a range of 2–12 deg AOA. For the 0/0/0 configuration, this range was only 4–8 deg AOA and for the baseline wing, 5–7 deg. Such performance improvements would increase a flight vehicle's glide ratio and endurance.

Variable Stability Winglet Configurations. The final trade study considered here focused on the effect of "inverse" dihedral orientations. This involved a comparison between the 60/70/80 and 80/70/60 ($i/70/j$) configurations and a comparison between the 40/60/80 and 80/60/40 ($i/60/j$) configurations. As shown in Fig. 8(a), the difference in lift between the $i/70/j$ configurations was 4% of the baseline wing, with the 80/70/60 configuration producing the higher lift over the whole range of AOA tested. The $i/60/j$ configurations demonstrated a similar lift characteristic up to 10 deg AOA, after which the 40/60/80 configuration dropped off substantially. For 12-16 deg AOA, the change in lift was about 0.14, with the 80/60/40 configuration producing the higher lift.

Figure 8(b) shows the drag increment for all four inverse configurations. The 80/70/60 configuration averaged ΔC_D values that were consistently about 9% higher than the 60/70/80 configuration. Because these trends were consistent with the increases in lift, the L/D ratios for these two configurations were comparable within experimental uncertainty. However, the 80/60/40 configuration actually shows a lower ΔC_D than its inverse from 11–17 deg AOA. When combined with the larger differences in lift, the L/D can be varied by inverting the winglet dihedral orientation. As an example for $\alpha=13$ deg, the 80/60/40 configuration produced $L/D=16.8$ while the 40/60/80 configuration pro-

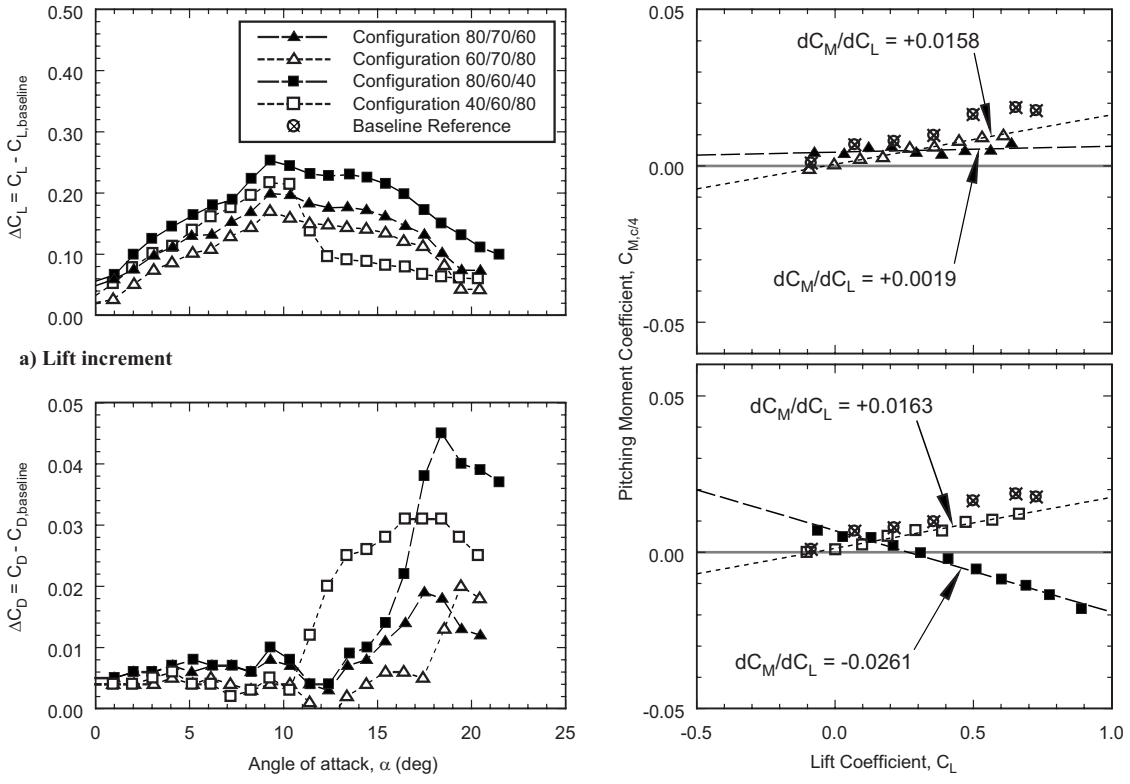

a) Lift increment

b) Drag increment

c) Pitching moment curves

Fig. 8 Effects of inverse winglet deflections

duced $L/D=12.0$.

However, the big advantage of the present trade study is seen in the pitching moment characteristics in Fig. 8(*c*). The linear trends in the plot at low-to-moderate AOA was evidence that the inversion of the winglet orientation created an opposite slope in the pitching moment curve as referenced about the $c/4$ chordwise position. Inverting the 80/70/60 configuration into the 60/70/80 configuration varied the value of dC_M/dC_L from +0.0019 to +0.0158, which effectively shifted the aerodynamic center aft by 1.4% of c_{ref}. The VLM analysis predicted that this shift would be 1.9%. For the $i/60/j$ configurations, this change increased from −0.0261 to +0.0163, which effectively shifted the aerodynamic center aft by 3.7% c_{ref} (2.5% was predicted by VLM). For comparison, the slope of the linear part of the pitching moment curve for the baseline wing was 0.0234, so all of the inverse-pair configurations resulted in an aft shift of the AC. Another subtle, but notable, characteristic was the shifting of $C_{M,0}$ for these configurations. For the $i/70/j$ and $i/60/j$ configurations, $C_{M,0}$ decreased by about 0.004.

These configurations were shown to have unique effects on "tuning" the operating C_L, L/D, and C_M of the wing by merely reversing the dihedral orientation of the winglets. In general, the steeper dihedral angle of the leading winglet produced higher C_L but lower $C_{M,c/4}$. Furthermore, because each pair of winglet configurations had the same physical span and thus projected planform area and true AR, these effects are due solely to the nonplanar orientation of the entire planform and its effect on the distribution of circulation and downwash. The results for the pitching moment, in particular, infer that actively controlled multiple winglets can benefit the trimming of an aircraft while reducing or eliminating the need for conventional horizontal control surfaces.

The present aerodynamic enhancements of the different families of configurations (louvered, high-lift, high-L/D, and inverse configurations) are summarized in Fig. 9. In general, all families produced an increase in lift compared to the baseline. All but the $i/45/j$ family produced increases in drag at the same AOA. However, the change in drag at the same C_L produced a benefit among all families. The $i/45/j$ family produced a net drag decrease at the same AOA, which resulted in the highest increases in L/D. The inverse families studied demonstrated the maximum shift in pitch stiffness.

Wake Analysis. There were four influences that produced the observed aerodynamic enhancements. The first two obvious effects were the addition to the true planform area and the increase in the true AR as a result of adding winglets. Because it was a planar configuration, the 0/0/0 winglet configuration provided the most additional area (30%) and AR (43%). However, the additional area would have theoretically increased both C_L and C_D by 30% throughout the linear aerodynamic regime. A "pure" AR effect would have theoretically increased C_L by 8% (at the same AOA) and decreased C_D by 22% (based on an elliptic lift distribution at $C_L=0.8$). It has been seen in the results that lift increments and the drag reductions are higher in practice, in the absence of flow separation.

The third influence deals with the effective AOA of the winglets. As the winglet dihedral angle was increased, the effective AOA on the winglets, $\alpha_{w,\text{eff}}$, became less than the AOA of the wing. This was seen in Eq. (2), which represents the coordinate transformation through a local dihedral rotation, then a pitch rotation. The magnitude of $\alpha_{w,\text{eff}}$ was determined by the scalar product of the velocity vector and the local surface normal vector.

$$\alpha_{w,\text{eff}} = \frac{\pi}{2} - \cos^{-1}(\sin\alpha\cos\gamma) \tag{2}$$

Therefore, the configurations with higher γ_1 settings had a delayed stall tendency, as seen in the drop-off in the lift curves (Figs. 4(*a*) and 6(*a*)) and the increase in the drag (Fig. 7(*a*)). The deflected winglets were able to maintain lift longer than the louvered wings because of a higher degree of three-dimensional flow. When the winglets stalled, they created an incremental loss of lift, beginning with the forward winglet, which reduced both the circulation and the downwash on the outboard portion of the wing. Thus, the progression to deep stall occurred in smaller increments, rather than in one, larger loss of lift and increase in drag.

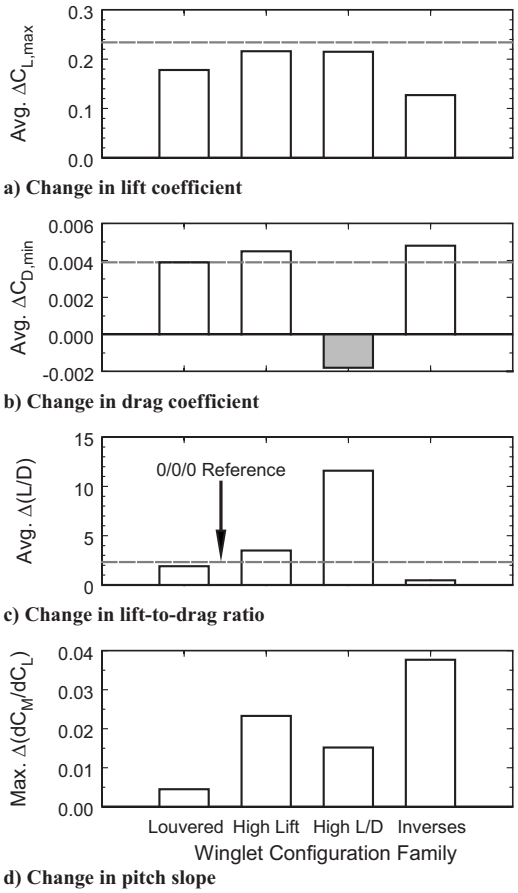

Fig. 9 A summary of aerodynamic improvements

The fourth influence of the winglets was the interaction of the vortices at the tip of each winglet, which created nonplanar distributions of wake velocity, circulation, and downwash as determined by a VLM wake analysis. This analysis was done by projecting 120 horizontal field lines in the yz-plane one chord length downstream of the wing trailing edge (TE), ranging from $2z/b=-0.27$ to +0.55. At 75 points along each field line, the vortex lattice induced velocity increments u, v, and w were calculated. From the incremental velocity components, the wake velocity magnitude, V_{wake}, was calculated using Eq. (3). The wake velocity is defined here as the perturbation velocity vector projected onto the yz-plane, and its magnitude describes the level of local circulation.

$$V_{\text{wake}} \equiv \sqrt{v^2 + w^2} \tag{3}$$

The downwash angle, ε, is a function of u and w and was calculated from Eq. (4).

$$\varepsilon = \alpha - \tan^{-1}\left(\frac{\sin\alpha - w/U}{\cos\alpha - u/U}\right) \tag{4}$$

Nondimensionalized wake velocity distributions are shown for the baseline, louvered, and the 60/30/0 configurations for $C_L=0.8$ in Fig. 10. While the irrotational assumption of VLM yields a zero vorticity at off-planform points, the distribution of vorticity over the vortex lattice will produce finite values of circulation in

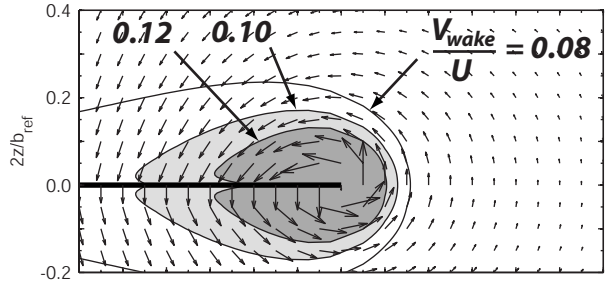

a) Baseline configuration

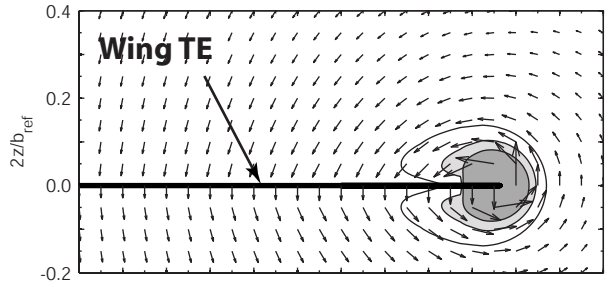

b) Winglet configuration *0/0/0*

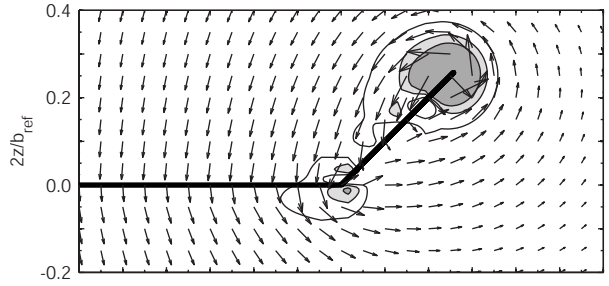

c) Winglet configuration *45/45/45*

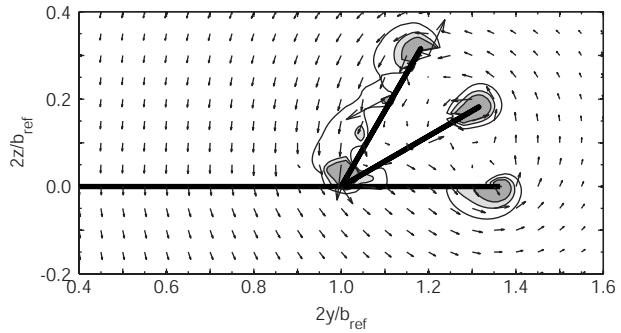

d) Winglet configuration *60/30/0*

Fig. 10 Wake velocity magnitude distributions for a lift coefficient of 0.8

the *yz*-plane, as long as the line integral encloses part of the lattice. This circulation is revealed through the wake velocity distribution, and is exactly balanced by the opposing wingtip (yielding zero net lift on the wake). As seen in Fig. 10(*a*), the baseline wing had most of the circulation (defined by $V_{\text{wake}}/U > 0.12$) concentrated in a region just inboard of the wing tip. The high magnitudes of V_{wake}/U were the result of the wing circulation present in the trailing wingtip vortex structure. Most of the wing was under the influence of a wake velocity that was at least 8% of U, and the level of circulation was high as evidenced by the overlay of the induced velocity vectors. The louvered configurations (Figs. 10(*b*) and 10(*c*)) had about the same net area of effect for $V_{\text{wake}}/U > 0.12$, but the region was much more confined to the winglet tips, creating a greater two dimensionality in the flowfield over the baseline section. Furthermore, the 0/0/0 configuration showed no circulation around the tip of the baseline wing section, while the 45/45/45 configuration revealed a small level of circulation there. It is clear that the nonplanar configurations (Figs. 10(*c*) and 10(*d*)) redirected the wake velocity vectors over the span of the baseline wing, and this circulation was shifted more "out of plane" as the winglets were deflected. This had the effect of further reducing the net downward component, or the downwash. The smallest downwash vectors resulted from the wake velocity distributions for the 60/30/0 configuration. In this case, the concentration of highest wake velocities became even more localized at the winglet tips and at the baseline wingtip, further diffusing the overall circulation effect while still maintaining an enhanced overall circulation (as per Fig. 6(*a*)). With this configuration, it was obvious that the tip vortices interacted with each other and partially canceled the induced velocities; all velocity magnitudes were notably smaller than the other three configurations. This had the effect of redistributing the circulation and diffusing the downwash distribution and allowing the vortex sheet to roll up out of the wing chord plane as reported by Tucker [10] and Kroo et al. [13]. Thus, the tip vortex cores became smaller (with lower "real" viscous losses) and induced drag was decreased from that of the baseline configuration.

The wake distributions in ε are shown for $C_L = 0.8$ in Fig. 11. The distribution of circulation, which was the result of the potential-flow induced velocities, had a direct impact on the distribution of the downwash. The baseline wing in Fig. 11(*a*) revealed a broad range of downwash angles in excess of $\varepsilon = 4$ deg. Outboard of the wingtip is the $\varepsilon = 0$ line, which is the demarcation between the induced downwash (generally inboard of the tip) and the upwash (generally outboard of the tip). When considering the winglet configurations, the breadth of the wake region affected by the downwash was diminished, and the areas of highest ε decreased substantially. Lower overall magnitudes of the downwash directly resulted in the reduction in the induced drag and thus the significant reduction in the overall drag at the same lift coefficient, as observed experimentally.

Furthermore, the "splaying" of the winglets to create nonplanar configurations resulted in altering the magnitude of the downwash angle. Figure 11(*c*) shows that moving the louvered configuration from 0/0/0 to 45/45/45 actually increased the region of highest ε. However, the distribution shifted much of this region out of plane of the main wing section. This created an area outboard of the baseline wingtip but inboard of the winglet tips in which upwash affected the overall configuration. The combination of these two effects, smaller regions of downwash angles and the presence of upwash fields within the overall span, validates the induced drag reductions observed in the wind tunnel tests (27–31% at $C_L = 0.8$).

The wake of the 60/30/0 configuration revealed additional downwash effects (Fig. 11(*d*)). The region of $\varepsilon > 4$ deg was confined to the wake immediately downstream of Winglet 1, and the other two showed very little contribution to the highest downwash angles. One reason for this consolidation was that the leading winglet carried 2/3 of the spanload for $2y/b_{\text{ref}} > 1$, and higher local C_ℓ values induced larger downwash magnitudes than the less loaded winglets. Another reason for the downwash consolidation was the interaction between winglets, in which the superposition of the induced downwash velocities was greatest in the plane of Winglet 1. Finally, the splaying of the winglets reduced the midspan distribution in ε, especially the contour defined by $\varepsilon = 3$ deg. The lower magnitudes inboard with higher magnitudes

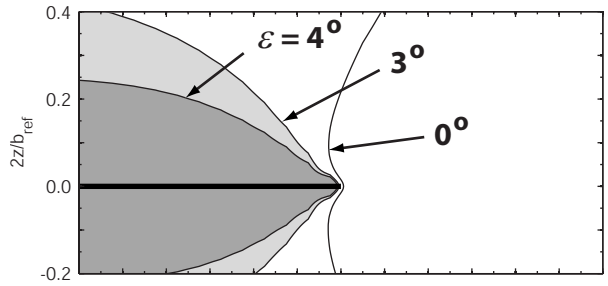

a) Baseline configuration

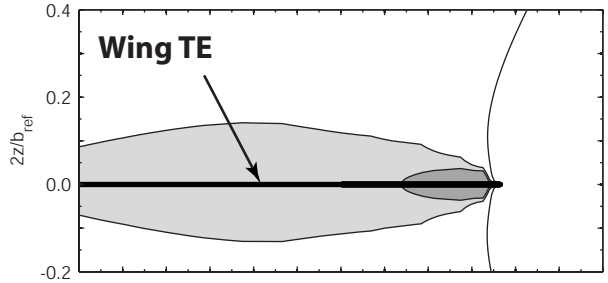

b) Winglet configuration *0/0/0*

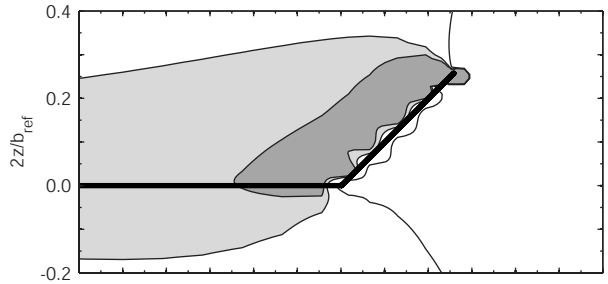

c) Winglet configuration *45/45/45*

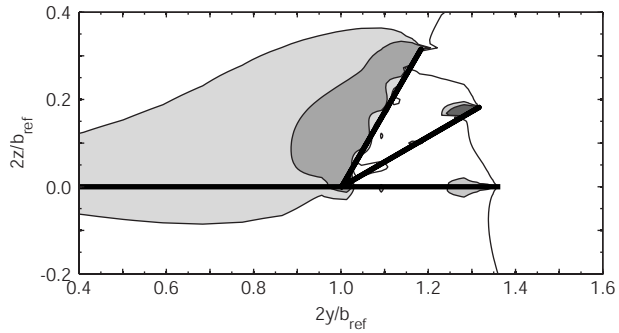

d) Winglet configuration *60/30/0*

Fig. 11 Wake downwash angle distributions for a lift coefficient of 0.8

outboard were manifested as span efficiencies in excess of 1, but the reduction in overall downwash at the midspan station caused the wing to perform more as an infinite wing. In other words, the configuration performed as if it had an effective AR that was beyond the physical span of the wing, even with the winglets fully extended.

4 Conclusions

Some general conclusions about the use of multiple winglets were made from the present series of analytic predictions and wind tunnel tests. The analytic VLM provided fair predictions of the wind tunnel performance, but the predicted trends in lift, drag, and (to a lesser degree) pitching moment were in good agreement with experimental results. However, the primary value of the analytic results was in scrutinizing the distributions of wake velocity, circulation, and downwash angle. This showed that the highly nonplanar configurations tended to reduce and diffuse the regions of highest circulation and to create more moderate downwash angles in the wake. These effects, along with partial cancellation of induced velocities between winglets, resulted in reductions in induced drag, which reduced the total drag by as much as 54% at equivalent lift coefficients.

Arranging the winglets with high-dihedral angles was detrimental to increasing the lift of the whole configuration. The highly vertical winglets produced less localized lift due to the loss of effective planform area in the chord plane. Because the leading winglet was more highly loaded than the aft winglets, its influence on increasing lift of the entire configuration was more pronounced. Therefore, the recommendation is that multiple winglets be kept away from dihedral angles greater than 45 deg if enhanced lift is the goal. The $2k/k/0$ family of configurations produced the highest $dC_L/d\alpha$ (as much as 65% higher than the baseline) and the highest $C_{L,\max}$ (on average 23% higher than the baseline). The opposite trend was true for high L/D ratios. The higher-dihedral angles on the leading winglet showed the most promise in producing high increments in L/D. The highest L/D measured was 34 on the 50/45/40 configuration, a 57% increase over the baseline. The $i/45/j$ family of configurations revealed the best compromise between low-dihedral lift enhancement and higher-dihedral L/D enhancement.

By inverting the dihedral arrangement of the winglets, substantial shifts in the longitudinal stability characteristics were realized. By shifting between the 80/60/40 and the 40/60/80 configurations, the aerodynamic center can be effectively moved almost 4% aft on the configuration, an effect that has ramifications on flight vehicle stability characteristics and control surface sizing.

From the present study, it can be concluded that multiple winglets can provide increases to lift and L/D at equivalent AOA, while providing decreases in drag at equivalent lift coefficients. This makes multiple winglets appropriate for actively controlled surfaces for flight-optimized aircraft configurations that depend on high lift and high efficiency, such as modern day UAV configurations. Other types of manned aircraft may also benefit from articulated winglets, based on the simplicity of actuating these relatively small and effective surfaces. However, the application would depend on the crossover point in the drag analysis and the weight added to the outboard wing to accommodate any actuation equipment and additional wing structure, all of which would increase the root bending moment. The present results call for continued research to study the effects of the winglets in more detail, in additional configurations with changes in the local pitch angle of the winglets. Furthermore, the effects on lateral and directional stability must be studied to better understand how multiple winglets can be employed to improve the performance of high lift, low speed flight. Lastly, the control authority of articulated winglets and the sizing of the surfaces must be analyzed for application to manned aircraft configurations.

Acknowledgment

The author would like to thank the support of the USNA Aerospace Engineering Department and the Office of Research and Scholarship. Lt. Patrick M. Bookey, United States Naval Reserve, was responsible for obtaining much of the analytic results and the wind tunnel data. Mr. Rusty Foard and Mr. Bill Beaver fabricated

the models. Additional gratitude is owed to Mr. John Lamar of NASA Langley regarding the vortex lattice code used.

Nomenclature

a = lift curve slope, $dC_L/d\alpha$
AOA = wing angle of attack
AR = wing aspect ratio, b^2/S
b = wing span
c = wing chord length
$\bar{c}$ = mean chord length
C = test section cross-sectional area
C_D = wing drag coefficient, $D/(qS)$
C_d = sectional drag coefficient
C_L = wing lift coefficient, $L/(qS)$
C_ℓ = sectional lift coefficient
C_M = wing pitching moment coefficient, $M/(qS\bar{c})$
D = drag force
e = span efficiency factor
L = lift force
M = pitching moment
MAC = mean aerodynamic chord, $(2/S)\int_0^{b/2} c^2 dy$
n_{crit} = log of the boundary layer amplification factor
q = freestream dynamic pressure, $(\rho U_\infty^2)/2$
Re_c = Reynolds number, $(\rho U_\infty c)/\mu$
S = wing planform area, $b\bar{c}$
u = axial velocity increment
U = steady-state axial velocity
v = spanwise velocity component
V_{wake} = wake velocity magnitude (yz-plane)
w = downwash velocity component
x = wing coordinate in the chordwise direction
y = wing coordinate in the spanwise direction
z = vertical coordinate
α = geometric angle of attack
α_{L_0} = angle of attack at zero lift
γ = winglet dihedral angle
ε = downwash angle
Γ = circulation
ξ = vorticity
μ = dynamic viscosity
ν = kinematic viscosity
ρ = fluid density

Subscripts

0 = wing zero-lift condition
1,2,3 = winglet number, indexed fore to aft
∞ = freestream condition
AC = referenced to the wing aerodynamic center position
$c/4$ = referenced to the wing quarter-chord position
ref = based on reference characteristic (i.e., baseline wing)
w = characteristic of a winglet

References

[1] F. Fiorino, ed., 2003, "Southwest 737-700s Earn Winglets," Aviat. Week Space Technol., **158**(25), p. 15.
[2] Proctor, P., 1996, "Winglets Span G2 Fleet," Aviat. Week Space Technol., **145**(22), p. 13.
[3] Proctor, P., 1993, "Winglet Designs to Cut Fuel Burn," Aviat. Week Space Technol., **139**(23), p. 49.
[4] Spillman, J. J., and McVitie, A. M., 1984, "Wing Tip Sails Which Give Lower Drag at All Normal Flight Speeds," Aeronaut. J., **88**, pp. 362–369.
[5] Whitcomb, R. T., 1976, "A Design Approach and Selected Wind-Tunnel Results at High Subsonic Speeds for Wing-Tip Mounted Winglets," NASA Technical Note D-8260.
[6] Maughmer, M. D., 2003, "Design of Winglets for High-Performance Sailplanes," J. Aircr., **40**(6), pp. 1099–1106.
[7] Maughmer, M. D., and Kunz, P. J., 1998, "Sailplane Winglet Design," Technical Soaring, **22**(4), pp. 116–123.
[8] Chattot, J. J., 2006, "Low Speed Design and Analysis of Wing/Winglet Combinations Including Viscous Effects," J. Aircr., **43**(2), pp. 386–389.
[9] Hoey, R. G., 1992, "Research on the Stability and Control of Soaring Birds," AIAA Paper No. AIAA-1992-4122.
[10] Tucker, V., 1995, "Drag Reduction by Wing Tip Slots in a Gliding Harris' Hawk, Parabuteo Unicinctus," J. Exp. Biol., **198**, pp. 775–781.
[11] Smith, M. J., Komerath, N., Ames, R., Wong, O., and Pearson, J., 2001, "Performance Analysis of a Wing With Multiple Winglets," AIAA Paper No. AIAA-2001-2407.
[12] La Roche, U., and La Roche, H. L., 2004, "Induced Drag Reduction Using Multiple Winglets, Looking Beyond the Prandtl-Munk Linear Model," AIAA Paper No. AIAA-2004-2120.
[13] Kroo, I., McMasters, J., and Smith, S. C., 1995, "Highly Nonplanar Lifting Systems," presented at *Transportation Beyond 2000: Technologies Needed for Engineering Design*, NASA Langley Research Center, Sept. 26–28.
[14] Cone, C. D., 1963, "The Aerodynamic Design of Wings With Cambered Span Having Minimum Induced Drag," NASA Technical Report No. TR R-152.
[15] Prandtl, L., 1923, "Applications of Modern Hydrodynamics to Aeronautics; Part II: Applications," NACA Report No. 116, Taken From NASA, 1979, "Classical Aerodynamic Theory," NASA Reference Publication No. 1050.
[16] Munk, M. M., 1923, "The Minimum Induced Drag of Aerofoils," NACA Report No. 121.
[17] Abbott, I. H., and Von Doenhoff, A. E., 1959, *Theory of Wing Sections Including a Summary of Airfoil Data*, Dover, Mineola, NY, Chaps., 1 and 6.
[18] Moffat, R. J., 1988, "Describing the Uncertainties in Experimental Results," Exp. Therm. Fluid Sci., **1**(1), pp. 3–17.
[19] Coleman, H. W., and Steele, W. G., 1995, "Engineering Application of Experimental Uncertainty Analysis," AIAA J., **33**(10), pp. 1888–1896.
[20] 1998, *Low Level Measurements*, 5th ed., J. Yeager, and M. A. Hrusch-Tupta, eds., Keithley Instruments, Inc., Cleveland, OH, Sec. 3.2.3.
[21] Barlow, J. B., Rae, W. H., and Pope, A., 1999, *Low-Speed Wind Tunnel Testing*, 3rd ed., Wiley, Hoboken, NJ, Chap. 10.
[22] Drela, M., and Youngren, H., 2001, XFOIL 6.94 User Guide, Aeronautics, and Astronautics Engineering, Massachusetts Institute of Technology, Cambridge, MA.
[23] Margason, R. J., and Lamar, J. E., 1971, "Vortex-Lattice FORTRAN Program for Estimating Subsonic Aerodynamic Characteristics of Complex Planforms," NASA Technical Note D-6142.
[24] Lamar, J. E., and Herbert, H. E., 1982, "Production Version of the Extended NASA-Langley Vortex Lattice FORTRAN Computer Code; Volume I, User's Guide," NASA Technical Memorandum TM-83303.
[25] Lamar, J. E., 2003, *Discussions of the Vortex Lattice Method Involving John Lamar, Pat Bookey, and David Miklosovic*, NASA Langley, Apr. 29.
[26] Miklosovic, D. S., Murray, M. M., Howle, L. E., and Fish, F. E., 2007, "Experimental Evaluation of Sinusoidal Leading Edges," J. Aircr., **44**(4), pp. 1404–1407.
[27] Samoylovitch, O., and Strelets, D., 2000, "Determination of the Oswald Efficiency Factor at the Aeroplane Design Preliminary Stage," Aircraft Design, **3**(3), pp. 167–174.

Victor Shatrov

Gunter Gerbeth[1]
e-mail: g.gerbeth@fzd.de

Forschungszentrum Dresden-Rossendorf,
P.O. Box 510119,
D-01314 Dresden, Germany

Regina Hermann
Leibniz Institute for Solid State and Materials Research (IFW) Dresden,
Helmholtzstrasse 20,
D-01069 Dresden, Germany

An Alternating Magnetic Field Driven Flow in a Spinning Cylindrical Container

This paper presents a numerical analysis of the free surface liquid metal flow driven by an alternating current magnetic field in a spinning cylindrical container. The axisymmetric flow structure is analyzed for various values of the magnetohydrodynamic interaction parameter and Ekman numbers. The governing hydrodynamic equations are solved by a spectral collocation method, and the alternating magnetic field distribution is found by a boundary-integral method. The electromagnetic and hydrodynamic fields are fully coupled via the shape of the liquid free surface. It is found that the container rotation may reduce the meridional flow significantly. [DOI: 10.1115/1.2948374]

1 Introduction

The rotating flow in a cylindrical container represents a generic problem in fluid mechanics. For instance, the symmetry breaking in a free-surface cylinder flow was analyzed by Lopez et al. [1], where the motion was driven by a constant rotation of the bottom wall. This flow is unstable to three-dimensional perturbations for sufficiently large rotation rates [1]. Very interesting free-surface phenomena were studied in a rotating fluid in a cylinder by Vatistas [2], where the flow was driven by a spinning disk at the bottom, and later by Suzuki et al. [3], where the flow was driven by the rotation of the whole bottom wall. The three-dimensional instability of the axisymmetric base flow driven by a rotating lid of a cylindrical enclosure was studied by Gelfgat et al. [4].

If the considered fluid is electrically conducting, external magnetic fields provide an interesting tool for a contactless stirring of the melt. Various flow topologies are possible depending on the feeding currents in the coil system, which create the external alternating magnetic field. The primarily azimuthal flow in a cylindrical container driven by a rotating magnetic field was considered, e.g., by Gelfgat et al. [5] or Grants and Gerbeth [6]. The flow stability in the case of a combined action of a rotating magnetic field and a mechanical rotation of the container was investigated by Pedchenko and Grants [7]. A purely meridional base flow is driven by an alternating magnetic field created by a corresponding alternating current in an axisymmetric coil system, which is vertically placed around the cylindrical container. The magnetic field is basically in vertical direction and the induced electrical current is an azimuthal one. The interaction of this induced electric current and the magnetic field gives rise to a time-independent Lorentz force distribution, which drives a radial-meridional flow. This type of melt stirring is well known for electromagnetic induction heating.

The combination of this electromagnetic meridional flow driving force with a mechanical rotation of the liquid container represents an interesting tool to arrange the flow field inside the liquid. Meridional and azimuthal flow components are fully coupled. For instance, a suppression of the meridional flow can be expected for an increasing spinning rate of the container, whereas the meridional flow driving should also change the azimuthal flow. This superposition of global rotation and electromagnetic flow driving was recently considered by Shatrov et al. [8] for the case of a spherical droplet as it typically occurs in electromagnetic levitation processing. The possibility of flow tailoring by the combination of mechanical rotation and electromagnetic stirring has recently received application in solidification studies [9,10]. Filip et al. [9] showed that a distinct reduction of the soft magnetic α-Fe phase can be obtained in the solidification of Nd–Fe–B alloys, if the melt crucible undergoes a mechanical rotation during solidification. Similarly, a strong influence of electromagnetic melt stirring on the morphology was found for solidified Ti–Al alloys [10].

In the present paper, the basic axisymmetric flow driven by an alternating external magnetic field and an additional rotation of the liquid container is analyzed numerically. The free liquid surface depends on the flow field and the contact angle to the sidewall. The externally applied magnetic field is strongly modified by the presence of the conducting liquid. Thus, the calculation of the electromagnetic forces is fully coupled to the flow field via the shape of the free surface of the liquid.

2 Problem Formulation

We consider the flow in a cylinder of radius R_0 and height H filled with a liquid metal of electrical conductivity σ, density ρ, kinematic viscosity ν, and surface tension γ. The cylinder rotates with angular velocity Ω_0 around its symmetry axis, as it is shown in Fig. 1 The cylindrical container is placed inside an inductor. The sizes of the inductor are much larger than H and the alternating magnetic field with frequency ω_0 is approximately uniform and parallel to the container symmetry axis (in absence of the liquid). The container is made from an electrically insulating material. This alternating magnetic field induces alternating electric currents inside the liquid metal. The interaction of the induced electric currents and the alternating magnetic field leads to a Lorentz force distribution inside the liquid. The Lorentz force has a stationary component and an oscillating one with double frequency $2\omega_0$. The eddy currents can be used to heat and melt the metal. We consider the thermodynamical equilibrium case: The metal is liquid and an almost uniform temperature distribution is established inside it. For simplicity, the temperature is considered as constant, and all physical properties of the liquid are constant as well. The stationary Lorentz force component drives a meridional flow inside the container. The part of the Lorentz force oscillating with the double frequency is neglected because inertia precludes any noticeable liquid reaction at the considered high frequencies in the range of hundreds of kilohertz. The free-surface shape of the liquid depends on the spinning rate, the gravity, the flow in the melt, the liquid surface tension, and the Lorentz force distribution along the surface. The distribution of the magnetic field, in turn, depends on the shape of the free surface. Thus, the

[1]Corresponding author.

Contributed by the Fluids Engineering Division of ASME for publication in the JOURNAL OF FLUIDS ENGINEERING. Manuscript received October 24, 2007; final manuscript received April 27, 2008; published online July 16, 2008. Assoc. Editor: Dimitris Drikakis.

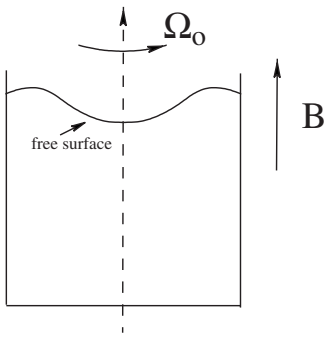

Fig. 1 Sketch of the spinning cylindrical container filled with a free-surface liquid metal

flow, the shape of the free surface, the ac magnetic field, and the Lorentz force distribution are fully coupled and must be determined simultaneously.

3 ac Magnetic Field Distribution

In order to calculate the ac magnetic field, we use the boundary-integral method [11]. Inside the electrically conducting liquid, the magnetic field is governed by the induction equation

$$i\omega_0 \boldsymbol{B} = \frac{1}{\mu_0 \sigma} \Delta \boldsymbol{B} \tag{1}$$

where μ_0 is the permeability of vacuum. Note that the effect related to the liquid flow (the $\boldsymbol{v} \times \boldsymbol{B}$ term) has been neglected in the equation above which according to Ref. [12] is a valid approximation for high-enough frequencies. Thus, the electromagnetic part of the problem is coupled to the hydrodynamic one only via the free-surface shape. For a given free surface, we can find the ac magnetic field distribution separately from the hydrodynamic part of the problem. Due to the axisymmetry of the problem, the poloidal magnetic field $\boldsymbol{B}$ under consideration here can be described by using a purely azimuthal vector potential $\boldsymbol{A} = A_\phi \boldsymbol{e}_\phi$ as $\boldsymbol{B} = \nabla \times \boldsymbol{A}$. Hence, the solution of Eq. (1) can be obtained in terms of the scalar $A_\phi(r, \theta, t)$.

The boundary-integral method [11] is based on the vector potential formulation, and makes use of Green's functions of Laplace and Helmholtz equations for the exterior and interior regions of the conducting melt. The method reduces the electromagnetic problem to the solution of two coupled boundary-integral equations, which are written in cylindrical coordinates as

$$\int_L \left(\frac{\partial \Psi(\boldsymbol{r}')}{\partial n'} r G^0_\phi(\boldsymbol{r}, \boldsymbol{r}') - \frac{\Psi(\boldsymbol{r}')}{r'} \frac{\partial (r r' G^0_\phi(\boldsymbol{r}, \boldsymbol{r}'))}{\partial n'} \right) d|\boldsymbol{r}'| + 2\pi c(\boldsymbol{r}) \Psi(\boldsymbol{r}) = 4\pi \Psi_0(\boldsymbol{r}) \tag{2}$$

$$\int_L \left(\frac{\partial \Psi(\boldsymbol{r}')}{\partial n'} r G^\lambda_\phi(\boldsymbol{r}, \boldsymbol{r}') - \frac{\Psi(\boldsymbol{r}')}{r'} \frac{\partial (r r' G^\lambda_\phi(\boldsymbol{r}, \boldsymbol{r}'))}{\partial n'} \right) d|\boldsymbol{r}'| - 2\pi c(\boldsymbol{r}) \Psi(\boldsymbol{r}) = 0 \tag{3}$$

where $\Psi(\boldsymbol{r}) = r A_\phi(\boldsymbol{r})$. For the assumed uniform external ac magnetic field, there is $\Psi_0(\boldsymbol{r}) = r^2/2$. The quantity $c(\boldsymbol{r})$ is a geometrical parameter, which for the case of linear boundary elements is simply $c(\boldsymbol{r}) = 1$. The variable $\boldsymbol{r}$ defines a control point on a contour L forming the conducting body of rotation. The Green functions [11] are

$$G^0_\phi(\boldsymbol{r}, \boldsymbol{r}') = \frac{4k}{\sqrt{(r' r)}} \left(\frac{K(k) - E(k)}{k^2} - \frac{K(k)}{2} \right) \tag{4}$$

$$G^\lambda_\phi(\boldsymbol{r}, \boldsymbol{r}') = \frac{2k}{\sqrt{(r' r)}} \int_0^{\pi/2} \frac{2\sin^2(\phi) - 1}{\sqrt{(1 - k^2 \sin^2(\phi))}} \times \exp(-\kappa \sqrt{(1 - k^2 \sin^2(\phi))}) d\phi \tag{5}$$

where $\kappa = 2\lambda \sqrt{r' r}/k$, and $\lambda^2 = 2i/\delta$ with the dimensionless skin depth $\delta = \sqrt{2/\mu_0 \sigma \omega_0 R_0^2}$. We use also the dimensionless frequency $\omega = \mu_0 \sigma \omega_0 R_0^2$. $K(k)$ and $E(k)$ are the complete elliptic integrals [13] of the first and second kinds, respectively, of the modulus $k = 2\sqrt{r' r/((r' + r)^2 + (z' - z)^2)}$.

Whereas different techniques for Green's function calculations are described [11], we applied a simple Gauss quadrature directly to the integral (5) using a cubic mapping near the collocation points. Though being rather slow, this method gives good accuracy. In order to solve systems (2) and (3), the integration contour L was disctretized by N_{elem} linear elements. Their sizes were reduced near the two corners of the contour using a cubic mapping. This leads to sufficiently small element sizes near the corners of the border, where the solution of the electromagnetic problem has a weak singularity [14,15].

A first test of the code was done for a sphere. The total dissipated power defined in terms of dimensionless surface quantities is [11]

$$N_p = \pi \omega \int_L \Im \left(\frac{\partial \Psi}{\partial n} \frac{\Psi^\star}{r} \right) d|\boldsymbol{r}| \tag{6}$$

where $\Im$ stands for the imaginary part and the asterisk denotes the complex conjugate. The power is scaled by $N_0 = R_0 B_0^2/(\sigma \mu_0^2)$. The exact value of this dissipated power is known analytically [11] as

$$N_p^{\text{exact}} = 2\pi \omega \Im \left(\frac{j_1^\star(s)}{s^\star j_0^\star(s)} \left(1 - \frac{j_2(s)}{2 j_0(s)} \right) \right)$$

where $s = \sqrt{\omega/i}$, and $j_n(s)$ is the spherical Bessel function of order n. The relative errors in the calculated power for a sphere in a uniform ac magnetic field are plotted in Fig. 2. It is shown that the errors for all considered frequencies are small and the method has a second order accuracy of convergence. In the case of high frequencies, there is a nonmonotonic behavior when the number of elements is small, but for $N_{\text{elem}} > 100$ the convergence is of second order, too.

In the second test, we calculate the ac magnetic field for the case of a cylinder with aspect ratio $H/(2R_0) = 1$. Now, there are two corners on the contour L, and the exact value of the total dissipated power in the cylinder is unknown. We repeated the power calculation for various N_{elem}, extrapolated them to the case of $N_{\text{elem}} = \infty$, and found the errors. The relative errors are plotted in Fig. 3. The convergence is of second order for all considered frequencies. The distribution of $\Re(\Psi) = \Re(r A_\phi)$ along a contour $L(s)$, where s denotes the distance along the contour, in the case of $\omega = 2 \times 10^4$ (which corresponds to a dimensionless skin depth $\delta = 0.01$) is plotted in Fig. 4 as an example. The two solutions with various element numbers $N_{\text{elem}} = 80$ and $N_{\text{elem}} = 160$ are almost identical. The vector-potential A_ϕ is finite in all points, but its first derivatives near the two edges ($z = 0$, $r = 1$ and $z = 2$, $r = 1$) are large. The cubic mapping helps us to achieve the necessary accuracy using a reasonable number of linear boundary elements.

In the present study, we shall consider only the case of a fixed frequency of $\omega = 2 \times 10^2$, corresponding to a dimensionless skin depth of $\delta = 0.1$. When A_ϕ is found, the time-averaged Lorentz force can be obtained in dimensionless form as $\boldsymbol{f} = \frac{1}{2} \Im[A \nabla A^*]$.

4 Numerical Method

We consider the flow inside the cylindrical container in the rotating frame of reference. Scaling length, time, velocity, and

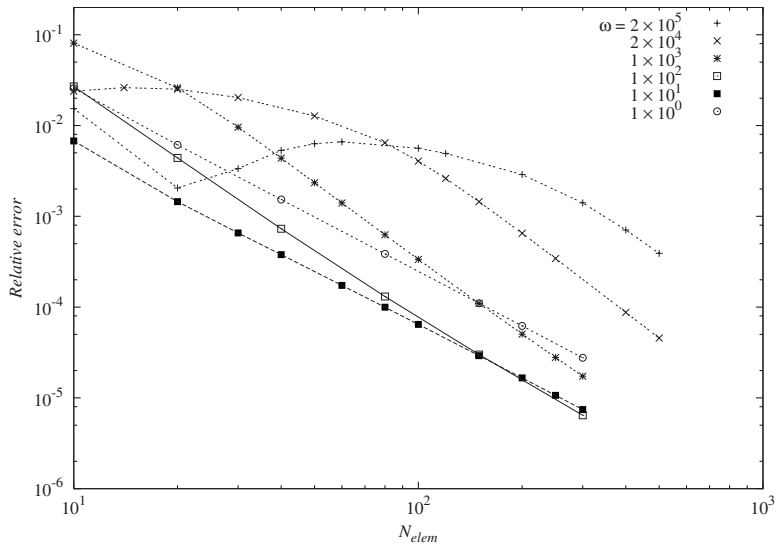

Fig. 2 The relative errors in total power for a sphere for various nondimensional frequencies ω and number of elements N_{elem}

pressure by R_0, R_0^2/ν, ν/R_0, and $\rho(\nu/R_0)^2$, respectively, we obtain the following dimensionless governing equations in the rotating frame of reference:

$$\frac{\partial \boldsymbol{v}}{\partial t} + (\boldsymbol{v}\cdot\nabla)\boldsymbol{v} + \frac{2}{E}\boldsymbol{e}_z \times \boldsymbol{v} = -\nabla P + \Delta \boldsymbol{v} + N\boldsymbol{f}, \quad \nabla \cdot \boldsymbol{v} = 0 \quad (7)$$

where $\boldsymbol{f}$ is the Lorentz force given above, $N=\sigma\omega R_0^4 B_0^2/(\rho\nu^2)$ is the interaction parameter characterizing the amplitude of the electromagnetic force, and $E=\nu/(\Omega_0 R_0^2)$ is the Ekman number. The true thermodynamic pressure p in the fluid is related to the total pressure P by

$$P = p - \frac{r^2}{2E^2} + Gh(r)$$

where G stands for the dimensionless gravity $G=gR_0^3/\nu^2$ with $g=9.87\ \mathrm{m/s^2}$, and $z=h(r)$ denotes the unknown free surface of the fluid.

For the fluid regions in contact with the container walls (the bottom at $z=0$ and the sidewall at $r=1$), the boundary condition for the velocity is the no-slip one $\boldsymbol{v}=0$. On the free-surface $z=h(r)$, there is a free-slip condition $e_{ij}t_i n_j=0$ and also $v_i n_i=0$ where e_{ij} denote the fluid shear stress and t_i, n_j components of the free-surface tangential and normal vectors, respectively [16].

For the axysimmetric case, it is convenient to introduce the stream function $\psi(r,z)$. Then, the meridional velocity components are $v_r=-1/r\partial\psi/\partial z$ and $v_z=1/r\partial\psi/\partial r$, and the azimuthal component of the vorticity is $w=\partial v_r/\partial z-\partial v_z/\partial r$. In terms of these quantities, the Navier–Stokes equation (7) for the steady case are

$$\frac{\partial(v_z w)}{\partial z} + \frac{\partial(v_r w)}{\partial r} - \frac{2v_\phi}{r}\frac{\partial v_\phi}{\partial z} - \frac{2}{E}\frac{\partial v_\phi}{\partial z} = \frac{\partial^2(w)}{\partial z^2} + \frac{\partial^2(w)}{\partial r^2} + \frac{1}{r}\frac{\partial w}{\partial r} - \frac{w}{r^2} + N(\nabla \times \boldsymbol{f})_\phi$$

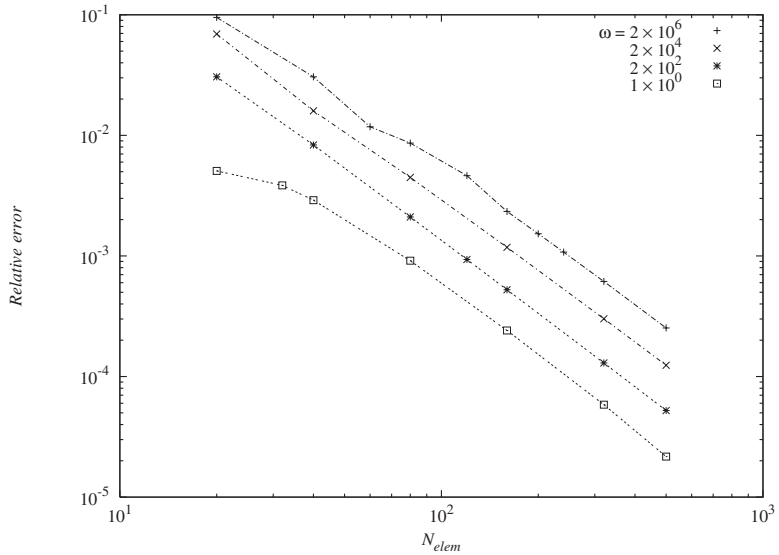

Fig. 3 The relative errors in total power for a cylinder for various nondimensional frequencies ω and number of elements N_{elem}

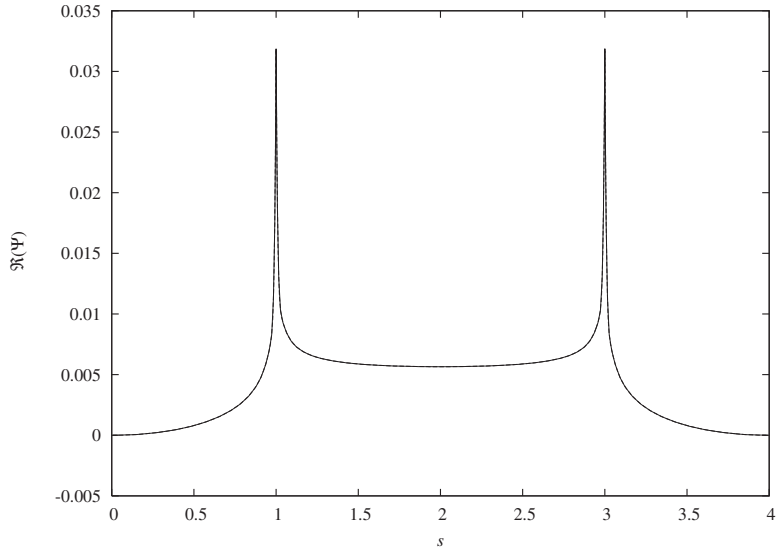

Fig. 4 The distribution $\Re(\Psi)=\Re(rA_\phi)$ along a contour $L(s)$ for nondimensional frequency $\omega=2\times10^4$ ($\delta=0.01$), and boundary element numbers $N_{elem}=80$ and $N_{elem}=160$, which are, however, not distinguishable with the precision of the line drawing

$$\frac{\partial^2\psi}{\partial z^2}+\frac{\partial^2\psi}{\partial r^2}-\frac{1}{r}\frac{\partial\psi}{\partial r}=-rw$$

$$v_z\frac{\partial\Omega}{\partial z}+v_r\frac{\partial\Omega}{\partial r}+2v_r\frac{\Omega}{r}+\frac{2}{rE}v_r=\frac{\partial^2\Omega}{\partial z^2}+\frac{\partial^2\Omega}{\partial r^2}+\frac{3}{r}\frac{\partial\Omega}{\partial r} \tag{8}$$

where $\Omega(r,z)=v_\phi/r$.

We should solve this system of equations in the computational domain $0<r<1$, $0<z<h(r)$, where $h(r)$ is a free boundary, which should be determined simultaneously. We shall consider the flow with an only slightly deformed free surface in the sense that it does not reach the bottom of the container. Hence, the container spinning should be not too intensive and the corresponding Ekman number should exceed some lower value; otherwise, our considerations are not valid. We use the mapping $r=\xi$, $z=(1+\eta)h(\xi)/2$, where $0<\xi<1$, $-1<\eta<1$. In the new variables ξ and η, the computational domain is a simple rectangular one. The first derivatives of any variable u can be written as $\partial u/\partial z=(2/h)\partial u/\partial\xi$, $\partial u/\partial r=\partial u/\partial\xi-(h_\xi/h)(1+\eta)\partial u/\partial\eta$. The second derivatives can be found in a similar way; thus, system (8) can be written in the new variables ξ and η. These equations contain also mixed terms $\partial^2/\partial_{\eta\xi}$. The boundary conditions on the rigid surface of the container are

$$\psi=0,\quad \partial\psi/\partial\xi=0,\quad \Omega=0\quad \text{at } \xi=1$$

$$\psi=0,\quad \partial\psi/\partial\eta=0,\quad \Omega=0\quad \text{at } \eta=-1$$

and the boundary conditions on the free surface ($\eta=1$) are

$$\frac{4h_{\xi\xi}}{h(1+h_\xi^2)}\frac{\partial\psi}{\partial\eta}=\xi w$$

$$\frac{(1+h_\xi^2)}{h}\frac{\partial\Omega}{\partial\eta}-\frac{h_\xi}{2}\frac{\partial\Omega}{\partial\xi}=0$$

The Navier–Stokes equations are solved by a spectral collocation code. We express the stream function, vorticity, and angular velocity via base functions constructed from orthogonal Chebyshev polynomials $T_n(x)$ to meet already a part of the boundary conditions as follows:

$$\psi(\xi,\eta)=\sum_{j=0}^{n_r-2}\sum_{l=0}^{n_z-2}C_{jl}\frac{\xi^2}{2}R_j(\xi)(1+\eta-\eta^2-\eta^3)T_l(\eta)$$

$$R_j(\xi)=T_{2j}(\xi)-\frac{4(j+1)}{2j+3}T_{2j+2}(\xi)+\frac{2j+1}{2j+3}T_{2j+4}(\xi)$$

$$w(\xi,\eta)=\sum_{j=0}^{n_r}\sum_{l=0}^{n_z}D_{jl}\xi T_{2j}(\xi)T_l(\eta)$$

$$\Omega(\xi,\eta)=\sum_{j=0}^{n_r-1}\sum_{l=0}^{n_z-1}E_{jl}(T_{2j}(\xi)-T_{2j+2}(\xi))(1+\eta)T_l(\eta)$$

Only even Chebyshev polynomials are needed in ξ-direction [8,17]. The Chebyshev collocation points $\xi_i=-\cos(\pi(i+n_r)/(2n_r))$, $i=0,\ldots,n_r$ and $\eta_k=-\cos(\pi k/n_z)$, $k=0,\ldots,n_z$ are used. Note that collocation points η_k on the symmetry axis $\xi=0$ are used, too.

The free-surface position can be found from the dynamical boundary condition [16], which in the absence of an external gas pressure is obtained as

$$p-2(e_{rr}n_r^2+e_{zz}n_z^2+2e_{rz}n_rn_z)+G(K_1+K_2)/Bo=0 \tag{9}$$

where e_{ij} are stress tensor components, $n_r=-h_\xi/\sqrt{1+h_\xi^2}$, $n_z=1/\sqrt{1+h_\xi^2}$ are components of the surface normal vector, and the Bond number is given by $\mathrm{Bo}=\rho gR_0^2/\gamma$. The curvatures K_1 and K_2 can be found from

$$K_1+K_2=\frac{h_\xi}{\xi\sqrt{1+h_\xi^2}}+\frac{h_{\xi\xi}}{(1+h_\xi^2)^{3/2}}$$

The pressure is obtained from the Navier–Stokes equation in the following way. We multiply the steady Navier–Stokes equation (7) with a tangential to the free-surface unit vector $\boldsymbol{\tau}$, (its components are $\tau_\xi=1/\sqrt{1+h_\xi^2}$, $\tau_\eta=h_\xi/\sqrt{1+h_\xi^2}$),

$$\boldsymbol{\tau}\cdot\nabla P=\boldsymbol{\tau}\cdot(\Delta\boldsymbol{v}+N\boldsymbol{f}-(\boldsymbol{v}\cdot\nabla)\boldsymbol{v})$$

Integrating this expression from $\xi=0$ to ξ along the free surface yields

$$P(\xi) = P_0 + \int_0^{\xi} \boldsymbol{\tau} \cdot (\Delta \boldsymbol{v} + N\boldsymbol{f} - (\boldsymbol{v} \cdot \nabla)\boldsymbol{v}) ds$$

where P_0 is a reference value, which will be determined later. In order to calculate this integral, we must know the Lorentz force components, which may be easily found from the magnetic potential A_ϕ as follows:

$$f_z = \frac{1}{2}\Im\left(A_\phi \frac{\partial A_\phi^\star}{\partial z}\right), \quad f_r = \frac{1}{2}\Im\left(A_\phi \frac{\partial A_\phi^\star}{\partial r}\right)$$

In a point where the free surface contacts the sidewall of the container ($\xi=1$, $\eta=1$), we apply an additional boundary condition related to the contact angle α_0 there, which represents an additional independent parameter of the problem as follows:

$$h_\xi(\xi = 1) = \cot(\alpha_0) \tag{10}$$

Independent of the surface deformation, the total volume of a liquid should be constant, which for a unit aspect ratio yields

$$\int_0^1 h(\xi)\xi d\xi = 1$$

We express the free boundary positions as

$$h(\xi) = \sum_{j=0}^{n_r} H_j T_{2j}(\xi) \tag{11}$$

The unknown coefficients C_{jl}, D_{jl}, E_{jl}, H_j, and P_0 must be determined from the system of nonlinear equations (8)–(11). The total number of unknown variables is $3n_r n_z + n_r + 4$. This system of nonlinear equations is solved by a Newton method, in which a simple Gauss elimination method is used for the solution of related linear equation systems.

Thus, for a given free surface, we find the vector potential A_ϕ, then the Lorentz force $\boldsymbol{f}$, then the fluid flow solution, and then the related new free-surface position. The process repeats until convergence is reached. We could find the vector-potential A_ϕ by the boundary-integral method in all collocation points, but instead we use a slightly different approach. We find first A_ϕ on the boundary of the liquid, after that we determine A_ϕ inside the liquid from the equation

$$\frac{\partial^2(A_\phi)}{\partial z^2} + \frac{\partial^2(A_\phi)}{\partial r^2} + \frac{1}{r}\frac{\partial A_\phi}{\partial r} - \frac{A_\phi}{r^2} - \frac{2iA_\phi}{\delta^2} = 0$$

which is obtained from Maxwell equations using the Coulomb gauge $\nabla \cdot \boldsymbol{A} = 0$ [11]. If this equation is written in ξ, η variables, the solution can be expressed as

$$A_\phi = \sum_{j=0}^{n_r-1} \sum_{l=0}^{n_z} a_{jl} T_{2j+1}(\xi) T_l(\eta)$$

and the coefficients a_{jl} are found by a spectral collocation method.

The meridional flow in the liquid is basically driven by the Lorentz force, the strength of which scales with the magnetic interaction parameter N. The resulting dimensionless meridional velocity $v_m = \sqrt{v_z^2 + v_r^2}$ depends on the input parameter of the problem, but may be much larger than 1. Note that due to the chosen scaling in Eq. (7) the resulting velocity gives directly the related Reynolds number, and we define the meridional Reynolds number as $\mathrm{Re} = \max(v_m)$. In Table 1, we show some results of flow calculations for the purpose of code validation. Here, the free surface is fixed to be flat, the Ekman number is $E=1$, the interaction parameter $N = 5 \times 10^6$, the frequency $\omega = 2 \times 10^2$, the Bond number Bo $=1$, the dimensionless gravity $G = 3.5 \times 10^6$, the contact angle $\alpha = \pi/2$, and the aspect ratio is fixed to 1. We repeated the calculations with various values of collocation points $n_r = n_z = n$. Table 1 gives the Re values and also the maximum angular velocity $\Omega_m = \max(\Omega(\xi, \eta))$. It is seen that the so-called spectral convergence is reached.

Table 1 Meridional Reynolds number Re and maximum angular velocity Ω_m calculated for various collocation point values $n_r = n_z = n$

n	26	30	36	40
Re	74.4420	74.4389	74.4393	74.4393
Ω_m	4.67275	4.67214	4.67223	4.67224

5 Results of the Flow Calculations

We consider the flow of a liquid metal or a liquid metal alloy with a typical density $\rho \sim 3 \times 10^3$ kg/m^3, electrical conductivity $\sigma \sim 10^6 - 10^7$ S/m, and surface tension $\gamma \sim 1$ N/m in a container of $R_0 \sim 5-10$ mm in an external ac magnetic field with a frequency of $f_0 \sim 10^5$ Hz. The independent, nondimensional parameters of the problem are the ac field frequency ω, the interaction parameter N, the Ekman number of the container rotation E, the relative gravity G, the Bond number Bo, and the contact angle α_0. In our study, we fix $G = 3.5 \times 10^6$, Bo$=1$, $\omega = 2 \times 10^2$ (i.e., skin depth $\delta = 0.1$), and limit all calculations to an aspect ratio of 1 for the liquid in the container. We mainly consider variations of two control parameters of the problem, the interaction parameter N and the Ekman number E, but investigate also the influence of various contact angles. At first, we fix the contact angle to $\alpha_0 = \pi/2$.

Figure 5 shows the stream function ψ (left) and angular velocity Ω (right) isolines at a fixed interaction parameter value $N = 2 \times 10^7$ and various Ekman numbers $E=1$ (*a*), 0.1 (*b*), 1×10^{-2} (*c*), 1×10^{-3} (*d*), 1.5×10^{-4} (*e*). In all five cases, the flow consists of four toroidal eddies. The flow is vertically nonsymmetric due to the different boundary conditions of a rigid wall at the bottom and a free surface on top. The arrows show the direction of the flow, and the signs (+) and (−) indicate the direction of the related azimuthal motion. An increasing spinning (i.e., reducing E) leads to a suppression of the meridional flow. The upper boundary is almost flat at $E > 1 \times 10^{-3}$ and only at $E = 1.5 \times 10^{-4}$ the deformation of the free surface becomes significant. Figure 6 shows the meridional Reynolds number Re versus the Ekman number E for various interaction parameter N. For large E, which corresponds to slow rotation, the Reynolds number effectively depends only on the interaction parameter N but not on E. Increase in N results in larger Re that corresponds to a stronger meridional flow. Reduction of E, corresponding to a faster spinning container, results in a suppression of the meridional flow characterized by a reduced Reynolds number. The damping of the meridional flow becomes effective for $E < 0.01$ where a rather strong reduction of the meridional flow takes place for further decreasing E. This reduction becomes even more pronounced at larger N. The maximum absolute value of the azimuthal velocity v_ϕ is shown in Fig. 7 versus the Ekman number E for various interaction parameters N. A deviation of the fluid rotation from its average solid body rotation, characterized by v_ϕ in the rotating frame of reference, develops as the container starts to spin. In a slowly spinning container ($E \gg 1$), the azimuthal velocity is small because the Coriolis force, which is responsible for the differential rotation in the fluid, is weak in this case. In a rapidly spinning container ($E \ll 1$), the azimuthal velocity decreases with increasing spinning rate in accordance to the Proudman theorem, which requires the fluid flow to be nearly uniform along the axis of a rapidly rotating fluid. Hence, the azimuthal velocity has a maximum at an intermediate Ekman number $E \sim 0.001-0.01$. The kinks on the lower curve ($N = 5 \times 10^6$) are due to the changing location of the related velocity maxima.

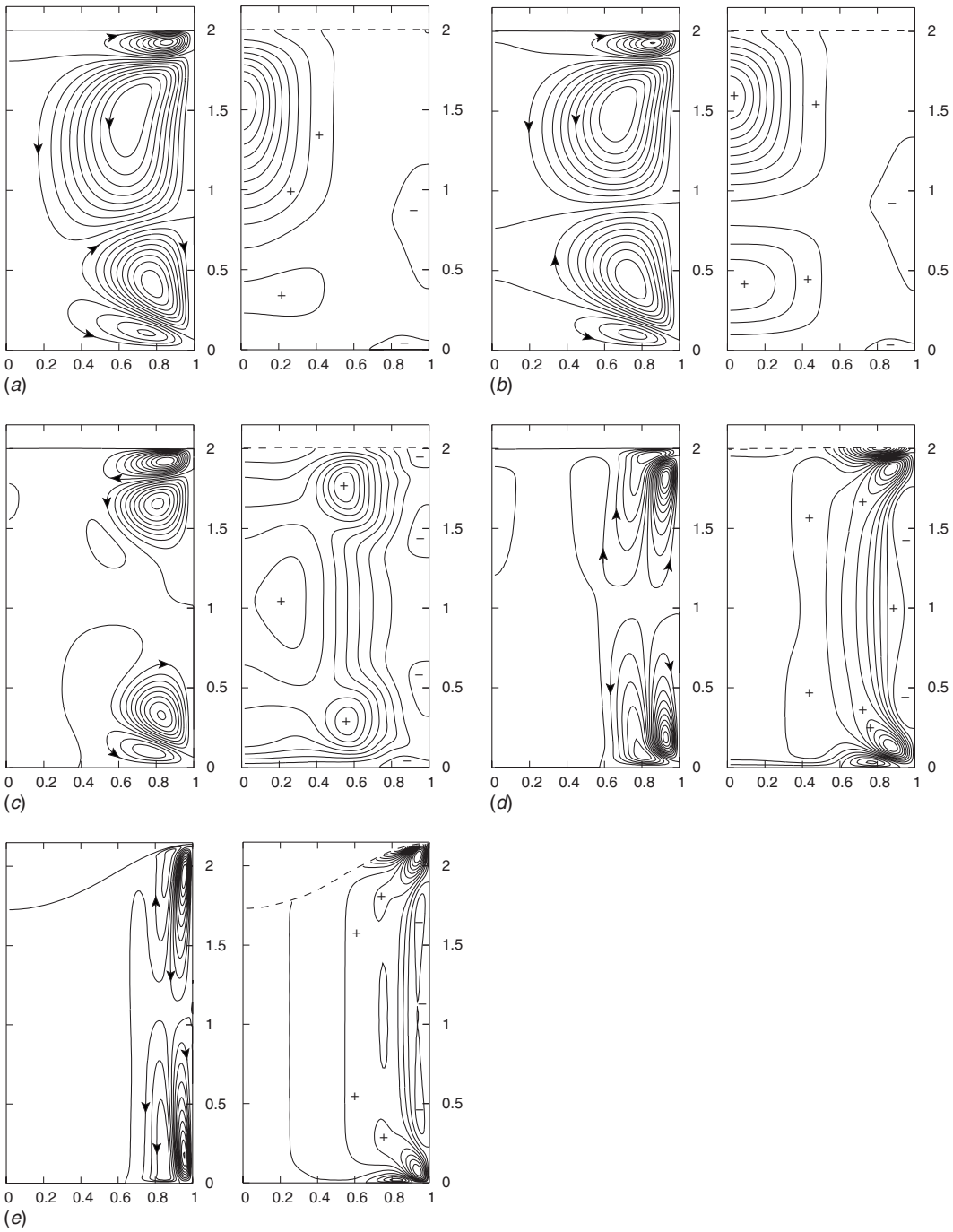

Fig. 5 Stream function ψ (on the left) and angular velocity Ω (on the right) isolines for interaction parameter $N=2\times10^7$ and Ekman numbers $E=1$ (*a*), 0.1 (*b*), 1×10^{-2} (*c*), 1×10^{-3} (*d*), 1.5×10^{-4} (*e*)

We repeated the flow calculations for different values of the contact angle α_0. Figure 8 shows the stream function isolines for the case of $N=2\times10^7$, $E=2\times10^{-3}$ for $\alpha_0=3\pi/4$ and $\alpha_0=\pi/4$, respectively. The flow has the same structure, there are always four toroidal eddies. Figure 9 shows the meridional Reynolds number Re versus the Ekman number E for $N=2\times10^7$ and various values of the contact angle α_0. The difference of the meridional Reynolds numbers at large Ekman numbers E is caused by the difference of the ac magnetic field distribution near the upper edge in case of varying contact angles. At Ekman number $E<1\times10^{-2}$, the meridional flow is suppressed by the container spinning for all considered contact angles α_0. Figure 10 shows the maximum of the azimuthal velocity component v_ϕ versus the Ekman number E and three different contact angles α_0. As seen, the varying contact angles have only a minor influence on the resulting azimuthal velocities.

In practice, the surface of liquid metals often consists of oxide layers or films, thus modifying the boundary conditions at the upper free surface significantly. Therefore, we repeated our analysis for this case where instead of free-slip boundary conditions we apply a no-slip boundary condition $\boldsymbol{\tau}\cdot\boldsymbol{v}=0$ on the upper surface ($\eta=1$) with $\boldsymbol{\tau}$ as a tangential to the surface unit vector. Here we fix the contact angle between the upper liquid surface and the container wall to $\alpha_0=\pi/2$. The stream function and angular velocity isolines are shown in Fig. 11 for the case of $N=2\times10^7$, $E=1.5\times10^{-4}$. The structure of the flow is very similar to the one

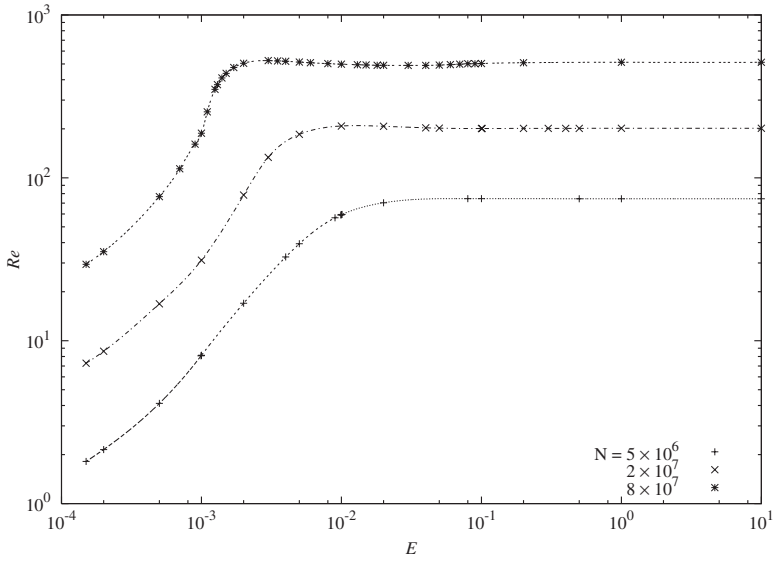

Fig. 6 The meridional Reynolds number Re versus Ekman number *E* for various interaction parameter values

shown in Fig. 5(*e*). Figure 12 shows the meridional Reynolds number Re versus Ekman number E for various interaction parameters N. Here the free-slip results of Fig. 6 are drawn by dashed lines for comparison. The main tendencies are the same as before. A strong container spinning suppresses the meridional flow. As expected, the velocities in the case of an upper oxide layer are always smaller compared to the free-surface case. The difference between the free-slip and the oxide-layer case becomes smaller at larger interaction parameters N, when the boundary layers on the upper boundary become thinner in both cases. The maximum absolute azimuthal velocity v_ϕ versus Ekman number E is shown in Fig. 13. Here again the free-slip curves from Fig. 7 are drawn by dashed lines. The pairs of curves for the free-slip and oxide-layer cases are close to each other with a vanishing difference at small Ekman numbers.

6 Conclusions

The liquid metal flow in a cylindrical rotating container driven by an alternating magnetic field as it is typical for a uniform induction heater is studied numerically. The free boundary was found simultaneously with the flow by a Newton method. Varying the Ekman number E, the magnetic interaction parameter N, as well as the contact angle α_0, it is found that in all considered parameter ranges the flow consists of four main toroidal eddies. This is mainly caused by the nonuniformity of the magnetic field near the edges of the liquid volume. The interaction parameter N controls the intensity of the meridional flow. The container spinning leads to a deformation of the flow structure. At Ekman numbers $E<1\times10^{-2}$, the meridional flow is significantly reduced. The azimuthal flow has its maximum in the Ekman number range

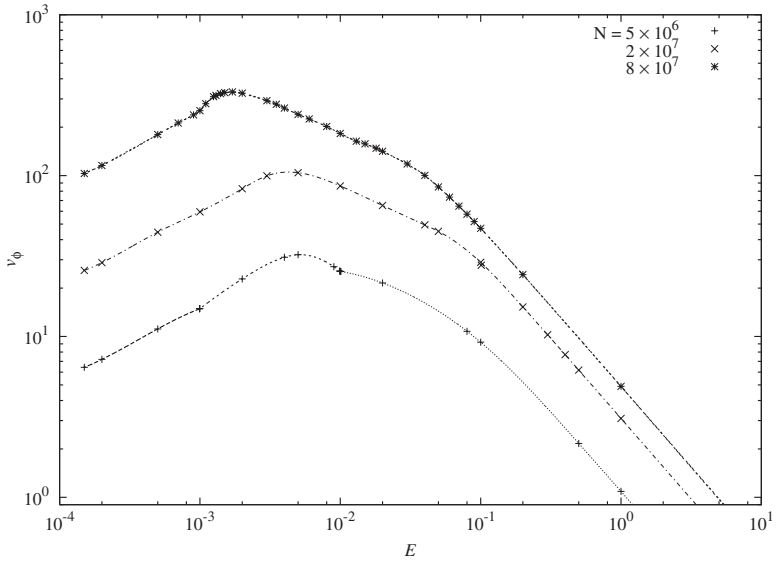

Fig. 7 The maximum of the azimuthal velocity versus Ekman number *E* for various interaction parameter values

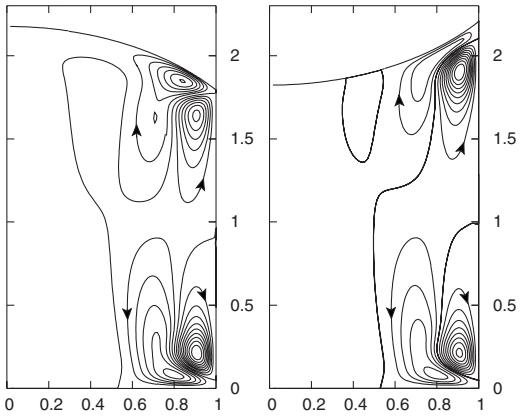

Fig. 8 Stream function ψ isolines for $N=2\times10^7$, $E=2\times10^{-3}$ and contact angles $\alpha_0=3\pi/4$ (*a*) and $\alpha_0=\pi/4$ (*b*)

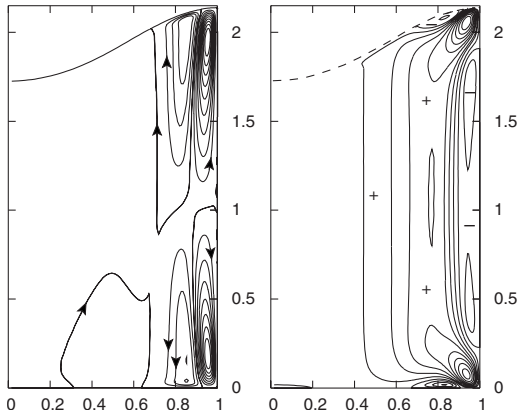

Fig. 11 Stream function ψ (on the left) and angular velocity Ω (on the right) isolines for $N=2\times10^7$, $E=1.5\times10^{-4}$. The surface of the liquid metal is covered by a thin oxide layer

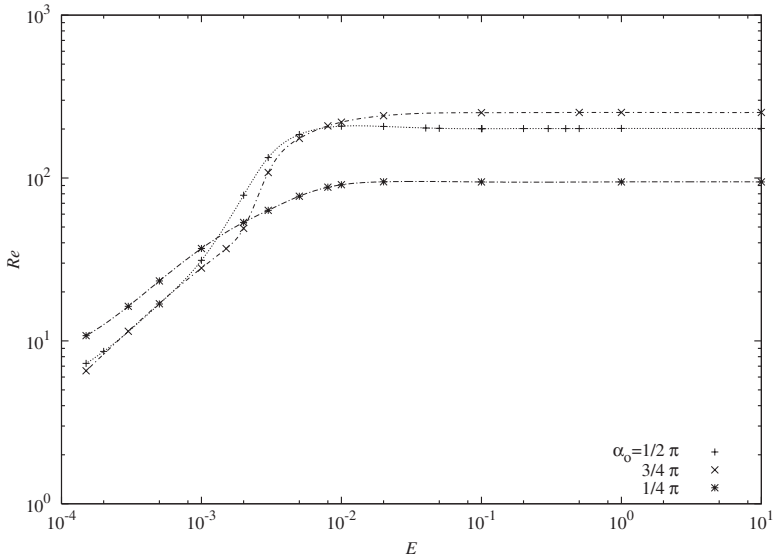

Fig. 9 The meridional Reynolds number Re versus Ekman number *E* for $N=2\times10^7$ and three values of the contact angle α_0

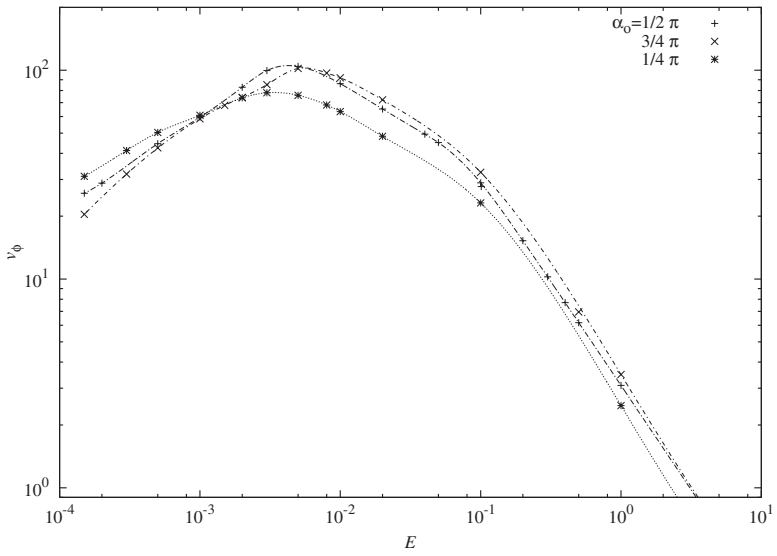

Fig. 10 The maximum of the azimuthal velocity versus Ekman number *E* for $N=2\times10^7$ and three values of the contact angle α_0

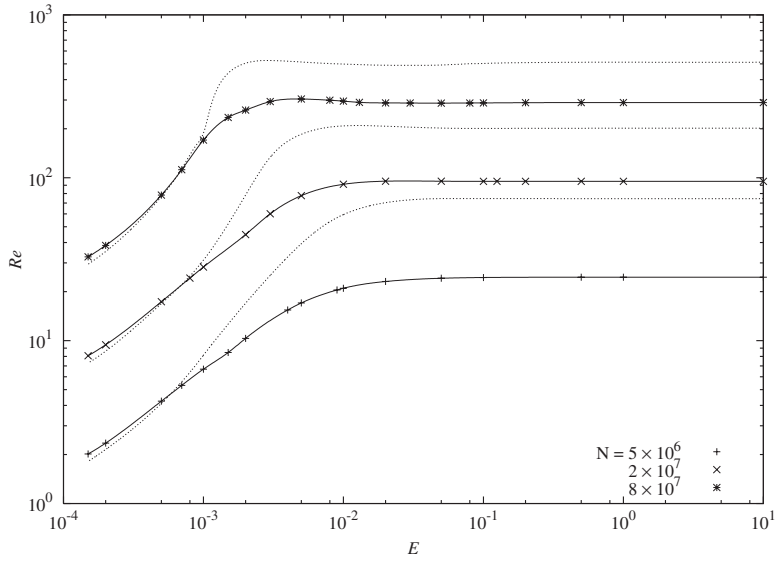

Fig. 12 The meridional Reynolds number Re versus Ekman number *E* for various interaction parameter values. The surface of the liquid metal is covered by a thin oxide layer. The dashed lines correspond to the free-slip case of Fig. 6.

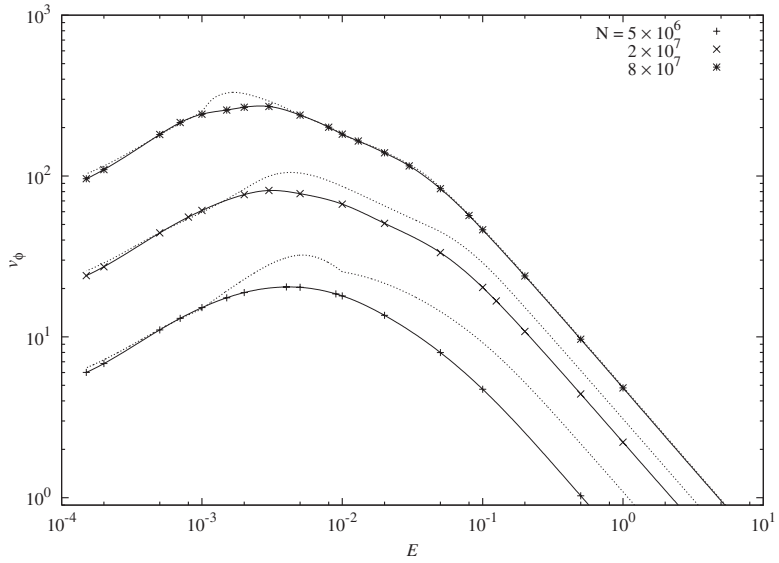

Fig. 13 The maximum of the azimuthal velocity versus Ekman number *E* for various interaction parameter values. The surface of the liquid metal is covered by a thin oxide layer. The dashed lines correspond to the free-slip case of Fig. 7.

of $E \sim 1 \times 10^{-3} - 1 \times 10^{-2}$; at smaller Ekman numbers the azimuthal flow is suppressed, too. The main conclusion is that a relatively strong container spinning suppresses the flow inside the liquid for all considered interaction parameter values.

Acknowledgment

This work has been supported by Deutsche Forschungsgemeinschaft under Grant No. HE 2955/2-2,3 and in frame of the Collaborative Research Center SFB 609.

Nomenclature

a_{ij} = coefficients
$\boldsymbol{A}$ = vector potential
A_ϕ = azimuthal vector potential component
$\boldsymbol{B}$ = magnetic field induction vector
B_0 = magnetic field induction amplitude, T
$c(\boldsymbol{r})$ = mathematical function, geometrical parameter
C_{jl} = coefficients
D_{jl} = coefficients
$\boldsymbol{e}_r$ = unit vector in r-direction
$\boldsymbol{e}_z$ = unit vector in z-direction
$\boldsymbol{e}_\phi$ = unit vector in ϕ-direction
e_{ij} = fluid shear stress
E_{jl} = coefficients
E = Ekman number, $\nu/(\Omega_0 R_0^2)$
$\boldsymbol{f}$ = dimensionless time-average Lorentz force vector

f_0 = frequency of external alternating magnetic field, Hz
f_r = dimensionless time-average Lorentz force r-component
f_z = dimensionless time-average Lorentz force z-component
g = acceleration due to gravity, ms^{-2}
G = dimensionless acceleration due to gravity, gR_0^3/ν^2
G_ϕ^0 = Green's function for the azimuthal vector potential component outside the conducting fluid
G_ϕ^λ = Green's function for the azimuthal vector potential component inside the conducting fluid
h = dimensionless free-surface position
H = height of cylinder, m
H_j = coefficients
$j_n(x)$ = spherical Bessel function of order n
K_1, K_2 = free-surface curvatures
n_r = number of collocation points in r-direction
n_z = number of collocation points in z-direction
n_j = component of normal to the free-surface unit vector
N = interaction parameter, $\sigma\omega R_0^4 B_0^2/(\rho\nu^2)$
N_p = dissipated power
N_0 = dissipated power scale, $R_0 B_0^2/(\sigma\mu_0^2)$
N_{elem} = number of elements
p = thermodynamic pressure
P = pressure
P_0 = reference pressure value
r = dimensionless radial coordinate
R_j = mathematical function
R_0 = radius of cylinder, m
t_i = component of tangential to the free-surface unit vector
T_l = Chebyshev polynomial
$\boldsymbol{v}$ = dimensionless fluid velocity
v_m = maximum of dimensionless meridional fluid velocity
v_r = r-component of the dimensionless fluid velocity
v_z = z-component of the dimensionless fluid velocity
v_ϕ = ϕ-component of the dimensionless fluid velocity
w = dimensionless fluid vorticity
z = dimensionless z-coordinate
α_0 = contact angle, rad
δ = dimensionless skin depth, $\sqrt{2/\mu_0\sigma\omega_0 R_0^2}$
μ_0 = permeability of vacuum, $\mathrm{N\,A}^{-2}$
ν = kinematic viscosity of the liquid, $\mathrm{m}^2\,\mathrm{s}^{-1}$
γ = surface tension of the liquid, N/m
ψ = stream function of the meridional flow
σ = electrical conductivity of the liquid, $\mathrm{S\,m}^{-1}$
ρ = liquid density, $\mathrm{kg\,m}^{-3}$
Ω = dimensionless angular fluid velocity
ω_0 = angular frequency of external alternating magnetic field, $2\pi f_0$, $\mathrm{rad\,s}^{-1}$
ω = dimensionless frequency of external alternating magnetic field

References

[1] Lopez, J. M., Marques, F., Hirsa, A. H., and Miraghaie, R., 2004, "Symmetry Breaking in Free-Surface Cylinder Flows," J. Fluid Mech., **502**, pp. 99–126.
[2] Vatistas, G. H., 1990, "A Note on Liquid Vortex Sloshing and Kelvin's Equilibria," J. Fluid Mech., **217**, pp. 241–248.
[3] Suzuki, T., Lima, M., and Hayase, Y., 2006, "Surface Switching of Rotating Fluid in a Cylinder," Phys. Fluids, **18**, 101701.
[4] Gelfgat, A. Yu., Bar-Yoseph, P. Z., and Solan, A., 2001, "Three-Dimensional Instability of Axisymmetric Flow in a Rotating Lid-Cylinder Enclosure," J. Fluid Mech., **438**, pp. 363–377.
[5] Gelfgat, Yu., Priede, J., and Sorkin, M. Z., 1991, "Numerical Simulation of MHD Flow Induced by Rotating Magnetic Field in Cylindrical Container of Finite Length," in *Proceedings of the International Conference on Energy Transfer in MHD Flows*, Grenoble, France, pp. 181–186.
[6] Grants, I., and Gerbeth, G., 2002, "Linear Three-dimensional Instability of a Magnetically Driven Rotating Flow," J. Fluid Mech., **463**, pp. 229–240.
[7] Pedchenko, A., and Grants, I., 2005, "Instability of Rotating Magnetic Field Driven Flow in a Counter-Rotating Cylinder," Phys. Fluids, **17**, 104102.
[8] Shatrov, V., Priede, J., and Gerbeth, G., 2006, "Basic Flow and its 3D Linear Stability in a Small Spherical Droplet Spinning in an Alternating Magnetic Field," Phys. Fluids, **19**, 078106.
[9] Filip, O., Hermann, R., Gerbeth, G., Priede, J., and Biswas, K., 2005, "Controlling Melt Convection—An Innovative Potential for Concerted Microstructure Evolution of Nd-Fe-B Alloys," Mater. Sci. Eng., A, **413–414**, pp. 302–305.
[10] Biswas, K., Hermann, R., Das, J., Priede, J., Gerbeth, G., and Acker, J., 2006, "Tailoring the Microstructure and Mechanical Properties of Ti-Al Alloy Using a Novel Electromagnetic Stirring Method," Scr. Mater., **55**, pp. 1143–1146.
[11] Priede, J., and Gerbeth, G., 2006, "Boundary-Integral Method for Calculating Poloidal Axisymmetric ac Magnetic Field," IEEE Trans. Magn., **42**(2), pp. 301–308.
[12] Mestel, A. J., 1982, "Magnetic Levitation of Liquid Metals," J. Fluid Mech., **117**, pp. 27–43.
[13] Gradshteyn, I. S., and Ryzhik, I. M., 2000, *Tables of Integrals, Series and Products*, 6th ed., Academic, New York, p. 851.
[14] Meixner, J., 1972, "The Behavior of Electromagnetic Fields at Edges," IEEE Trans. Antennas Propag., **AP-20**, pp. 442–446.
[15] Yakovlev, V. I., 1995, "On the Singularity of Alternating Electromagnetic Fields in the Vicinity of the Apex of a Conducting wedge," J. Appl. Mech. Tech. Phys., **37**(4), pp. 459–463.
[16] Batchelor, G. K., 1967, *An Introduction to Fluid Dynamics*, *Cambridge University Press*, Cambridge, UK, pp. 149–150.
[17] Tuckerman, L. S., 1989, "Divergence-Free Velocity Fields in Nonperiodic Geometries," J. Comput. Phys., **80**, pp. 403–441.

Comparison Between Theoretical CFV Flow Models and NIST's Primary Flow Data in the Laminar, Turbulent, and Transition Flow Regimes

Aaron Johnson
e-mail: aaron.johnson@nist.gov

John Wright

National Institute of Standards and Technology (NIST),
100 Bureau Drive,
Mail Stop 8361,
Gaithersburg, MD 20899

State-of-the art dimensional metrology was used to measure the throat diameter and throat curvature of nine critical flow venturis (CFVs) with nominal throat diameters ranging from 5 mm to 25 mm. The throat curvature was used in calculating the theoretical discharge coefficients, while the throat diameter was used in computing the experimental discharge coefficients. The nine CFVs were calibrated in dry air using two NIST primary flow standards with expanded uncertainties of 0.05% and 0.09%, respectively. The calibration data span a Reynolds number range from 7.2×10^4 to 2.5×10^6, including laminar, transition, and turbulent flow regimes. By correcting for both the throat diameter and curvature, the agreement between predicted and measured discharge coefficients was less than 0.17% in the turbulent regime and less than 0.07% in the laminar regime. [DOI: 10.1115/1.2903806]

Introduction

Critical flow venturis (CFVs) are widely used in the flow metering community as flow meters, check standards, and transfer standards. The popularity of these devices is a result of their excellent long term reproducibility [1], simple geometric design [2], straightforward application, and well understood physics. Much of the pioneering work for CFV flowmeters was done during the 1960s and 1970s when numerous theoretical flow models were developed for predicting the CFV discharge coefficient. Recent calibration data taken in air by Ishibashi [3–6] quantified the accuracy of these models over a portion of the laminar flow regime. Ishibashi's measurements of the discharge coefficient agreed with theoretical predictions to better than 0.03% over a Reynolds numbers range from 8×10^4 to 2.5×10^5. For this comparison, he used *high precision nozzles* (HPNs), manufactured on ultrahigh precision lathes, whose throat diameters (d) are known to better than a fraction of a micron and whose throat radius of curvature (r_c) and overall CFV profiles match the ISO [2] recommended shape to better than 1 μm. Consequently, HPNs come closest of any manufactured CFV to the ideal nozzle shape and are the best choice for comparing measured versus predicted values of the discharge coefficient.

Unfortunately, for CFV theorists, the high cost of HPNs, which is nearly ten times that of a normally manufactured CFV, significantly reduces their use within the flow metering community. By normally manufactured, we mean produced on something less than an ultrahigh precision lathe and generally polished after machining. For practical reasons, it is of interest to determine how well the discharge coefficients of normally manufactured CFVs compare with theoretically predicted values.

In this work, NIST characterized both the flow performance and geometry of nine normally manufactured CFVs. The nominal CFV throat diameters ranged from 5 mm to 25 mm, and the Reynolds numbers extended from 7.2×10^4 to 2.5×10^6. The flow calibrations were done in dry air using two pressure-volume-temperature-time (PVTt) primary flow standards [7–10]. NIST's Moore M48 coordinate measuring machine was used to determine the CFV contours [11], from which we determined the throat diameter, and the throat curvature ratio ($\Omega\equiv d/2r_c$). Other geometric features that were qualitatively assessed include the degree of eccentricity and twist of the various cross sections along the CFV centerline.

The measured d's were used in calculating the experimental discharge coefficients ($C_{d,\mathrm{exp}}$), while Ω's were used in calculating the predicted discharge coefficients ($C_{d,\mathrm{th}}$). Figure 1 shows that the overall agreement between $C_{d,\mathrm{exp}}$ and $C_{d,\mathrm{th}}$ is better than 0.17% over a Reynolds number range extending from 7.2×10^4 to 2.5×10^6. This good agreement is surprising since no effort was made to model the boundary layer transition from laminar to turbulent flow. Instead, we implemented a simple piecewise model that assumed laminar flow for Reynolds numbers below 10^6 and turbulent flow at higher Reynolds numbers.

The theoretically predicted discharge coefficient ($C_{d,\mathrm{th}}$) is obtained using a composite model consisting of three submodels. Each submodel accounts for different physical phenomena including boundary layer development along the CFV wall, curvature of the sonic line at the CFV throat, and departure from ideal gas behavior (i.e., virial effects). In general, these three mechanisms characterize the discharge coefficient of CFV flows. Other secondary mechanisms affecting the discharge coefficient, such as swirl, heat transfer, and vibrational relaxation, are made insignificant by selecting the appropriate gases and flow conditions (i.e., swirl free dry air at near ambient temperature). We use experimental data to assess the accuracy of several of the commonly used submodels, and we introduce a systematic approach based on a Taylor series expansion method to combine the three submodels into a single composite model for predicting $C_{d,\mathrm{th}}$. The Taylor series method is also used to estimate errors in $C_{d,\mathrm{exp}}$ attributed to species dependent virial effects. These errors are inherent in the present definition of the discharge coefficient, which attempt to eliminate the

Contributed by the Fluids Engineering Division of ASME for publication in the JOURNAL OF FLUIDS ENGINEERING. Manuscript received August 16, 2006; final manuscript received May 18, 2007; published online July 22, 2008. Assoc. Editor: James A. Liburdy.

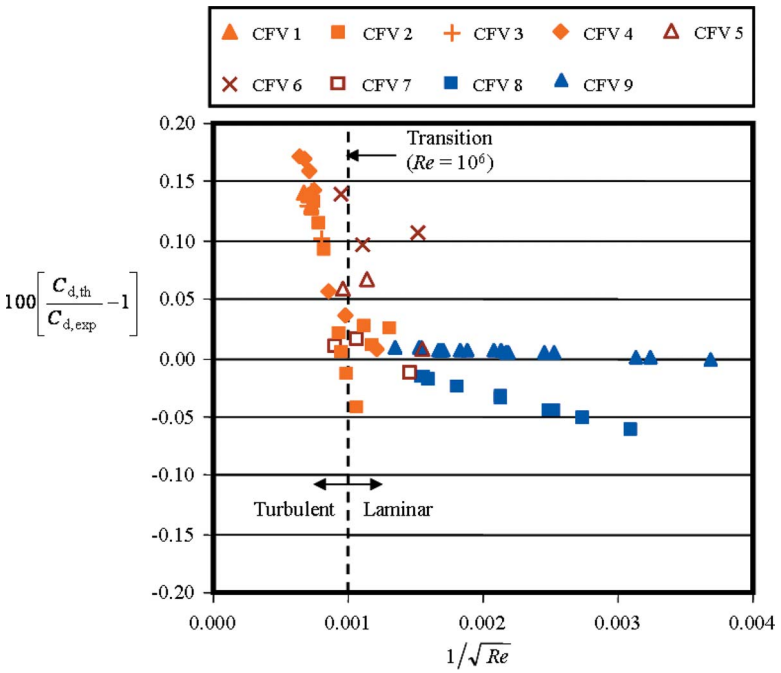

Fig. 1 Percent difference between theoretical models and experimental data for nine normally manufactured CFVs

influence of virial effects so that $C_{d,\mathrm{exp}}$ is primarily dependent on Reynolds number alone. These errors must be considered whenever a CFV is calibrated in one gas, but the calibration curve is applied using a different gas.

PVTt Flow Standards and the Historical Calibration Records of CFVs

The two NIST PVTt flow standards used to calibrate the CFVs have nominal collection tank volumes of 677 l and 26 m^3, respectively. Together, these PVTt systems cover a flow range extending from 100 l/min to 78,000 l/min.[1] The two smallest CFVs were calibrated using both the 677 l PVTt flow standard and the 26 m^3 PVTt flow standard. The remaining seven CFVs were calibrated using only the 26 m^3 PVTt standard. For all of the calibrations, the CFV stagnation temperature was maintained close to room temperature while the stagnation pressure ranged from 150 kPa to 850 kPa. The expanded mass flow uncertainties for the 677 l and 26 m^3 PVTt systems are 0.05% [7,8] and 0.09% [9,10], respectively.

Table 1 shows the calibration history for the set of nine CFVs. For convenience, each CFV is identified by the numerical value in Column 1 throughout this document. Column 2, gives the total number of calibration points (where the number of calibrations is in parentheses), Column 3 provides the standard deviation of residuals between a best fit curve of all the calibration data and the measured discharge coefficients, and Column 4 gives the relative uncertainty of the measured discharge coefficients (where the values in parentheses are the uncertainties obtained on the 677 l PVTt standard). Altogether, the calibration records contain 1007 data points.

The largest source of uncertainty in the discharge coefficient stems from the PVTt mass flow measurements. Other factors including the stagnation pressure, stagnation temperature, critical flow factor, throat diameter, etc., also contribute to the uncertainty so that the uncertainty of the discharge coefficient is slightly above the uncertainty of the mass flow. The uncertainty of CFV 6 is larger than its counterparts since all of its calibration data precede 2003, when performance upgrades reduced the uncertainty of the 26 m^3 PVTt flow standard from 0.21% to 0.09% [10].

Dimensional CFV Measurements

The throat diameter (d) and the throat curvature ratio (Ω) are the key geometric parameters for comparing measured and predicted values of the discharge coefficient. In a routine calibration, the discharge coefficient can be calculated using only a nominal value of the throat diameter. In this case, any error in diameter uniformly shifts the calibration curve above or below its true value, but the offset is compensated when the calibration curve is used to compute the mass flow provided the same nominal diameter is used. In fact, it is common to obtain measured discharge coefficients that exceed unity when $C_{d,\mathrm{exp}}$ is calculated using a nominal diameter that is less than the actual diameter. However,

Table 1 Calibration history for selected CFVs using dry air as the working fluid

CFV No.	No. of points (No. of cals)	Std. dev. of best fit residuals ($\times 10^6$)	Rel. unc. of discharge coefficient ($k=2$) (%)
1	37 (1)	80	0.11
2	79 (1)	170	0.11
3	42 (1)	137	0.11
4	62 (1)	68	0.11
5	150 (3)	405	0.11
6	60 (2)	482	0.21
7	90 (3)	460	0.11
8	234 (4)	300	0.11 (0.08)
9	253 (4)	290	0.11 (0.08)

[1]Unless otherwise noted, all volumetric flows in this paper are taken to be at standard conditions with a temperature at 293.15 K and a pressure of 101.325 kPa.

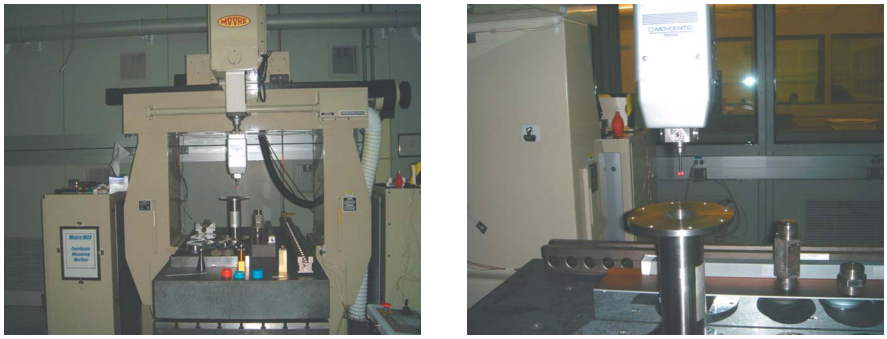

(*a*) (*b*)

Fig. 2 Moore M48 CMM (the left picture shows a full view of CMM while the right one shows a close-up of probe and CFV just prior to dimensional calibration)

any offset in $C_{d,\exp}$ is undesirable when comparing measured to predicted values of the discharge coefficient, and therefore highly accurate values of d are necessary. For example, since the discharge coefficient is proportional to the diameter squared, a diameter uncertainty of 0.05% leads to a 0.1% uncertainty in the measured discharge coefficient. On the other hand, the theoretical discharge coefficient is not strongly dependent on Ω, and relatively large uncertainties can be tolerated. For the Reynolds number range considered in this paper, an uncertainty of 10% or less is acceptable to ensure an effect of less than 0.02% on the predicted discharge coefficient.

Figure 2 shows pictures of NIST's Moore M48 coordinate measuring machine (CMM). This machine is commonly regarded as one of the most accurate CMMs in the world, capable of making position measurements with uncertainties as low as 0.05 μm. In this application, the uncertainty of throat diameter measurements is 0.5 μm (i.e., for $k=1$). This machine is housed in a temperature controlled environment that is maintained at $(20\pm0.01)\,^{\circ}\mathrm{C}$ to provide superior thermal stability. Moreover, the machine's heavy supporting structure gives it excellent mechanical stability. Detailed descriptions explaining the construction and operating principle of the Moore M48 can be found in Ref. [11].

Both d and Ω are indirectly determined by probing along the circumference of various cross sections and measuring contours along different azimuthal planes of symmetry. The contours of the CFVs are determined by traversing the probe of the Moore M48 along the nozzle wall through the throat region. At each cross section, the probe makes 12 radial measurements spaced 30 deg apart. These 12 measurements are used to calculate the cross sectional area. In this work, the cross sectional area is estimated by fitting the *best fit* ellipse through the 12 points. The ellipsoidal fit accounts for eccentricity observed in some of the CFVs but collapses to a circle in the special case where the data are perfectly round. By dividing the area determined by the ellipsoidal fit by π and taking its square root, we determine the *effective* radius at each cross section. The average CFV contour was estimated by fitting the measured data to either a fifth or sixth degree polynomial that expressed the calculated radius as a function of axial position. The axial position of the throat is determined by setting the derivative of the polynomial equal to zero. The throat diameter equals twice the value of the polynomial evaluated at the axial throat location, and the throat curvature equals the second derivative of the polynomial evaluated at the throat location.

Figure 3 shows the cross sectional shapes for all nine CFVs at five axial positions traversing the throat. At each axial location, the deviation from circularity (in microns) was calculated by taking the difference between the 12 radial measurements and the calculated average radius. For comparison purposes, all of the plots have the same scaling, varying from -15 μm to 10 μm. The figure shows that CFV 8 significantly deviates from the circular shape while the remaining CFVs are essentially circular. In addition, the cross sectional shapes of all the CFVs remain relatively consistent along the axis of symmetry (i.e., negligible twisting).

Figure 4 shows the near throat profiles of the nine CFVs (i.e., plots of the polynomial fits). The various profiles are labeled with the measured values of Ω where the subscripts identify the CFV. The shaded region in the figure shows the recommended range of curvature ratios for an ISO CFV. For CFVs 1–4, 8, and 9, the measured Ω is less than the minimum requirement given by the ISO standard. We hypothesize that polishing the throat flattens the profile, causing smaller Ω in the region close to the throat. In the Results section, we show that predicted C_d values that are calculated with the measured values of Ω generally have better agreement with measured data than those calculated using an assumed ISO value of $\Omega_{\mathrm{ISO}}=0.25$.

Table 2 shows the throat diameter, the throat curvature ratio, and their expanded relative uncertainties (i.e., $k=2$) for all nine CFVs. The uncertainties of the throat diameters are calculated by root sum squaring the 0.5 μm ($k=1$) uncertainty of the CMM measurements and the uncertainty attributed to the eccentricity of the CFV cross section. The standard uncertainty attributed to eccentricity is taken to be proportional to the absolute difference of two throat radii, calculated by two different methods. In one case, the best fit ellipse (as previously explained) is used to determine the effective radius, while in the other case, the best fit circle is used. Since we expect the uncertainty to fall between these two radii, a rectangular distribution is assumed and the standard uncertainty is taken equal to the absolute difference of the two radii divided by $\sqrt{3}$ [12,13]. For all these CFVs (with the exception of CFV 8), the effect of eccentricity is negligible.

The ellipsoidal shape of CFV 8 results in a strong angular dependence of its curvature ratio. The uncertainty of the throat curvature ratio is equal to the standard deviation the twelve Ω determinations of Ω, each calculated along one of the 12 contours spaced 30 deg apart.

CFV Principle of Operation and Physics

Figure 5 shows an axisymmetric cut of a toroidal shaped CFV with dimensions complying with the ISO 9300 standard [2]. The CFV profile consists of a circular arc extending slightly beyond the throat cross section to a point of tangency, followed by a conical divergent section with a half angle between 2 deg and 6 deg. When sufficient pressure ratios (i.e., P_b/P_0) exist across the CFV, the gas flow achieves sonic velocity near the throat. Here, P_0 is the upstream stagnation pressure and P_b is the static

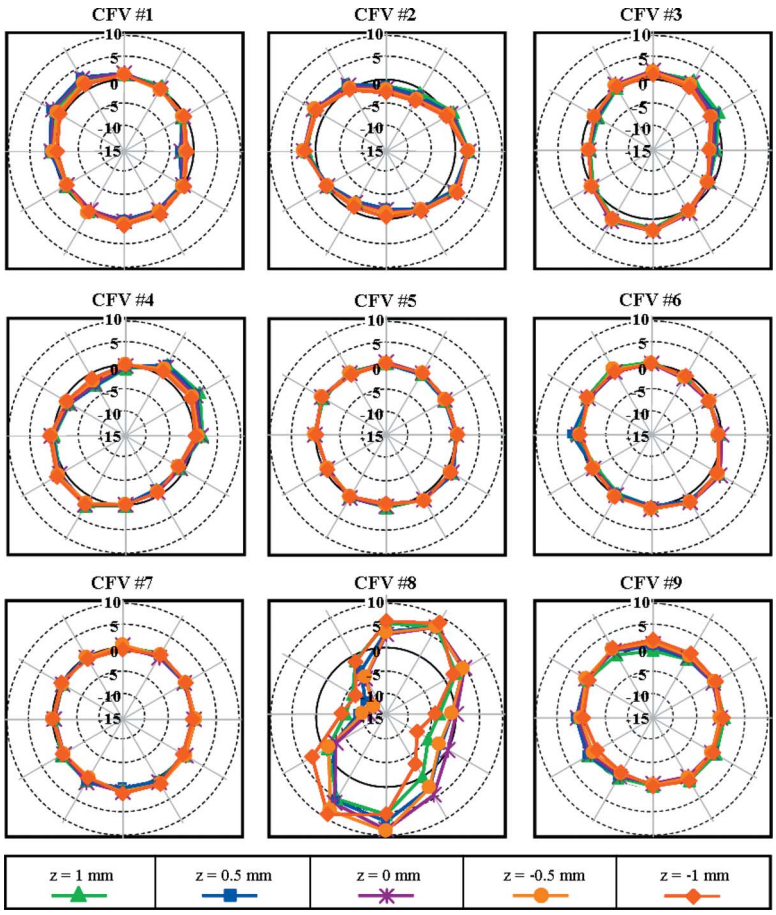

Fig. 3 Degree of roundness (in microns) for CFVs at five axial positions traversing the throat cross section (positive axial values correspond to positions upstream of the throat while negative values correspond to positions downstream of the throat)

pressure downstream of the CFV exit. The largest pressure ratio that satisfies this condition is called the *choking pressure ratio* (CPR) and CFVs are operated at or below this value.

Under choked flow conditions (i.e., P_b/P_0 less than the CPR), the CFV mass flow is independent of the thermodynamic conditions downstream of the throat section. Physically, pressure fluctuations cannot propagate upstream of the sonic throat.[2] Consequently, the mass flow is proportional to the upstream stagnation

[2]In small CFVs, the mass flow could exhibit some dependence on P_b attributed to pressure disturbances propagating upstream via the subsonic boundary layer.

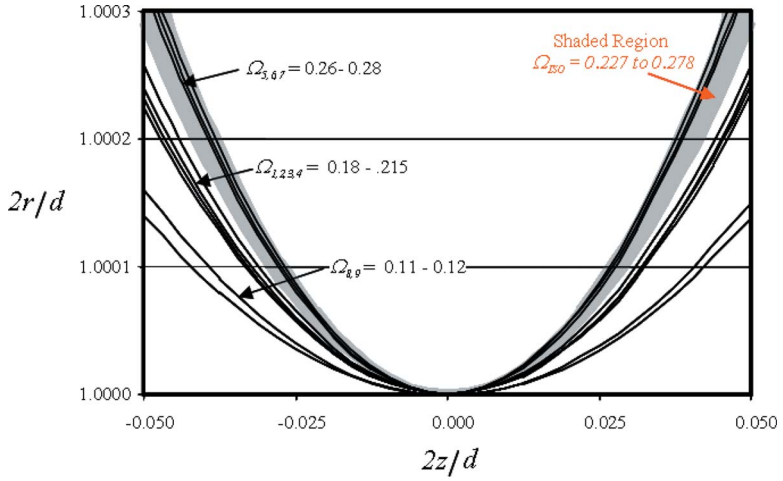

Fig. 4 Near throat CFV profiles (the shaded region indicates the ISO recommended values of the throat curvature ratio)

Table 2 Measured values of throat diameter (d) and curvature ratio (Ω) and their relative uncertainties ($k=2$)

CFV No.	d (mm)	$\left[\frac{U(d)}{d}\right]$ (%)	Ω	$\left[\frac{U(\Omega)}{\Omega}\right]$ (%)
1	25.3928	0.004	0.215	6.0
2	25.3912	0.004	0.19	8.1
3	25.3933	0.004	0.205	8.4
4	25.3884	0.004	0.18	7.4
5	19.7517	0.005	0.26	1.6
6	18.7857	0.005	0.265	2.9
7	17.3489	0.006	0.28	2.4
8	6.3784	0.020	0.12	51.7
9	4.8284	0.021	0.11	9.4

pressure alone, in contrast to a venturi operating at subsonic conditions where the flow is proportional to the difference between the upstream and downstream pressures.

Quantitative predictions of the CFV mass flow are commonly obtained via the published theoretical models [14–24]. The complexity as well as the accuracy of these models can significantly vary. The simplest of these models provides a common basis for all of the more sophisticated models and is herein called the *base line* model. The base line model is derived by reducing the Navier–Stokes equations [25] using the following three assumptions.

(1) The flow is one dimensional.
(2) The flow processes are isentropic.
(3) The fluid is a calorically perfect gas (i.e., the compressibility factor equals one and the constant pressure heat capacity is constant).

Together, Assumptions (1)–(3) are herein called the *sonic assumption*. Under the sonic assumption, the base line CFV mass flow is [14]

$$\dot{m}_b = \frac{\pi d^2 P_0 C_i^* \sqrt{\mathcal{M}}}{4\sqrt{R_u T_0}} \tag{1}$$

where P_0 is the upstream stagnation pressure, T_0 is the upstream stagnation temperature, R_u is the universal gas constant, $\mathcal{M}$ is the molecular weight, and C_i^* is the *ideal* gas critical flow function

$$C_i^* = \sqrt{\gamma}\left[\frac{\gamma+1}{2}\right]^{(\gamma+1)/2(1-\gamma)} \tag{2}$$

where $\gamma = C_p/C_v$ is the specific heat ratio evaluated at the upstream static pressure and temperature.

The sonic assumption typically leads to predicted mass flows that agree with measurements to much better than 5% of the actual value (primarily depending on Reynolds number). However, the sonic assumption is not fully satisfied in actual CFV flows primarily for three reasons.

(1) The boundary layer. The isentropic assumption is not valid in the boundary layer adjacent to the CFV wall. In this region, viscous effects retard the fluid motion, thereby reducing the gas velocity below the sonic velocity. Simultaneously, shear between adjacent fluid layers heat the gas, leading to larger temperatures, and subsequently lower densities than the fluid density in the inviscid core beyond the boundary layer. Together, the lower velocity and lower density lead to the decreased mass flow through the boundary layer region than would be predicted by the base line model.
(2) The inviscid core. The flow in the center, beyond the boundary layers, is multidimensional so that the profile of the sonic line (i.e., locus of points where the Mach number is unity) is nearly parabolic instead of the flat profile predicted by the base line model. The effect of the curved sonic line is to reduce the mass flow in the core region below the base line model.
(3) Virial effects. Real gas effects alter both the sound speed and the density, causing them to differ from the values predicted for a perfect gas with a constant heat capacity. In this case, virial effects can either increase or decrease the CFV mass flow depending on the upstream stagnation conditions and gas specie.

For the past 40 years, researchers have analyzed these three phenomena and developed corrections to the base line model, resulting in the state-of-the-art theoretical models that predict CFV performance. We compare our experimental data to these theoretical models. It should be noted that other phenomena, notably, vibrational relaxation [26] and heat transfer from the CFV wall, are also significant in many cases, but they have not yet been incorporated into the theoretical models due to their complexity.

In practice, the base line mass flow is used as the normalizing parameter in the definition of the ideal discharge coefficient

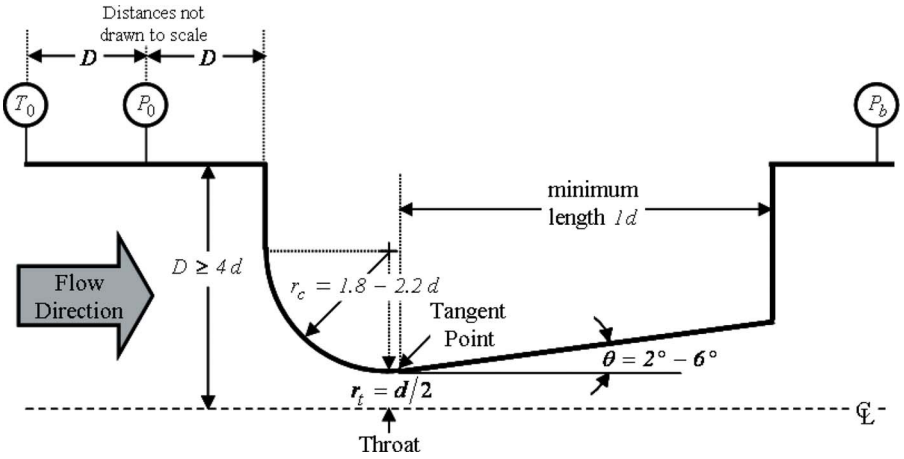

Fig. 5 Axisymmetric cut of a toroidal shaped CFV with dimension specifications of the ISO 9300 standard [2]

$$C_d^i \equiv \frac{\dot{m}}{\dot{m}_b} = \frac{4\dot{m}\sqrt{R_u T_0}}{\pi d^2 P_0 C_i^* \sqrt{\mathcal{M}}} \tag{3}$$

where $\dot{m}$ is either measured or determined theoretically, and the superscript i distinguishes the ideal discharge coefficient from the *real* discharge coefficient. The real discharge coefficient is indicated by the superscript r and is defined by

$$C_d^r \equiv \frac{4\dot{m}\sqrt{R_u T_0}}{\pi d^2 P_0 C_r^* \sqrt{\mathcal{M}}} = \left(\frac{C_i^*}{C_r^*}\right) C_d^i \tag{4}$$

replacing the *ideal gas* critical flow factor (C_i^*) with the *real gas* critical flow factor (C_r^*). The details explaining how to calculate C_r^* for various gases are given in Ref. [20]. In general, the real discharge coefficient (C_d^r) is preferred over the ideal discharge coefficient (C_d^i) for the following three reasons.

(1) The value of the real gas discharge coefficient is always less than unity, $C_d^r < 1$,[3] while in contrast, virial effects could potentially result in $C_d^i > 1$.
(2) C_d^r is nearly independent of real gas effects so that the discharge coefficient of different gases will be identical regardless of the degree of virial effects, provided that the set of dimensionless variables characterizing the discharge coefficient of both gases are all identical.
(3) In the absence of virial effects, the real gas critical flow function equals the ideal value (i.e., $C_r^* \to C_i^*$) and both definitions of the discharge coefficient are identical.

For these reasons, C_d^r is used instead of C_d^i unless otherwise noted for all measurements of the discharge coefficient. Consequently, the superscript r is omitted in the real gas discharge coefficient and it is expressed as C_d. For the thermodynamic range considered in this analysis, Condition (3) nearly realized so that C_i^* can be used in the place of C_r^* with negligible error (i.e., less than 0.01%).

In general, the discharge coefficient is a function of several variables including the Reynolds number, the specific heat ratio, heat transfer effects at the CFV wall, etc. A complete list of all of the pertinent dimensionless parameters characterizing the discharge coefficient is given in Ref. [27]. However, among the numerous parameters influencing the discharge coefficient, the Reynolds number is usually the most important. This fact has been demonstrated by numerous calibration data and by the various theoretical models. A commonly used Reynolds number definition is

$$\mathrm{Re} = \frac{4\dot{m}_b}{\pi d \mu_0} \tag{5}$$

where μ_0 is the molecular viscosity evaluated at the upstream stagnation conditions. An alternative Reynolds number definition also commonly used in the literature replaces the base line mass flow $\dot{m}_b$ in Eq. (5) with the measured mass flow $\dot{m}$. Although either definition is acceptable, we use the definition in Eq. (5) throughout this paper.

Review of Existing Theoretical Models

Although numerous theoretical models have been formulated to predict the discharge coefficient, no single model has been developed that simultaneously eliminates all three conditions of the sonic assumption. Instead, three distinct types of theoretical models have been developed, each focusing on improving a single aspect of the sonic assumption. This has resulted in three distinct definitions of theoretical discharge coefficients including

(1) the viscous discharge coefficient $C_{d,1}$
(2) the inviscid discharge coefficient $C_{d,2}$, and
(3) the virial discharge coefficient $C_{d,3}$

which are herein distinguished by the subscripts 1, 2, and 3, respectively. Each of these three discharge coefficients results from a different simplification of the Navier–Stokes equations. In particular, $C_{d,1}$ is derived by retaining Conditions (2) and (3) of the sonic assumption, but modifying Condition (1) to account for the boundary layer development along the CFV wall. In a similar manner, $C_{d,2}$ (and $C_{d,3}$) modifies the second (and third) condition of the sonic assumption while enforcing the remaining two. Each model is explained below.

Viscous Discharge Coefficient ($C_{d,1}$)

The viscous discharge coefficient accounts for the boundary layer development along the CFV wall. Predictive models have been developed both for laminar [15,16] and for turbulent flows [17]. For a smooth CFV contour, the boundary layer transition from the laminar to the turbulent flow typically occurs within a Reynolds number range extending from 8×10^5 to 1.8×10^6. The transition, however, has been observed at significantly lower Reynolds numbers in CFVs with rough walls. In this work, all of the CFVs have sufficiently smooth walls so that the transition to the turbulent flow occurs within the normal Reynolds number regime.

Among the various laminar flow models, the two most sophisticated and accurate models were independently developed by Tang in 1969 and by Geropp in 1971. Both of these models used similarity transformations to solve the axisymmetric compressible boundary layer equations. The turbulent flow model was developed in 1964 by Stratford who used an integral boundary layer technique to determine the turbulent displacement thickness and subsequently the viscous discharge coefficient. For either laminar or turbulent flow, the viscous discharge coefficient has the following form:

$$C_{d,1} = 1 - a_1 \Omega^{-m} \mathrm{Re}^{-n} + a_2 \Omega^{-2m} \mathrm{Re}^{-2n} \tag{6}$$

where a_1 and a_2 are coefficients, and m and n are exponents whose values depend on whether the flow is laminar or turbulent. Table 3 gives the values of these coefficients and exponents for the various models. The viscosity ratios (μ^*/μ_0) in both Tang's and Stratford's model convert between the Reynolds number definition based on the stagnation molecular viscosity (μ_0) given in Eq. (5) and the Reynolds number based on the molecular viscosity evaluated at the CFV throat (μ^*) that was used in these models. The coefficients a_1 and a_2 were calculated using a nominal value of the specific heat ratio for dry air ($\gamma = 1.405$). No attempt was made to account for the slight variation in $\gamma(P,T)$ attributed to different CFV operating conditions (i.e., different pressures and temperatures at the CFV inlet). The change in $C_{d,1}$ attributed to the slight variation in γ was less than 0.006% and taken to be negligible for the range of Reynolds numbers considered in this work.

For CFV flows with Reynolds number larger than 10^4, the last term in Eq. (6) is small relative to the other terms and is often omitted. For example, for the Reynolds number range considered in this paper, this term accounts for less than 0.005% of $C_{d,1}$. Consequently, the measured discharge coefficient scales almost linearly with $\mathrm{Re}^{-1/2}$ in the laminar flow regime.

In this work, the viscosity ratios (μ^*/μ_0) in the coefficients a_1

[3]Here, we assume that the discharge coefficient is calculated using the actual CFV throat diameter and that the mass flow is not affected by nontraditional mechanisms such as vibrational relaxation phenomena observed for CO_2 and SF_6 in geometrically small CFVs [26,27].

Table 3 Coefficient and exponent for selected boundary layer models used for predicting $C_{d,1}$[a]

Viscous solutions for $C_{d,1}$	Flow type	Exponents m	Exponents n	Coefficients a_1	Coefficients a_2
Tang [15]	Laminar	1/4	1/2	$2\left[\frac{\gamma\sqrt{2}+6\sqrt{3}-7\sqrt{2}}{\sqrt{3}}\right]\left(\frac{\gamma+1}{2}\right)^{-1/4}\left(\frac{\mu^*}{\mu_0}\right)^{1/2}$	$\left[\frac{2\sqrt{2}}{3}\frac{(\gamma-1)(\gamma+2)}{\sqrt{\gamma+1}}\right]\left(\frac{\mu^*}{\mu_0}\right)$
Geropp [16]	Laminar	1/4	1/2	$2\left[\frac{\gamma\sqrt{2}+6\sqrt{3}-7\sqrt{2}}{\sqrt{3}}\right]\left(\frac{\gamma+1}{2}\right)^{-3/4}$	$\left[\frac{\gamma\sqrt{2}+6\sqrt{3}-7\sqrt{2}}{\sqrt{3}}\right]^2\left(\frac{\gamma+1}{2}\right)^{-3/2}$
Stratford [17]	Turbulent	2/5	1/5	$\left(\frac{21}{400}\right)\left(\frac{1}{2}\right)^{2/5}\left(\frac{\mu^*}{\mu_0}\right)^{1/5}$	0

[a]Stratford's model was derived assuming a value of $\gamma=1.4$.

and a_2 are determined using the Sutherland viscosity law [25].[4] The largest difference between the laminar boundary layer models of Tang and Geropp occurred at the lowest Reynolds number and was only 0.028%. At the higher Reynolds numbers, the difference monotonically decreased. Between these two models, Geropp's boundary layer model agreed better with measured results and was therefore used for the comparison.

Inviscid Discharge Coefficient ($C_{d,2}$)

Several researchers [17–19] have developed methods for determining the inviscid discharge coefficient. Perhaps, the most widely used model was developed by Hall in 1962. Hall assumed that the gas behaved ideally and had a constant heat capacity. He used a perturbation series expansion in powers of $1/R$ (where $R=1/\Omega$) to solve the steady, irrotational, axisymmetric, compressible flow equation in the transonic regime [18]. Since the series diverges for $R<1$, it is not unexpected that the accuracy of this solution diminishes for small values of R. In fact, for sufficiently small R, Hall's solution yields nonphysical results, predicting negative values of the inviscid discharge coefficient. Consequently, the common practice has been to avoid using this solution for $R<2$. In 1969, Kliegel and Levine [19] extended and improved Hall's work by using a perturbation series solution expanded about $1/(1+R)$ that converges for all values of R. In developing the improved series solution, Kliegel and Levine found an error in Hall's original solution and provided the appropriate correction.

The mathematical formulation of the inviscid discharge coefficient is

$$C_{d,2} = 1 - \frac{\alpha_2}{\Lambda^2} + \frac{\alpha_3}{\Lambda^3} - \frac{\alpha_4}{\Lambda^4} \tag{7}$$

where α_2, α_3, and α_4 are species dependent coefficients and Λ is the expansion parameter. Table 4 gives the values of the coefficients and the expansion parameters for Hall's original solution, the corrected version of Hall's solution, and the improved solution of Kliegel and Levine. Figure 6 compares the predicted discharge coefficients given by these three models versus Ω for $\gamma=1.405$. The left y-axis gives the values of $C_{d,2}$ for the each of the three models, while the right y-axis gives the percent difference between the original series solution of Hall (which unfortunately is still being used by researchers) and the improved series solution of Kliegel and Levine. Within the ISO specified design limits (indicated by the shaded rectangle), the difference between these two solutions is no more than 0.03%, but increases to as much as 0.2% for $\Omega=0.5$ ($R=2$) with increased differences at larger throat curvature ratios (or smaller R).

Virial Discharge Coefficient ($C_{d,3}$)

The virial discharge coefficient is defined as the following ratio of mass flows:

$$C_{d,3} \equiv \frac{\dot{m}_3}{\dot{m}_b} \tag{8}$$

where $\dot{m}_3$ is the mass flow that would result if the CFV flow was both one dimensional and inviscid, but influenced by virial effects. Unlike the analytical solutions for the viscous and inviscid discharge coefficients previously given in Eqs. (6) and (7), no closed-form solutions have been found that adequately predict $C_{d,3}$ for arbitrary CFV operating conditions and gas species. Consequently, $\dot{m}_3$ has been numerically calculated [20] using a real gas equation of state to determine the density and sound speed at the CFV throat. Johnson was the first to make these calculations, and he

[4]The first order terms of the models of Tang and Geropp are identical if the viscosity in Tang's model is taken proportional to temperature, and the ideal gas isentropic relationships are used to relate the throat temperature to the stagnation temperature.

Table 4 Coefficients and expansion parameter for various series solutions of $C_{d,2}$

Inviscid discharge coefficient ($C_{d,2}$)	Series expansion parameter Λ	Series expansion coefficients α_2	Series expansion coefficients α_3	Series expansion coefficients α_4
Original Hall [18]	R	$\frac{\gamma+1}{96}$	$\frac{(\gamma+1)(8\gamma+21)}{4608}$	$\frac{(\gamma+1)(754\gamma^2+1971\gamma+2007)}{552{,}960}$
Corrected Hall [19]	R	$\frac{\gamma+1}{96}$	$\frac{(\gamma+1)(8\gamma+21)}{2304}$	$\frac{(\gamma+1)(754\gamma^2+2123\gamma+2553)}{552{,}960}$
Kliegel and Levine [19]	$1+R$	$\frac{\gamma+1}{96}$	$\frac{(\gamma+1)(8\gamma-27)}{2304}$	$\frac{(\gamma+1)(754\gamma^2-757\gamma+3633)}{276{,}480}$

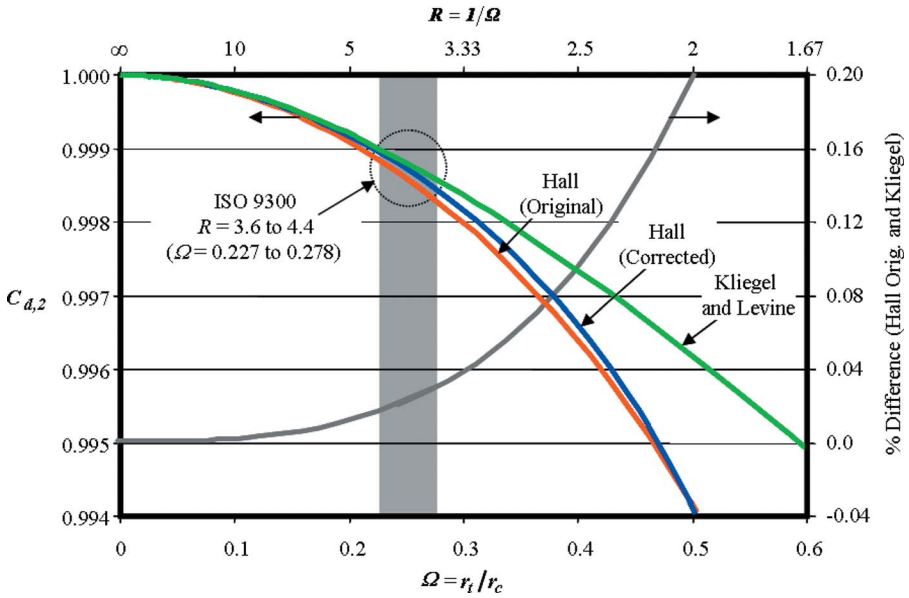

Fig. 6 Comparison of three models of the inviscid discharge coefficient

expressed $\dot{m}_3$ in a form analogous to the base line model given in Eq. (1).

$$\dot{m}_3 = \frac{\pi d^2 P_0 C_r^* \sqrt{\mathcal{M}}}{4\sqrt{R_u T_0}} \tag{9}$$

with the sole difference being that C_i^* is replaced by C_r^*. Thus, all real gas effects are lumped into the real gas critical flow function (C_r^*), which is a function of P_0, T_0 for a given gas species. Subsequently, the virial discharge coefficient is a function of the specific heat ratio, stagnation conditions, and gas species, and can be expressed as the ratio of the real gas critical flow factor and the ideal critical flow factor by substituting Eqs. (1) and (9) into Eq. (8).

$$C_{d,3} = \frac{C_r^*}{C_i^*} \tag{10}$$

Combining the Theoretical Models to Predict the Measured Discharge Coefficient

Throughout the years, researchers have combined $C_{d,1}$, $C_{d,2}$, and $C_{d,3}$ in various ways to estimate the ideal discharge coefficient (C_d^i).[5] In special cases where two of the three conditions comprising the sonic assumption are satisfied, $C_d^i = C_{d,k}$, where $k=1$, 2, or 3 as appropriate based on the relevant flow physics. For example, if both viscous effects and real gas behavior are negligible relative to the effect of the sonic line curvature, then $C_d^i = C_{d,2}$, and the two remaining theoretical discharge coefficients, $C_{d,1}$ and $C_{d,3}$, are both unity. However, in cases where all three conditions of the sonic line assumption are simultaneously not satisfied, the ideal discharge coefficient is

$$C_d^i = f(C_{d,1}, C_{d,2}, C_{d,3}) \tag{11}$$

assumed to be a function of all three theoretical discharge coefficients.

Historically, the functional form of f has been assumed (without justification) to be either a product [24] or a linear combination [17] of the theoretical discharge coefficients $C_{d,1}$, $C_{d,2}$, and $C_{d,3}$, respectively. In this work, we expand f using a Taylor series centered about the base line flow conditions for which all three of the theoretical discharge coefficients are unity. The zeroth and first order terms of the series are defined equal to C_d^i, while the second order terms are used to estimate how accurately the zeroth and first order terms approximate C_d^i.

Before deriving the functional form of f, we introduce two mathematical properties of f essential to the analysis. The two properties are the following:

(1) $f(1,1,1) \equiv f_b = 1$ and
(2) $C_{d,1} = f(C_{d,1}, 1, 1)$ $C_{d,2} = f(1 C_{d,2}, 1)$, and $C_{d,3} = f(1, 1, C_{d,3})$

Both properties logically follow from the definition of the ideal discharge coefficient. The first property expresses the fact that the three theoretical discharge coefficients and C_d^i are unity when the sonic assumption is satisfied. The second property demonstrates that C_d^i is completely described by a single theoretical discharge coefficient whenever any two conditions of the sonic assumption are satisfied. By expanding the function $f(C_{d,1}, C_{d,2}, C_{d,3})$ in a Taylor series centered about the unity base line conditions, we obtain

$$C_d^i = f_b - \sum_{k=1}^{3} \left(\frac{\partial f}{\partial C_{d,k}} \right)_b \Delta C_{d,k} + \text{higher order terms} \tag{12}$$

where f_b and $(\partial f / \partial C_{d,k})_b$ are the zeroth and first order Taylor coefficients, the subscript b indicates the unity base line condition, the higher order terms are the truncated terms of the series, and $\Delta C_{d,k}$ is the departure from unity of the kth theoretical discharge coefficient defined by

$$\Delta C_{d,k} \equiv 1 - C_{d,k} \tag{13}$$

for $k=1$, 2, and 3. Based on Property (1), the first term on the right hand side of Eq. (12) equals unity (i.e., $f_b = 1$). By taking the appropriate partial derivatives of Property (2), the partial derivatives in the second term in Eq. (12) are unity for k=1, 2, and 3, respectively. When Properties (1) and (2) are applied together, Eq. (12) simplifies to

$$C_d^i = 1 - \Delta C_{d,1} - \Delta C_{d,2} - \Delta C_{d,3} + \text{higher order terms} \tag{14}$$

In the special case where real gas behavior is negligible (i.e., $\Delta C_{d,3} = 0$), the result of Eq. (14) (ignoring the higher order terms)

[5] Since the theoretical models are corrections for the base line model, from which the ideal discharge coefficient is defined, these models describe C_d^i and *not* C_d^r.

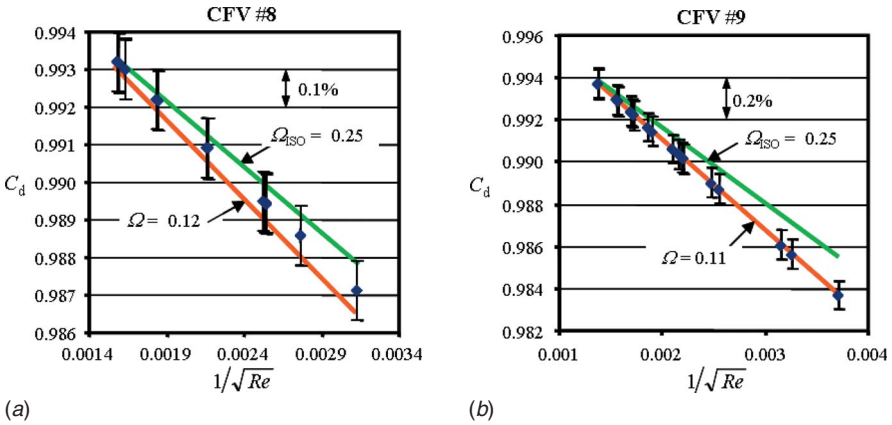

Fig. 7 Measured discharge coefficient of CFVs 8 (left) and CFV 9 (right) versus predicted C_d values calculated using their measured Ω's and an assumed value equal to $\Omega_{ISO}=0.25$

is consistent with the expression derived by Massier et al. who arrived at this result using an entirely different approach [23]. Without any loss in the order of accuracy, Eq. (14) can be factored into the following form:

$$C_d^i = (1-\Delta C_{d,1})(1-\Delta C_{d,2})(1-\Delta C_{d,3}) + \text{higher order terms} \tag{15}$$

Given that each term in parentheses ($C_{d,k} \equiv 1-\Delta C_{d,k}$) is equal to one of the three theoretical discharge coefficients, C_d^i equals

$$C_d^i = C_{d,1}C_{d,2}C_{d,3} + \text{higher order terms} \tag{16}$$

a product of the theoretical discharge coefficients. This multiplicative characteristic of C_d^i is the basis for introducing a new definition of the discharge that is independent of virial effects. In particular, virial effects are nearly eliminated by defining the real discharge coefficient, which is equal to C_d^i divided by $C_{d,3}$,

$$C_d \equiv \frac{C_d^i}{C_{d,3}} = C_{d,1}C_{d,2} + \text{higher order terms} \tag{17}$$

The ratio $C_d^i/C_{d,3}$ is recognized as the real discharge coefficient by recalling from Eq. (10) $C_{d,3}=C_r^*/C_i^*$ and by using the definition of the real discharge coefficient given in Eq. (4). Because the discharge coefficient as defined in Eq. (17) equals the product of $C_{d,1}$ and $C_{d,2}$, which both by definition are independent of virial effects, C_d is also independent of virial effects (at least to the accuracy of the higher order terms).

In practice, the definition of the real gas discharge coefficient as given in Eq. (4) is commonly taken to be independent of virial effects. However, virial effects can influence C_d via the higher order terms in Eq. (17). Physically, the higher order terms account for weak coupling between viscous effects, curvature of the sonic line, and virial effects. The magnitude of the higher order terms can be characterized using only the second order terms and not the entire infinite series since $|\Delta C_{d,k}|<1$ for $k=1$, 2, and 3. Furthermore, only a subset of the second order terms is necessary to characterize the error in C_d associated with decoupling virial effects and flow processes. We estimate the magnitude (in percent C_d change) of this error by

$$\xi_{\text{vir}} = 100\left[\frac{|\Delta C_{d,2}\Delta C_{d,3}| + |\Delta C_{d,1}\Delta C_{d,3}|}{C_d}\right] \tag{18}$$

where the first term in the brackets accounts for coupling between virial and boundary layer effects and the second term accounts for coupling between virial effects and sonic line curvature. Since Taylor coefficients of the same variable can be shown to be zero by using Properties (1) and (2), there are no squared terms included in the expression. Unfortunately, Properties (1) and (2) are insufficient to determine Taylor coefficients of mixed variables, which are herein assumed to be unity, $(\partial^2 f/\partial C_{d,k}\partial C_{d,3})_b=1$ for $k=1$ and 2. If these coefficients could be determined, a second order correction could be given for C_d. As it stands, Eq. (18) only estimates the size of the error introduced when C_r^* is used to reduce real gas behavior in the definition of the discharge coefficient.

Since the three theoretical discharge coefficients are generally close to unity, ξ_{vir} is typically small so that C_d is nearly independent of virial effects. However, in cases where ξ_{vir} becomes significant, it should be included in the uncertainty budget.[6] We suggest treating this term as a rectangular distribution [12,13] and including its uncertainty contribution with the uncertainty components of C_r^*. For the results presented in this paper, this term is insignificant, being less than $\xi_{\text{vir}}<0.003\%$.

Results

The overall agreement between the measured and predicted discharge coefficients of nine standardly manufactured CFVs was better than 0.17% over a Reynolds number range extending from 7.2×10^4 to 2.5×10^6. The best agreement was found for CFVs 8 and 9. The predicted discharge coefficients for these CFVs agreed with measured values to better than 0.065% over a Reynolds number range extending from 7.2×10^4 to 5.0×10^5. Figure 7 shows the measured data (♦) and two C_d predictions (solid lines), one calculated using the measured value of Ω for the CFV, and the other using an assumed value based on ISO guidelines ($\Omega_{ISO}=0.25$). Both predicted values of the discharge coefficient in the figure are determined by using Eq. (17) (with the higher order terms omitted). We used the boundary layer model of Geropp for the laminar flow and the model of Stratford for the turbulent flow along with the inviscid flow model of Kliegel and Levine. Following the results of the laminar boundary layer models, the C_d values in the figure are plotted versus $1/\sqrt{\text{Re}}$ to linearize the laminar calibration data.

The results show that reasonably accurate values of Ω are needed (i.e., better than 10%) to obtain the best agreement between predicted and measured C_d values. In Fig. 7, CFV 9 (right) has a curvature ratio ($\Omega_9=0.11$) that is significantly less than ISO recommended values. Given that this CFV was supposed to be machined according to ISO specifications, we were surprised to find that its curvature ratio deviated from the design limit by more

[6]Errors associated with virial effects only apply when CFV calibrations performed using one gas are applied to a different gas.

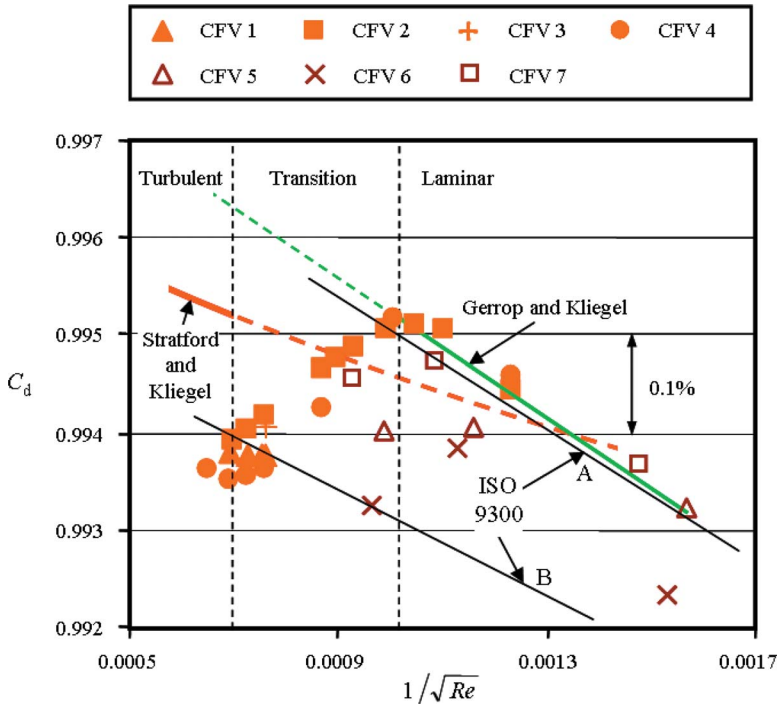

Fig. 8 Measured discharge coefficient of CFVs 1–7 compared to the piecewise theoretical model spanning the laminar, transition, and turbulent flow regimes (curves labeled A and B are the values of the discharge coefficient recommended by the IS0 9300 standard for accurately and normally machined CFVs [2])

than 100%. If we had not measured Ω, but instead used an assumed ISO value of $\Omega_{ISO}=0.25$, the resulting error would have been almost 0.21% at the lowest Reynolds number. In contrast, when we used the measured value of Ω in the predictive model, the agreement with calibration data was better than 0.01%.

Applying the measured value of the curvature ratio ($\Omega_8=0.12$) for CFV 8 (left) did not yield a substantial improvement over using an assumed value of $\Omega_{ISO}=0.25$. Defects in the geometry of this CFV are probably responsible. In particular, the elliptical shaped cross section of CFV 8 (see Fig. 2) results in a throat radius of curvature that substantially changes at various angles along the throat circumference. Consequently, the uncertainty in the measured throat curvature ratio was 52%. If we hypothetically increased the throat curvature ratio from 0.12 to 0.159, the agreement between theory and measurement would be better than 0.01%. Nevertheless, using the measured Ω value yielded results within the calibration uncertainty.

Figure 8 shows the measured C_d's for CFVs 1–7 plotted against a piecewise theoretical model that spans the laminar, transition, and turbulent flow regimes. Strictly speaking, the seven different theoretical plots are necessary to account for the geometrical differences (i.e., differing Ω) between the seven CFVs. However, instead of plotting seven different curves, we calculate the theoretical discharge coefficient using a single value of the curvature ratio equal to $\Omega=0.25$. This simplification allows a single theoretical curve for all seven CFVs shapes while introducing only 0.023% uncertainty in the predicted discharge coefficient. The dependence on Ω is less significant for these larger sized CFVs attributed to the diminished influence of boundary layer effects at higher Reynolds numbers, and because the measured Ω of these CFVs (0.18–0.28) is closer to $\Omega_{ISO}=0.25$. A further simplification of the theoretical model is the assumption that transition to turbulence occurs at a single Reynolds number, $Re=10^6$. As observed in the figure, the actual C_d data transition from the laminar to the turbulent flow over a Reynolds number range extending from 1×10^6 to 2.1×10^6. At $Re<10^6$, the data generally follow a linear trend typical of the laminar flow regime while for $Re>2.1\times10^6$, the data appear to be fully turbulent and begin to increase with increasing Reynolds number. Not surprisingly, the simple piecewise model does not capture the downward trend in C_d that occurs during the transition from the laminar to the turbulent flow.

Excluding CFV 6 which had the largest C_d uncertainty (see Table 1), the agreement in the laminar regime was better than 0.07%. The worst agreement was in the turbulent regime where the predictive model overestimated the measured data by as much as 0.17%.

In addition to the piecewise theoretical model, we also compared the measured C_d values to the two ISO 9300 calibration curves for toroidal throat CFVs [2]. In Fig. 8, the ISO 9300 curve labeled A applies to accurately machined CFVs (or HPNs) while the curve labeled B applies to normally manufactured CFVs.[7] The predicted discharge coefficients of both Curves A and B agree with the measured C_d values within the uncertainties given by ISO 9300 standard of 0.2% and 0.3%, respectively.

Conclusions

Nine normally manufactured CFVs with nominal diameters ranging from 5 mm to 25 mm were calibrated in dry air, and their measured discharge coefficients agreed with predicted values to better than 0.17% over a Reynolds number range extending from 7.2×10^4 to 2.5×10^6. For all nine CFVs, the walls were smooth so that the effect of surface roughness was assumed negligible. The throat diameters (d) and the throat curvature ratio (Ω) of

[7]The discharge coefficient for Curve A (i.e., accurately machined CFVs) is $C_d^A=0.9985-3.412\mathrm{Re}^{-0.5}$, while for Curve B (i.e., normally manufactured CFVs) is $C_d^B=0.9959-2.720\mathrm{Re}^{-0.5}$. Note that the Reynolds numbers in these expressions are based on the actual mass flow and not on the base line mass flow as previously defined in Eq. (5).

these CFVs were measured using a CMM. The flow calibration results included data in the laminar, transition, and turbulent flow regimes. The theoretical discharge coefficient was determined by combining either Geropp's laminar boundary layer model [16] ($Re < 10^6$) or Stratford's turbulent boundary layer model [17] ($Re > 10^6$) with the inviscid core model of Kliegel and Levine [19].

The best agreement was found in the laminar regime where the difference between measured and predicted discharge coefficients was less than 0.07%. In contrast, the turbulent model overpredicted the measured discharge coefficients by an almost constant offset of 0.14%. Part of the offset could be attributed to the 0.1% uncertainty of the measured data; however, most of the bias is likely attributed to the turbulent model.

The throat curvature ratio (Ω) played an important role for the two smallest CFVs. Dimensional measurements showed that these CFVs had Ω that significantly deviated from the intended ISO design value of $\Omega_{ISO}=0.25$. When the predicted discharge coefficient was calculated using the measured values of Ω, the results were within the uncertainty of the calibration data. The smallest CFV exhibited the best results, agreeing with the experimental data to better than 0.01%.

The good agreement between measured and predicted C_d's gives credibility to using theoretical models to predict the discharge coefficient of geometrically well characterized CFVs with negligible surface roughness. Additional research should be done to investigate what level of agreement can be achieved between measurement and theory in smaller CFVs where high accuracy dimensional measurements are more difficult. Additionally, the predictive models may not be as accurate for smaller CFVs where the Reynolds numbers are lower. In this lower Reynolds number regime (i.e., $Re < 5 \times 10^3$), the second order terms in the boundary layer models of Tang [15] and Geropp [16] play a larger role, causing the predicted C_d values of these two models to differ more substantially.

References

[1] Wright, J. D., 1998, "The Long Term Calibration Stability of Critical Flow Nozzles and Laminar Flowmeters," *Proceedings of the 1998 NCSL Workshop and Symposium*, Albuquerque, NM, NCSL, pp. 443–462.

[2] ISO 9300: (E), 1990, "Measurement of Gas Flow by Means of Critical Flow Venturi Nozzles," Geneva, Switzerland.

[3] Ishibashi, M., Takamoto, M., Watanabe, N., Nakao, Y., and Yokomizo, T., 1994, "Precise Calibration of Critical Nozzles of Various Shapes at the Reynolds Number of $0.8-2.5 \times 10^5$," *Proceedings of Flow Measurement*, Glasgow, UK.

[4] Ishibashi, M., Morioka, T., and Arnberg, B. T., 2005, "Effect of Inlet Curvature on the Discharge Coefficients of Toroidal-Throat Critical-Flow Venturi Nozzles (Keynote Paper)," *ASME Summer Meeting and Exhibition*, Houston, TX, ASME Paper No. FEDSM2005-77470.

[5] Ishibashi, M., 2003, "Fluid Dynamics in Critical Nozzles Revealed by Measurements (Keynote Paper)," *Fourth ASME/JSME Joint Fluids Engineering Conference*, Honolulu, HI, ASME Paper No. FEDSM2005-45592.

[6] Ishibashi, M., 2002, "Super-Fine Structure in the Critical Flow-Rate of Critical Flow Venturi Nozzles," *Joint US-European Fluids Engineering Conference*, Montreal, Canada, ASME Paper No. FEDSM2002-31079.

[7] Wright, J. D., Johnson, A. N., and Moldover, M. M., 2003, "Design and Uncertainty Analysis for a PVTt Gas Flow Standard," J. Res. Natl. Inst. Stand. Technol., **108**, pp. 21–47.

[8] Wright, J. D., Moldover, M. R., Johnson, A. N., and Mizuno, A., 2003, "Volumetric Gas Flow Standard With Uncertainty of 0.02% to 0.05%," ASME J. Fluids Eng., **125**(6), pp. 1058–1066.

[9] Johnson, A. N., and Wright, J. D., 2006, "Gas Flowmeter Calibrations With the 26 m^3 PVTt Standard," Journal of Research of the National Institute of Standards and Technology, NIST Special Publication 250-1046.

[10] Johnson, A. N., Wright, J. D., Moldover, M. R., and Espina, P. I., 2003, "Temperature Characterization in the Collection Tank of the NIST 26 m^3 PVTt Gas Flow Standard," Metrologia, **40**, pp. 211–216.

[11] Stoup, J. R., and Doiron, T. D., 2001, "The Accuracy and Versatility of the NIST M48 Coordinate Measuring Machine," Proc. SPIE, **4401**, pp. 136–146.

[12] Taylor, B. N., and Kuyatt, C. E., 1994, "Guidelines for Evaluating and Expressing the Uncertainty of NIST Measurement Results," NIST TN-1297.

[13] ISO, 1995, "Guide to the Expression of Uncertainty in Measurement," International Organization for Standardization (ISO), Geneva, Switzerland.

[14] John, J. E., 1984, *Gas Dynamics*, 2nd ed., Allyn and Bacon, Boston.

[15] Tang, S., 1969, "Discharge Coefficients for Critical Flow Nozzles and Their Dependence on Reynolds Numbers," Ph.D. thesis, Princeton University, Princeton, NJ.

[16] Geropp, D., 1971, "Laminare Grenzschichten in Ebenen und Rotationssymmetrischen Lavalduesen," Deutsche Luft-Und Raumfart, Forschungsbericht, pp. 71–90.

[17] Stratford, B. S., 1964, "The Calculation of the Discharge Coefficient of Profiled Choked Nozzles and the Optimum Profile for Absolute Air Flow Measurement," J. R. Aeronaut. Soc., **68**, pp. 237–245.

[18] Hall, I. M., 1962, "Transonic Flow in Two-Dimensional and Axially-Symmetric Nozzles," Q. J. Mech. Appl. Math., **15**, pp. 487–508.

[19] Kliegel, J. R., and Levine, J. N., 1969, "Transonic Flow in Small Throat Radius of Curvature Nozzles," AIAA J., **7**, pp. 1375–1378.

[20] Johnson, R. C., 1964, "Calculations of Real-Gas Effects in Flow Through Critical Nozzles," ASME J. Basic Eng., **86**, pp. 519–526.

[21] Back, L. H., and Cuffel, R. F., 1971, "Flow Coefficients for Supersonic Nozzles With Comparatively Small Radius of Curvature Throats," J. Spacecraft, **8**(2), pp. 196–198.

[22] Smith, R. E., and Matz, R. J., 1962, "A Theoretical Method of Determining Discharge Coefficients for Venturis Operating at Critical Flow Conditions," ASME J. Basic Eng., **84**(4), pp. 434–446.

[23] Massier, P. F., Back, L. H., Noel, M. B., and Saheli, F., 1970, "Viscous Effects on the Flow Coefficient for a Supersonic Nozzle," AIAA Technical Note, pp. 605–607.

[24] Ishibashi, M., and Takamoto, M., 1997, "Very Accurate Analytical Calculation of the Discharge Coeffcients of Critical Venturi Nozzles With Laminar Boundary Layer," *Proceedings of the FLUCOME*, Hayama, Japan, Sept. 14.

[25] White, F. M., 1991, *Viscous Fluid Flow*, McGraw-Hill, New York.

[26] Johnson, A. N., Wright, J. D., Nakao, S., Merkle, C. L., and Moldover, M. R., 2000, "The Effect of Vibrational Relaxation on the Discharge Coefficient of Critical Flow Venturis," Flow Meas. Instrum., **11**(4), pp. 315–327.

[27] Johnson, A. N., 2000, "Numerical Characterization of the Discharge Coefficient in Critical Nozzles," Ph.D. thesis, Pennsylvania State University, University Park, PA.

Measurement of Velocities in Two-Phase Flow by Laser Velocimetry: Interaction Between Solid Particles' Motion and Turbulence

N. Sad Chemloul
Research Laboratory of Industrial Technologies,
University Ibn Khaldoun of Tiaret,
Tiaret 14000, Algeria
e-mail: sad_2412@yahoo.fr

O. Benrabah
Institute of Physics,
University of Oran,
Oran 31000, Algeria

In this work, an experimental method based on laser anemometry with Doppller effects is developed. This allows the measurement of velocities and their fluctuations in a flow of solid-liquid suspension in an ascendant vertical pipe. In order to distinguish between the signals coming from the continuous phase, water, and those of the glass bead particles larger than the Kolmogorov length scale, an electronic logic circuit was incorporated in the measuring equipment. This enabled the study of both the slip velocity of the solid-liquid suspension and the influence of the large particles on turbulence. The results show that a fine particle suspension, which represents a tracer, behaves as a homogeneous fluid. For large particles, we confirmed the existence of a slip velocity and the effect of particle size on the turbulence. The use of two distinct measurement volumes produces good results for the direct measurement of the turbulent length scales. The results show that the presence of solid particles modifies the turbulence characteristics.
[DOI: 10.1115/1.2948358]

Keywords: flow, solid-liquid suspension, turbulence, laser velocimetry, measurement volume, slip velocity

1 Introduction

Suspension flows, mixtures of liquid and solid particles in various quantities, appear in many industrial fields. While the theoretical knowledge of the flows of only one fluid has progressed much these past years, no rigorous theory is yet accepted for flows of solid-liquid suspensions. Research carried out on solid-liquid suspensions has investigated the continuous phase and particularly the influence of turbulence modulation. In the works by Elghobashi and Truesdell [1], Michaelides and Stock [2], Owen [3], and Parthasarthy and Faeth [4,5], dissipation or production of turbulent kinetic energy in the continuous phase was reported.

The effects of particles on the carrier flow turbulence were investigated numerically by Varaksin and Zaichik [6] and Lei et al. [7]. So far, experimental investigations regarding turbulence modification have focused on flows in vertical pipes (Chandok and Pei [8]; Meada et al. [9]; Durst [10]; Tsuji et al. [11]) and turbulent jets (Modarress et al. [12]; Solomon et al. [13,14]; Mostafa et al. [15]; Park and Chen [16,17] and Geiss et al. [18]). In addition, Schreck and Kleis [19] have reported on modification of grid generated turbulence in a solid-liquid two-phase flow.

Gore and Crowe [20] proposed that the ratio of particle diameter to turbulent length scale can be used to predict whether the turbulent kinetic energy of the continuous phase is dissipated or produced. This analysis has been supported for small particles in a two-phase channel flow by Kulick et al. [21] but is in contradiction to experimental findings by Hardalupas et al. [22]. Concerning methods of two Doppler signal concepts (pedestals and visibility) used for the measurement of the particle velocity and diameter, one can quote Durst and Zare [23], Saffmann et al. [24], Bachalo and Houser [25,26], Tadrist et al. [27], Van Den Moortel et al. [28], Zhang and Arastoopour [29], and Mathiesen et al. [30,31]. Note that the measurement techniques cited in the above references are limited by the nature of the suspensions.

The aim of this experimental study is the development of a method of laser velocimetry based on the Doppler effect in order to determine the local parameters, which are the velocity fields of the solid particles in flows in a vertical pipe, the influence of these particles on the turbulence intensity of the carrying fluid, and the determination of the turbulent length scales. The difference between our system and those used in Refs. [8–31] resides in the use of an electronic logic circuit at the reception to detect the presence of the large particles in the measurement volume.

Laser velocimetry was selected rather than a hot wire or film, or ultrasound, because the first would be destroyed by the particles, and with the second, the measurement volume dimensions are relatively very large.

2 Two-Phase Laser Anemometry

2.1 Principles of Two-Phase Laser Anemometry. In two-phase laser anemometry, the velocity information is obtained from two signals of basically different nature. The first signal is diffused by small particles used as a tracer of the continuous phase. This signal is comparable to the signal of a traditional single-phase laser anemometry. The second signal comes from the large particles, which constitute the suspension. In this case, the signal collected by the photomultiplier is of a different nature and is produced by the light reflected or refracted by the particles.

Velocity data from within the fluid were obtained via dual-beam laser Doppler anemometry (LDA). Information on this technique can be found in the recent book by Albrecht et al. [32]. If a suspended particle, whose diameter is large compared to the distance between interference fringes, crosses the measurement volume, the light reflected or refracted by the large particles causes

Contributed by the Fluids Engineering Division of ASME for publication in the JOURNAL OF FLUIDS ENGINEERING. Manuscript received January 8, 2007; final manuscript received April 1, 2008; published online June 25, 2008. Assoc. Editor: Juergen Kompenhans.

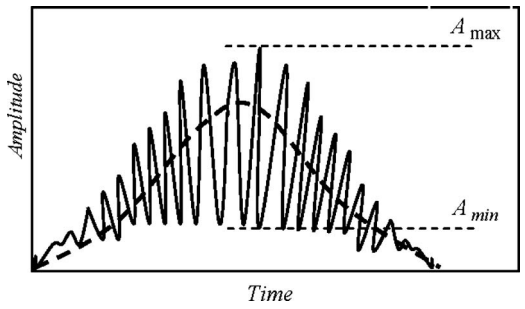

Fig. 1 Signal bursts and definition of visibility: Doppler component (solid line) and pedestal component (dashed line)

an output signal to be issued from the photomultiplier. The particle can be opaque and reflective or transparent [23]. For these two cases, we use the traditional relation of laser anemometry as follows:

$$f_D = \frac{2U \sin \theta}{\lambda_0} \tag{1}$$

When a suspended particle with a large diameter compared to the distance between interference fringes crosses the measurement volume, the output signal of the photomultiplier does not correspond to the light intensity scattered by the small particles, i.e., generally the contrast is strongly attenuated and leads to a bad signal quality.

The voltage delivered by the photomultiplier illustrated in Fig. 1 is composed partly of high (Doppler) frequency, which is modulated by a low, or pedestal frequency. To study the amplitude of the visibility signal [33,34], it is necessary to use the unfiltered output signal of the photomultiplier.

We define a degree of modulation called visibility V that corresponds to the quality of the signal, given by

$$V = \frac{A_{\max} - A_{\min}}{A_{\max} + A_{\min}} \tag{2}$$

This shape of the signal results from the light diffused simultaneously by the interference fringes. For well modulated signals, the part $A_{\min}$ of the Doppler signal tends to zero and the visibility to the maximum value 1.

For spherical particles, the relationship between the pedestal output signal of the photomultiplier and the particle diameter is approached by

$$A_p \cong q d_p \tag{3}$$

where q is a constant that depends on the opening and the angle of reception optics as well as the incidence angle of the beam.

The validity of Eq. (3) was confirmed by the experimental results of Durst and Zare [23] using a suitable assembly.

3 Experiment

Two optical measurement systems of LDA were used. The first system measures the velocity profiles and the intensity of the turbulence. This method is based on an electronic logic to detect the presence of the large particles in the volume measurement. The second system, based on the visibility of the Doppler signal, is used to determine the integral scale of the turbulence. Two measurement volumes are necessary for the second system. For these two optical measurement systems, the same flow circuit was used.

3.1 Flow Circuit. The flow circuit is shown in Fig. 2(*a*). It consists of a vertical closed loop made of glass pipes with an internal diameter D of 20 mm. The flow is driven by a variable speed centrifugal pump. In order to ensure a homogeneous turbulent flow, a grid is placed at the exit of the pump. The test section was located at $45D$ downstream of the pump, where the flow was fully developed. This study was performed using water as the continuous phase and glass beads for solid particles. Two samples of different particle size distributions were tested. The particles are spherical with a 5% sphericity defect and density of 2640 kg/m^3. The first sample has a volume-averaged mean particle diameter of 0.5 mm with particle size ranging between 0.33 mm and 0.57 mm. The second sample has a volume-averaged mean particle diameter of 1 mm with the particle size ranging between 0.83 mm and 1.2 mm. These particles were chosen to be larger than the Kolmogorov length scale η, estimated to 310 μm near the wall, and correspond to about 3.22η and 1.61η, respectively. The volumetric concentrations of the glass beads used in the suspension are 0.5%, 1%, 1.5%, and 2%, and were determined from the volume of the flow circuit.

Performed measurements within this work consider a two way coupling, i.e., taking into account the effects of the particles on the carrier fluid and vice versa. The classification of the suspension flow used is made according to Sato [35], Elghobashi [36], and Crowe et al. [37], who proposed the particle volume fractions as the criterion of classification. This classification was made taking into account only the volume of suspension in the test pipe which is equal to 1/4 of the volume of the flow circuit. The particle volume fractions are in the range $1.25\times10^{-3}-5\times10^{-3}$. For the very fine tracer particles, the impurities contained in the tap water were used.

3.2 Optical Measurement System of the Velocity Profiles and the Turbulence Intensity. A single-component dual-beam LDA system in forward scatter mode and electronic logic were

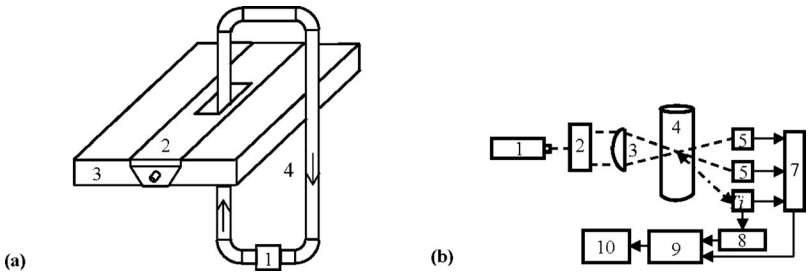

Fig. 2 Experimental setup of the velocity profiles and the turbulence intensity measurement: (*a*) flow circuit: (1) pump and tank, (2) horizontal table with micrometric displacement, (3) base, and (4) glass pipe; (*b*) optical measurement with acquisition and treatment system: (1) laser source, (2) beam splitter prism, (3) convergent lens, (4) flow pipe, (5) photodiode, (6) photomultiplier, (7) electronic logic, (8) bandpass filter, (9) digital storage oscilloscope, and (10) computer, (---) laser beams, (–·–·–) light diffused by the particle, and (—) interfacing cable

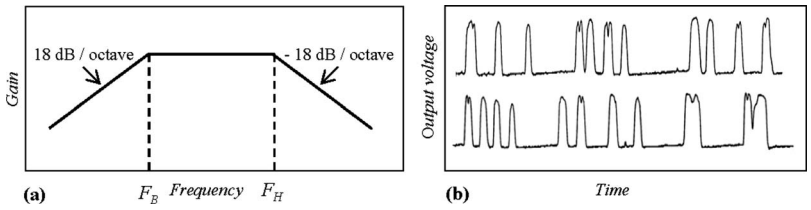

Fig. 3 Response characteristics of (*a*) the bandpass filter frequency and (*b*) the photodiodes, wave form

used to measure the axial velocity profiles and the turbulence intensity of the solid and liquid phases. Figure 2(*b*) shows the optical measurement system with the acquisition and treatment of the signal. The optical measurement system, consisting of the laser source, beam splitter prism, lens, and photomultiplier, is attached to the table with micrometric displacement.

In this setup, a 5 mW He–Ne laser was used with 632.8 nm wavelength. The laser beam was divided by a beam splitter prism to obtain two parallel beams 50 mm apart. These two beams were then sent through a focused lens with a focal length of 130 mm and emitted to form the measurement volume of $180 \times 550 \times 180\ \mu m^3$ inside the pipe. The plane containing the laser beams was perpendicular to the pipe axis.

The distance between interference fringes was 1.65 μm and the angle between the two beams was 23 deg. The photomultiplier was positioned in forward scattering mode at 45 deg, where the scattering light is controlled by the refraction and reflection [38]. The ratio of the photomultiplier aperture of 4 mm, to the distance between the particle and the photomultiplier, 125 mm, is lower than 0.1. The condition for the large spherical particles with smooth surface is thus satisfied in our case for glass beads with diameters of 0.5 mm and 1 mm. The ratio of the distance between the particle and the photomultiplier to the particle diameter is about of 250 times; we can then use the universal equation of single-phase laser anemometry (1).

The output signal of the photomultiplier is characterized as "burst" signal, as seen in Fig. 1. It consists of a pedestal component providing information on the particle size and a Doppler component providing information on particle velocity. The bandpass filter is used to remove the low frequency pedestal and the high frequency noise from the signal, see Fig. 3(*a*). The cut-off frequency (F_H) of the high pass filter is 100 kHz, and for low pass filter this frequency (F_B) ranges between 400 kHz and 1 MHz. The output signal of the filter is composed of the Doppler component and the residual signals due to optical and electronic noise that crosses the filter.

3.2.1 Separation of the Signals. The optical measurement system in Fig. 2(*b*) was used to distinguish between the continuous phase signal and large particle signal based on the amplitude of the unfiltered photomultiplier output signal. Yule et al. [39] showed that the amplitude of the signal from large particles is higher than that of tracer particles. The Schmitt trigger was used for this distinction. However, this property of the amplitude is not sufficient because the signal collected by the trigger is composed of both the signal of the liquid phase and that of the large particles. Figure 6(*b*) shows the typical signal obtained when the tracer and a large particle crossed the volume measurement simultaneously. This ambiguity is eliminated by the use of two photodiodes placed on the laser beam axes downstream from the measurement volume. These photodiodes have a response time of less than 1 ns, and are able to follow the particle motion accurately when the particle intersects the laser beams. The duration of the light pulse delivered by the photodiode is inversely proportional to the particle velocity. Figure 3(*b*) shows the response wave form of two photodiodes measured simultaneously with a digital storage oscilloscope prior to reaching the electronic logic circuit.

3.2.2 Logic Functional Diagram. The electronic logic circuit is used to distinguish signals from tracer particles and those from large particles. This is done by comparing the photomultiplier signal with the two photodiode signals. Figure 4 illustrates the electronic logic circuit used and presents the truth table of the different logical gates.

The impedance circuit adapter (1) delivers the output digital signal exactly received. In other words, the photomultiplier output signal of high impedance is equal to the electronic logic input signal without inversion of the phase. The attenuator circuit (2) attenuates the output signal, inverts its phase, and regulates the threshold of the Schmitt trigger (3). A high voltage level or "1" corresponds to 5 V_{dc} and a low voltage level or "0" corresponds to 0 V_{dc}. When the input voltage becomes greater than the upper limit of the trigger (1.7 V_{dc}), the output voltage is at low voltage

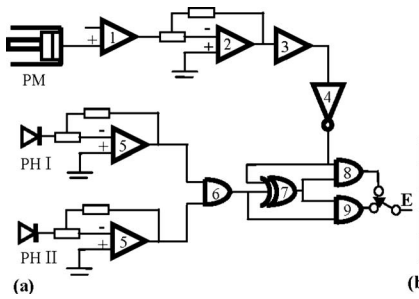

		SN7404		SN 74 LS 86	SN 7408
A	B	A	B	A + B	A.B
0	0	1	1	0	0
0	1	1	0	1	0
1	0	0	1	1	0
1	1	0	0	0	1

(b)

Fig. 4 Electronic logic circuit and truth table: (*a*) electronic logic circuit: (1) impedance circuit adapter (LM 308), (2) attenuator circuit (LM 308), (3) Schmitt trigger (SN 7414), (4) inverter signal (SN 7404 TTL), (5) inverter amplifier (LM 308), (6) AND gate (SN 7408 TTL), (7) OR EXCLUSIVE gate (SN 74 LS 86 TTL), (8) AND gate, and (9) AND gate, (PHI, PHII) photodiodes, (PM) photomultiplier, (*E*) digital logic circuit output; (*b*) truth table of logical gates

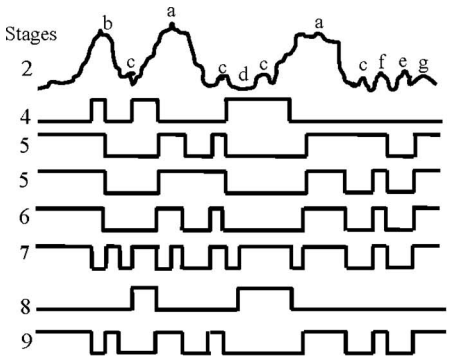

(a)

cases	Logical gates 4	5 PDI	5 PDII	6 PDI.PDII	7	8	9	Comment
a	1	0	0	0	1	1	0	large particle
b	1	1	1	1	0	0	0	ambiguity
c	0	1	1	1	1	0	1	small particule
d	0	0	1	0	0	0	0	no signal
e	0	1	0	0	0	0	0	ambiguity
f	0	1	1	1	1	0	1	/
g	0	0	0	0	0	0	0	No ambiguity

(b)

Fig. 5 Output wave forms and truth table of digital logic circuit: (*a*) output wave forms for different logical gates; (*b*) truth table of logical gates output for various cases

level or 0. The output voltage is at a high level or 1 if the input voltage is less than the lower threshold of the trigger ($0.9\ V_{dc}$). We use the terms Level 1 and Level 0 to indicate high and low voltage levels.

The logical inverter (4) outputs the exact opposite of the digital signal from the Schmitt trigger. This output signal of the logical inverter is at Level 1 each time that a photomultiplier signal exceeds the higher threshold.

The signals from the two photodiodes PH I and PH II are amplified using two identical inverter amplifiers (5).

These photodiodes deliver a Level 1 when there is a presence of light. When a solid particle cuts the laser beam, the photodiodes do not receive any light and deliver Level 0. The amplified signals of the two photodiodes then pass into a logical AND Gate (6). The two signals coming from the inverter and the AND gates (4) and (6) enter the logical OR EXCLUSIVE gate (7).

The output signal of Gate (7) is at Level 1 when the two input signals are different and at Level 0 when they are identical. This function enables the removal of some ambiguities met during the data acquisition.

The distinction between the signals from the large particles and the tracers is made in the following manner. For the large particles, the output signals from Gates (4) and (7) simultaneously enter a logical AND gate (8). The signal of the large particles is validated when both signals are at Level 1. For the tracers, the output signals of Gates (6) and (7) enter a logical AND gate (9). A two-position switch is used to select one of the output logical gates (8) or (9).

3.2.3 Operating Principle. From the wave forms of the output voltage of the different logical gates and the truth table (Fig. 5), we have identified the different cases that can arise as well as some ambiguities produced during the data acquisition.

Case a. A large particle crosses the measurement volume in the medium. The output of (4) is at Level 1. The particle cuts the laser beams at the same time and so the output of Gate (6) is Level 0 and gate (7) is at Level 1. The output of Stage (8) is at Level 1 so it confirms the passage of the large particle through the measurement volume.

Case b. Tracers cross the measurement volume simultaneously in time and in phase. In this case, the outputs of (4) and (6) deliver the same level, Level 1 because the tracers do not intersect the laser beams. The outputs of (8) and (9) are both at Level 0. This represents an artifact; therefore, this signal is eliminated.

Case c. One tracer passes through the measurement volume. The output of Gate (4) is at Level 0 and the output of Gate (6) delivers Level 1 because the laser beams are always present even when the tracer is present in the measurement volume. The output of Gates (7) and (8) are at Levels 1 and 0, and Gate (9) delivers Level 1. This confirms the presence of the tracer in the measurement volume.

Case d. A large particle cuts the laser beam upstream of the measurement volume. In this case, there is no Doppler signal even if the tracers are present in the measurement volume. All output stages are at Level 0, and the output of the electronic logic delivers Level 0.

Case e. A large particle cuts a laser beam downstream of the measurement volume. The outputs of Gates (4) and (6) are at the same level, Level 0 because the particle intersects the photodiode detected light. Then, the output of Gates (7)–(9) are at Level 0. This case is not accounted for because of ambiguity.

Case f. A large particle crosses at the edge of the measurement volume. In this case, the Doppler signal is very weak because of the low intensity of the light at the edge of the measurement volume. The outputs of Gates (4) and (6) are at Levels 0 and 1. Thus, Gate (7) delivers Level 1 and Gate (9) delivers Level 1. This same output level from Stages (7) and (9) represent ambiguity. This ambiguity can be eliminated by using the internal trigger of the digital storage oscilloscope to determine the amplitude of a filtered Doppler signal.

Case g. Two large particles simultaneously cut the two laser beams downstream of the measurement volume. Even with the presence of the tracer in the measurement volume, all outputs are at Level 0 and the output voltage of the electronic logic is at Level 0.

The output of (8) and (9) ensures the acquisition and the validation of the Doppler signals from, respectively, the large particles and the continuous phase. The sampling time of the large particles is defined by Signal (8) and that of the continuous phase by Signal (9).

3.2.4 Signal Processing. The signal from the filter can contain the velocity information of large particles in the form of Doppler frequency, Fig. 6(*a*), or the continuous phase, Fig. 6(*b*). The signal processing consists of determining the velocity corresponding to this frequency.

Frequency domain and Fourier transform were used for the analysis, due to the lower signal-to-noise ratio of the large particles (low signal visibility). The Doppler signal from the filter is sampled using a digital storage oscilloscope with 100 MHz of maximum sampling. The sampled function $\hat{x}(t)$ of the Doppler signal $x(t)$ is given by

$$\hat{x}(t) = x(t) \sum \delta\left(t - \frac{K}{f_e}\right) \tag{4}$$

where K is a constant and δ Dirac's impulse. According to the formula of Poisson, we have

$$\hat{x}(\nu) \rightleftharpoons X(\nu) \sum \delta(\nu - nf_e) \tag{5}$$

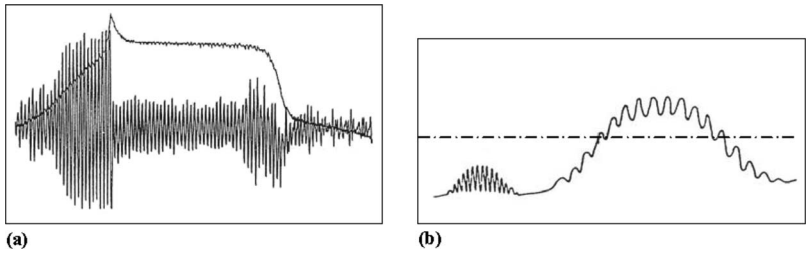

Fig. 6 Typical signals: (*a*) Doppler signal of glass bead with 1 mm of diameter; (*b*) signal obtained when the tracer and a large particle crosses the volume measurement simultaneously

where $X(\nu)$ is the Fourier transform of the Doppler signal $x(t)$.

To avoid the spectrum overlap phenomenon and thus the loss of information, the sampling frequency used was about five to ten times the greatest frequency of the spectrum. The values treated using the Fourier transform allow us to calculate the power spectral density $P(f)$ of the Doppler signal from the product of the frequency spectrum and its conjugate. The average Doppler frequency f_D is given by the normalized moment of order 1 of the ensemble average spectrum.

$$\overline{f_D} = \frac{\sum_{n=1}^{N} f_n G(f_n)}{\sum_{n=1}^{N} G(f_n)} \tag{6}$$

with

$$G(f_k) = \sum_{n=1}^{N} P_n(f_k) \tag{7}$$

with $k=1,2,3,\ldots,N$.

Considering that the enlargement of the spectrum is due only to the turbulent velocity fluctuations, we can calculate the normalized moment of second order of the energy spectrum integral associated with the Doppler signals. This moment with a Gaussian trend represents the turbulent intensity given by the relation

$$\sqrt{\overline{f_D'^2}} = \left[\sum_{n=1}^{N} (f_n - \overline{f_D})^2 G(f_n) \Big/ \sum_{n=1}^{N} G(f_n) \right]^{1/2} \tag{8}$$

3.2.5 Calibration Measurement. In order to validate the chosen method of signal processing, we developed the device illustrated in Fig. 7(*a*). This consists of a plastic disk of 200 mm diameter turning in the ambient air using a variable speed motor. Along the perimeter of the disk, cylindrical metal rods of 0.8 mm diameter and 40 mm length were fixed. The metal rods cross the measurement volume with a known tangential velocity U_t. The Doppler signal collected by the photomultiplier placed at 90 deg with respect to the optical axis is processed using fast Fourier transform. Figure 7(*b*), which represents the results for various disk rotation speeds, shows that there is a linear relationship between tangential velocity U_t and the Doppler frequency f_D.

3.3 Optical Measurement System of the Turbulent Length Scale. In addition to the analysis of the fluctuating velocity that generates the spectrum distribution of energy, the measurement of the turbulent scale allows the study of the particle-turbulence interactions and the characterization of the turbulent flows. In heterogeneous fluid flow, the Taylor assumptions used to determine the turbulent length scale in one measurement volume and for the time domain cannot be applied.

The integral turbulent length scale L_t is determined from the two-point spatial correlation function $R(x,x+\Delta x)$ for statistically steady turbulence. $R(x,x+\Delta x)$ given by Eq. (9) is obtained by simultaneously measuring the velocity in two distinct points distant from Δx.

$$R(x,x+\Delta x) = \frac{\overline{u_i'(x)u_i'(x,x+\Delta x)}}{\sqrt{\overline{u_i'^2(x)}}\sqrt{\overline{u_i'^2(x,x+\Delta x)}}} \tag{9}$$

For homogeneous isotropic turbulence, the integral length scale is given by

$$L_t = \tfrac{1}{3}L(x) \tag{10}$$

where $L(x)$ is the length scale tensor given by

$$L(x) = \frac{1}{2}\int_{-\infty}^{+\infty} R(x,x+\Delta x)d(\Delta x) \tag{11}$$

The direct measurement of the turbulent length scales is carried out by taking measurements of fluctuation velocity simultaneously

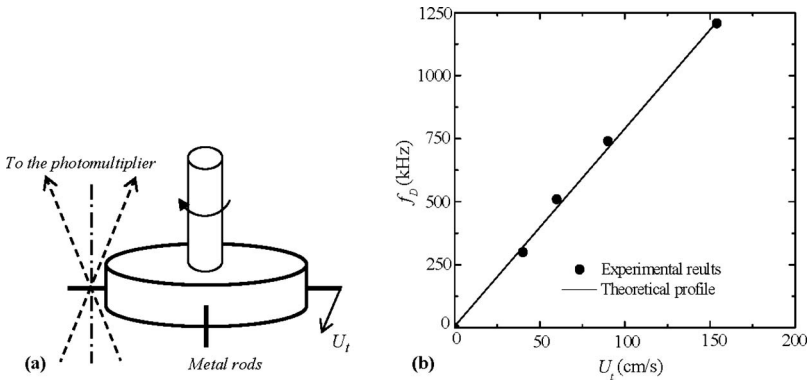

Fig. 7 Calibration measurement: (*a*) calibration system: (–·–) laser beam and (---) optical axis; (*b*) calibration curve

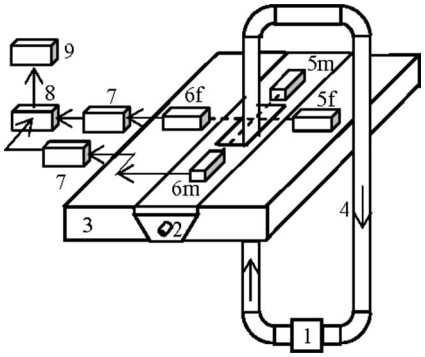

Fig. 8 Optical measurement system of the turbulence length scales: (1) pump and tank, (2) horizontal table with micrometric displacement, (3) base, (4) glass pipe, (5) laser source (m: moving with 2, f: fixed near the wall), (6) photomultiplier (m: moving with 2, f: fixed), (7) bandpass filter, (8) digital storage oscilloscope and (9) computer, (---) laser beams, (—) and interfacing cable

in two measurement volumes, Fig. 8. These measurements were obtained by using two laser sources of equal power 5 mW, one of which is fixed near the internal wall pipe (5f) and the other (5m) moving along the test section radius using the horizontal table (2). The two laser sources were placed on the same horizontal level but separated by an angle of 90 deg. At the reception points, two photomultipliers (6f) and (6m) were placed on the laser beam axes for the detection of the Doppler signal, and are followed by two identical bandpass filters.

For this optical measurement system, no electronic logic was used so the distinction between the signal from the continuous phase and that from large particles is based on the visibility property of the filtered Doppler signals from the photomultipliers. Indeed, the signals coming from the continuous phase have a good signal-to-noise ratio considering the size of the particles forming the tracer. For this tracer, the Doppler signal amplitude from the filter is larger than that of the large particles. It is enough to determine a threshold to distinguish between the signals from the continuous phase and the glass beads.

For the measurement of the turbulent length scales, the detection of two Doppler signals at the same time and at two different positions is necessary. The digital storage oscilloscope has a data acquisition period of 100 μs to ensure simultaneous measurements. This data acquisition period must be shorter than the time scale of turbulent fluctuations but also as large as possible in order to acquire data at high speed. The Doppler signal is obtained by counting the number of zero crossings, which are detected using the positive crossing function of the oscilloscope. A computer program is used to calculate the timings of the zero crossings.

The validation of the counting method consists of a comparison among five to eight periods with a tolerance of 3%. The calculation of the average frequency of the signals is determined by an elaborate software. Also, this same software computes the average frequency distribution of the small particles from the probability density distribution. Each point of this distribution represents 512 values of the signal average frequencies.

The probability density distributions of the Doppler frequencies obtained for four positions of the test section radius have the same trend as the Gaussian distributions.

4 Experimental Results

4.1 Mean Velocity Profiles of Fine Particles. The suspension consists of water and its impurities (very fine particles), which are used as tracer particles. We can thus assume that the mean slip velocity is negligible and the concentration is uniform [40]. Figure 9 shows the velocity profile plotted versus the radius using the tracer. Note that the mean velocity profile of water, marked by this tracer, coincides well with the theoretical profiles determined with the same flow for a homogeneous Newtonian fluid. The theoretical profile of water alone is drawn using the power-law profile

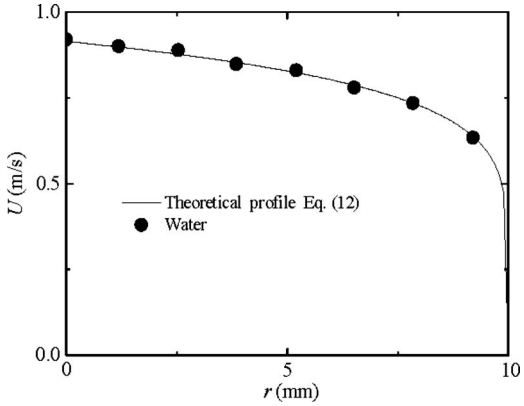

Fig. 9 Mean velocity profiles of water for $\bar{U}$=0.806 m/s

$$\frac{U}{U_{\max}} = \left(\frac{y}{R}\right)^{1/n} \tag{12}$$

This is the simpler form that adequately describes the turbulent flow velocity distribution in a pipe, where $y=R-r$ is the wall normal distance, $U_{\max}$ is the maximum velocity generally taken on the pipe axis, and n is a constant, which depends on the Reynolds number. For $n=7$, we obtain a good agreement between the theoretical profile and the experimental data with a value correlation coefficient close to 1.

4.2 Mean Velocity Profiles of the Large Particles. Large particles of high density compared to the carrier fluid, i.e., those where the diameter exceeds the wavelength of the laser, do not follow the flow. Figure 10 shows the influence of the flow mean velocity on the large particle velocity profile. It is noted that the velocity profiles of the solid particles are below that of water, except for those near the wall, for all mean flow velocities. The difference between the velocity profiles of water and the particles shows the existence of a slip velocity, which according to certain authors is approximately the terminal velocity of the particles in stationary water. Ohashi and Sugawara [41] reported that this is not always true, and found that the solid-liquid slip velocities depend on the mean flow velocity. Indeed, the difference between the velocity profiles of water and the particles decreases as the velocity of the flow increases. This same phenomenon was ob-

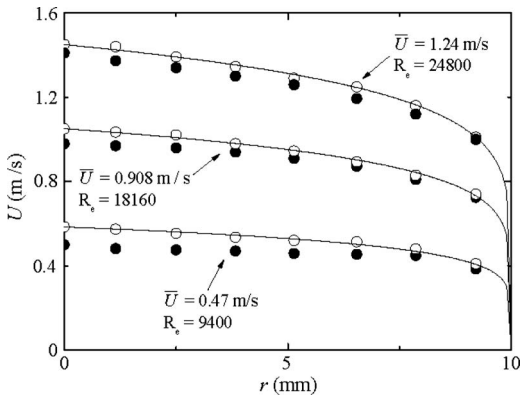

Fig. 10 Mean velocity profiles of water and glass beads at different flow mean velocities (C_v=1%); (—) theoretical profile Eq. (12); (○) water alone; (●) solid particles

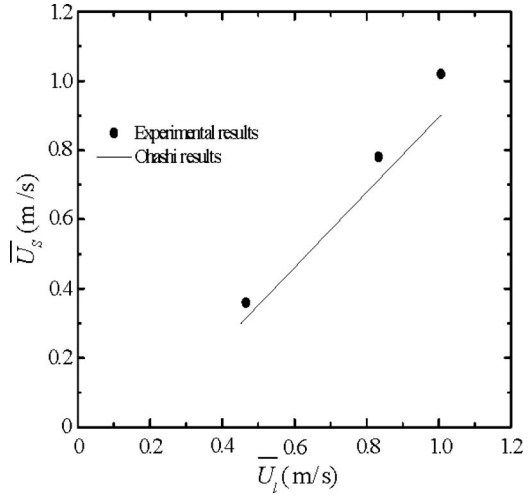

Fig. 11 Comparison between the experimental results and those obtained by the model of Ohashi and Sugawara [41]

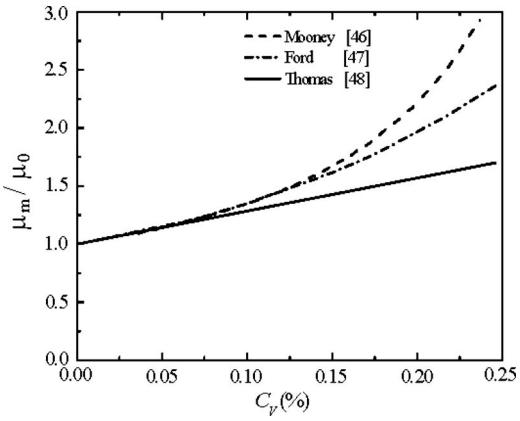

Fig. 13 Variation of relative viscosity versus the volumetric concentration

served by Idrissi [42] and Belibel [43] by using ultrasound velocimetry. Modarress et al. [12] have shown that the mean slip velocity between the two phases increases with increasing particle diameter but decreases with increase in the initial mass loading. Similar results have been obtained for other concentrations.

Figure 11 shows the difference between the particles' mean velocity and the water velocity $\bar{U}_s$ and $\bar{U}_l$. The present data are in good agreement with Ohashi and Sugawara's data [41]: Both sets of data are from the same volumetric concentration of $C_v=1\%$ and the same diameter pipe of $D=20$ mm. This result shows the effect of the flow mean velocity on the slip velocity $\bar{U}_l-\bar{U}_s$. This slip velocity induces the fluid-particle interactions.

Figure 12 shows the velocity profiles of the solid particles of diameter $d_p=0.5$ mm for various volumetric concentrations. The flatness of the profiles is accentuated at higher concentrations of the solid particles. This is also the case for the 1 mm diameter particles: The velocity profiles are even more flattened than those obtained for the 0.5 mm diameter. These results confirm those obtained by Kowalewski [44]. The same results have been obtained for other mean velocities.

4.3 Results Analysis. The obtained results show that the velocities of the glass beads depend on the mean flow velocity, the concentration, and the particle diameter. To analyze the distribution of local mean velocities of the solid particle quantitatively and to study the influence of each parameter referred above, we have to examine the variations of the dimensionless velocity profiles

$$U^+ = f(y^+) \tag{13}$$

This procedure was used in Ref. [45] for open channel flows, and Ref. [42] for flows in circular pipes. It is necessary to know the friction velocity U_s^* and the suspension dynamic viscosity μ_m. By analogy with a homogeneous fluid, the friction velocity of a solid-liquid suspension is given by

$$U_s^* = \sqrt{\frac{\tau_p}{\rho_m}} \tag{14}$$

where τ_p is the wall shear stress and ρ_m the suspension density.

The dimensionless wall distance in the case of the suspension is given by

$$y^+ = yU_s^* \frac{\rho_m}{\mu_m} \tag{15}$$

where μ_m is the suspension viscosity that depends on the volumetric concentration. The models proposed by Mooney [46], Ford [47], and Thomas [48] for the suspension dynamic viscosity according to the volumetric concentration are shown in Fig. 13. For volumetric concentrations lower than 5%, the suspension dynamic viscosity can be represented by the carrying fluid viscosity.

Figure 14 shows the variation of the dimensionless velocity profiles of solid particles of 1 mm of average particle diameter d_p for various volumetric concentrations. It is noticed that the dimen-

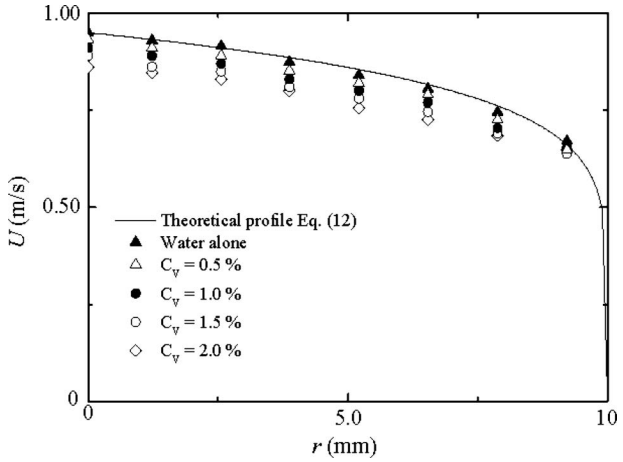

Fig. 12 Mean velocity profiles of the glass beads with various concentrations (d_p=0.5 mm, Re=16,200)

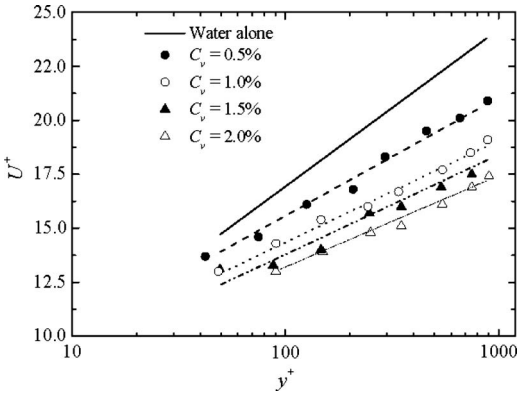

Fig. 14 Dimensionless velocities of the solid particles (d_p =1 mm)

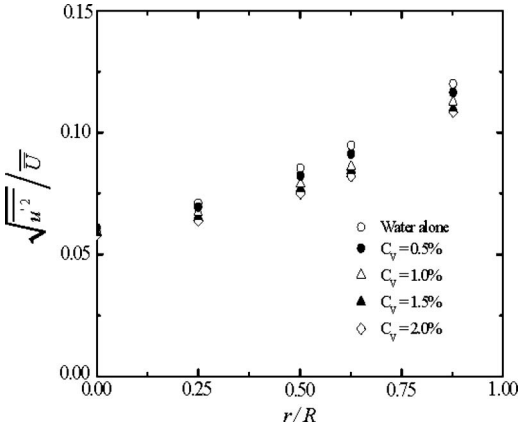

Fig. 15 Turbulence intensity of water and solid particles (Re =16,200, d_p=1 mm)

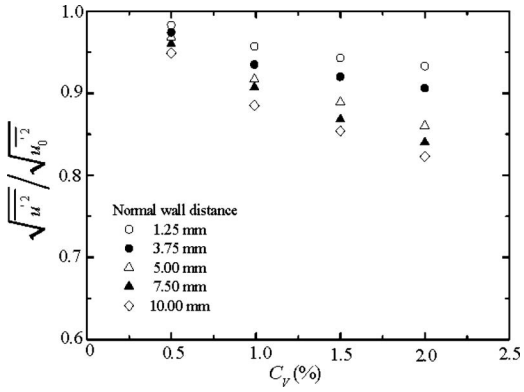

Fig. 16 Reduction of turbulence intensity (Re=16,200, d_p =1 mm)

sionless velocity profiles of the solid particles are all located below the dimensionless velocity profile of water alone as given by the universal law.

$$U^+ = 5.75 \log y^+ + 5.5 \tag{16}$$

valid for $y^+ > 30$.

At each volumetric concentration of the glass beads, the experimental points are well aligned starting from $y^+ = 100$. For $y^+ > 100$, the dimensionless velocity profiles of the solid particles in suspension can be put in the form

$$U^+ = A \log y^+ + B \tag{17}$$

where y^+ is taken from Eq. (15), and

$$U^+ = \frac{U}{U_s^*} = f(y^+) \tag{18}$$

The results obtained for the 0.5 mm diameter are of lesser values than the 1 mm diameter.

Coefficients A and B decrease with increasing concentration and the diameter of the solid particles, thus confirming the observed flatness of the velocity profiles. The difference between the dimensionless velocity profile of water alone and profiles of the solid particles, which increase with concentration, is related to the increase of solid-liquid slip velocities. The same observations were made by Idrissi [42] by using ultrasound velocimetry; he established a model of coefficients A and B, which is a function of the diameter and the concentration of the solid particles.

4.3.1 Effect of Particles' Concentration on the Turbulence Intensity. Considering the widening of the power spectrum associated with the Doppler signal is only due to the turbulence; we have calculated the turbulence intensity from the second order moment. Figure 15 shows that for water alone, the turbulence intensity in the parietal area is greater than that of the pipe axis. The turbulence intensity decreases when the glass beads' concentration increases along the test section radius.

For each diameter particle used (0.5 mm and 1 mm), the ratio of particle diameter (d_p) to turbulent length scale L_t (determined by Eq. (10)) is less than 0.1. According to Gore et al. [20], the turbulent kinetic energy of the continuous phase is dissipated.

Figure 16 shows that the turbulence intensity decreases with concentration and increases with distance from the wall. We notice a reduction from 4.5% to 10% of the turbulence intensity at 2% of concentration. This result is similar to Bouvard and Petkovic's result [49]. Kulick et al. [21] have shown that fluid turbulence was attenuated by the addition of particles smaller than the Kolmogorov length scale and that the degree of attenuation decreased with the distance from the wall. According to Ahmed and Elghobashi [50], this decrease is due to the change of turbulent kinetic product rate of the continuous phase, which is caused by the particle effect on the vorticity dynamics.

4.3.2 Effect of Particle Concentration on the Turbulence Integral Length Scale. Figure 17 represents the spatial correlation of water alone and the solid particles of 1 mm in diameter and volumetric concentration $C_v = 1\%$ obtained by the use of two same laser sources (see Fig. 8).

The lateral integral length scale was calculated by using a 10 mm separation between two measurement volumes that correspond to the radius of the pipe. From Eqs. (9)–(11), the determined lateral integral length scales of water alone and solid particles were respectively, 3.75 mm and 3.32 mm. It is apparent that the lateral integral scale decreases when the solid particles' concentration increases. We notice a reduction of the turbulence scale of 12% for a 1% concentration.

5 Conclusion

In this study, we have developed a measurement technique in order to determine the velocity profiles of the solid particles (glass bead) and the continuous phase (water) of an ascending two phase flow in a vertical pipe. An electronic logic circuit built into the measuring equipment made it possible to distinguish between the signals coming from the continuous phase and those from the solid particles. The use of this technique is limited to small concentrations lower than 2%. Indeed, when a concentration of 2% is exceeded, the suspension becomes a very diffusing medium and prevents the propagation of the laser beams. This technique shows the effects of the particle diameter and concentrations on the local mean velocity profiles of the suspensions.

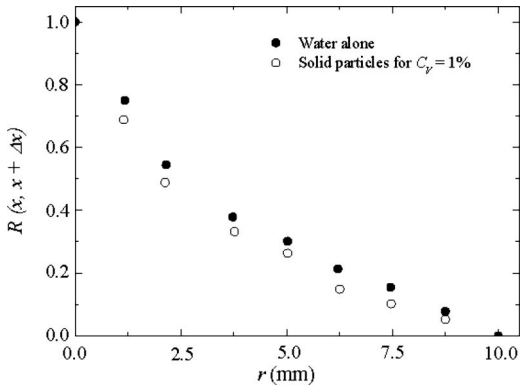

Fig. 17 Reduction of the lateral integral scale of turbulence, Re=16,200

The results obtained show that for fine particles, the suspension behaves like a homogeneous fluid. For the large particles, we confirmed that the existence of a slip velocity is responsible for the fluid-particle interaction.

The dimensionless velocity profiles of the large particles follow a logarithmic law with slope depending on the concentration and particle diameter. The turbulence characteristics are also affected by the presence of the solid particles. Indeed, the results show that the turbulence intensity is reduced when the volumetric concentration of particles is increased.

The use of two identical laser sources in order to obtain two distinct measurement volumes allows the determination of the turbulent length scale of the continuous phase and solid particles. The results show that the presence of particles can modify the turbulent length scale of the continuous phase. From these good results, we conclude that the two measurement volumes method can be easily applied to the turbulent length scale measurements.

In our next study concerning the solid liquid suspension of high volumetric concentrations greater than 2%, we will be experimenting with a very fine adjustment of the suspension refractive index in order to avoid multiple scattering in a light scattering experiment.

Nomenclature

$A_{\max}$ = the irradiance corresponding to the maximum in the fringe system
$A_{\min}$ = the irradiance corresponding to the adjacent minimum in the fringe system
C_v = volumetric concentration
d_p = particle diameter
D = pipe diameter
L_t = integral turbulent length scale
$P(f)$ = power spectral density of the Doppler
R = pipe radius
Re = Reynolds number
$R(x,x+\Delta x)$ = spatial correlation function
U = axial velocity component
U^+ = dimensionless velocity
U_s^* = suspension friction velocity
$\bar{U}$ = flow mean velocity
V = visibility or degree of modulation
f_e = sampling frequency
$\overline{f_D}$ = average Doppler frequency
f_D = Doppler frequency signal
r = variable pipe radius
u' = velocity fluctuation
$\sqrt{\overline{u_0'^2}}$ = turbulence intensity of water
$\sqrt{\overline{u'^2}}$ = turbulence intensity of water with the presence of the solid particles
$\sqrt{\overline{u'^2}}/\sqrt{\overline{u_0'^2}}$ = ratio that represents a reduction of turbulence intensity
y = wall normal distance
y^+ = dimensionless wall distance

Greek

δ = Dirac's impulse
η = Kolmogorov length scale
λ_0 = laser beam wavelength
μ_m = suspension dynamic viscosity
μ_0 = water dynamic viscosity
θ = half-angle between intersecting laser beams
ρ_m = suspension density
τ_p = wall shear stress

References

[1] Elghobashi, S. E., and Truesdell, G. C., 1993, "On the Two-Way Interaction Between Homogeneous Turbulence and Dispersed Solid Particles. I: Turbulence Modification," Phys. Fluids A, **5**(7), pp. 1790–1801.
[2] Michaelides, E. E., and Stock, D. E., 1989, *Turbulence Modification in Dispersed Multiphase Flows*, ASME, New York, FED Vol. 80.
[3] Owen, P. R., 1969, "Pneumatic Transport," J. Fluid Mech., **39**, pp. 407–432.
[4] Parthasarathy, R. N., and Faeth, G. M., 1990, "Turbulence Modulation in Homogeneous Dilute Particle-Laden Lows," J. Fluid Mech., **220**, pp. 485–514.
[5] Parthasarathy, R. N., and Faeth, G. M., 1990, "Turbulent Dispersion of Particles in Self-Generated Homogeneous Turbulence," J. Fluid Mech., **220**, pp. 515–537.
[6] Varaksin, A. Y., and Zaichik, L. I., 2000, "Effect of Particles on the Carrier Flow Turbulence," J. Thermophys. Aeromech., **7**, pp. 237–248.
[7] Lei, K., Taniguchi, N., and Kobayashi, T., 2000, "LES of Particle-Laden Turbulent Channel Flow Considering SGS Coupling. A Proposal of Dynamic SGS Model," Trans. Jpn. Soc. Mech. Eng., Ser. B, **66**(651), pp. 2807–2814.
[8] Chandok, S. S., and Pei, D. C. T., 1972, "Particle Dynamics in Solid-Gas Flows in a Vertical Pipe," Prog. Heat Mass Transfer, **6**, pp. 465–474.
[9] Meada, M., Hishida, K., and Furutani, T., 1980, "Optical Measurements of Local Gas and Solid Velocity in an Upward Flowing Dilute Gas-Solid Suspension," *Proceedings of the Polyphase Flow and Transport Technology*, Century 2-ETC, San Francisco, CA, pp. 211–216.
[10] Durst, F., 1982, "Review—Combined Measurements of Particle Velocities, Size Distributions, and Concentrations," ASME Trans. J. Fluids Eng., **104**, pp. 284–296.
[11] Tsuji, Y., Morikawa, Y., and Shiomi, H., 1984, "LDV Measurements of an Air-Solid Two-Phase Flow in a Vertical Pipe," J. Fluid Mech., **139**, pp. 417–434.
[12] Modarress, D., Tan, H., and Elgobashi, S., 1984, "Two-Component LDA Measurement in a Two-Phase Turbulent Jet," AIAA J., **22**(5), pp. 624–630.
[13] Solomon, A. S. P., Shuen, J. S., Zhang, Q. F., and Faeth, G. M., 1985, "Structure of Non Evaporating Sprays, Part I: Initial Conditions and Mean Properties," AIAA J., **23**(10), pp. 1548–1555.
[14] Solomon, A. S. P., Shuen, J. S., Zhang, Q. F., and Faeth, G. M., 1985, "Structure of Non Evaporating Sprays, Part II: Drop and Turbulence Properties," AIAA J., **23**(11), pp. 1724–1730.
[15] Mostafa, A. A., Mongia, H. C., McDonell, V. G., and Samuelsen, G. S., 1989, "Evolution of Particle-Laden Jet Flows: A Theoretical and Experimental Study," AIAA J., **27**(2), pp. 167–183.
[16] Park, C. J., and Chen, L. D., 1989, "Experimental Investigation of Confined Turbulent Jets, Part I: Particle-Laden Flow Data," AIAA J., **27**(11), pp. 1506–1510.
[17] Park, C. J., and Chen, L. D., 1989, "Experimental Investigation of Confined Turbulent Jets, Part II: Single-Phase Data," AIAA J., **27**(11), pp. 1511–1516.
[18] Geiss, S., Dreizler, A., Stojanovic, Z., Chrigui, M., Sadiki, A., and Janicka, J., 2004, "Investigation of Turbulence Modification in a Non-Reactive Two-Phase Flow," Exp. Fluids, **36**(2), pp. 344–354.
[19] Schreck, S., and Kleis, S. J., 1993, "Modification of Grid-Generated Turbulence by Solid Particles," J. Fluid Mech., **249**, pp. 665–688.
[20] Gore, R. A., and Crowe, C. T., 1989, "Effect of Particle Size on Turbulent Intensity," Int. J. Multiphase Flow, **15**, pp. 279–285.
[21] Kulick, J. D., Fessler, J. R., and Eaton, J. K., 1994, "Particle Response and Turbulence Modification in Fully-Developed Channel Flow," J. Fluid Mech., **277**, pp. 109–134.
[22] Hardalupas, Y., Taylor, A. M. K. P., and Whitelaw, J. H., 1989, "Velocity and Particle-Flux Characteristics of Turbulent Particle-Laden Jets," Proc. R. Soc. London, Ser. A, **426**, pp. 31–78.
[23] Durst, F., and Zare, M., 1975, "Laser-Doppler Measurements in Two-Phase Flows," *Proceedings of the LDA-Symposium*, Copenhagen, pp. 403–429.
[24] Saffmann, M., Buchhave, P., and Tanger, H., 1984, "Simultaneous Measurements of Size Concentration and Velocity of Spherical Particles by a Laser Doppler Method," *Laser Anemometry in Fluid Mechanics—II*, R. J. Adrian, D. F. G. Durano, F. Durst, H. Mishina, and J. H. Whitelaw, eds., Ladoan Instituoto Superior Tecnico, Lisboa, Portugal.
[25] Bachalo, W. D., and Houser, M. J., 1984, "Phase Doppler Spray Analyzer for Simultaneous Measurements of Drop Size and Velocity Distributions," Opt. Eng. (Bellingham), **25**(5), pp. 583–590.
[26] Bachalo, W. D., and Houser, M. J., 1985, "Experiments in Polydispersed Two-Phase Turbulent Flows," *Second International Symposium on Laser Anemometry*, Miami, FL, ASME, New York, FED Vol. 33, pp. 135–141.
[27] Tadrist, L., Azario, E., and Cattieuw, P., 1993, "Analysis of Two-Phase Flow in a Circulating Fluidized Bed," *Proceedings of the 4th International Conference on Circulating Fluidized Bed*, Vol. 2, pp. 702–707.
[28] Van Den Moortel, T., Santini, R., and Tadrist, L., 1996, "Measurement of Local Mass Flux in a Circulating Fluidized Bed Using a Phase Doppler Particle Analyzer," *Proceedings of the ASME Heat Transfer Division*, Vol. 3, pp. 239–250.
[29] Zhang, Y. F., and Arastoopour, H., 1995, "Dilute FCC Particles/Gas Flow Behaviour in the Riser of a Circulating Fluidized Bed," Powder Technol., **84**(3), pp. 221–229.
[30] Mathiesen, V., Solberg, T., Arastoopour, H., and Hjertager, B. H., 1999, "Experimental and Computational Study of Multiphase Gas/Particle Flow in a CFB Riser," AIChE J., **45**(12), pp. 2503–2518.
[31] Mathiesen, V., Solberg, T., and Hjertager, B. H., 2000, "An Experimental and Computational Study of Multiphase Flow Behavior in a Circulating Fluidized Bed," Int. J. Multiphase Flow, **26**(3), pp. 387–419.
[32] Albrecht, H. E., Damaschke, N., Borys, M., and Tropea, C., 2003, *Laser Doppler and Phase Doppler Measurement Techniques*, Springer, Berlin.

[33] Farmer, W. M., 1972, "Measurement of Particle Size, Number Density, and Velocity Using a Laser Interferometer," Appl. Opt., **11**, pp. 2603–2612.
[34] Bachalo, W. D., 1980, "Method for Measuring the Size and Velocity of Spheres by Dual—Beam Light—Scatter Interferometry," Appl. Opt., **19**, pp. 363–370.
[35] Sato, Y., 1996, "Turbulence Structure and Modelling of Dispersed Two-Phase Flows," Ph.D. thesis, Keio University, Japan.
[36] Elghobashi, S. E., 1994, "On Predicting Particle-Laden Turbulence Flows," Appl. Sci. Res., **52**, pp. 309–329.
[37] Crowe, C. T., Troutt, T. R., and Chung, J. N., 1996, "Numerical Models for Two-Phase Turbulent Flows," Annu. Rev. Fluid Mech., **28**, pp. 11–43.
[38] Eckel, A., 1983, "Contribution to the Development of Simultaneous Measurement Methods of Dimensions, Velocities and Concentration of Particles in Two-Phase Flows," Ph.D. thesis, University of Louis Pasteur, Strasbourg, France.
[39] Yule, A. J., Chigier, N. A., Atakan, S., and Ungut, A., 1977, "Particle Size and Velocity Measurement by Laser Anemometry," J. Energy, **1**(4), pp. 220–228.
[40] Furuta, T., Tsujimoto, S., Thoshima, M., Okasaki, M., and Toei, R., 1977, "Concentration Distribution of Particles in Solid-Liquid. Two Phase Flow Through Vertical Pipe," Mem. Fac. Eng., Kyoto Univ., **36**, Part 4, pp. 155–162.
[41] Ohashi, A., and Sugawara, T., 1980, "Average Particle Velocity in Solid-Liquid Two Phase Flow Through Flow Vertical and Horizontal Tubes," J. Chem. Eng. Jpn., **13**(5), pp. 343–349.
[42] Idrissi, B. A., 1987, "Solid-Liquid Mixture Flow in Pipe. Velocity Profiles in Vertical Flow," Ph.D. thesis, University of Louis Pasteur, Strasbourg, France.
[43] Belibel, C., 1985, "Mixture Solid-Liquid Flow in Pipes. Velocity Fields in Vertical Flow," Ph.D. thesis, University of Louis Pasteur, Strasbourg, France.
[44] Kowalewski, T. A., 1984, "Concentration and Velocity Measurements in Flow of Droplet Suspension Through a Tube," Exp. Fluids, **2**, pp. 213–219.
[45] Bouvard, M., and Petkovic, S., 1985, "Vertical Dispersion of Spherical Heavy Particles in Suspension in a Channel With Turbulent Free Flow," J. Hydraul. Res., **23**(1), pp. 5–23.
[46] Mooney, M., 1951, "The Viscosity of Concentrated Suspension of Spherical Particles," J. Colloid Sci., **6**, pp. 162–170.
[47] Ford, T. F., 1960, "Viscosity and Fluidity Concentration, Relation Ships for Suspension of Spherical Particles in Newtonian Liquids," J. Phys. Chem., **64**, pp. 1168–1174.
[48] Thomas, B., 1953, "Viscosity of Suspension," *Proceedings of the 3rd Midwestern Conference on Fluid Mechanics*.
[49] Bouvard, M., and Petkovic, S., 1973, "Modification of a Turbulence Characteristics Under the Influence of Solid Particles in Suspension," La Houille Blanche, 1.
[50] Ahmed, A. M., and Elghobashi, S. E., 2000, "On the Mechanisms of Modifying the Structure of Turbulent Homogeneous Shear Flows by Dispersed Particles," Phys. Fluids, **12**(11), pp. 2906–2930.

Pressure Drop Predictions in Microfibrous Materials Using Computational Fluid Dynamics

Ravi K. Duggirala[1]
e-mail: duggirk@vt.edu

Christopher J. Roy

Aerospace Engineering Department,
Auburn University,
211 Aerospace Engineering Building,
Auburn, AL 36849-5338

S. M. Saeidi

Jay M. Khodadadi

Mechanical Engineering Department,
Auburn University,
Auburn, AL 36849

Don R. Cahela

Bruce J. Tatarchuk

Chemical Engineering Department,
Center for Microfibrous Materials Manufacturing,
Auburn University,
Auburn, AL 36849

Three-dimensional computational fluid dynamics simulations are performed for the flow of air through microfibrous materials for void fractions of 0.41 and 0.47 and face velocities ranging between 0.04 ms and 1.29 m/s. The microfibrous materials consist of activated carbon powder with diameters of 137×10^{-6} m entrapped in a matrix of cylindrical fibers with diameters of 8×10^{-6} m. These sintered microfibrous materials are a new class of patented materials with properties that are advantageous compared to traditional packed beds or monoliths. Microfibrous materials have demonstrated enhanced heat and mass transfer compared to packed beds of particles of similar dimensions. In this paper, the simulations are used to predict the pressure drop per unit length through the materials and to analyze the details of the flow that are difficult to interrogate experimentally. Various geometric approximations are employed in order to allow the simulations to be performed in an efficient manner. The Knudsen number, defined as the ratio of the mean free path between molecular collisions to the fiber diameter, is 0.011; thus, velocity-slip boundary conditions are employed and shown to have only a minor effect on the pressure drop predictions. Significant effort is made to estimate numerical errors associated with the discretization process, and these errors are shown to be negligible (less than 3%). The computational predictions for pressure drop are compared to available experimental data as well as to two theory-based correlations: Ergun's equation and the porous media permeability equation. The agreement between the simulations and the experiments is within 30% and is reasonable considering the significant geometric approximations employed. The errors in the simulations and correlations with respect to experimental data exhibit the same trend with face velocity for both void fractions. This consistent trend suggests the presence of experimental bias errors that correlate with the face velocity. The simulations generally underpredict the experimental pressure drop for the low void fraction case and overpredict the experimental pressure drop for the high void fraction case. [DOI: 10.1115/1.2948363]

Introduction

One of the challenges in a logistic power system using an onboard polymer electrolyte membrane (PEM) fuel cell is to design high-efficiency gas clean-up units. These units are required to reduce the sulfur concentration down to 0.1 ppb (parts per billion) [1] and total carbon oxides including CO and CO_2 to below 1 ppm. Traditional approaches using extrudates in packed beds usually require large reactor sizes for these low threshold applications [2] because of their low contacting efficiency, channeling, and severe mass transfer resistances. Therefore, the traditional approaches may not be applicable for logistic applications and novel sorbent/catalysts and reactor designs are required.

Microfibrous entrapped catalysts and sorbents (MFESs) developed at the Center for Microfibrous Materials Manufacturing (CM^3) at Auburn University provide a novel approach for more effective design of small, efficient, and lightweight fuel processors [3]. MFES have demonstrated excellent performance in heterogeneous reactions such as H_2S removal [4] and CO oxidation [5]. For H_2S removal, MFES demonstrated lower pressure drop, reduced critical bed depth, improved ZnO utilization, ease of regeneration, and high dynamic capacity compared packed bed counterparts [6]. Since the active component is ZnO in both MFES and extrudates, the difference is due to the kinetic behavior of the materials.

The underlying mechanisms behind the enhanced reactivity of microfibrous media are not fully understood, especially for the applications at low Reynolds and Schmidt numbers. In order to understand the basic physical and chemical processes in microfibrous materials and to optimize their effectiveness, computational fluid Dynamics (CFD) is being used.

CFD deals with the solution to the discrete form of the nonlinear, coupled, partial differential equations that govern fluid flow, i.e., the Navier–Stokes equations. Microscale gas flow simulations can be difficult since at very small scales, the continuum hypothesis of the Navier–Stokes equations is invalid. One challenge in the application of CFD to microscale gas flows is in the modeling of additional phenomena that occur at the microscale, which are generally neglected in macroscale simulations [7]. These phenomena are primarily surface interaction effects and are characterized by the Knudsen number, $\mathrm{Kn}=\lambda/L$, the ratio of the mean free path between molecular collisions to the characteristic length scale. The Knudsen number determines the degree of rarefaction of the gas and the validity of continuum flow assumptions. Flows with Knudsen numbers below 0.01 are considered fully continuum flows and are amenable to modeling with the standard Navier–Stokes equations. For Knudsen numbers between 0.01 and 0.1, the flow is in the slip regime where noncontinuum effects can be incorporated by allowing for velocity, temperature, and concentration discontinuities (i.e., slip) at surfaces through boundary condition modifications. Flows with Knudsen numbers between 0.1 and 10 are said to be in the transitional regime between continuum

[1]Corresponding author.

Contributed by the Fluids Engineering Division of ASME for publication in the JOURNAL OF FLUIDS ENGINEERING. Manuscript received March 16, 2007; final manuscript received April 9, 2008; published online June 25, 2008. Review conducted by Joseph Katz.

flow and free molecular flow, where the application of continuum methods with appropriate rarefaction models is still being investigated. For Knudsen numbers greater than 10, the gas is essentially in free molecular flow, where statistical methods such as direct simulation Monte Carlo or molecular dynamics simulations must be used. Surface effects will dominate the flow behavior in microscale systems. The increase in surface area relative to the volume will affect the mass, momentum, and energy transfer [8].

For microscale flows, another important dimensionless parameter is the Reynolds number

$$\mathrm{Re} = \frac{\rho V D}{\mu}$$

which is the ratio between inertial and viscous forces. Inertial forces will be small while surface friction and viscous effects will dominate at the microscale, which leads to the laminar flow. In order to understand the different flow regimes, it is helpful to examine the canonical flow over a cylinder, which are discussed in various text books [9]. Transition from a laminar to turbulent wake flow does not occur until Reynolds numbers greater than 200, and typical upper limit of Reynolds number for microscale flows is between 40 and 100. Thus, turbulence is extremely unlikely in most microscale flows. For the flow through porous media, a similar analogy can be made based on pipe flow theory.

Various numerical approaches have been developed in order to understand microscale gas flows. These flows can be modeled by solving continuum equations with slip boundary conditions (i.e., the continuum approach). Many conventional computational techniques can be used to solve the continuum equations including finite volume method [10] and the finite element method [11]. To extend the application of the continuum approach to model flows in the slip regime, wall boundary conditions having discontinuous jump in velocity, temperature jump, and concentration are required due to rarefied gas phenomena.

Using the spectral element method, Karniadakis' group developed a Navier–Stokes solver [12], which uses a slip boundary condition that is designed to be valid over the entire range of Knudsen number [13,14]. They studied the rarefied gas effects for flows in channels, pipes, and ducts and showed that the continuum-based approach can be employed to simulate microflows in the continuum and slip regimes [7].

Using upwind differences and a finite volume approach, a numerical method was developed by Hennighausen [15], which integrates the compressible Navier–Stokes equations on a deforming grid. The Maxwell slip boundary condition was used and a preconditioning technique was also implemented in order to expedite the iterative convergence at low Mach numbers.

Porous materials are used in a variety of processes, such as fixed bed reactors, packed distillation columns, adsorbent beds, filters, and heat pipes. In general, spherical particles are used in the catalyst beds. The fluid flow pattern in these types of beds is not well understood. A macroscopic framework cannot provide an exact solution for the flow through porous media because of the complicated boundaries in the pore structure [16]. For modeling the flow through porous media, it is generally assumed that the flow is through a set of parallel tubes with the radius of the tube determined by the geometry (i.e., the hydraulic radius). It is assumed that the flow through a packed bed and fully developed flow through a straight pipe (with approximate hydraulic radius) will have the same pressure drop-flow rate relationship.

Information on the flow through packed beds was thoroughly examined by Ergun in 1952. He found that the pressure losses are due to simultaneous kinetic and viscous energy losses, which follow a comprehensive equation that is applicable to flow through packed beds. Pressure losses depend on flow rate, properties of the fluids, fractional void volume, as well as the orientation, size, shape, and surface of the particles in the packed bed.

Papathanasiou et al. [17] evaluated the Ergun and Forchheimer equations for the permeability of fibrous porous media using square and hexagonal arrays of fibers. Arrays with uniform fibers as well as arrays in which the fiber size was allowed to change were used in their study with the porosity ranging from 0.30 to 0.60 (these lower porosities represent actual materials used in biotechnology applications) and the Reynolds number ranged between 0 and 160. No-slip boundary conditions were used on the fiber surfaces and symmetry boundary conditions were used in the fluid. The inlet and outlet were linked as periodic boundary condition and the pressure was obtained from the applied force in the direction of fluid flow. The authors compared the numerical results obtained from FIDAP to the predictions of KOKOPELLI, a research CFD code developed at Los Alamos National Laboratory. The authors reported that the numerical results coincided with Ergun equation at high porosity and low Reynolds number ($\mathrm{Re} < 1$), whereas for low porosity and high Reynolds number, Ergun equation over-predicted the friction factor in square arrays. For the hexagonal geometry, numerical predictions were in good agreement for $\mathrm{Re} < 1$, but disagreed for larger Reynolds number. The authors also observed that the Forchheimer equation slightly overpredicted the friction factor for the square geometry while it underpredicted it for the hexagonal array. At very low Reynolds number (creeping flow), the Forchheimer equation was in good agreement with the numerical simulations, while the Ergun equation did not capture the behavior of the fiber arrays in the flow with strong contracting/expanding elements.

Andrade et al. [18] investigated the origin of the deviation from the classical Darcy law numerically by simulating the Navier–Stokes equations in two-dimensional disordered porous media. They used the Forchheimer equation to correlate the variations of friction factor with porosity and the flow conditions. They observed the transition from linear to nonlinear at high Reynolds number where inertia becomes important. They found that the transition can be understood and characterized in terms of spatial distribution of kinetic energy in the system.

Hicks [19] briefly discussed regarding the validity of the Ergun equation in predicting the pressure drop in a packed bed of spheres. He showed that the coefficients (a,b) in the Ergun equation vary with Reynolds number and are not true constants. He also showed that the Ergun equation is not a good fit of pressure drop for smooth spheres with the value $\mathrm{Re}/(1-f)$ greater than 500 and that in the range $300 < \mathrm{Re}/(1-f) < 60{,}000$, the viscous friction factor is represented by the nonlinear relationship.

As an alternative to packed beds, high surface area extrudates, particles, or sheets can be used in chemical/thermal processes. These extrudates can be produced from sintered or fused materials at the microscale. CM^3 at Auburn University has developed a new class of composite materials consisting of roughly spherical adsorbent/reactant particles embedded in a matrix of sinter-bonded microfibers with diameters of order 10×10^{-6} m. Most of the chemical and thermal processes depend on kinetic phenomena that occur on active surfaces and are important to obtain desired intraparticle and intrabed transport rates. As we decrease the size of the particles entrapped in the microfibrous network, intraparticle transport increases. Furthermore, the ability of the mesh to separate the particles also increases the intrabed transport [20].

Applications of these microfibrous materials include microfibrous wicks used for heat pipes in thermal management systems, which result in higher heat transfer rates at lower thermal gradients, sintered metal fiber filters used in several commercial processes, such as polymer filtration, automotive airbags, and assorted high-efficiency particulate air (HEPA) filter applications [20]. In order to know when these microfibrous catalysts are best suited to accelerate reaction rates, it is important to determine the flow characteristics including the pressure drop within the system as well as thermal and chemical properties.

This study is focused on flow through microfibrous materials in which the flow characteristics and pressure drops are analyzed via CFD simulations. The governing equations and numerical approach employed are discussed in detail, and efforts are made to

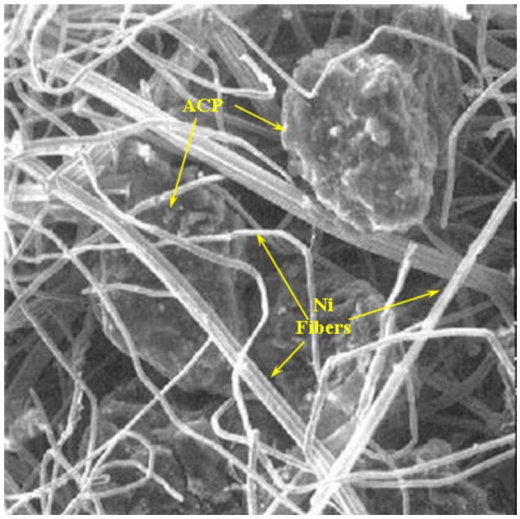

Fig. 1 SEM of sintered composite material of (55–58) $\times 10^{-6}$ m ACP with 2×10^{-6} m, 4×10^{-4} m, and 8×10^{-6} m Ni fibers

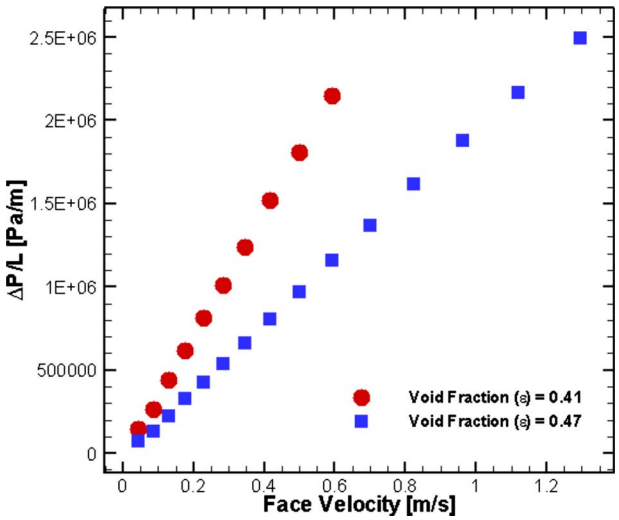

Fig. 2 Pressure drop through 8×10^{-6} m Ni/ACP mesh (experimental data from Ref. [21])

quantify the numerical errors in the simulations. The pressure drop predictions are then compared with the experimental data and empirical correlations.

Problem Description

This study is focused on the flow through microfibrous materials, a type of porous media. These microfibrous materials are a new class of composite materials developed by CM^3 at Auburn University using traditional paper making techniques that are discussed in detail by Ref. [20]. Materials consisting of activated carbon powder (ACP) embedded into a mesh of nickel (Ni) and pyrolyzed cellulose (PC) fibers are used in this study. The particles are roughly spherical with diameters ranging between 100×10^{-6} m and 150×10^{-6} m, whereas the fibers are roughly cylindrical with diameters ranging between 10×10^{-6} m and 15×10^{-6} m. Experiments were conducted by Ref. [21] to measure the pressure drop in microfibrous materials consisting of fiber diameters of Ni and PC of 8×10^{-6} m and 10×10^{-6} m, respectively, and 100–120 mesh activated carbon powder. The solid volume percentages of Ni, ACP, and PC were 7.1%, 91.4%, and 1.5%, respectively. A detailed description of the materials used and the experimental setup is given by Ref. [21]. Pressure drops were measured in these materials with 40–50% void fraction at face velocities between 0.04 m/s and 1.29 m/s. (The face velocity is defined as the velocity that would occur if the microfibrous material was not present.) A scanning electron microscopy (SEM) image of $(55-58)\times10^{-6}$ m ACP entrapped in a micrometal fiber matrix of 2×10^{-6} m, 4×10^{-6} m, and 8×10^{-6} m Ni fibers is shown in Fig. 1 where the fibers and ACP are clearly identifiable. The measured pressure drops across the unit length of the bed are plotted against the face velocity for both void fractions and are shown in Fig. 2. The pressure drop varies linearly with the face velocity for both void fractions. It should be noted that the experimental data set of Ref. [21] also includes pressure drop measurements at a voidage of $\varepsilon=0.67$; however, problems securing the microfibrous media in the test apparatus (related to the deformation of the edges of the high voidage, spongelike material) are believed to have created significant bias errors. Therefore, these high voidage data are omitted from the present study.

Numerical Simulation Approach

The commercial CFD code, FLUENT, is used to analyze the flow and predict the pressure drop for microfibrous materials. In this section, the governing equations, geometric approximations, mesh, boundary conditions, discretization, iterative convergence, and grid convergence are discussed in detail.

Governing Equations. The governing equations used to simulate compressible, laminar, steady flow through microfibrous materials include conservation equations for mass, momentum, and energy:

$$\nabla\cdot(\rho\mathbf{V})=0 \tag{1}$$

$$\nabla\cdot[(\rho u)\mathbf{V}]=-\frac{\partial p}{\partial x}+\frac{\partial\tau_{xx}}{\partial x}+\frac{\partial\tau_{yx}}{\partial y}+\frac{\partial\tau_{zx}}{\partial z} \tag{2a}$$

$$\nabla\cdot[(\rho v)\mathbf{V}]=-\frac{\partial p}{\partial y}+\frac{\partial\tau_{xy}}{\partial x}+\frac{\partial\tau_{yy}}{\partial y}+\frac{\partial\tau_{zy}}{\partial z} \tag{2b}$$

$$\nabla\cdot[(\rho w)\mathbf{V}]=-\frac{\partial p}{\partial z}+\frac{\partial\tau_{xz}}{\partial x}+\frac{\partial\tau_{yz}}{\partial y}+\frac{\partial\tau_{zz}}{\partial z} \tag{2c}$$

$$\frac{\partial}{\partial t}(\rho h)+\nabla\cdot(\rho\mathbf{V}h)=\nabla\cdot(k\nabla T)-\frac{\partial}{\partial x}(up)-\frac{\partial}{\partial y}(vp)-\frac{\partial}{\partial z}(wp)+\frac{\partial}{\partial x}(u\tau_{xx})+\frac{\partial}{\partial y}(u\tau_{yx})+\frac{\partial}{\partial z}(u\tau_{zx})+\frac{\partial}{\partial x}(v\tau_{xy})+\frac{\partial}{\partial y}(v\tau_{yy})+\frac{\partial}{\partial z}(v\tau_{zy})+\frac{\partial}{\partial x}(w\tau_{x})+\frac{\partial}{\partial y}(w\tau_{yz})+\frac{\partial}{\partial z}(w\tau_{zz}) \tag{3}$$

where the viscous stresses are given by the following.

For normal stresses,

$$\tau_{xx}=2\mu\frac{\partial u}{\partial x}-\frac{2}{3}\mu\nabla\cdot\mathbf{V},\quad \tau_{yy}=2\mu\frac{\partial v}{\partial y}-\frac{2}{3}\mu\nabla\cdot\mathbf{V}$$

$$\tau_{zz}=2\mu\frac{\partial w}{\partial z}-\frac{2}{3}\mu\nabla\cdot\mathbf{V}$$

For shear stresses,

$$\tau_{xy}=\tau_{yx}=\mu\left(\frac{\partial v}{\partial x}+\frac{\partial u}{\partial y}\right),\quad \tau_{xz}=\tau_{zx}=\mu\left(\frac{\partial w}{\partial x}+\frac{\partial u}{\partial z}\right)$$

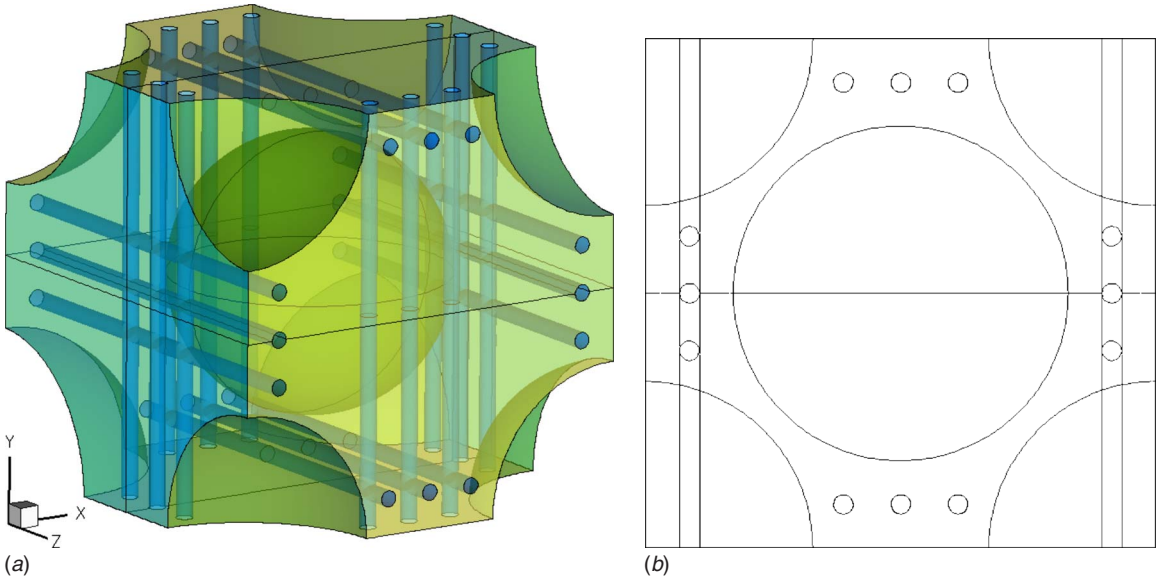

Fig. 3 (*a*) **Isometric view of the simplified geometry;** (*b*) **front view of the simplified geometry**

$$\tau_{yz} = \tau_{zy} = \mu\left(\frac{\partial w}{\partial y} + \frac{\partial v}{\partial w}\right)$$

Equations (1), (2), (2*a*)–(2*c*), and (3) represent the continuity, *X*, *Y*, and *Z* momenta, and energy equations in conservative form, respectively. In this study, the equation of state (Eq. (4)) for an ideal gas is used to calculate the density

$$\rho = \frac{p}{RT}M \tag{4}$$

for the compressible flow with change in pressure. The absolute viscosity of air is assumed to be constant ($\mu = 1.85 \times 10^{-5}$ kg/m s).

Geometric Approximations. A simplified 3D geometric approximation for the microfibrous material is used in the CFD simulations and is shown in Fig. 3. The straight cylindrical fibers and spherical particles are evident in the isometric view, and the regular orientation of the fibers in the domain is shown in the front view. The geometric approximations made while modeling the microfibrous material are as follows: (1) The activated carbon particles are assumed to be spherical in shape with a diameter of 137×10^6 m and are arranged in a regular matrix, as shown in Fig. 3; (2) the fibers are assumed to be straight cylinders; (3) only one size of cylindrical fibers (8×10^6 m, weighted average diameter) is considered instead of two fibers (Ni and PC) with different diameters (7.6×10^6 m and 10.4×10^6 m, respectively); (4) the fibers are oriented perpendicular to the flow direction, parallel to the *Y* and *Z* axes; (5) the fibers oriented parallel to the *Y* and *Z* axes intersect each other whereas in reality fibers do not intersect; (6) the length to height ratio of each unit cell is assumed to be one.

Flow-Field Mesh. FLUENT's preprocessor, GAMBIT, is used to generate flow-field meshes. An unstructured mesh consisting of tetrahedral volumetric elements in 3D is used in the entire domain except around the fibers and the particles, where a structured boundary layer mesh consisting of pentahedral volumetric elements is used. Figure 4(*a*) shows a sample mesh consisting of triangular elements on the particle and fiber walls of the modeled microfibrous material. Figure 4(*b*) shows the unstructured mesh on the top symmetry face along with the boundary layer mesh around the fiber and the particle (in the enlarged region at the right). The effect of using a structured boundary layer mesh around the fibers and particles is also examined by considering a case with an unstructured mesh in the entire domain. Pressure drops on the structured and unstructured meshes around the fibers and the particles varied by up to 2–8%; moreover, the unstructured mesh results had significantly larger numerical error as estimated by a grid refinement study. The accuracy of the unstructured (tetrahedral) mesh results could be increased by refining the mesh, but the additional refinement is expensive in both computation cost and solution time. As a result, a boundary layer mesh is used around the fibers and the particles to reduce the computation cost and time and improve accuracy.

Boundary Conditions. Since the velocities are periodic in the *X* direction, the inlet and outlet planes are linked as periodic boundary condition, which enforces periodicity of the velocity but allows a pressure drop. By employing symmetry arguments, only one-quarter of the total domain shown in Fig. 3 is modeled to reduce the computational effort and a symmetry boundary condition is use on all four sides (top, bottom, front, and back). Surfaces of the fibers and particles are defined as high Knudsen number slip walls by enabling the low-pressure slip boundary formulation in FLUENT, which uses the first-order Maxwell velocity-slip boundary condition as discussed below [22].

Verification of Slip Boundary Condition Formulation. The commercial CFD code FLUENT is used for the current simulations [22]. The purpose of this section is to verify the formulation of slip boundary condition in FLUENT. 2D Poiseuille flow (pressure driven flow) is used as a test case and a schematic is given in Fig. 5 showing the boundary conditions. The top and bottom boundaries are stationary walls, while the left and right sides are linked together with the periodic boundary condition, which matches velocity components but allows a pressure gradient. Maxwell's first-order velocity-slip boundary condition (Eq. (5)) as given by Ref. [7] is applied to the stationary walls.

$$U_s - U_w = \frac{2 - \sigma_v}{\sigma_v}\lambda\frac{\partial U}{\partial n} \tag{5}$$

Velocity profiles are available for this type of benchmark solution from the simulation by McNenly et al. [23] and an analytic solution also exists. McNenly et al. [23] evaluated the performance of the three popular slip models from literature. The three slip models chosen are Maxwell's model, empirical model pro-

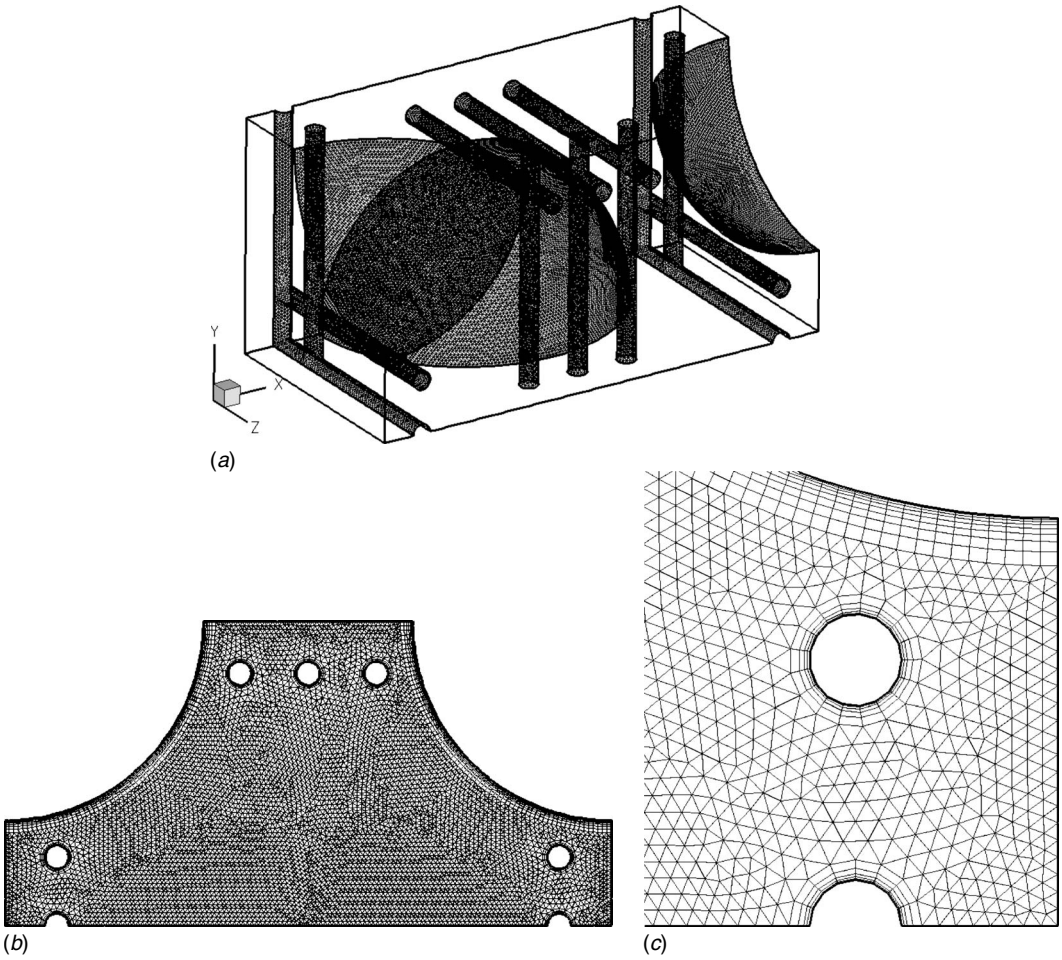

Fig. 4 (*a*) Triangular mesh on the fiber and particle walls; (*b*) triangular mesh on the top symmetry face with a structured boundary layer mesh around the particles and the fibers

posed by Karniadakis and Beskok, and a first-order empirical model based on DSMC results. Velocity profiles obtained from CFD simulations using FLUENT are compared to the profiles obtained by McNenly [23] and to the analytic solution. Air is used as a working fluid, which enters the domain with a flow velocity of 20 m/s. The temperature of the walls is fixed at 273 K. Several tests are conducted by varying the Knudsen number from 0.01 to 1.0. Since the Knudsen number applied in this paper is not too large, comparison of the results at high Knudsen numbers is not discussed. The tangential momentum accommodation coefficient (σ_v), defined as the fraction of tangential momentum the gas molecules exchange with the surfaces, is taken as unity, which means the molecules are reflected from the wall with zero average tangential velocity, or diffuse reflection [7]. The analytic solution for velocity profiles in Poiseuille flow using the second-order velocity-slip boundary condition was derived in Ref. [7] and is given by

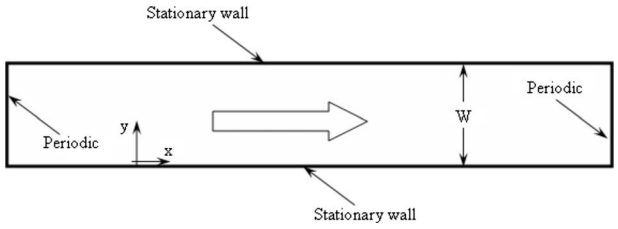

Fig. 5 Illustration of test case geometry for Poiseuille flow

$$U(x,y) = -\frac{dp}{dx}\frac{W^2}{2\mu}\left[-\left(\frac{y}{W}\right)^2 + \left(\frac{y}{W}\right) + C_1\mathrm{Kn} + 2C_2\mathrm{Kn}^2\right] \quad (6)$$

For Maxwell's first-order velocity-slip boundary condition, C_1 and C_2 are equal to 1 and 0, respectively. The results obtained from the CFD simulations are compared with literature and the analytic solution in Fig. 6. The distance measured from the bottom wall is nondimensionalized with the total distance between the two stationary walls (W). Velocities are plotted against the nondimensional height of the domain for different Knudsen numbers in Fig. 6. The results obtained from CFD simulations are in good agreement with both the analytic solution and the results from Ref. [23] for the three Knudsen numbers tested. Figure 6 also shows the increase in the velocity at the wall with the increase in the Knudsen number. For Knudsen numbers of 0.01 and 0.1, the wall velocities are approximately 1 m/s and 6 m/s, respectively.

Discretization. The process of converting partial differential equations into a set of algebraic relations, which can be solved on a computer is called discretization. It involves two main steps: (1) converting the continuum partial differential equations into algebraic relations and (2) converting the continuous physical domain into nodes, volumes, or elements where the algebraic equations will be solved. An iterative solution approach is employed where the solution is advanced in pseudotime until the steady-state equations are satisfied to a specified tolerance. At each iteration, the governing equations are solved sequentially using a segregated solver. A finite volume-based technique is used to solve the dis-

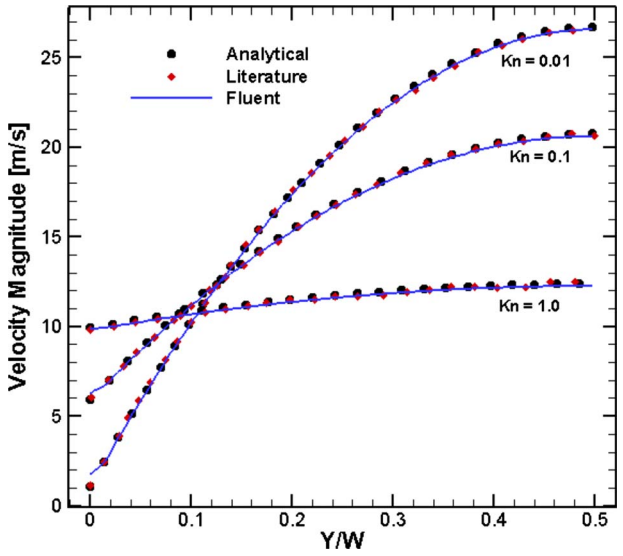

Fig. 6 Comparison of velocity profiles for Poiseuille flow at three Knudsen numbers

crete form of the governing equations on the computational grid. In the finite volume technique, we approximate the volume averaged quantities with the values at the cell center. The standard SIMPLE algorithm is used in which the momentum equations are first solved for the velocity components. A pressure correction is then determined, which will drive the velocity field toward satisfying the mass conservation equation. See Ref. [24] for more details.

The imbalance in the discrete equations is called the residual, and the residuals for each equation are normalized by their initial values and monitored during each iteration. Due to difficulties in converging the residuals to 10^{-7} using the second-order spatial discretization, the following procedure is used to converge the solution in all cases. Initially for these simulations, a first-order upwind scheme is used to discretize conservation equations where the face value on a cell is assumed to be equal to the cell-centered value in the upstream cell. The solution is then converged to a relative residual tolerance of 10^{-3} using the first-order upwind spatial discretization scheme. At this point, a second-order discretization scheme is used to discretize the conservation equations where the face value on a cell is evaluated using the cell-centered value and the gradient in the upstream cell.

Iterative Convergence. Iterative convergence is assessed by monitoring the steady-state residuals. The convergence criterion is set to 10^{-7} for all conservation equations. A sample residual history for the computation with a void fraction of 0.47 and a face velocity of 0.04 m/s is shown in Fig. 7. We observe that the residuals decrease gradually with each iteration. There is a sudden rise when residuals reach 10^{-3} as the discretization scheme is changed from first to second order, then the residuals gradually decrease and approach 10^{-7}. The iterative error in the pressure drop is found by comparing the pressure drop at the current iteration to the converged pressure drop (residuals $\sim 10^{-7}$):

$$\%\,\text{error in}\ \left(\frac{\Delta P}{L}\right)_{i\text{th iteration}} = \left|\frac{\left(\frac{\Delta P}{L}\right)_{\text{converged}} - \left(\frac{\Delta P}{L}\right)_{i\text{th iteration}}}{\left(\frac{\Delta P}{L}\right)_{\text{converged}}}\right| \times 100\% \tag{7}$$

The iterative error in the pressure drop is also shown in Fig. 7. We observe that the percentage error in the pressure drop (right axis) decreases gradually from each iteration and approaches 10^{-2} as the maximum residual (left axis) approaches 10^{-6}. The value of 10^{-7} is thus used as the residual convergence tolerance for all the simulations presented herein. For this residual convergence tolerance, the iterative error in the pressure drop is estimated to be less than 0.001% and can thus be neglected.

Grid Convergence. As the original conservation equations are discretized, the numerical solution will not match with the exact solution to the partial differential equations. The difference between the numerical solution and the exact solution is called discretization error. The discretization error is usually the primary

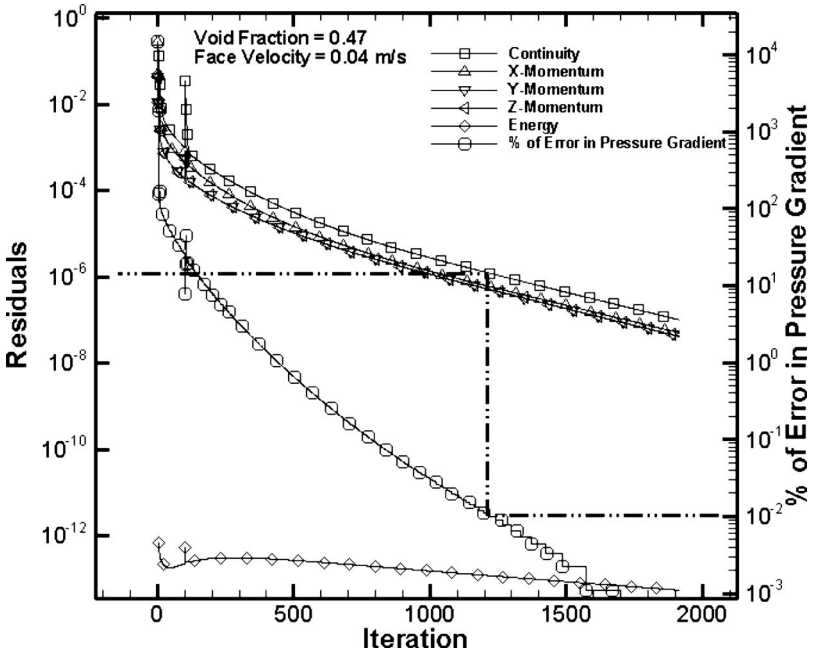

Fig. 7 Iterative convergence as determined by residual reduction (left axis) and estimated error in the pressure drop (right axis)

Table 1 Discretization error data

Void fraction	Face velocity (m/s)	Grid type	No. of elements	Grid refinement factor	Pressure gradient (Pa/m)	Estimated discretization error	Order of accuracy
0.41	0.04	Fine	2,743,441	1.4999	143,670	1.841%	1.632
		Medium	812,958	1.4455	141,140	3.570%	
		Coarse	369,136	—	136,380	6.822%	
	0.59	Fine	2,743,441	1.4999	1,978,100	1.251%	1.632
		Medium	812,958	1.4455	1,943,600	2.973%	
		Coarse	369,136	—	1,878,700	6.213%	
0.47	0.04	Fine	3,398,596	1.3959	91,668	1.379%	1.606
		Medium	1,249,410	1.5102	90,759	2.357%	
		Coarse	362,743	—	89,102	4.139%	
	1.29	Fine	3,398,596	1.3959	2,872,600	1.085%	1.829
		Medium	1,249,410	1.5102	2,846,100	1.997%	
		Coarse	362,743	—	2,793,600	3.805%	

source of numerical errors in CFD simulations. The exact solution for the pressure drop per unit length that can be estimated using generalized Richardson extrapolation [25] is given by

$$\left.\frac{\Delta P}{L}\right|_{\text{exact}} = \left.\frac{\Delta P}{L}\right|_1 + \frac{\left.\frac{\Delta P}{L}\right|_1 - \left.\frac{\Delta P}{L}\right|_2}{r^{p'} - 1} \tag{8}$$

Once the exact solution has been estimated, the relative discretization error (RDE) in the fine grid solution can then be estimated using

$$\text{RDE} = \frac{\left.\frac{\Delta P}{L}\right|_1 - \left.\frac{\Delta P}{L}\right|_{\text{exact}}}{\left.\frac{\Delta P}{L}\right|_{\text{exact}}} \times 100\% \tag{9}$$

The generated flow-field grids along with Eqs. (8) and (9) are used to estimate the discretization error for both void fractions at high and low face velocities. The quantity p' in Eq. (8) is set to the formal order of accuracy of $p'=2$. Discretization error estimates in these numerical simulations are tabulated in Table 1 along with the details of the generated flow-field grids and pressure gradients. It is observed that the estimated discretization errors range from 1.2% (fine grid) to 6.8% (coarse grid) for the void fraction of 0.41 and from 1.0% (fine grid) to 4.1% (coarse grid) for the void fraction of 0.47. This estimated discretization error provides guidance in choosing an appropriate grid. The medium grid is used for all simulations presented in this study, which has maximum discretization error estimates of 3.5% for the cases examined.

The accuracy of the estimated exact solution for pressure drop per unit length can be determined by comparing the observed order of accuracy with the formal order. The formal order of accuracy is determined by a truncation error analysis, and is defined as the order of the leading term of the truncation error obtained in the process of discretizing the governing equations. The observed order of accuracy is the order of accuracy of the numerical solution, which can be calculated using solutions on three grids as [26]

$$\frac{\left.\frac{\Delta P}{L}\right|_3 - \left.\frac{\Delta P}{L}\right|_2}{r_{23}^{p''}} = r_{12}^{p''}\left(\frac{\left.\frac{\Delta P}{L}\right|_2 - \left.\frac{\Delta P}{L}\right|_1}{r_{12}^{p''} - 1}\right), \quad r_{ij} = \sqrt[n]{\frac{N_i}{N_j}} \tag{10}$$

Three flow-field grids are generated by uniformly refining each cell in the domain by a factor of 1.5 in all three directions (X, Y, and Z). The observed order of accuracy is obtained for these grids using Eq. (10) for both void fractions at high and low face velocities. Table 1 also shows the observed order of accuracy found from the pressure gradients on the three meshes. The formal order of accuracy for these numerical simulations is 2 as a second-order upwind discretization is used. Table 1 shows that the observed order of accuracy is between 1.6 and 1.8, which is nearly equal to the formal order of accuracy and gives confidence that the numerical errors are indeed reduced with grid refinement.

Empirical Correlations

Ergun's Equation. The factors to be considered in determining the pressure drop in packed beds are the rate of fluid flow and the void fraction as well as the size, shape, and surface roughness of the particles [27]. In the laminar flow regime, using Hagen–Poiseuille's law, $f=16/\text{Re}$, and the modified Reynolds number, $\text{Re}=(2/3)(\rho V_0 D_p/\mu(1-\varepsilon))$, for the packed bed, we get

$$f = \frac{\Delta P}{L}\frac{D_p\varepsilon^3}{\rho V_0^2(1-\varepsilon)} = 72\frac{(1-\varepsilon)}{\left(\frac{\rho V_0 D_p}{\mu}\right)} \tag{11}$$

By performing a least squares fit on experimental data, Ergun came up with a constant of 150 instead of 72 in Eq. (11) [27,28]. The modified equation (which employs a constant of 150) is called the Blake–Kozeny equation [28] and is given by

$$f = \frac{\Delta P}{L}\frac{D_p\varepsilon^3}{\rho V_0^2(1-\varepsilon)} = 150\frac{(1-\varepsilon)}{\left(\frac{\rho V_0 D_p}{\mu}\right)} \tag{12}$$

In the case of turbulent flow at high Reynolds number, the Burke–Plummer equation can be used [28]

$$f = \frac{\Delta P}{L}\frac{D_p\varepsilon^3}{\rho V_0^2(1-\varepsilon)} = 1.75 \tag{13}$$

By incorporating both Eqs. (12) and (13), we get Ergun's equation

$$f = \frac{\Delta P}{L}\frac{D_p\varepsilon^3}{\rho V_0^2(1-\varepsilon)} = 150\frac{(1-\varepsilon)}{\left(\frac{\rho V_0 D_p}{\mu}\right)} + 1.75 \tag{14}$$

Ergun's equation (Eq. (14)) is valid for a packed bed with spherical particles of a constant diameter. Defining an equivalent diameter allows one to use Ergun's equation to estimate the pressure drops in the flows through any porous media [28]. In this study, the porous media consist of particles and fibers. An equivalent diameter (D_{eq}) is calculated using Eq. (15) as defined by [21]

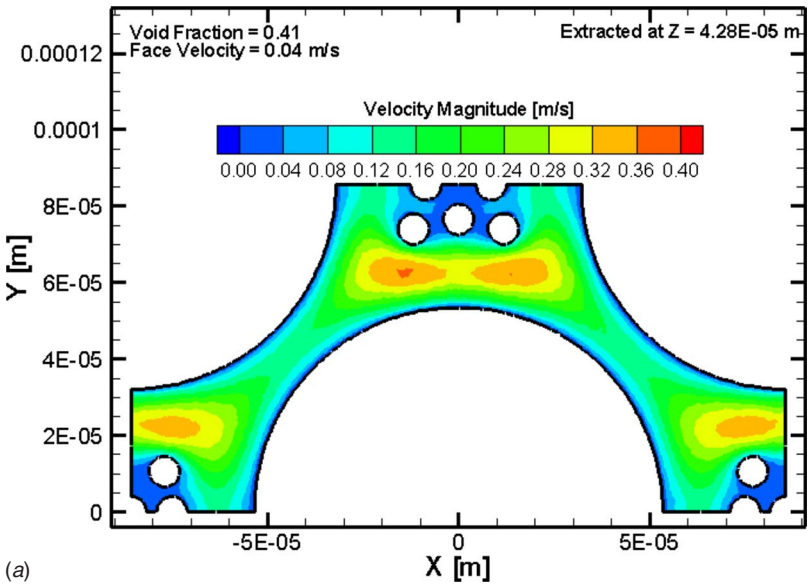

Fig. 8 (*a*) Velocity magnitude contours; (*b*) pressure contours $Z=4.28\times10^{-5}$ m; $\varepsilon=0.41$; $V_0=0.04$ m/s

$$\frac{1}{D_{\text{eq}}}=\sum_{i=1}^{n'}\frac{1}{D_i\phi_i} \tag{15}$$

The shape factor ϕ for the particles is calibrated using Ergun's equation for a packed bed. Initially, pressure drop is measured in a packed bed consisting of the particles whose shape factor is to be determined. Once the pressure drop is measured, the shape factor of the particles is then determined from Ergun's equation along with Eq. (15).

Porous Media Permeability Equation. Ergun's equation is designed for packed beds and does not apply for void fractions greater than 50% as it does not consider form drag losses, which are small in low void fraction flows. Most filters composed of fibrous materials have porosity greater than 80% [20]. The viscous form drag losses are calculated using Stokes law and are added to the viscous friction loss, which improves Ergun's equation for materials with high void fraction. This modified form of Ergun's equation, called the porous media permeability (PMP) equation, was developed by Ref. [21].

The pressure drop due to form drag can be calculated from Stokes law as

$$\left(\frac{\Delta P}{L}\right)_{\text{drag}}=6\frac{\tau^2}{\cos^2(\theta)}\frac{\mu V_0(1-\varepsilon)^2}{\varepsilon(\phi D)^2} \tag{16}$$

The total pressure drop due to viscous losses is the sum of the friction losses and the drag losses and is thus given by

$$\left(\frac{\Delta P}{L}\right)_{\text{viscous}}=72\frac{\tau^2}{\cos^2(\theta)}\frac{\mu V_0(1-\varepsilon)^2}{\varepsilon^3(\phi D)^2}[1+x_{\text{FD}}],\quad x_{\text{FD}}=\frac{\varepsilon^2}{12(1-\varepsilon)} \tag{17}$$

Equation (17) gives the pressure drop in a packed bed with solid particles of any shape. Cahela and Tatarchuk [21] developed an equation to calculate the pressure drop through microfibrous materials consisting of solid particles and fibers of any shape, which is given by

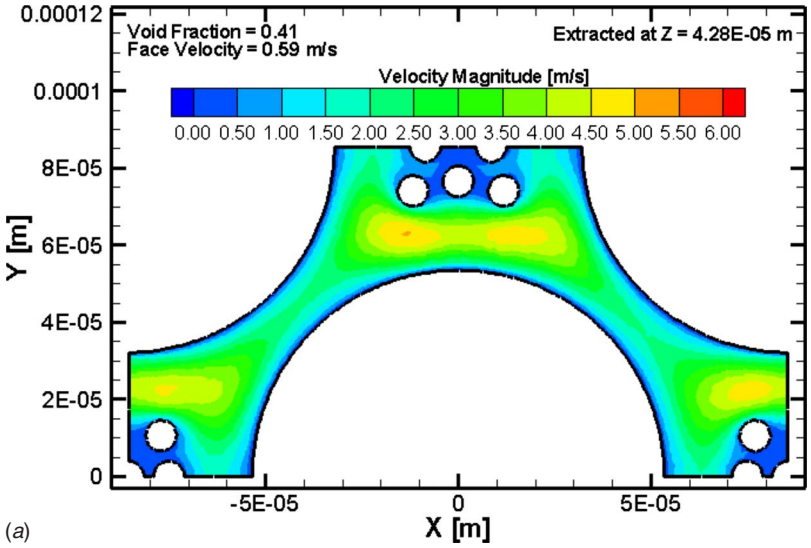

(*a*)

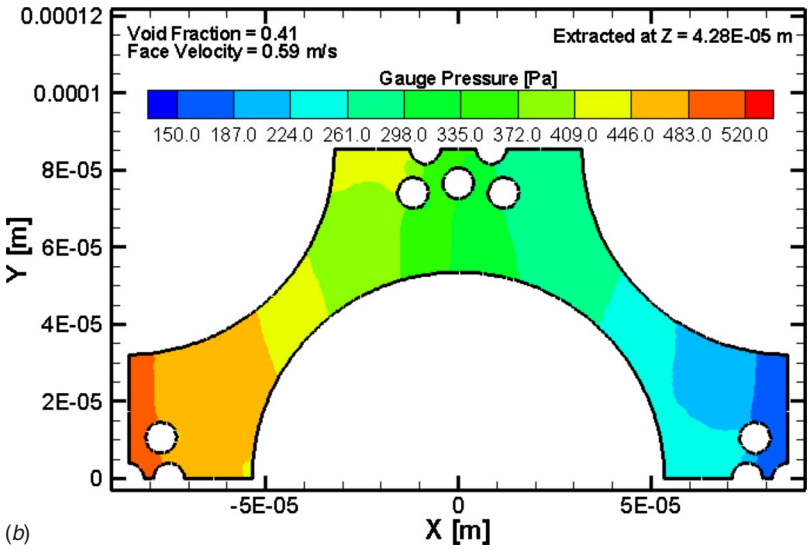

(*b*)

Fig. 9 (*a*) Velocity magnitude contours; (*b*) pressure contours $Z=4.28\times10^{-5}$ m; $\varepsilon=0.41$; $V_0=0.59$ m/s

$$\left(\frac{\Delta P}{L}\right)_{\text{viscous}} = 72\frac{\tau^2}{\cos^2(\theta)}\frac{\mu V_0}{\varepsilon^3}(1-\varepsilon)^2 \times\left[\left(\sum_{i=1}^{n'}\frac{x_i}{\phi_i D_i}\right)^2 + x_{\text{FD}}\sum_{i=1}^{n'}\frac{x_i}{(\phi_i D_i)^2}\right] \quad (18)$$

The flow angle (θ) is calibrated from the experimental data for the pressure drop and is found to be 20 deg [21]. Since this same experimental data set is used in the present study, the PMP results show are theory-based correlations of the data and not true predictions.

Results and Discussion

A number of 3D CFD simulations are conducted by varying the face velocities ranging from 0.04 m/s to 1.29 m/s for two void fractions ($\varepsilon=0.41$ and 0.47) to demonstrate the effects of these parameters on the pressure drop. In this study, Reynolds number ranges between 0.3 and 10, which is calculated based on the diameter of the particle (137×10^{-6} m). The effect of the slip boundary condition is also examined in this study. The pressure drops obtained from the simulations are compared to the empirical correlations (Eqs. (14) and (18)) and to the experimental data obtained from Ref. [21]. The error in the pressure drop predictions using the empirical correlations and the CFD simulations relative to the experimental data is calculated and is also discussed.

Effect of Slip Boundary Condition. The Knudsen number for this microfibrous material is calculated based on the diameter of the fibers from

$$\text{Kn} = \frac{\lambda}{L} = \frac{M}{\sqrt{2}\pi d^2 \rho N_{\text{AV}} L} \quad (19)$$

The calculated Knudsen number is approximately equal to 0.0113. The Knudsen numbers in the range of $0.01<\text{Kn}<0.1$ are considered to be in the slip flow regime; thus the first-order Maxwell velocity-slip boundary formulation (Eq. (5)) is used to incorporate high Knudsen number effects.

The effect of the slip boundary condition is analyzed for both void fractions by varying the face velocity. The pressure gradients decreased by 2.6% for both the void fractions (0.41 and 0.47) when the Maxwell velocity-slip boundary condition is used. Although these effects are small, they are included in the remainder

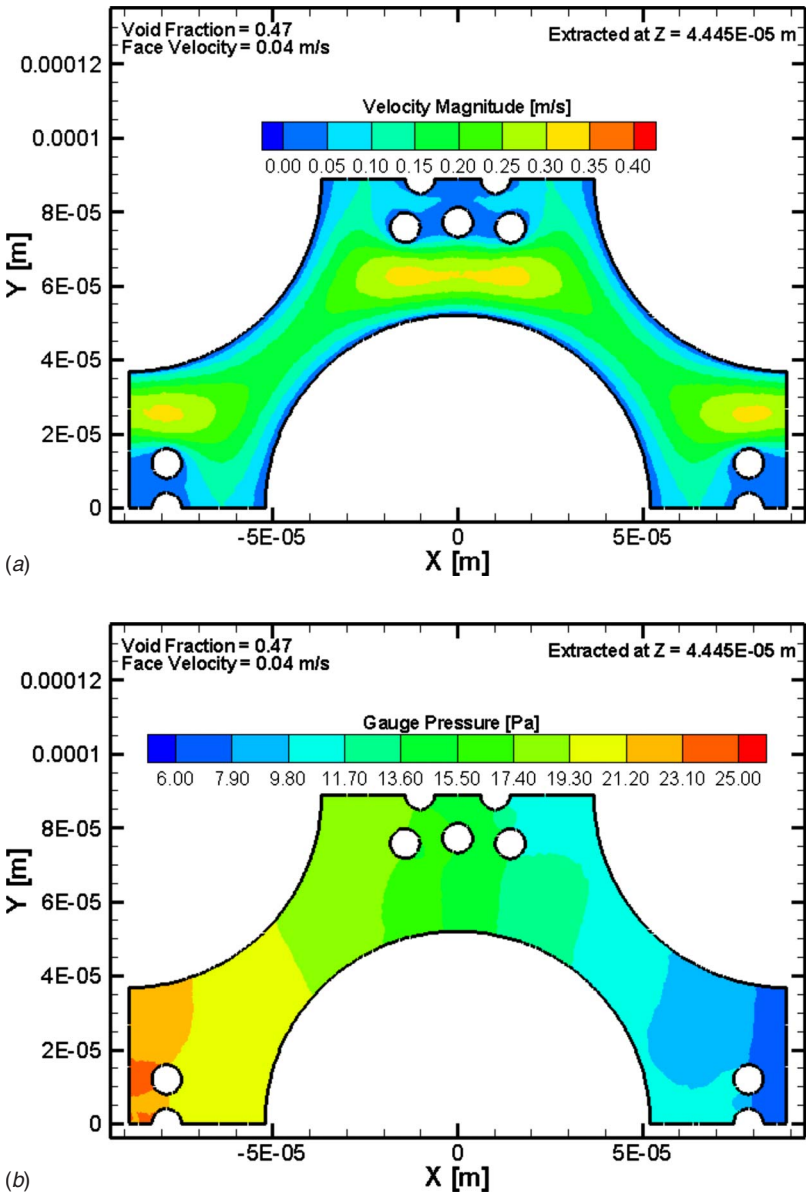

Fig. 10 (*a*) **Velocity magnitude contours;** (*b*) **pressure contours** $Z=4.445\times10^{-5}$ **m;** $\varepsilon=0.47$**;** $V_0=0.04$ **m/s**

of the CFD simulations. It should be noted that if the fiber diameters are decreased, the wall slip effect will become more pronounced.

CFD Simulations: Flow Analysis. CFD simulations are performed using the generated flow-field meshes in order to predict the pressure drop and analyze the details of the flow in microfibrous materials. A plane is extracted at the center of the domain (i.e., $Z=2.48\times10^{-5}$ m) for the case with a void fraction of 0.41. The velocity magnitude and pressure contours are shown in Figs. 8 and 9 for air flowing at face velocities of 0.04 m/s (lowest velocity case) and 0.59 m/s (highest velocity case), respectively. A plane is also extracted at the center of the domain (i.e., $Z=2.445\times10^{-5}$ m) for the case with a void fraction of 0.47, and the velocity magnitude and pressure contours are shown in Figs. 10 and 11 for air flowing at face velocities of 0.04 m/s (lowest velocity case) and 1.29 m/s (highest velocity case), respectively. Figures 8(*a*), 9(*a*), 10(*a*), and 11(*a*) show that the flow speeds up between the fibers and the particles for both void fractions. In addition, the flow slows down between the fibers due to the geometric approximations, which force the fibers closer to each other than seen in the actual microfibrous materials. The ratio of the peak velocity to the face velocity is approximately 9 for the void fraction of 0.41 and 7 for the void fraction of 0.47. The flow is symmetric across $X=0$ for both void fractions at low face velocity, and the flow deviates from symmetric behavior at high face velocity. Figures 8(*b*), 9(*b*), 10(*b*), and 11(*b*) show a gradual decrease in pressure across the length of the domain. The pressure drop across the length of the domain is small at low face velocity and is large at high face velocity for both the void fractions. A similar analysis was performed with the planes extracted at constant Y locations (not shown here) and similar behavior was observed.

Comparison of Pressure Drop With Experiments. CFD predictions for the pressure drop per unit length of the bed for air flowing through microfibrous materials are compared to the pressure drops from empirical correlations and those measured in the experiments [21] for both the void fractions and at various face velocities. Some approximations are made while predicting the

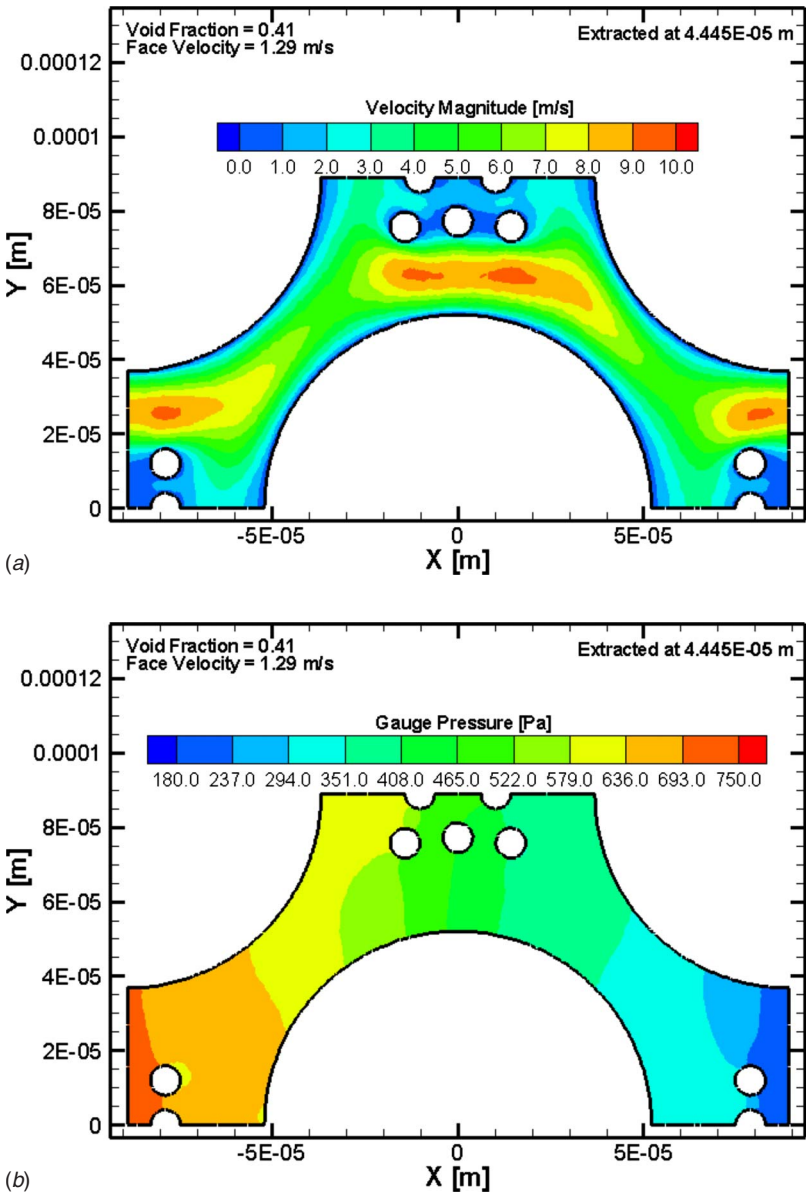

Fig. 11 (*a*) **Velocity magnitude contours;** (*b*) **pressure contours** $Z=4.445\times10^{-5}$ **m;** $\varepsilon=0.47$**;** $V_0=1.29$ **m/s**

pressure drop using these empirical correlations. As discussed in earlier sections, Ergun's equation is valid for the materials with one type of particle only. In order to use Ergun's equation to predict the pressure drop in a microfibrous material, an equivalent diameter is calculated using Eq. (15) with the shape factors of 1.5, 0.72, and 1.5 for Ni, ACP, and PC, respectively [21]. The shape factors used in Ergun's equation to determine the equivalent diameter are also used in the PMP equation. A flow angle of $\theta=20$ deg, obtained by calibrating with the experimental data, is used for the PMP equation. The tortuosity (τ) is estimated using

$$\tau = 1 + \frac{1}{2}(1-\varepsilon) \tag{20}$$

which is obtained by considering a cubic unit cell with one spherical particle [21].

The pressure drop found from the CFD simulations, the PMP equation, and Ergun's equation is plotted against the face velocity on a log-log plot for both void fractions along with the experimentally measured pressure drop and is shown in Fig. 12. As discussed above, a shape factor of 0.72 is used for ACP while determining the pressure drop using the PMP and Ergun's equation, whereas in the CFD simulations, smooth spheres (i.e., a shape factor of 1) are used. Figure 12 shows good agreement between CFD simulations and empirical correlation in predicting the pressure drop for both the void fractions. The pressure drop obtained from the CFD simulations underpredicted by 15–20% and 8–15% from PMP and Ergun's equations, respectively, for high void fraction ($\varepsilon=0.47$) and overpredicted by 8–10% and 10–12% from PMP and Ergun's equations, respectively, for low void ($\varepsilon=0.41$). The empirical correlations are essentially theory-based correlations since there are adjustable parameters (shape factor ϕ and flow angle θ), which were chosen to obtain agreement with this experimental data set. Figure 12 also shows that the CFD predictions of pressure drop are in reasonably good agreement with the experimental measurements. For a void fraction of 0.41, CFD simulations underpredicted the pressures drop at all face velocities compared to the experimental measurements, whereas for a void fraction of 0.47, the CFD simulations overpredicted the pressure drop at all face velocities compared to the experimental measurements.

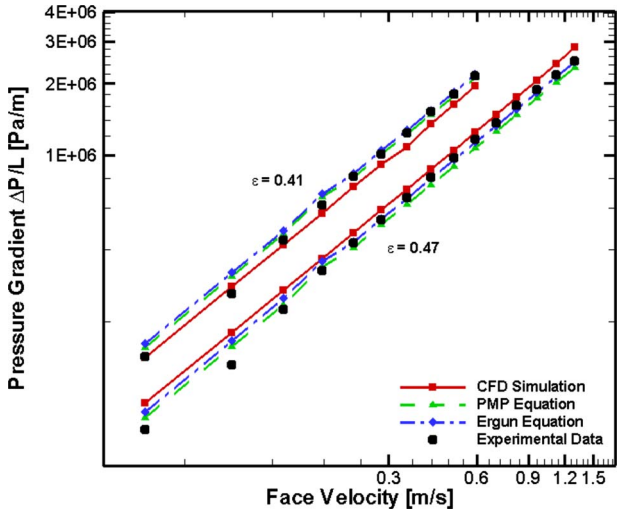

Fig. 12 Comparison of the pressure drop from CFD simulations and empirical correlations with experimental data from Ref. [21]

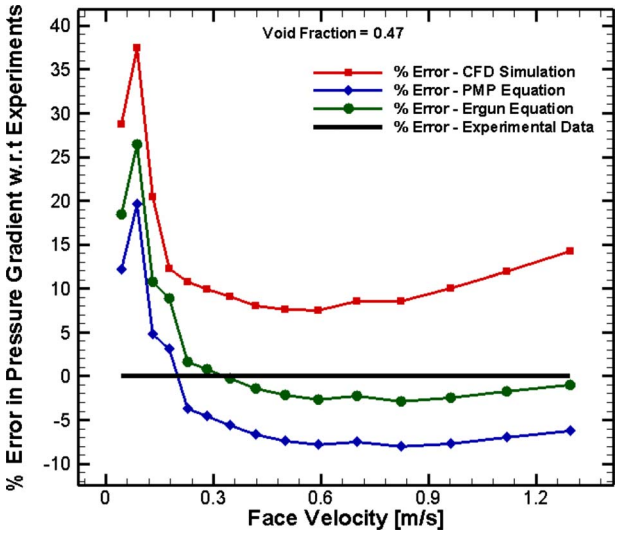

Fig. 14 Error in predicting pressure drop with respect to experiments [21]; void fraction=0.47

Error in Predicting the Pressure Drop. The error in predicting the pressure drop for the CFD simulations and the empirical correlations relative to experimental measurements is calculated as

$$\text{Error in } \frac{\Delta P}{L} = \frac{\left(\frac{\Delta P}{L}\right)_{\text{CFD/empirical}} - \left(\frac{\Delta P}{L}\right)_{\text{expt}}}{\left(\frac{\Delta P}{L}\right)_{\text{expt}}} \times 100\% \quad (21)$$

Calculated errors in pressure drop predictions using CFD and the empirical correlations are plotted against the face velocity for both the void fractions (0.41 and 0.47) and are shown in Figs. 13 and 14, respectively. The PMP equation overpredicted the pressure drop relative to the experimental measurements at low face velocities and underpredicted the pressure drop at high face velocities for both the void fractions. For low void fraction, Ergun's equation overpredicted the pressure drop relative to the experimental measurements, whereas for high void fraction, Ergun's equation overpredicted the pressure drop relative to the experimental measurements at low face velocities and underpredicted the pressure drop at high face velocities for both the void fractions. The pressure drop determined using the empirical correlations deviated by 2–15% for the void fraction of 0.41 and by 2–20% for the void fraction of 0.47 relative to the experimental measurements. For a void fraction of 0.41, CFD simulations are within 10% of the experimental measurements, whereas for a void fraction of 0.47, CFD simulations are within 10–30% of the experimental measurements. The different trends with different porosities may be related to experimental bias errors, which may show up at different void fractions (possibly due to the clamping or squeezing of the porous material at high void fractions). The deviation of pressure drop obtained using the CFD simulations and empirical correlations relative to experiments have the same trend for both the void fractions as shown in Figs. 13 and 14. There are consistent trends between the different models, and there are consistent trends relative to data at low velocity. This consistent trend suggests that either there are physical mechanisms missing from both the simulations and the theory-based correlations or that there are experimental bias errors which correlate with face velocity.

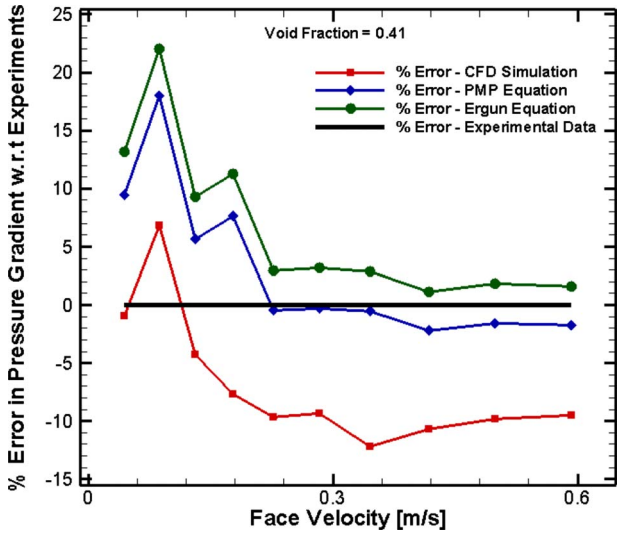

Fig. 13 Error in predicting pressure drop with respect to experiments [21]; void fraction=0.41

Conclusions

Simulations were performed for the flow through microfibrous materials using the FLUENT CFD code. These simulations can provide insight into the detailed fluid mechanics as well as the global properties of microfibrous flows. Knudsen number effects were taken into account by employing the first-order Maxwell velocity-slip boundary condition. The numerical accuracy of the simulations was also demonstrated in this study. The estimated numerical errors in the pressure drop predictions from CFD were 1% for the void fraction of 0.41 and 0.7% for the void fraction of 0.47. The pressure drop obtained from the CFD simulations was compared with theory-based correlations and available experimental data [21]. The CFD predictions for the pressure drop were lower than results from the empirical correlations and experimental measurements by 8–20% and 10–30%, respectively, at high void fraction (ε=0.47). The CFD predictions for the pressure drop were higher than results from the empirical correlations and experimental measurements by 8–12% and 1–12%, respectively, at low void fraction (ε=0.41). Given the significant approximations made in the geometric modeling of this microfibrous material for the CFD simulations, agreement with pressure drop data within 30% is fairly good, especially since no uncertainty estimates are available

for the experimental data. The trend of the modeling error in for the pressure drop relative to experimental data was the same for the CFD simulations and the empirical correlations for both void fractions. The likely source of this consistent error trend is a bias error in the experimental data, which correlates with the face velocity. The CFD results are truly predictive as there are no adjustable parameters (like in empirical correlations). Because of geometric approximations, the CFD model is not perfect but can be extended to new microfibrous materials.

Acknowledgment

Financial support from the U.S. Army SMDC (SMDC-DASG60-00-C0070) and also the U.S. Army TARDEC (TARDEC-W56HZV-05-C-0686) is gratefully acknowledged. The authors also would like to thank R. Kalluri and H. Yang for their suggestions while preparing this article.

References

[1] Novochinskii, I. I., Song, C., Ma, X., Liu, X., Shore, L., Lampert, J., Farrauto, R. J., 2004, "Low Temperature H2S Removal From Steam-Containing Gas Mixtures With ZnO for Fuel Cell Application. 1. ZnO Particles and Extrudates," Energy Fuels, **18**, pp. 576–583.

[2] Song, C. S., and Ma, X. L., 2004, "Ultra-deep Desulfurization of Liquid Hydrocarbon Fuels: Chemistry and Process," International Journal of Green Energy, **1**(2), pp. 167–191.

[3] Cahela, D. R., Chang, B. K., Karanjikar, M., Luna, E. A., and Tatarchuk, B. J., 2004, "Microfibrous and Micro-Structured Adsorbents and Catalysts Media: Enhancement in Effectiveness Caused by Static Mixing," *AIChE Annual Meeting Conference Proceedings*, Austin, TX.

[4] Lu, Y., Sathitsuksanoh, N., Yang, H. Y., Chang, B. K., Queen, A. P., and Tatarchuk, B. J., 2005, "Microfibrous Entrapped ZnO-Supported Srbent or High Contacting Efficiency H2S Removal From Reformate Streams in PEMFC Applications," *Microreactor Technology and Process Intensification* (ACS Symposium Series), Y. Wang and J. D. Holladay, eds., American Chemical Society, Washington DC, Vol. 914, pp. 406–422.

[5] Chang, B. K., Lu, Y., and Tatarchuk, B. J., 2006, "Microfibrous Entrapment of Small Catalyst or Sorbent Particulates for High Contacting Efficiency Removal of Trace Contaminants Including CO and H2S From Practical Reformates for PEM H2-O2 Fuel Cells," Chem. Eng. J., **115**, pp. 195–202.

[6] Lu, Y., and Tatarchuk, B. J., 2003, "Microfibrous Entrapped Supported-Zno Sorbents With High Contacting Efficiency for Trace H2S Removal in PEMFV Applications," *Abstracts of Papers, 226th ACS National Meeting*, New York, Sept. 7–11.

[7] Karniadakis, G., Beskok, A., and Aluru, N., 2005, *Microflows and Nanoflows: Fundamentals and Simulation* 2nd ed., Springer-Verlag, New York, Chaps. 1–4.

[8] Barber, R. W., Emerson, D. R., Gu, X. J., and Zhang, Y., 2006, "Rarefied Gas Dynamics in Micro-Devices," URL: http://www.cse.clrc.ac.uk/ceg/c4m/rgd.shtml.

[9] Panton, R. L., 1996, *Incompressible Flow*, 2nd ed., Wiley, New York, pp. 359–401.

[10] Versteeg, H. K., and Malalasekera, W., 1996, *An Introduction to Computational Fluid Dynamics*, Addison-Wesley, Reading, MA.

[11] Reddy, J. N., and Gartling, D. K., 1994, *The Finite Element Method in Heat Transfer and Fluid Dynamics*, CRC, Boca Raton, FL.

[12] Karniadakis, G. E., and Sherwin, S. J., 1999, *Spectral/HP Element Methods for CFD*, Oxford University Press, New York.

[13] Beskok, A., 1996, "Simulations and Models for Gas Flows in Microgeometries," Ph.D. thesis, Princeton University.

[14] Beskok, A., and Karniadakis, G. E., 1999, "A Model for Flows in Channels, Pipes, and Ducts at Micro and Nano Scales," Microscale Thermophys. Eng., **3**, pp. 43–77.

[15] Hennighausen, K., 2001, "Fluid Mechanics of Microscale Flight," Ph.D. thesis, University of Minnesota.

[16] Tang, G. H., Tao, W. Q., and He, L. Y., 2005, "Gas Slippage Effect on Microscale Porous Flow using the Lattice Boltzmann Method," Phys. Rev. E, **72**(5), 056301.

[17] Papathanasiou, T. D., Markicevic, B., and Dendy, E. D., 1990, "A Computational Evaluation of the Ergun and Forchheimer Equations for Fibrous Porous Media," Phys. Fluids, **13**(10), pp. 2795–2805.

[18] Andrade, J. S., Costa, U. M. S., Almeida, M. P., Makse, H. A., and Stanley, H. E., 1999, "Inertial Effect on Fluid Flow Through Disordered Porous Media," Phys. Rev. Lett., **82**(26), pp. 5249–5252.

[19] Hicks, R. E., 1970, "Pressure Drop in Packed Beds of Spheres," Ind. Eng. Chem. Fundam., **9**(3), pp. 500–502.

[20] Harris, D. K., Cahela, D. C., and Tatarchuk, B. J., 2001 "Wet Lay-up and Sintering of Metal—Containing Microfibrous Composites for Chemical Processing Opportunities," Composites, Part A, **32**, pp. 1117–1126.

[21] Cahela, D. R., Tatarchuk, B. J., 2001, "Permeability of Sintered Microfibrous Composites for Heterogeneous Catalysis and Other Chemical Processing Opportunities," Catal. Today, **69**, pp. 33—39.

[22] 2005, FLUENT 6.2 User's Guide, Vols. 1–3.

[23] McNenly, M. J., Gallis, M. A., and Boyd, I. D., 2003, "Slip Model Performance for Micro-scale Gas Flows," *36th AIAA Thermophysics Conference*, Paper No. AIAA-2003–4050.

[24] Anderson, J. D., Jr., 1995, *Computational Fluid Dynamics: The Basics with Applications*, McGraw-Hill, New York, pp. 253–264.

[25] Roy, C. J., 2005, "Review of Code and Solution Verification Procedures for Computational Simulation," J. Comput. Phys., **205**(1), pp. 131–156.

[26] Roache, P. J., 1998, *Fundamentals of Computational Fluid Dynamics*, Hermosa, NM, pp. 487–500.

[27] Ergun, S., 1952, "Fluid Flow Through Packed Columns," Chem. Eng. Prog., **48**(2), pp. 89–94.

[28] Middleman, S., 1998, *An Introduction to Fluid Dynamics: Principles of Analysis and Design*. 2nd ed., Wiley, New York, pp. 411–421.

Evert-Jan Foeth
e-mail: e.j.foeth@marin.nl

Tom van Terwisga

Technical University of Delft,
Mechanical, Maritime and Materials
Engineering Laboratory of Ship Hydrodynamics,
Mekelweg 2,
2628CD Delft,
The Netherlands

Cas van Doorne
Shell Research and Technology
Centre Amsterdam,
Postbus 38000,
1030 BN Amsterdam,
The Netherlands

On the Collapse Structure of an Attached Cavity on a Three-Dimensional Hydrofoil

A three-dimensional twisted hydrofoil with an attached cavitaty closely related to propellers was observed with a high-speed camera at the University of Delft Cavitation Tunnel. Reentrant flow coming from the sides of the cavity aimed at the center plane—termed side-entrant flow—collided in the closure region of the cavity, pinching off a part of the sheet resulting in a periodic shedding. The collapse of the remainder of the sheet appears to be a mixing layer at the location of the colliding reentrant flows. Collision of side-entrant jets in the closure region of a cavity is identified as a second shedding mechanism, in addition to reentrant flow impinging the sheet interface at the leading edge.
[DOI: 10.1115/1.2928345]

1 Introduction

Fully developed sheet cavitation on ship propellers is a major cause of noise, vibration, and erosion. Although the final evaluation of a propeller design is based on model experiments, calculations of cavitation are becoming increasingly more important. Potential flow solvers are now the industry standards (e.g., Young and Kinnas [1]), but in the past decades, an increase in both Euler (e.g., Choi and Kinnas [2], and Schnerr et al. [3]) and Reynolds-averaged Navier-Stokes (RANS) (e.g., Kunz et al. [4]) codes is observed. However, up until now, these simulations are not able to capture the pressures radiated by cavitation or to predict erosion location and severity on propellers (ITTC [5]). To improve the description of the cavity behavior and especially the unsteady shedding in the form of cloud cavitation and in support of the rapidly expanding field of numerical simulation, this experimental research was started with a threefold goal: First, analyze the physical mechanisms of the instability of the cavity; second, build a data set of simple cavitating flows to be used as benchmark material for computational fluid dynamics validation; and third, extend the insights gained to guidelines for propeller design. Here, we focus on the description of the flow field around an attached cavity and its shedding mechanism.

Cavitation has been extensively tested in the past on two-dimensional hydrofoils (i.e., Franc and Michel [6]). However, cavitation on ship propellers is distinctly three dimensional due to the propeller's three-dimensional geometry, the radially increasing velocity and change in blade loading, and a periodic change of inflow conditions due to the wake behind a ship's hull. As studying cavitation on a rotating object is inherently more difficult, three-dimensional hydrofoils were designed with a spanwise variation in loading, resulting in a cavitation topology closely related to propellers. This allows for observations of the influence of controlled three-dimensional effects of the attached cavity. For this study, a span-symmetric three-dimensional hydrofoil is chosen, creating an isolated sheet cavity around the plane of symmetry. The hydrofoil is lightly loaded at the tunnel walls to avoid any interaction of the cavity with the tunnel boundary layer.

Crimi [7] studied the effect of sweep (skew) and concluded that the inception velocity increased with an increase in the skew angle. Hart et al. [8] investigated an oscillating three-dimensional finite-span hydrofoil and concluded that the cavity collapse was most violent when the oscillating frequency coincided with the natural shedding frequency of the cavity. de Lange and de Bruin [9] concluded that the reentrant of the two-dimensional hydrofoil was directed upstream, but in the three-dimensional case, the reentrant jet component normal to the closure line was reflected inward. As the pressure gradient is perpendicular to the closure line, the flow is deflected perpendicularly to the cavity closure line. Laberteaux and Ceccio [10] studied a series of swept wedges. The cavity plan form was significantly changed and the reentrant jet was directed into the cavity, allowing for a steady sheet that only shed cloud cavitation at the far downstream edge. Dang and Kuiper [11] numerically studied the reentrant jet on a hydrofoil with a spanwise varying angle of attack and found the reentrant jet direction to be strongly influenced by the cavity topology. The change in cavity shape was determined by loading and not by the sweep angle.

In this paper, high-speed recordings are presented with our interpretation for the shedding behavior for two distinct cases, a cavity of roughly half the chord length and a supercavity. The shedding mechanism for both cases differed from two-dimensional shedding—where the reentrant jet reaches the leading edge—but was governed by the three-dimensional topology of both hydrofoil and the attached cavity. A brief description of the setup of the experiment is given in Sec. 2. The observations are described and interpreted in Sec. 3 and conclusions are in Sec. 4.

2 Setup

The experiments were performed in the University of Delft Cavitation Tunnel (see Figs. 1 and 2), with an effective measuring channel of 0.60 m in length with a 0.3×0.3 m^2 cross section with optical access from all sides; velocities up to 10 m/s can be attained and the local pressure can be reduced to 5000 Pa. The nondimensional cavitation number is defined as

$$\sigma = \frac{p_0 - p_V}{\frac{1}{2}\rho V_0^2} \tag{1}$$

or the ratio of the pressure head to the vaporization pressure (p_V) and the dynamic pressure located at the test section entrance.

The test object is a three-dimensional hydrofoil, previously used by Dang [12], with a chord length of $C=150$ mm, a span of $S=300$ mm (spanning the entire test section), and a spanwise varying angle of attack (Fig. 3). This geometric angle of attack

Contributed by the Fluids Engineering Division of ASME for publication in the JOURNAL OF FLUIDS ENGINEERING. Manuscript received May 15, 2007; final manuscript received March 13, 2008; published online June 25, 2008. Assoc. Editor Theodore Heindel.

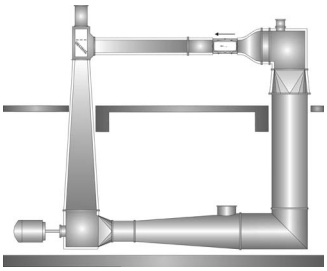

Fig. 1 A sketch of the Delft Cavitation Tunnel consisting of two cylindrical and two square channels

varies as sketched in Fig. 4, rotating the sectional profile (NACA0009) around the midchord position. (See Ref. [13] for specific details.) Calculations by Koop et al. [14] indicate that the change in effective angle of attack is only 2 deg. The hydrofoil was manufactured in both anodized aluminum and perspex. The aluminum hydrofoil was mounted with its suction side downward so that it can be easily filmed from below. The perspex hydrofoil was mounted with the suction side upward and was filmed from the pressure side so that the cavity could be viewed from inside of the cavity.

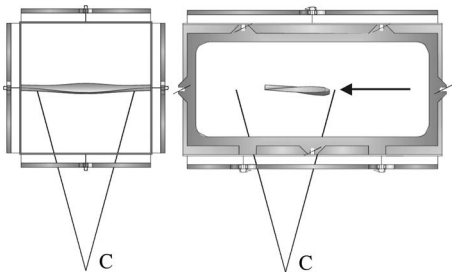

Fig. 2 A close-up of the test section showing the hydrofoil (suction side up, transparent hydrofoil mounted upside down), the camera location, and effective viewing area

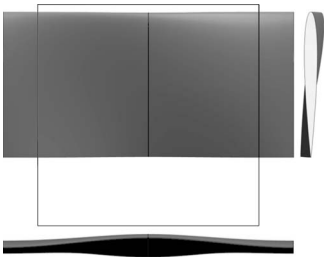

Fig. 3 Top, side, and front views of the hydrofoil. The black outline indicates the viewing area of Figs. 6 and 11.

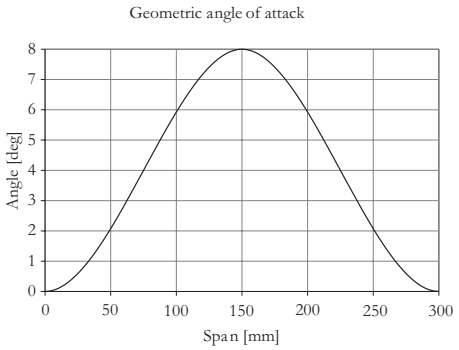

Fig. 4 Distribution of the geometric angle of attack of the hydrofoil. The angle at the sides is taken as the reference angle for the whole geometry.

The boundary layer near the minimum pressure region will remain laminar at low Reynolds numbers and no cavity sheet will appear. When the boundary layer separates and a separation region is formed, a smooth and glassy cavity can appear. With the limited Reynolds numbers typically present at small scales, transition to turbulence does not occur unless the boundary layer is locally disturbed. When it does occur, natural transition to turbulence can temporarily suppress leading edge flow detachment [6]. As a three-dimensional hydrofoil is used at moderate velocities, the sides of the attached cavity can be locally suppressed as the flow remains laminar, so roughness elements of 120 μm were applied at the leading edge (4% chord length) as a turbulence tripping mechanism. The roughness elements can lead to local streaks of cavitation appearing next to the main cavity. At too low speeds, the entire detachment region near the leading edge may resemble an agglomeration of such streaks, which was observed at 5 m/s. The gas content was measured to be less than 0.1%, but the roughness will supply the degassed flow with ample nuclei for sheet cavitation to develop [15]; incipient cavitation on roughness elements is typically observed when σ equals the minimum pressure coefficient [16] and the nuclei content of the flow is no longer critical.

The camera used for the high-speed imaging is a Photron Ultima APX with a 10 bit dynamic range, 1 megapixel resolution at 2 kHz with a maximum acquisition frequency of 120 kHz (0.4% full resolution) with 2.6 Gbyte memory. The lens is a Nikon AF Nikkor 50 mm, used with a f-stop of 2.8. A New Wave Pegasus dual-head, high repetition, diode pumped Nd:YLF laser was used as a stroboscope, with a 180 ns duration with a 10 mJ/pulse power at 1 kHz.

3 Observations

The shedding process of the attached cavity is classified into three regimes. At high cavitation numbers ($\sigma > 1.1$), the attached cavity was short in length and present over a wide part of the leading edge and hence mainly two dimensional. This cavity was shedding vortices intermittently; no large cloudy structures were identified. Such a closure was termed "open" by Laberteaux and Ceccio [10]. At moderate cavitation numbers ($0.65 > \sigma > 1.1$), large structures were shed regularly. This intermediate regime was dominated by the three dimensionality of the cavity. Lowering the pressure further ($\sigma < 0.65$) created an attached cavity reaching a length comparable to the chord length of the hydrofoil. Shedding was then intermittent and irregular. The cavity spanned the entire foil and was once more mainly two dimensional.

Visual analysis of the high-speed video recordings indicated that the Strouhal number

$$\mathrm{St} = \frac{fl}{V} \tag{2}$$

based on cavity shedding frequency f—determined by frame-by-frame analysis of the high-speed video over ten sheddings—and cavity length l was around $\mathrm{St} = 0.185$, when $0.65 < \sigma < 1.1$. Strouhal numbers of $\mathrm{St} = 0.25 - 0.40$—based on the same parameters as above—were reported or specified by Arndt et al. [17] as

$$\mathrm{St} = \frac{1}{4}\sqrt{1+\sigma} \tag{3}$$

from which can be concluded that due to the three-dimensional geometry of the foil, the resulting shedding of the sheet differed significantly from a two-dimensional cavity shedding. In Fig. 5, the Strouhal number is plotted versus the cavitation number σ including the Strouhal number following from Eq. (3). There was no indication that the Strouhal number was dependent on the cavi-

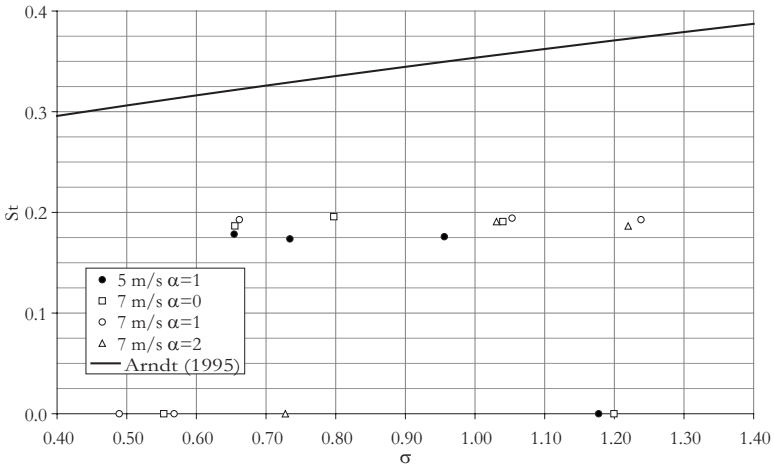

Fig. 5 Strouhal numbers at two different velocities and various angles of attack β based on maximum cavity length with an average of St=0.185, significantly lower than for a two-dimensional foil. Several points at St=0 are visible, indicating either irregular shedding ($\sigma<0.65$) or the absence of large structure shedding resulting in an "open" cavity ($\sigma>1.1$). The continuous line is the relation by Arndt et al. [17] for two-dimensional cavity shedding.

tation number for the angles of attack considered in the present work.

3.1 Case Study at a Low Cavitation Number. Figure 6 presents an example of an intermittently shedding (super) cavity at $\sigma=0.49$, showing the shedding in detail. In Figs. 6.1–6.6, the location of the front of the reentrant jet is given by the arrow at the center. Although difficult to identify on photographs, on the recordings, it is clearly seen to move slowly forward. The breakup of the sheet in Figs. 6.1–6.10 started from the end into distinct vortices, moving upstream. These vortices later collapsed. This upstream movement of the cavity closure was only observed when the cavity length exceeded the chord length of the hydrofoil.

The shed flow structure in Figs. 6.7 and 6.8 consisted of primary spanwise and secondary streamwise vortices, similar to the turbulent shear flow structure observed behind steps and other mixing layers [18]. Figure 7 shows the formation of a spanwise vortex from Figs. 6.5–6.7 (showing intermediate images as well). Such a spanwise vortex system can be a result of a Kelvin–Helmholtz instability with a street of vortices with a positive strength (where the vorticity has the same sign as the hydrofoil's circulation). A close-up of Figs. 6.6–6.9 is given in Fig. 8, including all intermediate images. Bernal and Rosko [19] describe a structure that greatly resembles the presented shedding structure of spanwise and streamwise vortices, describing the structure of a helium-nitrogen mixing layer. The streamwise vortices originated as a single spanwise vortex warped around the primary spanwise vortices. The smaller scale vortices can be seen to be stretched around the periphery of the spanwise structures with an increase in their vaporous cores. Cavitation inception is first observed in these streamwise vortices in shear layers [18], but in the case of a sheet cavity, break-up vapor is trapped in the initial formation.

From Figs. 6.4–6.8 is visible that the front of the mixing moved forward and the breakup was cascading toward the leading edge. The breakup of the sheet started out as concave but the front drew parallel to the span as it progressed upstream. The front of the disturbance accelerated at a constant rate up to the mean stream velocity when reaching the leading edge, as determined from frame-by-frame analysis. The approximated location of the front at the center plane was identified and plotted in Fig. 9.

The reentrant jet momentum depends on the pressure gradient in the closure region [20]. The increase in collapse speed may be explained as follows. At the start of the collapse cycle, the cavity is a well-defined spatial structure with a convex closure. Due to the three-dimensional geometry with a symmetry plane, a stagnation point is present in the closure region only (Fig. 10.1). After the first pinch-off, the closure region of the cavity has changed from a convex into a concave or straight shape and the reattachment region has widened (Fig. 10.2) and widening further with each pinch-off (Fig. 10.3) as the cavity loses its three dimensionality. From observations at higher values of σ—presented below—it is observed that on a three-dimensional cavity, the reentrant jet diverges radially from the closure into the sheet when the cavity is fully grown.

3.2 Case Study at a Higher Cavitation Numbers. In Fig. 11, a full shedding cycle at 5 m/s and $\sigma=0.66$ of a regularly shedding cavity is shown, with the flow from top to bottom. The shedding was repeatable, constant in its shedding frequency, and always followed the same macrostructural collapse.

The shedding cycle of the cavity in Fig. 11 is divided into four phases: destabilization, primary and secondary shedding, followed by growth into its initial condition. There is a short overlap between primary and secondary shedding (and growth). The primary shedding is located at the midplane of the hydrofoil; the secondary shedding is visible at the sides of the region of the primary shedding as two distinct smaller vortices.

Phase 1 11.1–11.4 Initial disturbance
Phase 2 11.5–11.12 Primary shedding (cavity center)
Phase 3 11.9–11.16 Secondary shedding (cavity sides)
Phase 4 11.17–11.20 Growth

3.3 Initial Disturbance. Figures 11.1–11.4 show the convex cavity, here considered fully grown. The lower part of the cavity interface was turbulent, while the cavity at the sides and near the leading edge was glassy and transparent. It is in the closure region where the cavity became turbulent first, not near the leading edge, as is typical of large structure shedding on two-dimensional hydrofoils. The reasons are twofold.

1. The closure region in a two-dimensional flow would normally be followed by a stagnation line (parallel to the leading edge); here, it was a stagnation point at the midplane implying that the local pressure gradient was weakened. As indicated above, the momentum in the reentrant jet depends on the pressure gradient in the closure region, so the three-

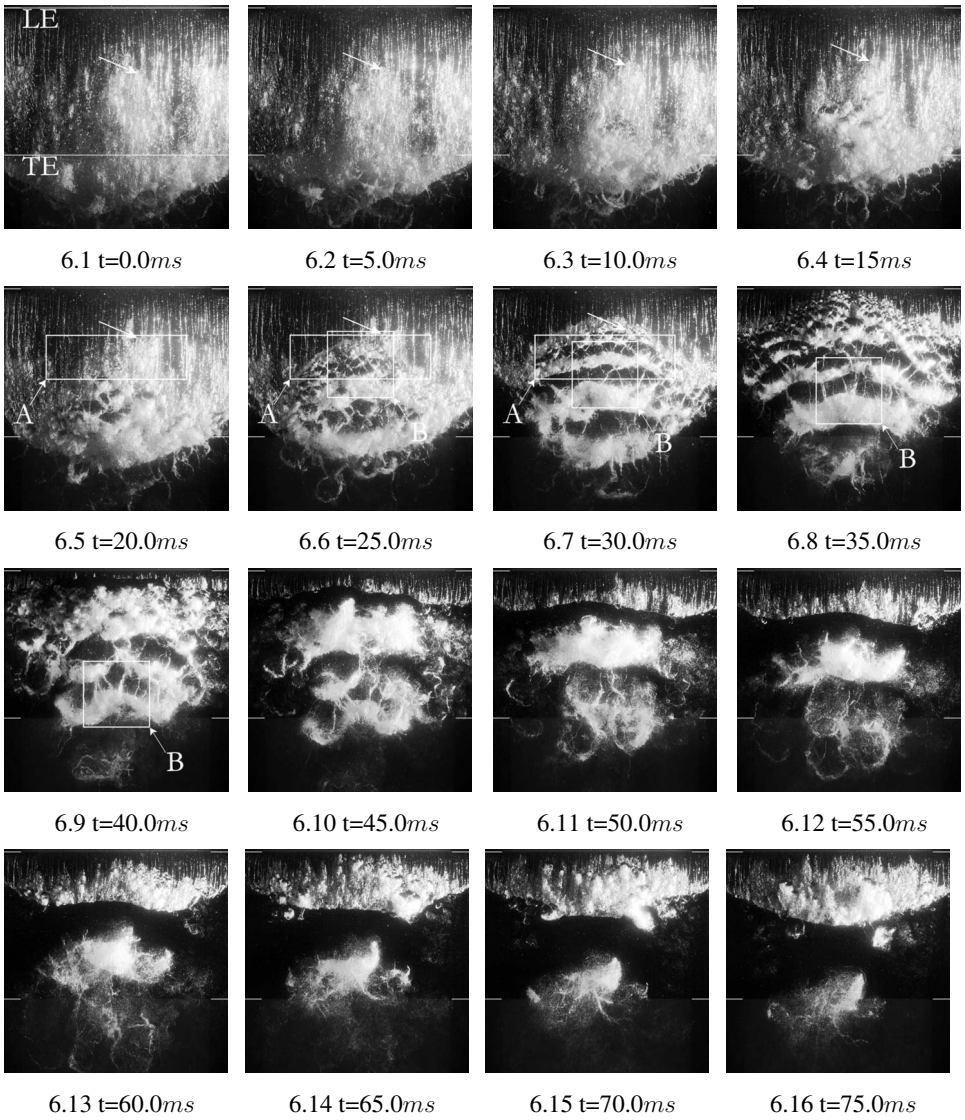

Fig. 6 Visualization at 6.89m/s|±7.70%, α=1, σ=0.49±28.4%, recorded at *f*=2000 Hz but showing every fifth frame. The leading edge (LE) and trailing edge (TE) are indicated in the first image. White outlines indicate Areas A and B enhanced in Figs. 7 and 8, respectively.

dimensional topology of the attached cavity resulted in a reentrant jet diverging radially into the cavity from its closure at the midspan position. Therefore, its forward momentum is diminished as it progressed into the cavity.

2. At the sides of the sheet, the pressure gradient forces the flow over the sheet into the cavity roughly "mirroring" the streamlines at the interface contour, as sketched in Fig. 12. de Lange and de Bruijn concluded that the reentrant jet of the two-dimensional hydrofoil was directly upstream, but in the three-dimensional case, the reentrant jet component normal to the closure line was reflected inward. As the pressure gradient was perpendicular to the closure line, the component tangential to the closure line remains unchanged. At the sides of the cavity, the reentrant flow had a very small spanwise component and was directed downstream. The spanwise component was largest when the cavity closure contour was at about 45 deg with the incoming flow where the velocity component in the downstream direction of the reentrant flow was zero. When the sheet cavity was growing, flow from the sides was not obstructed, nor was it directed at the leading edge.

To distinguish between various directions of the reentrant flow, the term side-entrant jet is introduced. This term refers to that part of the reentrant flow that has a strong spanwise velocity component. The term reentrant jet is reserved for the reentrant flow that has a velocity component that is mainly streamwise. The reentrant flow is thus split up in reentrant and side-entrant jet components, even though at certain points of the flow, both terms may apply. Note that the side-entrant jet component, in contrast to the reentrant jet component, is not necessarily directed upstream. The term side entrant is introduced to emphasize the three-dimensional character of the flow. For the case presented, the side-entrant jets from both sides were flowing into the closure region of the sheet where they collided. Side-entrant jets of the reentrant flow do not reach the leading edge but may form an equally important source for the shedding.

Any fluid ejected upward through the cavity interface created a significant disturbance, isolating a small portion of vapor and creating a bubbly flow consisting of jet-entrained vapor. The velocity of a streamline at the cavity surface is measured at $V_V = V_0\sqrt{1+\sigma}$ [13]. Although the velocity of the reentrant flow is difficult to

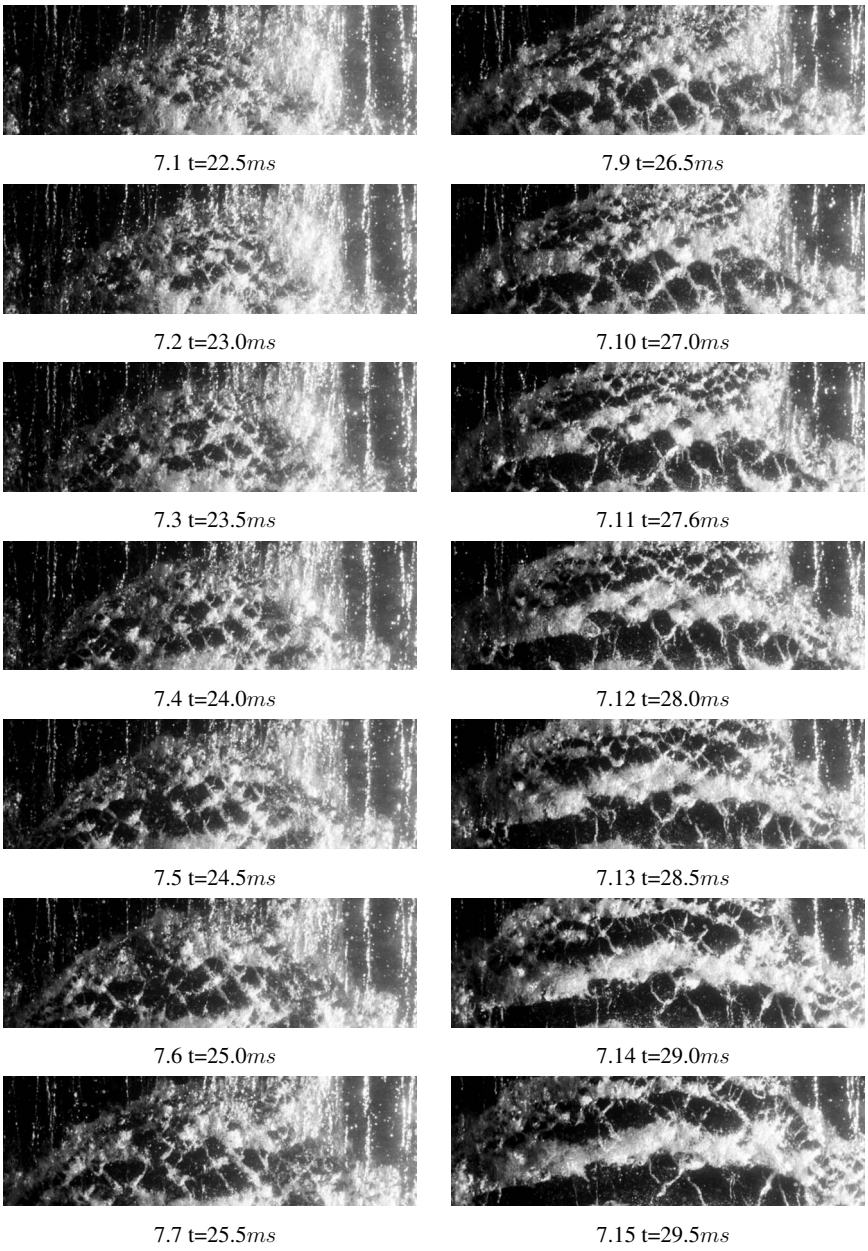

Fig. 7 A close-up of Fig. 6 (marked A) shows the formation of a large spanwise vortex at 2 kHz. As the main sheet collapses, a trail of very small spanwise vortices is created, merging in several distinct larger structures.

measure, the velocity of the jets is unlikely to be an order of magnitude lower. Also, if we assume that during the shedding cycle the two side-entrant jets were converging for about a third of the shedding cycle (15 Hz), the amount of fluid through a square millimeter—taking a homogeneous velocity distribution—at this velocity of 6.4 m/s was about 285 mm^3 per mm^2 cross section of the reentrant flow. At this rate, the cavity closure could be collecting fluid quickly even if the jets were thin.

3.4 Primary Shedding (Cavity Center). The primary shedding originated at the collision region in the center of the sheet, see Figs. 11.5–111.12. However, only a portion was broken off from the main sheet and advected with the flow. Most of the cavity remained attached. This structure could be seen to roll up quickly in Figs. 11.5–11.8 by self-induction into a hairpin vortex. This structure grew significantly in height, on the order of the cavity length. The cavity closure after the cutoff of the hairpin vortex was temporarily turbulent—shedding a large cloudy structure—but reattached smoothly shortly thereafter. In order to visualize the reentrant flow more clearly, a series of additional images of the transparent hydrofoil is presented in Figs. 14 and 15. The cavitation was filmed through the pressure side of the hydrofoil showing the internal structure of the cavity. The radially diverging reentrant flow is clearly visible in Fig. 14 (denoted as A) as waves on the jet surface reflected the laser light.

The reentrant flow directed upstream in a two-dimensional situation would be constrained in its lateral movement. The vapor interface at the leading edge was not visibly disturbed upon contact with this reentrant flow; its apparently low momentum did not lead to immediate shedding. As the side-entrant jets were aimed at the closure, it was here that the fluid first impinged on the interface. Therefore, the main cause for the detachment of the main structure was the side-entrant jet and not the reentrant jet.

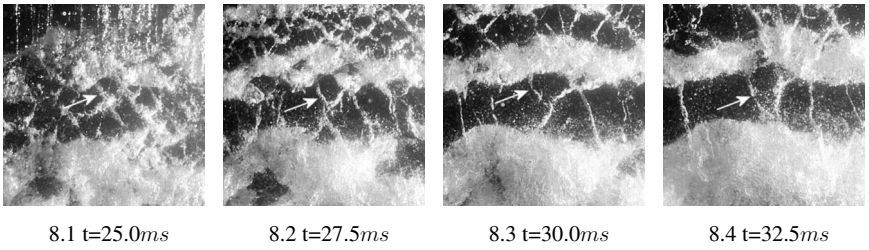

Fig. 8 Close-ups of Figs. 6.6–6.9 (marked B) including intermediate images. The streamwise cavitating vortices that originate perturbations near the primary spanwise vortices are stretched around the primary spanwise vortices.

3.5 Secondary Shedding (Cavity Sides). The remaining topology of the sheet closure line in Figs. 11.5–11.12 was concave. The locally convex regions of the cavity are seen to shed a series of larger vortices, followed by a turbulent flow region. From observation, the secondary shedding greatly resembled the primary shedding. The secondary shedding disappeared when the closure was no longer concave.

The reentrant flow direction in the center was still directed radially outward. The main side-entrant jets and radially diverging reentrant jet were now converging in both downstream lobes of the remaining cavity shape (Figs. 16 and 17). The secondary shedding was caused by the collision of these two flows. Basically, the main shedding as visible in Figs. 11.5–11.12 was repeated at both sides of the center plane, as visible in Figs. 11.9–11.18.

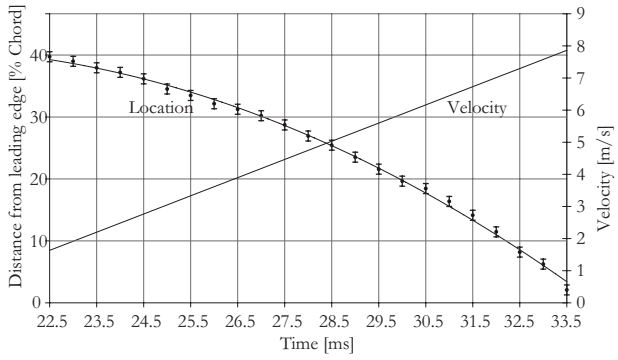

Fig. 9 The location (and its quadratic fit) and velocity of the visible break-up front in the center plane as visible in Figs. 6.5–6.10 determined from frame-by-frame analysis. Error bars indicate a 10 pixel error in the location of the break-up front. The front seems to accelerate at a constant rate.

After the secondary shedding, the remaining cavity had a near-convex shape with two concave regions, denoted H in Fig. 18, corresponding to Fig. 11.18. From these regions, the reentrant flow entered the cavity sideways, similar to the reentrant flow in Fig. 17 after the primary shedding. The reentrant flow from the closure of the cavity at the midplane and from the sides on the cavity—denoted B and C, respectively, in Fig. 18—remained present and collided with the side-entrant jets from H. Figure 15 shows this situation on the transparent hydrofoil. The movement of the front of the side-entrant flow (A) from these regions at Fig. 18-H can be seen, as the reentrant flow forced into the cavity collided with the reentrant flow from the plane of symmetry (B) and a frothy turbulent region was created upon impact at the lower corners. At the outer side, a continuous mixing is observed as the reentrant flow from the main flanks of the cavity (Fig. 18.C) continued to collide with the reentrant flow from (H). No large-scale shedding was observed at this point of the shedding cycle, as with each subsequent shedding, the scale and hence total jet momentum decreased, while the inflow and its momentum from the sides of the cavity remained constant. Without any further major disturbances allowing for a sheet topology change in the closure region, the cavity grew back into its original convex shape and side-entrant jets at the center plane collided once again repeating the process. The cavity did not reach a constant length.

3.6 Cavity Closure. The shedding of the sheet cavity of the three dimensionality is similar to a two-dimensional shedding, having its origin a disturbance of its interface, except that the disturbance occurs at the aft part of the sheet. The fluid impinging on the interface isolates a region of vapor, as sketched in Fig. 19. If the interface is considered a streamline with a tangent velocity $V_V = V_0\sqrt{1+\sigma}$, it is immediately apparent from contour integral of

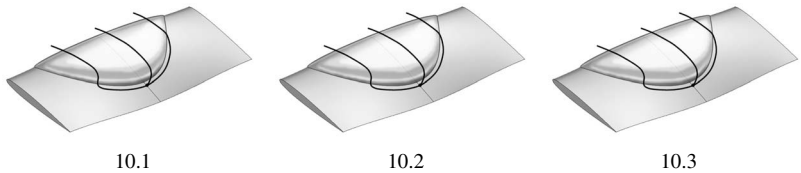

Fig. 10 Flow lines converge at the center plane with reattachment and reentrant flow emanating from this center plane point (as later observed in Fig. 14 and in sketched Fig. 13). With each pinch-off, the reattachment region widens and the closure of the cavity becomes increasingly more two dimensional.

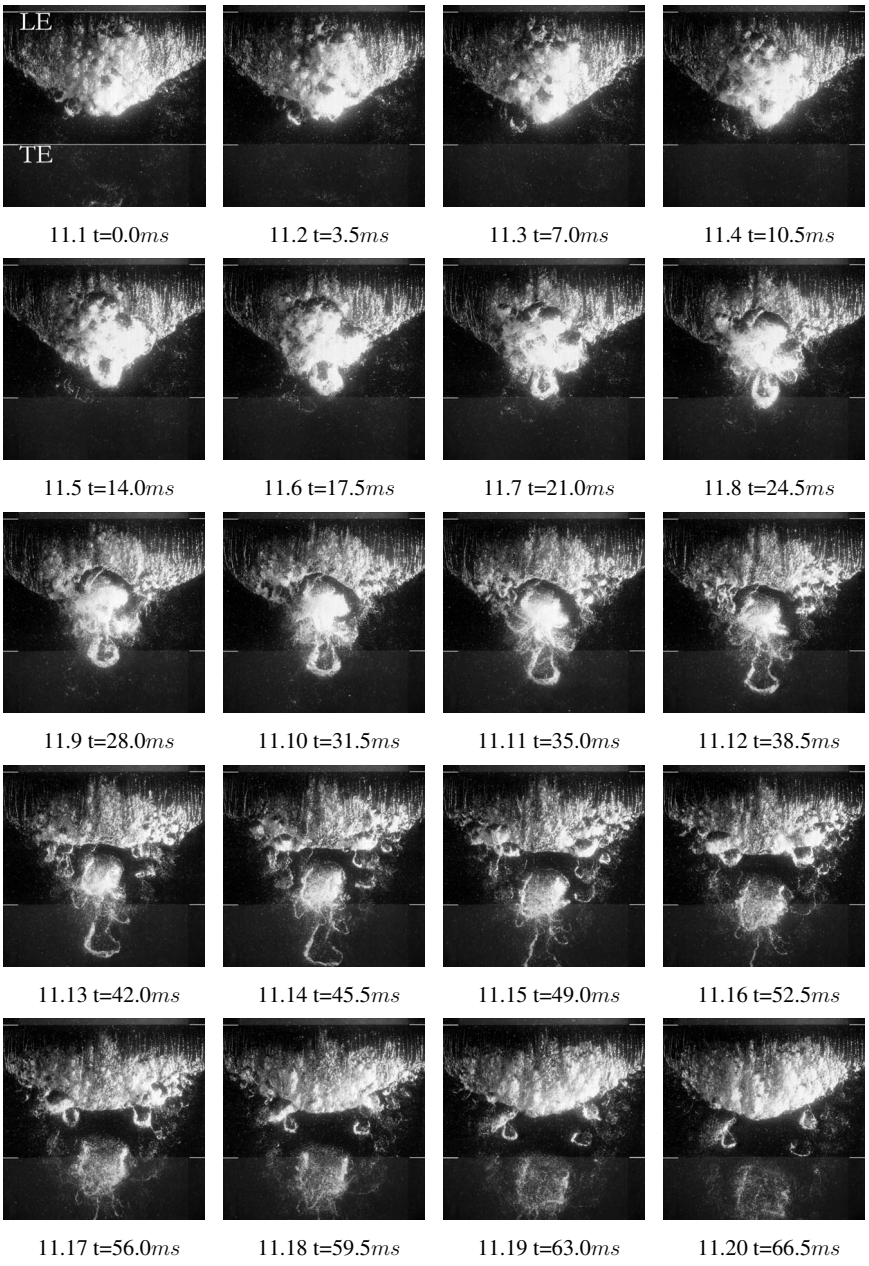

Fig. 11 Visualization at 4.96 m/s±6.4%, α=1 deg, σ=0.66±7.94%, recorded at 2 kHz but showing every seventh frame. Flow from top to bottom.

that velocity over the boundary of S that circulation is detached and adverted with the flow. The impingement and detachment of this vapor structure are inertial in nature. The mixing layer with its region of high shear and strong vortices visibly generates vorticity.

4 Conclusions

From the experiment, investigations with the three-dimensional cavities follow that reentrant flow from the sides dictates the be-

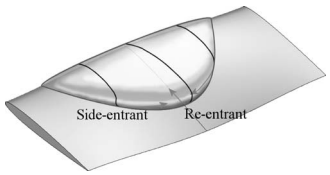

Fig. 12 Streamlines over the cavity interface are directed inward

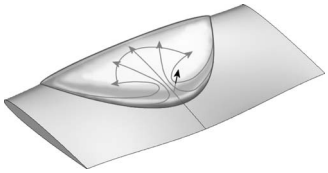

Fig. 13 Observed direction of the reentrant flow focusing causing the primary pinch-off. The reentrant flow is radially diverging into the cavity.

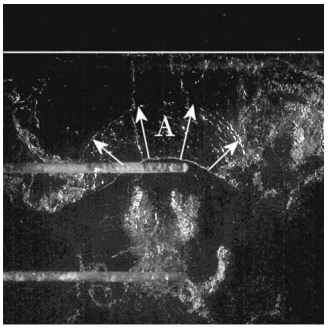

(*a*)

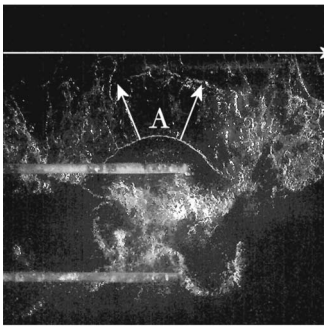

(*b*)

Fig. 14 The reentrant flow was filmed through a transparent hydrofoil, corresponding approximately to Figs. 11.7–11.10. The images show the reentrant jet after cleaning up the pictures (despeckle, color, and histogram enhancement). These figures show the radially diverging reentrant jet (A) emanating from the center of the foil at two different shedding cycles, as sketched in Fig. 17. The two horizontal lines are holes for ink injection (not presented).

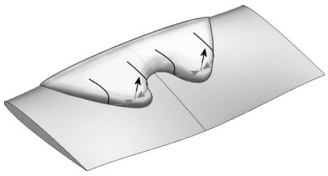

Fig. 16 The streamlines at the side planes in the concave part are partly directed away from the center plane, corresponding to Figs. 11.7 and 11.8

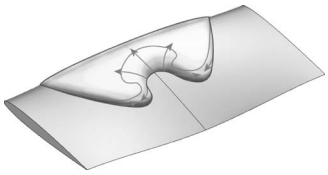

Fig. 17 Estimate of the direction of the reentrant flow in Fig. 16 focusing in the lobes causing a second pinch-off

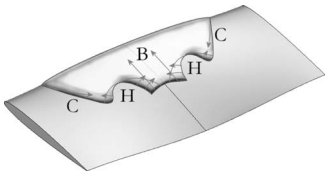

Fig. 18 The streamlines at the side planes in the concave part are partly directed away from the center plane; corresponding to Figs. 11.15–11.17

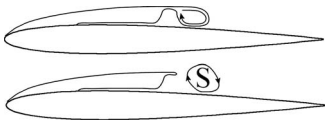

Fig. 19 Side-entrant jets converge in the closure region and cut off the first vortical structure. The remaining cavity closure is now "open."

havior of the shedding cycle. The reentrant flow from the sides depends on the cavity shape. Thus, the cavity topology largely dictates the reentrant flow direction.

The convex cavity planform leads to converging reentrant flow and that flow convergence leads to shedding in the cavity closure region. Reentrant flow was observed to reach the leading edge, which did not result in shedding. The reentrant flow can be moving both upstream and in the spanwise direction. The spanwise component of the reentrant flow is denoted as the side-entrant jet. For any convex cavity shape, the side-entrant components of the reentrant jet converge in the closure region of the sheet, creating a disturbance that causes local breakoff of the aft part of the main sheet structure. This converging of the side-entrant flow is suggested as a second shedding mechanism for attached sheet cavitation, in addition to the well-known mechanisms of the reentrant flow impinging on the cavity interface near or on sheet cavity detachment point. The cause of the shedding is the same: impingement of a high-momentum flow on the surface of the hydrofoil on the cavity interface. The attached cavity on the suction side of a

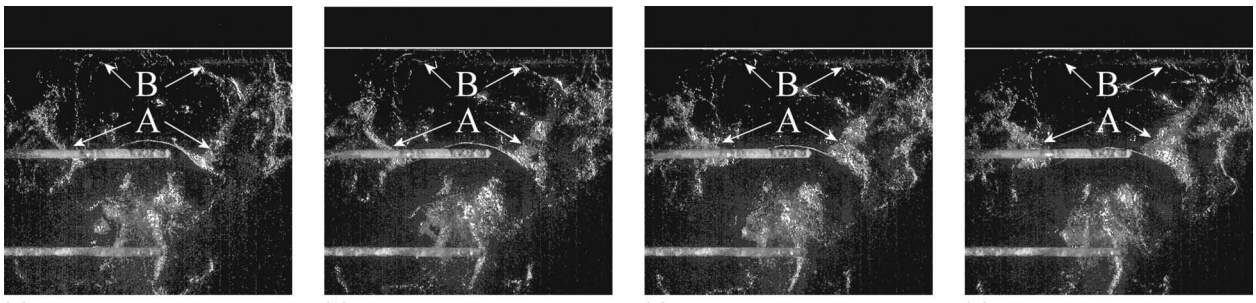

(*a*) (*b*) (*c*) (*d*)

Fig. 15 This series shows the cavity at the end of its secondary shedding corresponding to Figs. 11.15–11.17. The side-entrant jet is seen to develop at both corners of the sheet (A) as visualized in Fig. 18. The reentrant jet is visible near the leading edge (B).

propeller is always three dimensional. The isolated cavity as presented on the current hydrofoil—that is, not connected to the tip of the propeller—is present on some propeller designs and the isolated cavity is shown to be inherently unstable.

With a convex cavity closure line, side-entrant jets converge in the cavity closure region leading to a pinch-off of the aft part of the cavity. The observed (cavitating) vortices in the wake of the remainder of the attached cavity are similar to the spanwise and streamwise vortices in a planar mixing layer. It is concluded that the wake of an attached cavity shedding small-scale vortices is, in fact, a mixing layer with its characteristic wake structure.

The alternating shedding seen on the three-dimensional hydrofoil results in a distinct cycle. However, the two-dimensional or rotational-symmetric hydrofoil lacks the spanwise variation in pressure distribution in the center, resulting in the seemingly random local shedding along its cavity closure. Any disturbance at its closure will redirect the reentrant flow into converging side-entrant flow resulting in local shedding. The two-dimensional cavity has a highly three-dimensional structure, making it more difficult to study, either numerical or experimental, with the reentrant flow constantly changing direction and continuously converging in other locations along the span. The three-dimensional cavity is shown to have a repeatable collapse making it a more proper candidate for numerical validation studies of cloud shedding.

Acknowledgment

This research is funded by the Dutch Technology Foundation STW Project No. TSF.6170 and the Royal Netherlands Navy. See www.stw.nl for more details.

References

[1] Young, Y. L., and Kinnas, S. A., 2001, "A BEM for the Prediction of Unsteady Midchord Face and/or Back Propeller Cavitation," ASME J. Fluids Eng., **123**(2), pp. 311–319.

[2] Choi, J. K., and Kinnas, S. A., 1998, "A 3-D Euler Solver and its Application on the Analysis of Cavitating Propellers," *25th American Towing Tank Conference*.

[3] Schnerr, G. H., Schmidt, S. J., Sezal, I. H., and Thalhamer, M., 2006 "Schock and Wave Dynamics of Compressible Liquid Flows With Special Emphasis on Unsteady Load on Hydrofoils and on Cavitation in Injection Nozzles," *Sixth International Symposium on Cavitation*, Wageningen, The Netherlands.

[4] Kunz, R. F., Boger, D. A., Stinebring, D. R., Chyczewski, T. S., and Gibeling, H. J., 1999, "A Preconditioned Navier-Stokes Method for Two-Phase Flows With Application to Cavitation Prediction," AIAA Paper No. 99-3329.

[5] ITTC, 2002, "Final report and Recommendations to the 23rd ITTC by the Specialist Committee on Cavitation Induced Pressures," *23rd International Towing Tank Conference*, Venice, Italy, Vol. 2, pp. 417–459.

[6] Franc, J. P., and Michel, J. M., 1985, "Attached Cavitation and the Boundary Numerical Treatment," J. Fluid Mech., **154**, pp. 63–60.

[7] Crimi, P., 1970, "Experimental Study of the Effects of Sweep on Hydrofoil Loading and Cavitation," J. Hydronaut., **4**(1), pp. 3–9.

[8] Hart, D. P., Brennen, C. E., and Acosta, W. L., 1990, "Observations of Cavitation on a Three Dimensional Hydrofoil," *25th Cavitation and Multiphase Flow Forum*.

[9] de Lange, D. F. and de Bruin, G. J., 1998, "Sheet Cavitation and Cloud Cavitation, Re-Etrant Jet and Three-Dimensionality," Appl. Sci. Res., **58**, pp. 91–114.

[10] Laberteaux, K. R., and Ceccio, S. L., 2001, "Partial Cavity Flows Part 2. Cavities Forming on Test Objects With Spanwise Variation," J. Fluid Mech., **431**, pp. 43–63.

[11] Dang, J. and Kuiper, G., 1999, "Re-Entrant Jet Modeling of Partial Cavity Flow on Three-Dimensional Hydrofoils," ASME J. Fluids Eng., **121**(4), pp. 781–787.

[12] Dang, J., 2000, "Numerical Simulation of Unsteady Partial Cavity Flows," Ph.D. thesis, Technical University of Delft, The Netherlands.

[13] Foeth, E. J., van Doorne, C. W. H., van Terwisga, T. J. C., and Wienecke, B., 2006, "Time-Resolved PIV and Flow Visualization of 3D Sheet Cavitation," Exp. Fluids, **40**, pp. 503–513.

[14] Koop, A. H., Hoeijmakers, H. W. M., Schnerr, G. H., and Foeth, E. J., 2006, "Design of a Twisted Cavitating Hydrofoil Using a Barotropic Flow Method," *Sixth International Symposium on Cavitation*.

[15] Kuiper, G., 1982, "Some Experiments With Specific Types of Cavitation on Ship Propellers," ASME J. Fluids Eng., **1**, pp. 105–114.

[16] Caron, J. F., Farhat, M., and Avellan, F., 2000, "Physical Investigation of the Cavitation Phenomenon," *Sixth International Symposium on Fluid Control, Measurement and Visualization (Flucome 2000)*, Sherbrooke, Canada.

[17] Arndt, R. E. A., Ellis, C., and Paul, S., 1995, "Preliminary Investigation of the Use of Air Injection to Mitigate Cavitation Erosion," ASME J. Fluids Eng., **117**, pp. 498–592.

[18] O' Hern, T. J., 1990, "An Experimental Investigation of Turbulent Shear Flow Cavitation," J. Fluid Mech., **215**, pp. 365–391.

[19] Bernal, L. P., and Rosko, A., 1986, "Streamwise Vortex Structure in Plane Mixing Layers," J. Fluid Mech., **170**, pp. 449–525.

[20] Le, Q., Franc, J. P., and Michel, J. M., 1993, "Partial Cavities: Global Behavior and Mean Pressure Distribution," ASME J. Fluids Eng., **115**, pp. 243–248.

Cavitation Structures in a Venturi Flow With Various Backward Facing Steps

Hailing An

Michael W. Plesniak

School of Mechanical Engineering,
Purdue University,
West Lafayette, IN 47907-2088

Cavitation inception and development caused by a backward facing step in a Venturi-type test section were studied experimentally for different step heights (0.8–4 mm). High-speed cinematography and particle image velocimetry images were used to demonstrate the cloud shedding process and cavitation development stages. It was found that for small step height (0.8 mm, $h/\delta_0 = 1.7$) cavitation started in the reattachment region in the form of a reentrant jet, and caused cloud shedding in its developed stage. For high step height (4 mm, $h/\delta_0 = 8.5$) cavitation started midway downstream of the shear layer and resembled the spanwise vortices in the separated shear layer. This study contributes experimental results for better understanding of cavitation inception and development in the separated shear layer. [DOI: 10.1115/1.2948370]

1 Introduction

Cavitation and separation are closely related and thus generation of cavitation caused by separated flow is of considerable interest. Arakeri and Ramarajan [1] studied cavitation inception from a backward facing step with step height ranging from 0.2 mm to 2.5 mm behind a hemisphere. They found that when the step size was small (on the order of 0.5 mm), the cavitation bubbles were quite close to the body surface and slightly downstream of the separation point. For larger step heights, cavitation appeared in the free shear layer away from the solid surface. Ramamurthy et al. [2] studied the cavitation effects past backward facing steps with step heights of 6.35 mm and 12.7 mm. They found that cavitation started in the shear layer at about three or four step heights downstream of separation. Their separation bubble length was approximately 6.5 step heights. Cavitation inception location for separated flow behind a backward facing step is different from that for the laminar separation bubble on the hemispherical nose and International Towing Tank Conference (ITTC) standard headform, where inception was found to occur in the reattachment region of the separated free shear layer [3]. Katz [4] studied cavitation inception on four axisymmetric bodies with boundary layers that underwent a laminar separation and subsequent turbulent reattachment. He reported that the inception zone was located within the turbulent shear layer downstream of transition and upstream of the reattachment region of the bodies with large separation regions. The inception region on the body with the smallest separation zone, a hemisphere-cylinder body, was located in the reattachment region, but the cavities were also detached from the surface. The hemisphere-cylinder body results were in accord with the results reported by Arakeri and Acosta [3].

Katz [4] also found that the location and the shape of the cavitation in the shear layer suggested a relation to the mixing-layer eddy structure. Katz and O'Hern [5] reported that, in large-scale shear-layer flows, cavitation inception occurred in longitudinal, secondary, shear-layer eddy structures. As it reaches a more developed state, the cavitation takes the form of spanwise large eddies with the streamwise structures superimposed on. The same phenomena have been observed in other types of free shear layers, but not in every type of separated flow where the dimensions of the separated regions are too small to allow the development of the streamwise vortices. For backward facing step flow, the step height is a key factor determining the thickness of the shear layer and it plays an important role in determining whether the inception structure occurs in streamwise vortices or the spanwise vortices.

On hydrofoils, cavitation can be classified as partial cavitation and supercavitation. Partial cavities are ones that detach from the vicinity of the leading edge of a hydrofoil and close on the wall. Supercavitation refers to long cavities whose length is greater than the chord length of the hydrofoil and, therefore, enclose the fluid bulk [6]. Partial cavitation is more deleterious because cavitation bubbles collapse on the foil and cause damage to its surface. Therefore, it has been subject to more intensive studies.

In general, the development of partial cavitation goes through different phases for separated flow. Due to the complexity of the flow and variation of the phenomena, there are no standard terminologies to define these phases. To facilitate communication, detailed descriptions of the phenomenon are necessary. The following paragraphs describe different types of cavitation observed for a lifting surface, with a focus on cloud cavitation and the reentrant jet instability.

Callenaere et al. [7] observed different regimes of partial cavitation on the backward diverging step. They mapped the regimes as a function of the cavitation number and the height of the step. The central part of this regime map corresponds to the reentrant jet instability and subsequent cloud cavitation, which can be easily identified visually as periodic shedding. At its limits, the shedding loses its regularity as cavitation number further decreases. Callenaere et al. observed an intermittency between coherent bursts of large clouds and a chaotic entrainment of smaller vapor structures. For large step height and for large cavitation numbers, the regime of cloud cavitation is limited by shear cavitation, where vapor does not fill all the space behind the step but is limited to the shear layer. When the step height was small they found that the cloud cavitation domain is limited by a regime in which the cavity length is no longer oscillating, but a reentrant jet still exists. They also observed surge type of cavitation at extremely small cavitation number.

Reentrant jet instability is often attributed to the cavity destabilization and transition to cloud cavitation [8–12]. The principle of the reentrant jet instability has been described by several researchers. Knapp et al. [13] gave a precise description of the flow at the downstream end of a cavity. The decisive role of the reentrant jet in the generation mechanism of cloud cavitation was experimentally proved by Kawanami et al. [10]. They conducted a simple but conclusive experiment in which they placed an obstacle on the

Contributed by the Fluids Engineering Division of ASME for publication in the JOURNAL OF FLUIDS ENGINEERING. Manuscript received September 6, 2007; final manuscript received April 5, 2008; published online June 26, 2008. Review conducted by Joseph Katz.

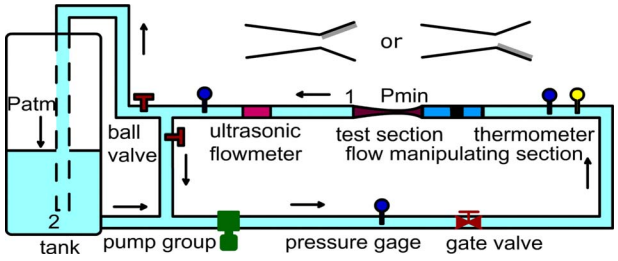

Fig. 1 Schematic of the water loop and the test section

floor in order to stop the progression of the reentrant jet. The addition of such an obstacle holds back the reentrant jet and prevents the generation of a large cloud. Much smaller vapor structures are formed. In addition, the pressure oscillations due to the shedding of the cloud are mostly suppressed. This experiment confirms the essential role of the reentrant jet on the onset of cloud cavitation. "Cloud cavitation" is known to induce high magnitude pressure pulses and to be a destructive form of cavitation [14]. The coherent collapse of the cloud of bubbles can cause more intense noise and more potential for damage than in a similar nonfluctuating flow [15]. The existence of the reentrant jet requires that the cavity must not be too thin, or larger-scale clouds cannot be formed and that the adverse pressure gradient must be large enough at the cavity closure to develop a reentrant jet.

In this paper, cavitation inception and development behind backward facing steps of different heights in a Venturi flow were examined using flow visualization and image processing. Turbulent flow structures indicated by regions of cavitation inception are discussed. This study contributes to understanding the complex phenomenon of cavitation inception and development caused in a separated shear layer downstream of a backward facing step.

2 Experimental Facilities

2.1 Water Loop Facility. A sketch of the water loop used for this study is shown in Fig. 1. A 1.36 m^3 (300 gal) tank which is open to atmosphere was used as the water reservoir. The open water surface in the tank allows the air bubbles to be expelled from the system, and therefore it served to deaerate the pipe flow before any experiments were done. The free surface height of the tank also determines the absolute pressure level in the test section. The water was pumped into the loop by operating one to four centrifugal pumps mounted in parallel. Each of the pumps is rated at a maximum flow rate of 0.0057 m^3/s (90 gal/min). Along the flow path, which was constructed using 10.16 cm (4 in.) and 5.08 cm (2 in.) PVC pipes, various flow measurement instruments were installed such as pressure gages, a thermometer, and an ultrasonic flow meter. Two passages of 5.08 cm (2 in.) diameter transparent PVC pipes were connected to the upstream and downstream of the test section to facilitate visual observations. In each experiment, the flow in the pipe was deaerated until no air bubbles were visible, which indicated that the undissolved air content in the incoming flow was decreased to the minimal level achievable in the current facilities. It was also found that when the flow loop was operated at cavitating conditions no bubbles were observed in the downstream pipe. Therefore, the vapor bubbles were well collapsed or the gas bubbles were redissolved before they exited the test section. Consequently, there was no need for concern about uncollapsed or undissolved bubbles damaging the pumps or contaminating the incoming flow. Absence of bubbles also allowed installing the ultrasonic flow meter downstream of the test section to measure the flow rate.

2.2 Venturi Test Section Design. The test section is a typical Venturi channel made of acrylic sheet to ensure good optical access for flow visualization, particle image velocimetry (PIV) and laser doppler velocimetry (LDV) measurements. The wall surfaces are smooth and the front and back walls are parallel. A rectangular cross section was used to avoid optical distortions. The contraction and expansion profiles are linear with included half angles of 15 deg and 3 deg, respectively. The 3 deg expansion was used for a gradual connection from the Venturi throat to the downstream pipe. The expansion imposes an adverse pressure gradient on the flow. The contraction area ratio is 4:1, leading to a throat thickness of $D_t=12.6$ mm (0.5 in.). Reneau et al. [16] and Carlson et al. [17] were used as guidance for diffuser design. On one of the nonparallel walls, 13 pressure taps of 1.6 mm (0.0625 in.) diameter were installed on the centerline to monitor the mean static pressure distribution along the wall.

A flow conditioning section was mounted upstream of the test section to ensure a uniform incoming flow with low turbulence level. This section is 48.3 cm (19 in.) long with a 5.08 $\times$ 5.08 cm^2 (2×2 $in.^2$) square cross section. The first part of this section is a transition passage from the circular pipe to the rectangular test section. Prisms with one concave surface are embedded in the corners to enable a smooth transition free from corner vortices. The same kind of transition passage was used downstream of the test section at the junction with the pipe flow. A stainless steel screen (15×15 mesh, 0.25 mm (0.010 in.) wire diameter) was installed 10.2 cm (4 in.) from the upstream end of the flow conditioning section. This initial coarse entrance screen was used to achieve a uniform flow with relatively small pressure drop. It is followed by a 2.54 cm (1 in.) long honeycomb section (with 3.2 mm (1/8 in.) hexagonal cells), and then by a finer stainless steel screen (26×26 mesh, 0.2 mm (0.0075 in.) wire diameter). This combination makes the flow more uniform and decreases the turbulence level dramatically. The next 29.2 cm (11.5 in.) long section serves as the settling chamber so that the turbulence level at the entrance of the test section was further decreased to acceptable levels (less than 2% at the exit). At 2.54 cm (1.0 in.) upstream of the entrance, pressure tap holes were drilled on each side of the tunnel surface to measure an averaged P_∞. This pressure was used as a reference to estimate the pressure at Venturi throat P_t, which was further used to calculate cavitation number $\sigma=(P_t-P_v)/\frac{1}{2}\rho V_t^2$.

The pressure distributions along the test section at noncavitating Reynolds numbers collapse very well, indicating that the Reynolds number effect on noncavitating flow is negligible over the range studied. The flow conditions in the test section in the absence of the test model were measured. Figure 2 shows typical LDV-measured streamwise velocity and turbulence intensity (U component) in the spanwise direction. Measurements were taken at the center of the test section ($Y=0$) and at two streamwise locations, i.e., the entrance ($X=-40$ mm) and the throat ($X=0$). Velocity is nondimensionalized by the mean velocity of the profile, and turbulence intensity is defined as the root mean square of the streamwise velocity fluctuations divided by the local mean velocity. From the velocity distribution (Fig. 2(a)), it can be seen that the sidewall effect at the throat section is much smaller than at the entrance. It is confined within $0.2D_t$ away from the wall. Turbulence levels at two locations are approximately the same, but the turbulence intensity level at the throat section is lower than at the entrance section. For the uniform velocity portion, the turbulence intensity is about 1%. Reynolds number effect on turbulence level is negligible over the range 1.78×10^5–2.70×10^5, based on the Venturi throat thickness.

Backward facing steps with heights range from 0.8 mm to 4 mm were installed on one of the converging walls to create a separation bubble downstream of the Venturi throat. The baseline Venturi boundary layer thickness was $\delta_0=0.47$ mm, which resulted in h/δ_0 ranging from 1.7 to 8.5. Cavitation inception and development caused by the separation bubble were studied for different step heights. In the experiments, the steps were installed either on the top wall or the bottom wall, as shown in

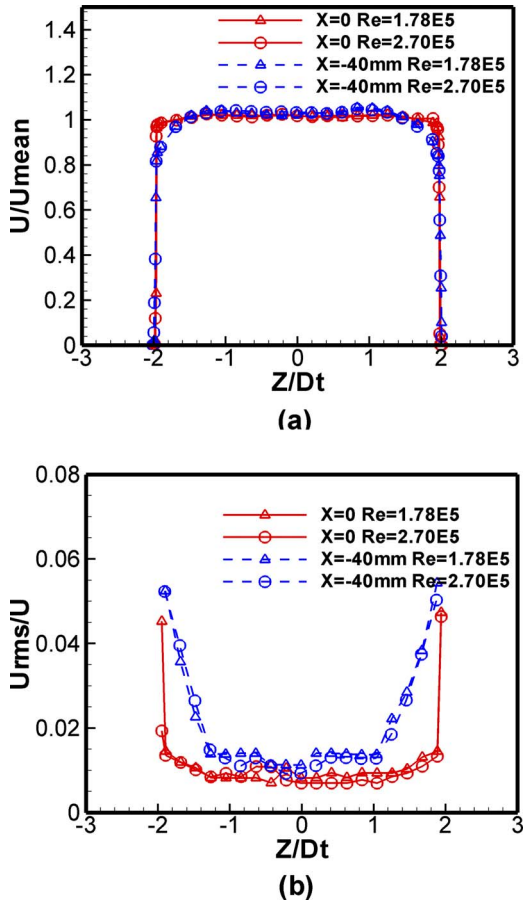

Fig. 2 Flow conditions of the incoming flow in test section: (*a*) axial velocity distribution and (*b*) turbulence intensity distribution

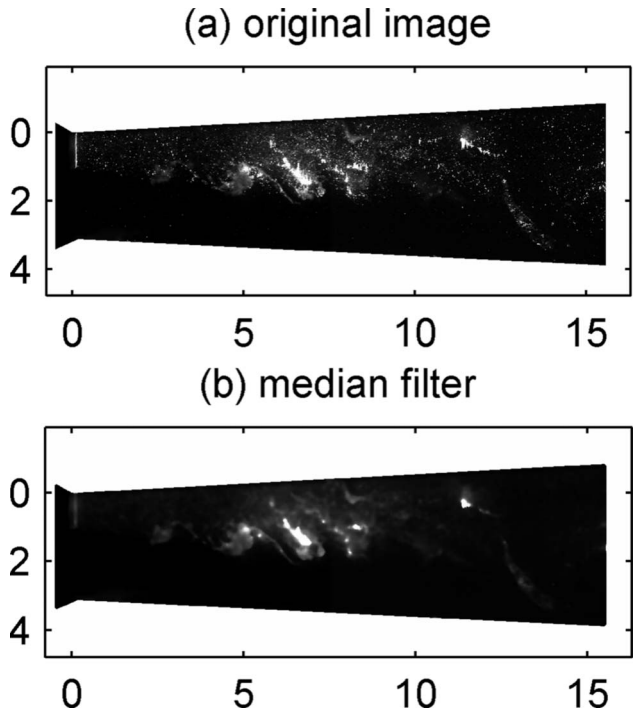

Fig. 3 PIV image processing example

Fig. 1. Froude number ($\mathrm{Fr}=V^2/gL \gg 1$) was estimated and found to be much greater than one for the microcavitation bubbles (where V is the convection velocity and L is the diameter of the microcavitation bubble). Hence, the buoyancy force is negligible compared to the inertial force and, therefore, the cavitation features are not expected to be different for the same step installed on different walls. Step location was chosen to facilitate the illumination used for the flow visualization.

3 Experimental Measurement Techniques and Experimental Uncertainties

Flow conditions (flow velocity and turbulence intensity distribution) in the test section were measured using a one-dimensional DANTEC LDV system. LDV results were discussed in Sec. 2.2 to document the quality of flow in the test section. Specifications of the LDV system can be found in Ref. [18]. All signal processing was performed using DANTEC DYNAMICS BSA flow processing software. Flow seeded for PIV measurements was also measured using LDV. The validated sample rate was in the range of 200–1000 Hz depending on Reynolds number. The sampling criterion for each ensemble of realizations was set as 10,000 data points or 10 s, whichever comes first. The uncertainties for the mean velocity are less than $\pm 2\%$ and approximately $\pm 3.5\%$ for the rms values (see Ref. [18] for details).

PIV experiments were performed using a standard commercial TSI PIV system. Silver-coated glass spheres of 14 μm in diameter and 1.65 specific gravity were used to seed the flow. For noncavitating flow field measurements, 200 realizations were acquired and averaged to determine the mean velocity and other properties of the flow field. The uncertainties of PIV results were estimated by considering the bias limits and precision limits [19]. In the shear layer, the uncertainty of mean streamwise velocity U is approximately $\pm 4\%$ (see Ref. [18] for details).

When using PIV to perform flow visualization, the cavitation microbubbles were used as the flow tracer and marker. Laser illumination intensity was adjusted to achieve adequate light scattering by the cavitation bubbles. "Noise" on PIV images caused by the reflections of seeding particles in the flow was removed using a digital median filter. Figure 3 shows an example of the original and filtered images.

A GE Panametrics PT878 ultrasonic flow meter with a range of ± 12.2 m/s was used to measure the velocity and volumetric flow rate. The measurement uncertainty is 0.02 m/s. A Dwyer series 490 wet/wet handheld digital manometer was used to measure mean static pressure. Its measurement range is $(0-1)\times 10^5$ Pa and accuracy $\pm 1\%$ of full scale, which is approximately ± 1020 Pa.

Cavitation was achieved by increasing the flow rate. A high-speed camera NAC MEMRECAM fx K3 (NAC Image Technology Corporation) was used to study the cavitation inception and development for the smallest step height 0.8 mm. The images were acquired at a framing rate of 2000 frames/s, frame size 1280×512 pixels. Volume illumination with a 150 W Westinghouse outdoor flood light was used. Cavitation images for different step heights were also recorded using PIV to observe cavitation structures. Detailed specifications can be found in Ref. [18].

The uncertainty in cavitation number σ depends on the uncertainty in pressure and velocity measurement. For the range that the measurements covered, the uncertainty in cavitation number did not exceed $\pm 2\%$. Since cavitation was achieved by increasing the flow rate, the increase in Reynolds number Re_h corresponded to the decrease in cavitation number σ. Therefore, higher Reynolds number indicates a more developed state of cavitation in this study.

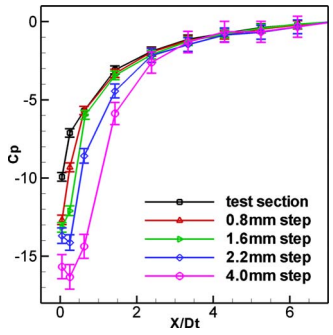

Fig. 4 Pressure distribution for different step heights in Venturi test section

4 Experimental Results and Discussions

Backward facing steps of heights $h=0.8$ mm, 1.6 mm, 2.2 mm, 4.0 mm were mounted on one of the converging walls of the Venturi test section. The noncavitating performance data of the test section with different backward facing steps are shown in Fig. 4 and compared to the baseline Venturi test section in the absence of backward facing steps. The pressure at the exit of the test section was used as the reference pressure. Larger step height caused lower mean pressure in the separation bubble downstream of the step. For a higher step, the cavitation condition is achieved by operating the system at a lower flow rate, i.e., inception cavitation number σ_i is larger.

PIV images were used to visualize cavitation inception or limited cavitation structures and also extended to visualize the developed cavitation by adjusting illumination intensity. High-speed cinematography was performed with the 0.8 mm step.

4.1 Cavitation Inception and Cloud Shedding Process for Smaller Step Heights. Flow visualizations on cavitation inception and evolution were captured using the NAC high-speed camera for the 0.8 mm step case. Figure 5 shows the cavitation development at decreasing cavitation numbers. The onset of the visual observation of the bubbles was associated with limited cavitation. Because the cavitation bubbles at this stage were still small, it is reasonably assumed that they acted as tracers and did not interact actively with the main flow. They served as the visualization agent to reveal some important features of the underlying flow field.

Noncavitating PIV results (Fig. 10(*a*)) show that the separation bubble length was approximately 16 h for the 0.8 mm step. The magnification of Fig. 5 is actual scale. Figure 5(*a*) shows that cavitation inception originated at the rear of the turbulent shear layer around separation bubble. At this stage it was characterized by the sporadic appearance of the bright filaments in that region. The second stage of cavitation is shown in Fig. 5(*b*) where flow upstream of the inception location started to cavitate, but was confined in the shear layer. With the decrease in the cavitation number, i.e., increase in Reynolds number, cavitation structures took the form of spanwise vortices in the shear layer as it grew stronger. At the third stage (Fig. 5(*c*)), the cavitation structures grew larger in the shear layer and cavitation microbubbles started to fill the separation bubble. At these stages, cavitation bubbles were convected downstream in the form of cavitation surges. With a further decrease in cavitation number (Fig. 5(*d*)), the cavity became longer and thicker and wavy forms traveled on the interface of the cavity and the outer flow. Periodic pinch-off was clearly observed at the cavity closure region. For an even lower cavitation number (Fig. 5(*e*)), cavitating flow was more developed, with similar cloud shedding features.

After cloud shedding began, images at different phase angles were taken to show how the cavitation structures changed periodically. In Fig. 6, a shedding process for a continuous 3.5 ms at $\sigma=0.47$ is shown. On each photograph, the major cavity was outlined with a dashed line and cloud structures were labeled with circled numbers. During the entire process, three shed cloud structures were identified. A complete shedding process, which started when the second cloud structure was formed at the rear of the major cavity and ended when the third cloud structure formed, lasted for 2.5 ms. This corresponds to a shedding frequency of 400 Hz. The Strouhal number of this instability is St=0.38, based on the maximum cavity length, which approximately equals the separation bubble length, 16 h, and the velocity of the reentrant jet, which is of the order of the flow velocity at Venturi throat. The uncertainty in this value is less than 15%. It falls into the range of 0.25–0.4 found in many experiments, e.g., Kawanami et al. [20]. The reentrant jet instability is usually considered to be the mechanism of cloud shedding. The roll-up motion at cavity closure gives birth to the formation of the reentrant jet [6]. Using the high-speed camera images, the average convection velocity of the shed structures was estimated to be approximately 40–50% of the throat velocity. This was determined by taking the ratio of the measured displacement of large vapor structures between two successive frames to the time interval between the two frames.

The delineation of the major cavity contour is somewhat subjective. It was determined by comparing a sequence of high-speed camera images. The shedding structures that are relatively obvious from the images were considered to break off away from the major cavity. By comparing the relative locations of the shedding

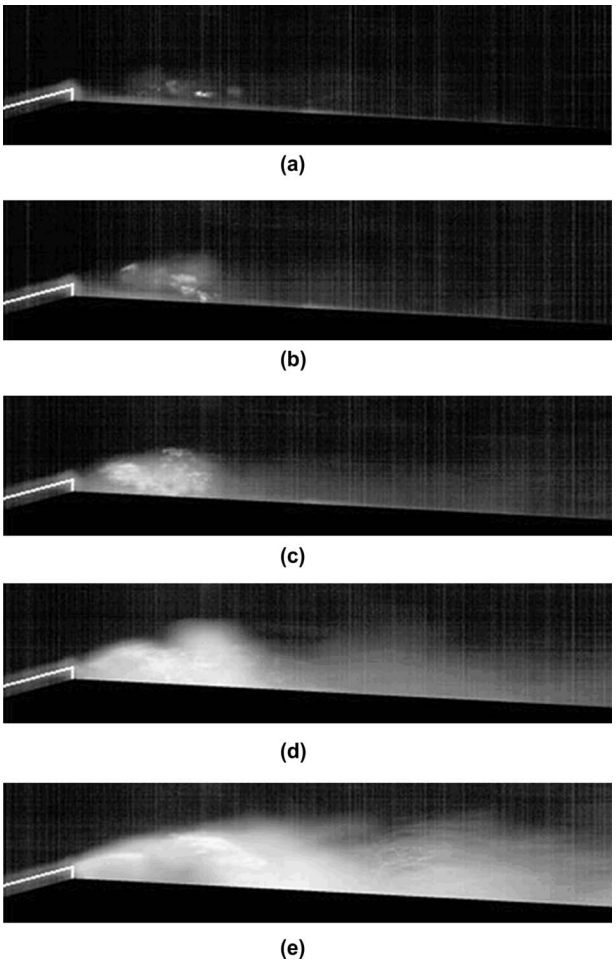

Fig. 5 Cavitation inception and development for baseline case. (*a*) $Re_h=8.8\times10^3$, $\sigma=0.99$; (*b*) $Re_h=9.2\times10^3$, $\sigma=0.87$; (*c*) $Re_h=9.4\times10^3$, $\sigma=0.79$; (*d*) $Re_h=9.9\times10^3$, $\sigma=0.67$; and (*e*) $Re_h=1.1\times10^4$, $\sigma=0.47$ (the step height $h=0.8$ mm).

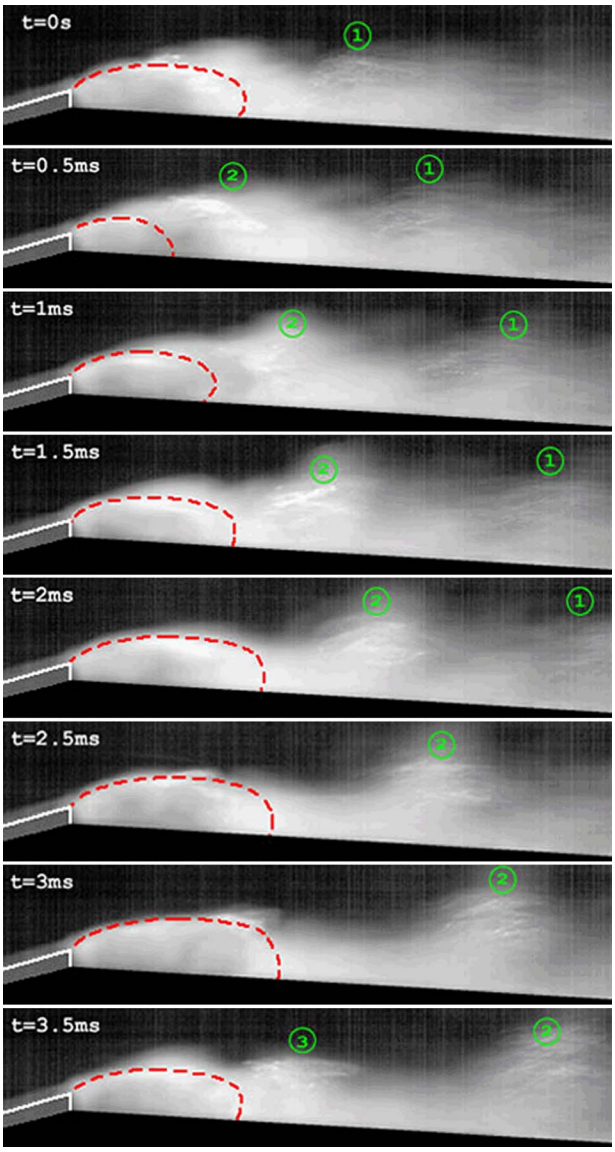

Fig. 6 Cloud cavitation shedding process for baseline case at σ=0.47. The major cavity is outlined with dashed line; cloud structures are labeled with circled numbers (the step height h =0.8 mm).

structures on sequential images, the contour/profile of the major cavity was estimated. The cavity lengths found this way have very large uncertainties.

4.2 Cavitation Inception and Development for Intermediate Step Heights. For intermediate step heights (1.6 mm and 2.2 mm), PIV images showed that cavitation inception location shifted between the middle of the shear layer and the rear of the separation bubble due to the unsteady nature of the flow. Selected flow visualization images were shown in Figs. 7 and 8, respectively, for 1.6 mm and 2.2 mm steps. The inception locations for the two intermediate steps are marked in noncavitating flow field relative to the separation bubbles in Figs. 10(*b*) and 10(*c*), respectively. Cavitation structures, therefore, appeared in various forms on flow visualization images ranging from a bright spot in the rear of the separation bubble to connected vortex structures in the middle of the shear layer. At much lower cavitation numbers, cavitation microbubbles filled the vortex structures in the shear

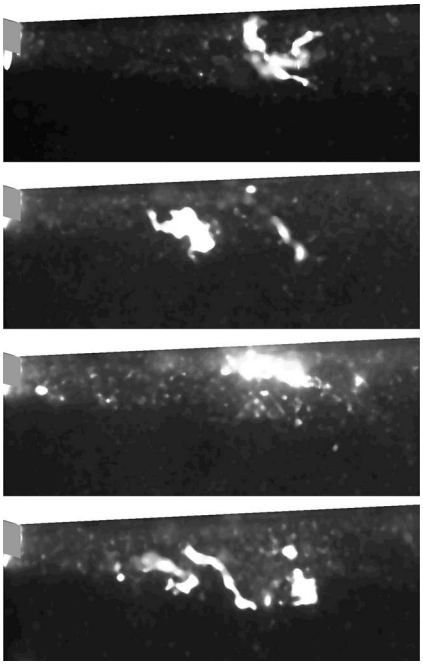

Fig. 7 Selected PIV images of cavitation inception structures for 1.6 mm step in Venturi test section at $Re_h=1.84\times10^4$, σ =1.07

layer. They were less abundant in the separation bubbles. The developed cavitation for the two intermediate steps was much more like that for the 4.0 mm step case.

4.3 Cavitation Inception and Development in Separated Shear Layer for Larger Step Heights. The 4 mm step was used to study the cavitation inception and development in separated shear layer for larger step heights. Median-filtered PIV images of cavitation visualization at different Reynolds numbers (i.e., cavitation numbers) are shown in Fig. 9.

Figure 9(*a*) shows the cavitation inception locations in the separated shear layers occurring approximately 5–8 h downstream of the step. Noncavitating PIV measurements (Fig. 10(*d*)) showed that the separation bubble length exceeded 16 h for the 4 mm step. Thus, the inception location was in the middle of the sepa-

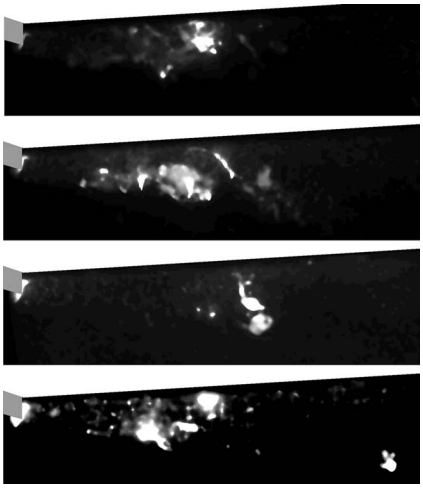

Fig. 8 Selected PIV images of cavitation inception structures for 2.2 mm step in Venturi test section at $Re_h=2.55\times10^4$, σ =1.14

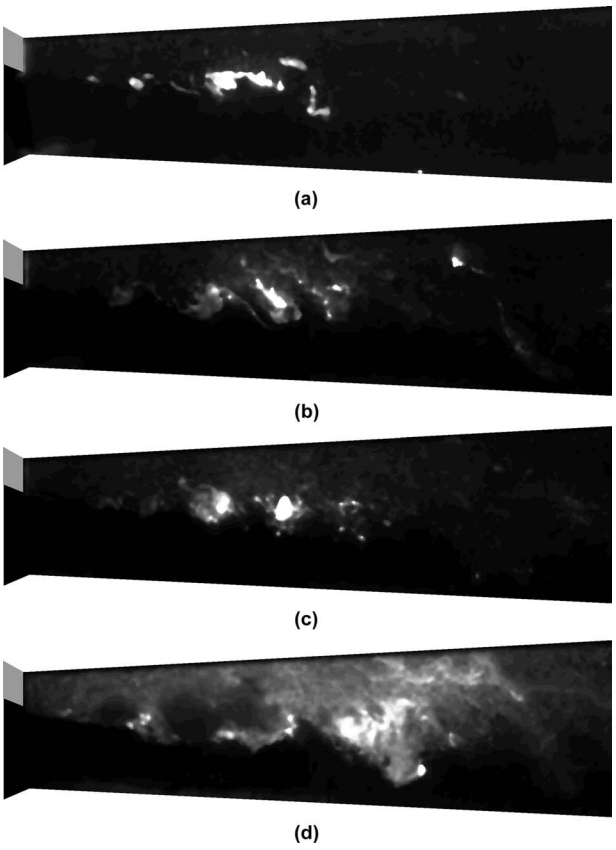

Fig. 9 PIV images of cavitation structures in the shear layer of 4.0 mm step in Venturi test section: (*a*) $Re_h=4.7\times10^4$, $\sigma=1.33$; (*b*) $Re_h=5.1\times10^4$, $\sigma=1.12$; (*c*) $Re_h=5.4\times10^4$, $\sigma=0.99$; and (d) $Re_h=5.8\times10^4$, $\sigma=0.85$

rated shear layer. The cavitation structures correspond to the turbulent flow structures in the separated shear layer. Figures 9(*a*) and 9(*b*) show cavitation in spanwise vortices and the secondary streamwise vortices connecting them. Figure 9(*c*) clearly shows cavitation structures bearing the shape of spanwise vortices in the middle of the shear layer. As Reynolds number increased (i.e., cavitation number decreased), the cavitation region developed sooner upstream. Smaller cavitation structures assuming the shape of the spanwise vortices could be seen at the trailing edge of the backward facing step where the shear layer was thinner. While the cavitation region occurred closer to the backward facing step, cavitation bubbles also tended to fill the separation bubble. Coherent structures convecting downstream were also observed and clearly identifiable as spanwise vortices filled with cavitation microbubbles convecting downstream. They should be differentiated from the cloud cavitation shedding generated due to the reentrant jet.

4.4 Discussion. Cavitation inception and development for different backward step heights were observed. Small steps and larger steps were associated with different cavitation inception locations and cavitation structure shedding modes. When the step was small (0.8 mm), cavitation originated in the reattachment region of separation bubble. When the steps became larger, cavitation shifted upstream to midway downstream of the shear layer enclosing the separation bubble. This can be seen from Fig. 10, which relates the cavitation inception locations obtained from flow visualization to the noncavitating flow features measured with PIV. It is speculated that for smaller steps, the pressure fluctuations played an important role, causing the instantaneous pressure to decrease to the vapor pressure. In contrast, for the larger step ($h=4.0$ mm), the mean pressure at the middle of the shear layer was much lower than that at the reattachment region compared to the smaller step ($h=0.8$ mm) case (Fig. 4). Cavitation started in the shear layer despite the high pressure fluctuations at the rear of the separation bubble. The cavitation inception loca-

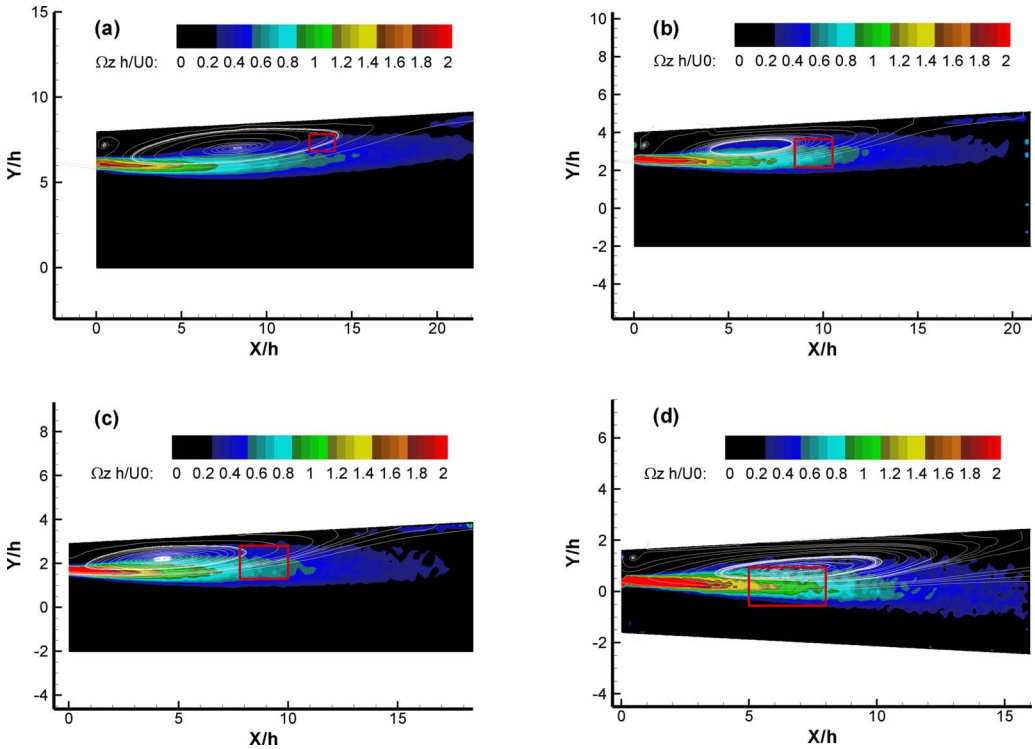

Fig. 10 Noncavitating vorticiy ($\Omega_z h/U_0$) field with separation bubble and cavitation zone marked: (*a*) $h=0.8$ mm, (*b*) $h=1.6$ mm, (*c*) $h=2.2$ mm, and (*d*) $h=4.0$ mm

tions for the two intermediate step heights were observed to shift between the rear of the separation bubble and the middle of the separated shear layer.

For the 0.8 mm step, the cavitation structures at higher cavitation numbers did not show the detailed turbulent structures because the length scale was too small and the shear layer was not strong enough. After the second stage of its development, cavitation structures took the form of the spanwise vortices in the shear layer. However, the other step heights were large enough so that when cavitation inception structures occurred in the shear layer, the streamwise vortices were occasionally observed between spanwise vortices. Moreover, the turbulent structures were clearly visualized with the assistance of cavitation microbubbles.

Different cavitation structure shedding modes were observed for different step heights. For the 0.8 mm step, the shedding was attributed to the reentrant jet instability, but the reentrant jet could not be directly measured or visualized because of its small scale. The presence of the instability was inferred, because the shed structures were of the scale of the cavity (separation bubble) length, which was much larger than the step height. Typically the spanwise vortices and the step height are on the same length scale. Therefore, the shed structures could not be the spanwise vortices. The cavitating flow characteristics, i.e., periodic cavity length change and cloud shedding, are consistent with reentrant jet instability reported [7]. In addition, the shedding frequency $St=0.38$ fell into the range of reentrant jet instability found in many other researchers' experiments. If this shedding was caused by the shear-layer instability, it would result in a Strouhal number of 0.09, far less than 0.2 found by Driver et al. [21] for shear-layer instability. For larger steps 1.6 mm, 2.2 mm, and 4 mm, vortex propagation was also observed. In these cases it was caused by the convection of spanwise vortices as clearly seen in the middle of the shear layer, and the cavitation structures resemble the spanwise vortices. The measurement of these shedding frequencies using spectral analysis on the pressure signal or streamwise velocity component would provide further evidence to differentiate the two cloud shedding modes. Due to the limitation of the experimental facility, separation bubbles did not cavitate completely as they could for the 0.8 mm step. Therefore, only the first three stages of cavitation development for the 0.8 mm step were observed for the other step heights. It would be interesting to check whether the reentrant jet instability would exist for higher steps if even lower cavitation numbers could be achieved.

5 Conclusions

Cavitation inception and development downstream of a backward facing step in a Venturi test section were studied experimentally for different step heights (0.8–4 mm). High-speed cinematography and PIV images were used to evaluate the cloud shedding process and cavitation development stages.

Inception locations and cavitation development observed in Venturi test section differed with step heights. For small step height (0.8 mm), cavitation inception originated in reattachment region; for larger step heights (1.6 mm, 2.2 mm, and 4 mm), cavitation shifted to the middle of the separated shear layer. The pressure distribution, which was largely affected by the step heights when the wall divergence remained the same, determined the cavitation inception locations. For small step height $h=0.8$ mm, the pressure fluctuations at the rear of the separation bubble were speculated to cause cavitation, while the low mean pressure at the middle of the separated shear layer initiated cavitation for the higher steps.

Different shedding modes were associated with different step heights. For $h=0.8$ mm, a shedding frequency of $St=0.38$ relates the cloud cavitation to the reentrant jet instability at low cavitation numbers ($\sigma=0.47$). For larger steps, flow visualization images showed that cloud shedding was related to the shear-layer instability within the operational limits of the current water loop. Other quantitative measurements of these shedding frequencies in future studies would further elucidate the difference. Shedding modes at even lower cavitation numbers on the larger step heights also would provide interesting research topics.

References

[1] Arakeri, V., and Ramarajan, V., 1981, "Inception of Cavitation From a Backward Facing Step," ASME J. Fluids Eng., **103**(2), pp. 288–293.

[2] Ramamurthy, A., Balachandar, R., and Govinda Ram, H., 1991, "Some Characteristics of Flow Past Backward Facing Steps Including Cavitation Effects," ASME J. Fluids Eng., **113**(2), pp. 278–284.

[3] Arakeri, V., and Acosta, A., 1973, "Viscous Effects in the Inception of Cavitation in Axisymmetric Bodies," ASME J. Fluids Eng., **95**(4), pp. 519–528.

[4] Katz, J., 1984, "Cavitation Phenomena Within Regions of Flow Separation," J. Fluid Mech., **140**, pp. 397–436.

[5] Katz, J., and O'Hern, T. J., 1986, "Cavitation in Large Scale Shear Flow," ASME J. Fluids Eng., **108**, pp. 373–376.

[6] Franc, J., 2001, "Partial Cavity Instabilities and Re-Entrant Jet," *CAV2001 Fourth International Symposium on Cavitation*, Pasadena, CA.

[7] Callenaere, M., Franc, J. P., Michel, J. M., and Riondet, M., 2001, "The Cavitation Instability Induced by the Development of a Re-Entrant Jet," J. Fluid Mech., **444**, pp. 223–256.

[8] Furness, R. A., and Hutton, S. P., 1975, "Experimental and Theoretical Studies of Two-Dimensional Fixed-Type Cavities," ASME J. Fluids Eng., **97**, pp. 515–522.

[9] Stutz, B., and Reboud, J. L., 1997, "Experiments on Unsteady Cavitation," Exp. Fluids, **22**, pp. 191–198.

[10] Kawanami, Y., Kato, H., Yamaguchi, H., Tanimura, M., and Tagaya, Y., 1997, "Mechanism and Control of Cloud Cavitation," ASME J. Fluids Eng., **119**(4), pp. 788–794.

[11] Pham, T. M., Larrarte, F., and Fruman, D. H., 1999, "Investigation of Unstable Sheet Cavitation and Cloud Cavitation Mechanisms," ASME J. Fluids Eng., **121**, pp. 289–296.

[12] Dang, J., and Kuiper, G., 1999, "Re-Entrant Jet Modeling of Partial Cavity Flow on Two-Dimensional Hydrofoils," ASME J. Fluids Eng., **121**, pp. 773–780.

[13] Knapp, R. T., Daily, J. W., and Hammitt, F. G., 1970, *Cavitation*, McGraw-Hill, New York.

[14] Le, Q., Franc, J. P., and Michel, J. M., 1993, "Partial Cavities: Pressure Pulse Distribution Around Cavity Closure," ASME J. Fluids Eng., **115**(2), pp. 249–254.

[15] Brennen, C. E., 1995, *Cavitation and Bubble Dynamics*, Oxford University Press, New York, pp. 217–240.

[16] Reneau, L., Johnston, J., and Kline, S., 1967, "Performance and Design of Straight, Two-Dimensional Diffusers," ASME J. Basic Eng., **89**, pp. 141–150.

[17] Carlson, J., Johnston, J., and Sagi, C., 1967, "Effects of Wall Shape on Flow Regimes and Performance in Straight, Two-Dimensional Diffusers," ASME J. Basic Eng., **89**, pp. 151–160.

[18] An, H., 2007, "On the Use of Vortex Generators to Control Cavitation in a Backward Facing Step Flow," Ph.D. thesis, Purdue University, West Lafayette, IN.

[19] Stern, F., Muste, M., Beninati, M., and Eichinger, W., 1999, "Summary of Experimental Uncertainty Assessment Methodology With Example," IIHR Technical Report No. 406.

[20] Kawanami, Y., Kato, H., and Yamaguchi, H., 1998, "Three-Dimensional Characteristics of the Cavities Formed on a Two-Dimensional Hydrofoil," in *Proceedings of the Third International Symposium on Cavitation*, J. Michel and H. Kato, eds., Vol., 1, pp. 191–196.

[21] Driver, D., Seegmiller, H., and Marvin, J., 1987, "Time-Dependent Behavior of a Reattaching Shear Layer," AIAA J., **25**(7), pp. 914–919.

Image Treatment of a 2D Vapor-Liquid Compound Droplet in a Linearized Steady Viscous Flow

D. Palaniappan[1]
Department of Mathematics,
Texas A&M University,
College Station, TX 77843-3368

The classical method of images is used to construct closed form exact solutions for the two-dimensional (2D) perturbed flow fields in the presence of a 2D vapor-liquid compound droplet in the limit of low-Reynolds number. The geometry of the multiphase droplet is composed of two overlapping infinitely long cylinders C_a and C_b of radii a and b, respectively, intersecting at a vertex angle $\pi/2$. The composite inclusion has the shape resembling a 2D snowman type of object with a vapor cylinder C_a partly protruded into the cylinder C_b filled with another fluid whose viscosity is different from that of the host fluid. The mathematical problem with this inclusion in the Stokes flow environment is formulated in terms of Stokes stream function with mixed boundary conditions at the boundary of the hybrid droplet. General expressions for the perturbed stream functions in the two phases are obtained in a straightforward fashion using Kelvin's inversion together with shift and reflection properties of biharmonic functions. Application of our method to other related problems in creeping flow and possible further generalizations are also discussed. The general results are then exploited to derive singularity solutions for the hybrid droplet embedded in (i) a centered shear flow, (ii) a quadratic potential flow, and (iii) an extensional flow past the 2D vapor-liquid compound droplet. The image singularities in each case depend on the two radii of the cylinders, the center-to-center distance, and the viscosity ratio. The exact solutions are utilized to plot the flow streamlines and they show some interesting patterns. While the flow fields exterior to the droplet exhibit symmetrical topological structures, the interior flow fields show existence of free eddies—enclosed in a figure-eight separatrix—and stagnation points (hyperbolic points). The flow characteristics are influenced by the viscosity and radii ratios. Furthermore, the asymptotic analysis leads to a rather surprising conclusion that there is a (subdominant) uniform flow far away from the droplet in all cases. The existence of an origin, the natural center of the drop of the composite geometry, which neutralizes the uniform flow for a particular choice of the physical parameters, is illustrated. This reveals the sensitivity of the geometry in 2D Stokes flow. The present results may be of some interest in models involving a combination of stick and slip boundaries. Moreover, the method discussed here can be useful both as a teaching tool and as a building block for further calculations. [DOI: 10.1115/1.2948351]

1 Introduction

The method of calculating viscous flows in and/or around cylindrical bodies is useful in connection with several contexts. The viscous flow itself perturbed due to the bodies in a given basic ambient flow field is of interest for its own sake or as the basis for further theoretical and/or numerical analysis as can be found in standard reference texts on the subject [1–3]. Another field of application can be found in the techniques to simulate viscous flows through the frame of singularity induced flows with embedded 2D point singularities (such as stokeslet, rotlet, etc.) as explained, for instance, in Refs. [4–7]. It is to be noted that the shape of the contour in most of those studies was assumed to be circular and the corresponding mathematical boundary value problems were therefore analytically tractable. However, for noncircular body profiles, not many exact calculations are available owing to the mathematical difficulties encountered in dealing with the corresponding boundary value problems. The exact analysis in the case of noncircular cylindrical bodies requires some remedies such as suggested in this paper. The possibility of an analytical treatment for a noncircular body with mixed boundary conditions in a fairly general setting is, in fact, one of the motivations of the present investigation.

Another motivation for the present work originates from the issues concerning 2D bounded viscous flows. One of the interesting and unusual phenomena associated with the 2D exterior creeping flows is the so called *Stokes paradox*, which is a consequence of the result that there is no solution to the governing equations that represents slow streaming flow past a finite body. However, Jeffery [8] showed that two identical circular cylinders rotating with equal but opposite angular velocities produce a uniform flow at large distances. Other examples of such a phenomenon are given by Dorrepaal et al. [6], who found a uniform stream in the case of (i) rotlet or (ii) stokeslet positioned in front of a circular cylinder. The potential singularities such as source or sink located in front of a cylinder also produce a uniform flow at infinity as shown in Refs. [9,10]. This implies that despite the Stokes paradox, streaming flow past a cylinder can indeed be realized through locally generated flows. Investigation of Stokes flow past noncircular objects reveals further surprising results as shown in this paper. Flows past a partially encapsulated 2D droplet are consid-

[1]Also at Texas A&M University at Qatar, P.O. Box 5825, Doha, Qatar.

Contributed by the Fluids Engineering Division of ASME for publication in the JOURNAL OF FLUIDS ENGINEERING. Manuscript received June 23, 2006; final manuscript received April 25, 2008; published online July 22, 2008. Assoc. Editor: Theodore Heindel.

ered here to elucidate such fascinating results. In particular, it is shown that the *exact* analysis for a partially encapsulated droplet submerged in nonuniform flow fields generated at infinity reveals the existence of slow streaming flow. A way to neutralize such subdominant flows is suggested, which also explains the sensitivity of the geometry in Stokes flow.

In recent years, the computation of viscous flows involving 3D completely/partially fused objects has been the subject of many studies. Two dissimilar fused configurations, compound drops for instance, occur in processes such as melting of ice particles in the atmosphere, liquid membrane technology, as well as in other industrial processes. The existence of such drops is elucidated in studies of lipid bilayer [11] and polymer grafted [12] membranes in concentrated solutions. A comprehensive review on 3D modeling compound drops may be found in Refs. [13,14]. Similar models have also been used in the electric field-induced cell-to-cell fusion process to predict the fusion of biological cells [15]. The semicircular bulge on a microchannel wall model by Gaver and Kute [16] to predict the amplification of stress, force, and torque on an adherent cell is another example of this kind. However, most of the models, with the exception of the latter, have dealt with the 3D objects ignoring their 2D counterpart. Although the 3D models may have a variety of applications under physically realizable conditions, the corresponding 2D models still provide some novel qualitative features that are worthwhile in several situations. For instance, the 2D object under investigation could be modeled as two dissimilar partially merged cylindrical surfaces under varying ambient flow conditions. Therefore, our exact analysis may provide some insight into various physical phenomena as well.

While there are numerous analytical and numerical methods available for solving boundary value problems, the classical method of images continues to receive attention even to date. This method originally developed in the context of electrostatics possesses a number of features, which distinguish it from other techniques for solving boundary value problems modeling a variety of physical phenomena. The essential constituents involved in the classical method of images are as follows:

- the region of distribution/image point and its location in a specific geometry
- suitable image singularities such as stokeslets, rotlets, dipoles, and higher order multipoles
- strengths of the image singularities in order to satisfy the desired boundary conditions

Lord Kelvin used this so called image principle to solve static problems involving a perfectly electrically conducting (PEC) grounded sphere. The use of this idea in hydrodynamics is quite well known (see Ref. [10], for instance). Spheres, cylinders, and half-spaces belong to the class of objects for which the image principle works pretty well in many circumstances. A natural question arises whether the image principle can be used for body profiles other than spheres, cylinders, and half-spaces. It turns out that for complex body shapes the image principle becomes extremely difficult to apply and requires quite a lot of guess work and iterative adjustments in order to obtain even approximate solutions. Here we extend the idea of the image principle to treat the mathematical boundary value problem for the 2D flow past a multiphase compound droplet. This idea is well suited especially for a class of boundary value problems involving merging (intersecting) surfaces. These surfaces depart from a circular shape and the fact that exact solutions can be found for problems involving these surfaces makes them members of a very exclusive family.

We solve a basic fluid flow problem for a special nontrivial geometry of 2D *snowman type* in this paper using the technique discussed above. More specifically, we consider a geometry consisting of a vapor cylinder partially merged in a fluid cylinder with a viscosity different from that of the surrounding host fluid and construct solutions for the flow fields in the limit of low-Reynolds

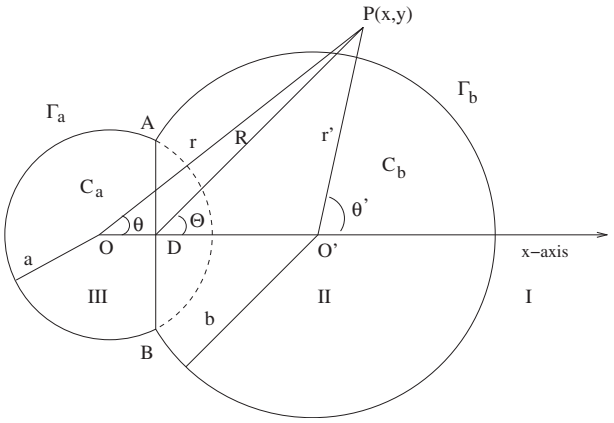

Fig. 1 Schematic of a 2D multiphase droplet Γ

number using the classical image principle. It is assumed that the angle of intersection of the two cylindrical surfaces of the two-phase object is $\pi/2$. This assumption allows the two bounding circles to share a common inverse point, a requirement that is *crucial* for the exact analysis. The boundary value problem for the determination of the stream functions is solved analytically and general solutions representing a set of basis functions are provided in terms of the basic unbounded flow. The solutions are expressed in terms of Green functions for specific externally generated flow fields. The advantage of these forms of solutions is that various physical quantities of interest can be computed directly. Furthermore, these closed form solutions provide results that, besides their significance to hydrodynamics, can be used to validate numerical codes designed to handle objects of more general shapes.

This paper is organized as follows. In Sec. 2, the geometry of the 2D compound droplet and surface tension forces on the surface of this compound droplet are discussed. Section 3 discusses the formulation of the problem and other details pertaining to the present analysis. The main results of the present work appear in Sec. 4. The general solutions for the stream functions in the continuous (exterior to the droplet) and dispersed (interior to the droplet) phases, respectively, are provided in closed form. Various special cases and the generalizations of the method are discussed in the same section. In Sec. 5, the utility of our general results are demonstrated for several choices of freestream flows. Finally, our main findings of the present study are summarized in Sec. 6.

2 Geometry of the 2D Multiphase Droplet

The geometry of the cylindrical multiphase droplet (2D vapor-liquid droplet) is depicted in Fig. 1. This geometry is composed of two unequal overlapping infinitely long circular cylinders C_a and C_b of radii a and b with centers O and O', respectively. It is assumed that the two circles intersect orthogonally. The boundary of the droplet is denoted by $\Gamma=\Gamma_a\cup\Gamma_b$, where Γ_a is the circle where $r=a$ and Γ_b is part of the circle where $r'=b$. Since the circles overlap at a contact angle $\pi/2$, the two centers share a common inverse point D. In the right-angled triangle OAO', $c^2=a^2+b^2$, where $OO'=c$. As shown in Fig. 1, the line AB intersects OO' at D. Hence, $OD=a^2/c$ and $DO'=b^2/c$. It then follows that

$$\frac{1}{(OA)^2}+\frac{1}{(O'A)^2}=\frac{1}{(DA)^2} \tag{1}$$

which is an interesting geometrical relation connecting the radii of the two circles and the distance between the inverse point D and the vertex A. Let (r,θ), (r',θ'), and (R,Θ) be the polar coordinates of any point outside the assembly Γ with O,O', and D as origins, respectively; then, the following geometrical relations are evident from Fig. 1:

$$r^2 = r'^2 + 2cr' \cos\theta' + c^2 \tag{2}$$

$$r'^2 = r^2 - 2cr \cos\theta + c^2 \tag{3}$$

$$R^2 = r^2 - 2\frac{a^2}{c} r \cos\theta + \frac{a^4}{c^2} = r'^2 + 2\frac{b^2}{c} r' \cos\theta' + \frac{b^4}{c^2} \tag{4}$$

We see from Eqs. (2)–(4) that on the circular boundaries C_a and C_b, r' and r reduce to

$$r' = \frac{c}{a} R \quad \text{on } r = a \tag{5}$$

$$r = \frac{c}{b} R \quad \text{on } r' = b \tag{6}$$

Part of the cylinder C_b contains a liquid with viscosity different from the viscosity of the ambient liquid surrounding the droplet, and the cylinder C_a is a vapor. We designate the fluid region exterior to Γ as I and the circular regions C_b and C_a as II and III, respectively. The surface tension forces are assumed to be large enough to keep the interfaces in a circular shape. The vapor-liquid configuration exists at rest with contact angle approximately 90 deg if $\gamma_{\mathrm{I,II}} \approx \gamma_{\mathrm{II,III}} \gg \gamma_{\mathrm{I,III}}$, which is in agreement with the Laplace law on all interfaces. Here the $\gamma_{a,b}$ denotes the surface tension at the interface separating regions a and b.

The assumption of $\pi/2$ contact angle, even though a necessity here is to make analytical progress, is a first step towards solving the problem for arbitrary contact angle, perhaps through conformal mapping techniques or numerical methods. The solution provided here can also be very useful for validation of many numerical methods and codes, which attempt to solve such complex problems computationally. The solution can also be useful in many practical situations where this may serve as a good approximation, for instance, in the phenomena of "two drops glued together" that occurs in three-phase emulsions, in direct-contact heat exchange between two immiscible liquids and in separation technology where drops and bubbles are used to capture particulate impurities (see Ref. [14]). Furthermore, the problem discussed here provides yet another example for the removal of contact-line singularity [17–19] that would otherwise lead to nonintegrable stress components at the boundary.

3 Formulation of the Problem

Consider a stationary 2D vapor-liquid droplet submerged in a 2D flow of a viscous fluid. The Reynolds number of the flow fields is assumed to be small so that all inertial effects are negligible. In this case, the governing equations for fluid flow are the linearized steady Navier–Stokes equations, also called creeping flow equations or Stokes equations in two dimensions,

$$\mu^{(i)} \nabla^2 \mathbf{q}^{(\mathbf{i})} = \nabla p^{(i)}, \quad \nabla \cdot \mathbf{q}^{(\mathbf{i})} = 0 \tag{7}$$

where $i = 1, 2$ is used to denote the continuous (that is Phase I) and the dispersed (that is Phase II) liquid phases, respectively, $\mathbf{q}^{(\mathbf{i})}$, $p^{(i)}$ and $\mu^{(i)}$ are the velocities, pressures, and viscosities in the respective phases. The boundary and interface conditions are as follows.

- the 2D velocity and pressure far from the droplet are that of a specified basic flow as follows:

  $$\mathbf{q}^{(1)} \to \mathbf{q}_0, \quad p^{(1)} \to p_0 \quad \text{as } r \to \infty$$

  where $r = \sqrt{x^2 + y^2}$.
- Zero normal velocity on Γ,

  $$\mathbf{q}^{(i)} \cdot \hat{\mathbf{n}}_a = \mathbf{q}^{(i)} \cdot \hat{\mathbf{n}}_b = 0 \quad \text{on } \Gamma$$

  where $\hat{\mathbf{n}}_a$ and $\hat{\mathbf{n}}_b$ are the 2D unit normals at the circular surfaces C_a and C_b, respectively.
- Continuity of tangential velocity and shear stress at the liquid-liquid interface bounding C_b,

  $$q_t^{(1)} = q_t^{(2)}, \quad \tau_t^{(1)} = \tau_t^{(2)} \quad \text{on } \Gamma_b$$

  where $q_t^{(i)}$ and $\tau_t^{(i)}$ are the tangential components of the velocity and surface force, respectively.
- Zero shear stress at the vapor-liquid interface C_a,

  $$\tau_t^{(1)} = 0 = \tau_t^{(2)} \quad \text{on } \Gamma_a$$

  The governing Stokes equation (7) subject to these far-field and interface conditions constitutes a well-posed problem whose solution provides the velocities and pressures in the dispersed and continuous phases prevailing in the presence of the compound droplet.

It is convenient to use the stream function formulation, which requires the solution of the biharmonic equation

$$\nabla^4 \psi = 0 \tag{8}$$

where ∇^2 in two dimensions is given by

$$\nabla^2 = \frac{\partial^2}{\partial x^2} + \frac{\partial^2}{\partial y^2} \tag{9}$$

$$= \frac{\partial^2}{\partial r^2} + \frac{1}{r}\frac{\partial}{\partial r} + \frac{1}{r^2}\frac{\partial^2}{\partial \theta^2} \tag{10}$$

for the Cartesian (x, y) and polar (r, θ) coordinates, respectively. Now the velocity components in terms of the stream function are given by

$$q_r^{(i)} = \frac{1}{r}\frac{\partial \psi^{(i)}}{\partial \theta}, \quad q_\theta^{(i)} = -\frac{\partial \psi^{(i)}}{\partial r} \tag{11}$$

and the pressure is obtained from

$$\nabla p^{(i)} = \mu^{(i)} \nabla^2 [\mathrm{curl}(\mathbf{e}_z \psi^{(i)})] \tag{12}$$

where $\mathbf{e}_z$ is the unit vector along the z-direction. The boundary and the interface conditions in terms of the stream function become

$$\psi^{(1)} = 0 \tag{13}$$

$$r\frac{\partial}{\partial r}\frac{1}{r}\frac{\partial \psi^{(1)}}{\partial r} = 0 = r\frac{\partial}{\partial r}\frac{1}{r}\frac{\partial \psi^{(2)}}{\partial r} \tag{14}$$

on C_a, the part of the droplet where $r = a$, and

$$\psi^{(1)} = 0 = \psi^{(2)} \tag{15}$$

$$\frac{\partial \psi^{(1)}}{\partial r'} = \frac{\partial \psi^{(2)}}{\partial r'} \tag{16}$$

$$\mu^{(1)}\left(\frac{\partial}{\partial r'}\frac{1}{r'}\frac{\partial \psi^{(1)}}{\partial r'}\right) = \mu^{(2)}\left(\frac{\partial}{\partial r'}\frac{1}{r'}\frac{\partial \psi^{(2)}}{\partial r'}\right) \tag{17}$$

on C_b, the part of the droplet where $r' = b$.

The corresponding formulation for a 3D droplet in three dimensions is given in Ref. [20]. In the cited article, singularity solutions for uniform flow field for a partially encapsulated 3D droplet were reported. We utilize that approach here to construct solutions for arbitrary 2D Stokes flows in and around a partially encapsulated 2D droplet. The essential steps involved in the derivation are as follows.

Step 1. Reflect a given flow field ψ_0 in the stress-free circular cylinder C_a and call the perturbation field as ψ_a. This is the image of ψ_0 in C_a.

Step 2. Reflect the given flow field ψ_0 in the liquid cylinder C_b and call the perturbation to the given flow field as $\psi_b^{(1)}$ and $\psi_b^{(2)}$, respectively. This gives the corresponding images in the cylinder C_b.

Step 3. Reflect ψ_a obtained in Step 1 in cylinder C_b and call the perturbation to ψ_a as $\psi_{ab}^{(1)}$ and $\psi_{ab}^{(2)}$. Reflecting $\psi_b^{(1)}$ and $\psi_b^{(2)}$ obtained in Step 2 in sphere C_a will result in the same potentials, i.e.,

$\psi_{ab}^{(1)}=\psi_{ba}^{(1)}$ and $\psi_{ab}^{(2)}=\psi_{ba}^{(2)}$. This implies that the respective images coincide.

Hence, the desired solutions are obtained. In the first two steps above, we make use of a theorem from Ref. [21].

For convenience we use the 2D Cartesian coordinates. Let (x, y), (x', y'), and (X, Y) denote the Cartesian coordinates of a point outside Γ with O, O', and D as origins, respectively. The Cartesian and polar coordinates are related to $x=r\cos\theta$, $y=r\sin\theta$, with similar relations for the coordinates with respect to other origins. Since x does not appear explicitly in the operator ∇^2 defined in Eq. (9), it is form invariant under translation origin along the x-axis. The following properties are true for Eq. (8).

(A) *Inversion*. If $\psi_0(x,y)$ is a solution of Eq. (8), then $(r/a)^2\psi_0((a^2/r^2)x,(a^2/r^2)y)$ is also a solution of Eq. (8), where a is the radius of inversion.
(B) *Reflection*. If $\psi_0(x,y)$ is a solution of Eq. (8), then $\psi_0(-x,y)$ is also a solution.
(C) *Translation of origin*. If $\psi_0(x,y)$ is a solution of Eq. (8), then $\psi_0(x+h,y)$, where h is a constant, is also a solution.

4 General Solutions

Below, the general expressions for the flow fields in the continuous and dispersed phases are presented in the form of a theorem followed by a simple proof. Numerous special cases, which follow from our main results, are also discussed briefly in this section.

4.1 Theorem. THEOREM. *Let $\psi_0(x,y)$ be the free-space stream function for the 2D motion of a viscous fluid whose singularities lie outside a composite geometry with boundary Γ formed by two generally unequal circular surfaces intersecting orthogonally, and suppose that $\psi_0(x,y)=O(r)$ as $r\to 0$. When a vapor-liquid compound droplet Γ is introduced in this flow field, the modified stream functions due to the droplet become*

$$\psi^{(1)}(x,y)=\psi_0(x,y)-\frac{r^2}{a^2}\psi_0\left(\frac{a^2}{r^2}x,\frac{a^2}{r^2}y\right)+\left[\lambda\left(-1+\frac{r'(r'^2-b^2)}{b^2}\frac{\partial}{\partial r'}-\frac{r'^2(r'^2-b^2)^2}{4b^4}\nabla^2\right)-(1-\lambda)\frac{r'^2}{b^2}\right]\Psi \tag{18}$$

in the continuous phase and

$$\psi^{(2)}(x,y)=(1-\lambda)\frac{(r'^2-b^2)}{b^2}\left[-1+r'\frac{\partial}{\partial r'}-\frac{(r'^2-b^2)}{4}\nabla^2\right]\left(\psi_0(x,y)-\frac{r^2}{a^2}\psi_0\left(\frac{a^2}{r^2}x,\frac{a^2}{r^2}y\right)\right) \tag{19}$$

in the dispersed phase. The function Ψ in Eq. (18) *is defined as*

$$\Psi=\psi_0\left(c+\frac{b^2}{r'^2}x',\frac{b^2}{r'^2}y'\right)-\frac{c^2R^2}{a^2r'^2}\psi_0\left(\frac{a^2}{c}-\frac{a^2b^2}{c^2R^2}X,\frac{a^2b^2}{c^2R^2}Y\right)$$

and

$$\lambda=\frac{\mu^{(2)}}{\mu^{(1)}+\mu^{(2)}}$$

Proof. By virtue of the Properties (A), (B), and (C) presented in the previous section, the terms without derivatives in $\psi^{(1)}-\psi_0$ (the perturbation terms in $\psi^{(1)}$ in Eq. (18)) and $\psi^{(2)}$ (given by Eq. (19)) are solutions of the governing equation (8). The terms with derivatives can also been shown to be solutions of Eq. (8) using the details given in Ref. [21]. By a direct verification, with some algebra, it can be seen that $\psi^{(1)}$ and $\psi^{(2)}$ satisfy the boundary conditions (13)–(17). Since the singularities of ψ_0 lie outside Γ, the singularities of the perturbation terms in $\psi^{(1)}$ will all lie inside Γ. Hence, the perturbed stream function for the continuous phase does not introduce new singularities in the unbounded flow. Finally, since $\psi_0(x,y)=O(r)$ at the origin, the perturbation terms in Eq. (18) are at most of order $O(r)$ for large r. Therefore, the perturbation velocity (which involves derivative of $\psi^{(1)}$) in the continuous phase tends to a constant (which may be taken as zero) as $r\to\infty$. This completes the proof. □

Note 1. The functions $\psi^{(1)}-\psi_0$ (the perturbation terms in $\psi^{(1)}$ in Eq. (18)) and $\psi^{(2)}$ (given by Eq. (19)) are linear in the dimensionless parameter λ, which takes values between 0 and 1 inclusive. For $\lambda=1$ and $\lambda=0$, the solutions given by Eqs. (18) and (19) reduce to the cases of vapor-rigid assembly and vapor-vapor assembly (2D composite bubbles), respectively. It should be mentioned that the latter geometry of a bubble is artificial (unrealistic), but the corresponding solution can be used as a testing tool for more general boundary value problems. The complete velocity and pressure fields in the respective phases can be computed using formulas (11) and (12).

Note 2. Expressions (18) and (19) are in a form similar to the celebrated Lorentz formula [22] for a 3D plane wall. The corresponding formulas for a single fluid as well as for a rigid cylinder, generally known as circle theorems, are also available in Refs. [21,23]. In the limiting case of a single circular cylindrical boundary, expressions (18) and (19) reduce to the results found in Refs. [21,23].

Note 3. Notice that the fluid parameters enter into the stream functions for the cylindrical multiphase droplet in the factor λ only. Therefore, explicit solutions can be generated in a straightforward fashion. It will be seen in the next section that the flow fields, in general, are influenced by the viscosity ratio λ, the geometrical parameters such as the radii of the two circles a and b, and the center-to-center distance c.

Note 4. It may be worthwhile to mention that the related problems such as (i) rigid/fluid cylinder bisected by a planar interface, (ii) 2D vapor half buried in a viscous planar interface, and (iii) two stress-free planes intersecting at a contact angle $\pi/2$ can also be treated using the method of images discussed here.

Note 5. For the flows in two dimensions in general, the flow fields can also be represented in complex functional form. In this sense, expressions (18) and (19) represent the imaginary parts of such analytic functions. The derivation of the biharmonic complex potential satisfying the complex form of the boundary conditions can be done in the same way as explained here for the stream functions. In fact, such analytic functions may be used to find flow fields for more complicated geometries using *conformal transformations*.

4.2 Possible Extension of the Present Method. The simple derivation of exact solutions given in Sec. 4.1 was possible because the two cylinders, modeling the vapor-liquid droplet, intersect at a contact angle $\pi/2$. In this case, the number of Kelvin image points is 3 and the features of the biharmonic equation are used to generate explicit solutions for the multiphase droplet submerged in a 2D viscous flow. Note that the number of image points, which is 3, dictates the number of reflections/steps, also 3, involved in the derivation of solutions in the present case. Now for the cylinders intersecting at a contact angle $\pi/3$ the number of Kelvin image points inside the double circular geometry is 5. This means that the suitable solutions of biharmonic equations can be superposed using five reflections to generate solutions for this case. Likewise, for the contact angle π/n, n an integer, the number of Kelvin image points is $2n-1$ inside the twin cylindrical object. Therefore, a similar superposition of functions at these image points (that is, $2n-1$ number of reflections/steps) will result in a finite series solution. For the general case when the contact angle is not a submultiple of π the image method will yield an infinite series solution. One might encounter difficulty related to convergence of this series solution, and therefore, the image method may not be convenient. In this case, the problem may be solved using a bicylindrical framework with the price of heavy

computations involving complicated functions. However, the accounted boundary value problem for complicated flow fields using this methodology could be quite cumbersome.

5 Illustrative Examples

In this section, we illustrate the results presented in the previous section by numerous examples. Although exact solutions can be obtained for any 2D flow generated outside Γ using the general solutions (18) and (19), we consider here the flows that are generated at infinity and document some of the features of these flows. While the uniform flow past any 2D object is not possible (the so called *Stokes paradox*), we show below that such a uniform flow can be induced far away from the multiphase cylindrical droplet by submerging the object in some nonuniform flows.

5.1 Centered Shear Flow Past Γ. Let the underlying flow be a centered shear flow. The stream function due to this flow in the absence of Γ is $\psi_0(r,\theta)=\alpha r^2 \sin^2\theta$, where α is a shear constant. It should be mentioned that this case has been discussed recently elsewhere [24] in a slightly different context. We simply rederive the solutions using our general formulas presented in the foregoing section. The flow fields in the presence of a cylindrical multiphase droplet suspended in the centered shear flow are obtained using Eqs. (18) and (19). The solutions in the respective phases are as follows. For the continuous phase,

$$\psi^{(1)}(r,\theta)=\alpha\Bigg\{r^2\sin^2\theta-a^2\sin^2\theta+\lambda\left(\frac{b^4}{r'^2}\sin^2\theta'-2b^2\sin^2\theta'-\frac{(r'^2-b^2)^2}{2r'^2}\right)-(1-\lambda)\left(b^2\sin^2\theta'-\frac{a^2b^2}{c^2}\sin^2\Theta\right)+\lambda\Bigg[\frac{a^2b^2}{c^2}\left(2-\frac{b^2}{c^2}\right)\sin^2\Theta+2\frac{a^2b^4}{c^4}\cos^2\Theta-2\frac{a^4b^4}{c^5}\frac{\sin^2\Theta\cos\Theta}{R}+2\frac{a^4b^4}{c^5}\frac{\cos\Theta}{R}-\frac{a^6b^4}{c^6}\frac{\sin^2\Theta}{R^2}-2\frac{a^2b^2}{c^3}R\cos\Theta+\frac{a^2}{2c^2}\frac{\left(R^2-\frac{a^2b^2}{c^2}\right)^2}{R^2}\Bigg]\Bigg\} \tag{20}$$

and for the dispersed phase,

$$\psi^{(2)}(r,\theta)=(1-\lambda)\frac{(r'^2-b^2)}{b^2}\alpha\Bigg[r'^2\sin^2\theta'\left(1-\frac{a^2}{r^2}\right)+2r'^3a^2\sin^2\theta'\frac{(r'+c\cos\theta')}{r^4}+\frac{(b^2-r'^2)}{2}\left(1-\frac{a^2}{r^2}+\frac{2a^2r'^2\sin^2\theta'}{r^4}\right)\Bigg] \tag{21}$$

The above solutions given in Eqs. (20) and (21) are the same as those derived in Ref. [24]. We give here, for the sake of completeness, additional information on these solutions and the features of the flow fields relevant to the present context. Expressions (20) and (21) may be interpreted in terms of the 2D singularities, i.e., *Green* functions. The image system for a centered shear flow consists of Stokes dipoles, Stokes quadrupoles, Stokes octupoles, potential dipoles, and higher order potential singularities located inside Γ together with a uniform flow along the y-direction at infinity. A brief discussion of the uniform flow at infinity is provided at the end of this subsection. It is important to note that expression (20) in the continuous phase yields solutions that can readily be expressed in singularity form.

The streamline patterns for the centered shear flow are sketched for various values of the nondimensional parameter λ in Fig. 2 using expressions (20) and (21). The flow fields display interesting features in continuous as well as in dispersed phases. The plots show that in the continuous phase, the streamlines (closer to the x-axis) coming from infinity are pushed back to infinity due to the presence of the droplet. In the dispersed phase, a pair of symmetrical free eddies occurs for various values of the viscosity ratio. The structure of these eddies does not change significantly with λ. It appears from Fig. 2 that the separatrix (though it is not plotted) that bounds the two eddies is a figure-eight, with one eddy on the top part of the figure-eight, another at the bottom part, and an interior stagnation point at the crossing point of the figure-eight. The interior saddle stagnation point also termed as a hyperbolic fixed point produces a homoclinic orbit (not clearly shown in the figure). The existence of homoclinic orbits suggests that the shear flow discussed here may be a very good candidate for studying chaotic advection (see Refs. [4,5,25] for details). It is found that the radii ratio also has an influence on the flow structure.

As noted earlier in this subsection, there exists a uniform flow term in the image and system for the centered shear flow in the continuous phase. This flow may be extracted from Eq. (20) by computing the asymptotic behavior of the flow at infinity. It is evident from Eq. (20) that for large r (i.e., far away from the droplet),

$$\psi^{(1)}(r,\theta)\sim-2\alpha\lambda\frac{b^4}{c^3}r\cos\theta+O(r^2) \tag{22}$$

which shows that the far-field behavior is that of a subdominant uniform flow with speed $U=-2\alpha\lambda(b^4/c^3)$ along the y-direction. It can be seen that the speed of this uniform flow depends on many parameters such as the radius b, the distance between the centers c, the rate of shear α, and the viscosity parameter λ. The speed U vanishes for $b=0$, that is, in the absence of the fluid cylinder C_b. It also vanishes when $\lambda=0$, which corresponds to a 2D (unrealistic) vapor-vapor assembly.

5.2 Quadratic Potential Flow Past Γ. Now consider a quadratic potential flow. The stream function due to this flow in the absence of Γ is $\psi_0(r,\theta)=-(\alpha/3)r^3\sin 3\theta$, where α is a constant. The flow fields in the presence of a cylindrical multiphase droplet suspended in the quadratic flow may be obtained by the use of the theorem in Sec. 4.1. The solutions for this flow in the respective phases are as follows. For the continuous phase,

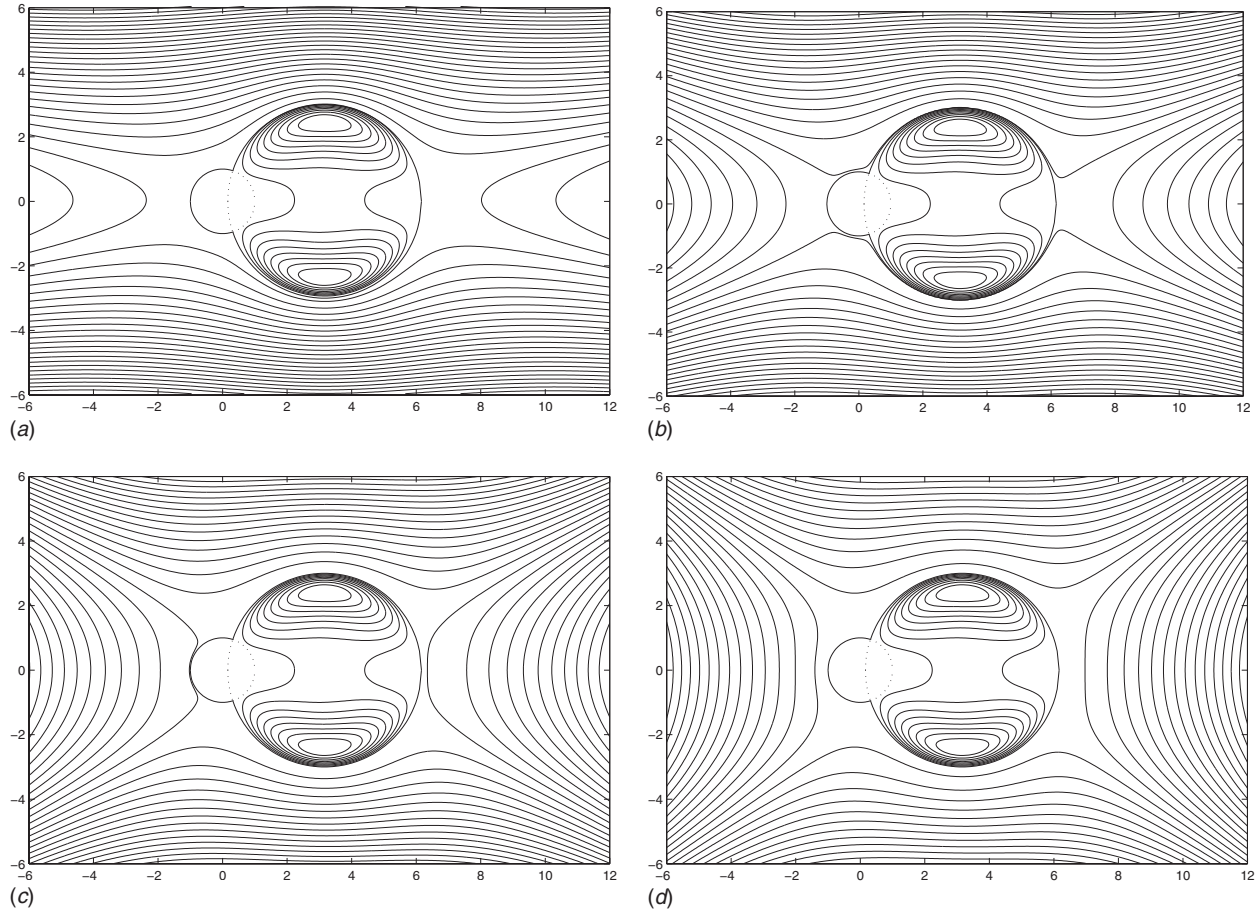

Fig. 2 Streamline patterns for centered shear flow past a multiphase droplet with $b/a=3$ and for various viscosity ratios. (*a*) $\lambda=0.1$, (*b*) $\lambda=0.3$, (*c*) $\lambda=0.5$, and (*d*) $\lambda=0.7$.

$$\psi^{(1)}(r,\theta) = -\frac{\alpha}{3}\left\{\left(r^3-\frac{a^4}{r}\right)(3\sin\theta)-4\sin^3\theta\right)-\lambda\left[3b^2r'\sin\theta'\left(\frac{b^4}{r'^4}-2\frac{b^2c}{r'^3}\cos\theta'+4\frac{c}{r'}\cos\theta'+\frac{c^2}{b^2}\right)-4\frac{b^6}{r'^3}\sin^3\theta'\left(3\frac{r'^2}{b^2}-2\right)\right]$$
$$+\lambda\left[3b^2R\sin\Theta\left(\left(\frac{b^6}{c^6}+2\frac{b^4}{c^4}+\frac{c^2}{b^2}-4\right)+2\frac{a^2}{c}\left(2\frac{b^6}{c^6}+3\frac{b^4}{c^4}-2\right)\frac{\cos\Theta}{R}+2\frac{a^4b^4}{c^6}\left(\frac{b^2}{c^2}+1\right)\left(\left(\frac{1+2\cos^2\Theta}{R^2}\right)\right.\right.\right.$$
$$\left.\left.\left.+2\frac{a^6b^4}{c^7}\left(2\frac{b^2}{c^2}+1\right)\frac{\cos\Theta}{R^3}\right)-4\frac{a^4b^6}{c^6}\frac{\sin^3\Theta}{R^3}\left(\left(3\frac{c^2}{b^2}-2\right)R^2-4\frac{a^2}{c}R\cos\Theta-4\frac{a^4}{c^4}\right)\right]-(1-\lambda)\left[3r'\sin\theta'\left(\frac{b^4}{r'^2}+2\frac{b^2c}{r'}\cos\theta'+c^2\right)\right.$$
$$\left.+4\frac{b^4}{r'}\sin^3\theta'\right)\right]+(1-\lambda)\left[3\frac{a^4}{c^2R}\sin\Theta\left(R^2+2\frac{b^2}{c}R\cos\theta+\frac{b^4}{c^2}\right)+4\frac{a^4b^4}{c^4R}\sin^3\Theta\right]\Bigg\} \tag{23}$$

and for the dispersed phase,

$$\psi^{(2)}(r,\theta) = (1-\lambda)\frac{\alpha}{3}(b^2-r'^2)r\sin\theta\left[6r'(r'+c\cos\theta')\left(1-\frac{a^2}{r^2}\right)\right.$$
$$-8\left(\frac{r^2}{r'^2}\sin^2\theta\left(r'^2-\frac{a^4r'^2}{r^4}+2\frac{a^4r'^3}{r^4}(r'+c\cos\theta')\right)\right)$$
$$\left.-\frac{(r'^2-b^2)}{r^4}(1-\sin^2\theta)\right] \tag{24}$$

The image system for the quadratic potential flow consists of Stokes dipoles and Stokes multipoles, and potential dipoles and potential multipoles located inside the droplet plus a uniform flow along the x-direction. Sample flow topologies are portrayed in Fig. 3 for various values of the nondimensional viscosity ratio λ plotted using solutions (23) and (24). The flow fields in the continuous as well as in the dispersed phases display interesting patterns. In the continuous phase, i.e., Phase I, there are six different compartments—two on the right side, two on the left side, one on top and another at the bottom of the multiphase droplet—representing the flow patterns as can be seen in Figs. 3(*a*)–3(*d*). In other words, the three compartments lie above the x-axis and the other three (identical compartments) lie below the x-axis. It is clear from Fig. 3 that there is a symmetry with respect to the x-axis. This compartmental division of fluid region seems to exist for all values of the nondimensional parameters. In general, the fluid drawn from the infinity towards the multiphase cylindrical droplet is pushed back to infinity in all these six compartments. In the dispersed phase, i.e., in Phase II, two sets of closed eddies,

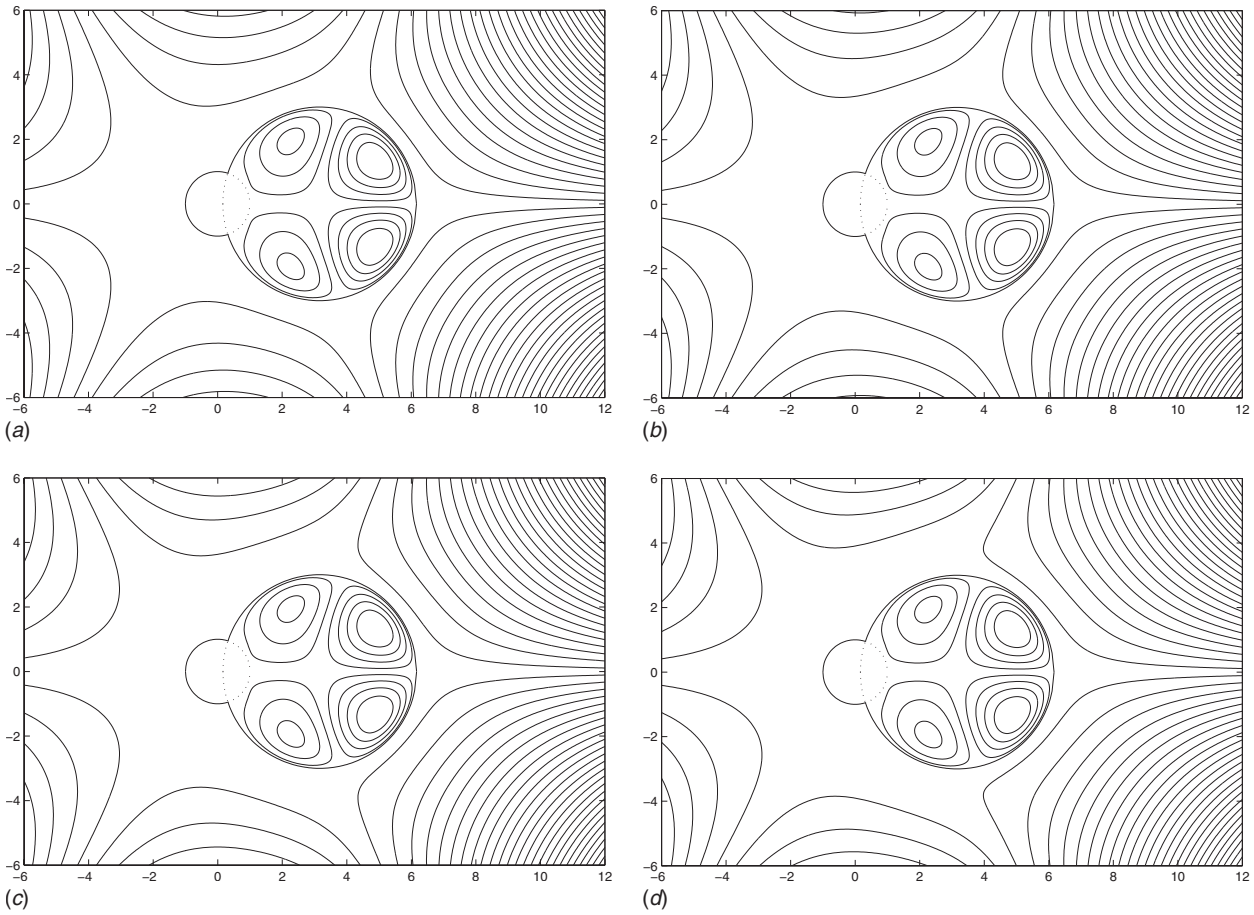

Fig. 3 Streamline patterns for quadratic potential flow past a multiphase droplet with $b/a=3$ and for various viscosity ratios. (*a*) $\lambda=0.1$, (*b*) $\lambda=0.3$, (*c*) $\lambda=0.5$; and (*d*) $\lambda=0.7$.

each set consisting of a pair of eddies, symmetrical with respect to the x-axis appear. The pattern of these eddies does not seem to change dramatically in the parameter range $0<\lambda<1$ for $b/a=3$.

For larger r, the stream function in the continuous phase yields

$$\psi^{(1)}(r,\theta) \sim \frac{\alpha}{3}\left[\lambda\left(b^2-\frac{b^6}{c^4}\left(\frac{b^2}{c^2}+2\right)\right)+(1-\lambda)\frac{b^2}{c^2}(c^2+a^2)\right]r\sin\theta + O(r^3) \tag{25}$$

and this indicates that there is a uniform flow along with the original quadratic flow. The speed of this uniform flow depends on the radii of the cylindrical regions, the distance between the centers and the viscosity ratio. It is evident from Eq. (25) that this uniform flow vanishes when $b=0$, that is, in the absence of the fluid cylinder C_b.

5.3 Extensional Flow. As a further illustration, consider a stationary cylindrical droplet with boundary Γ, immersed in a 2D extensional flow. The stream function corresponding to this flow is $\psi_0=\epsilon r^2\sin\theta\cos\theta$, where ϵ is a shear constant and θ, unless otherwise mentioned below, refers to the polar angle measured counterclockwise at O from the x-axis as shown in Fig. 1. It is worth pointing out that if the angle θ is measured with respect to a different origin along the axis, then the ψ_0 as given above will correspond to a different extensional flow. Therefore this stream function ψ_0 can be used to refer to several extensional flows simply shifting the point O for the purposes of measurement of angle θ.

Now the introduction of the two-phase cylindrical droplet modifies the given flow. The perturbed stream functions in the continuous and dispersed phases are obtained readily from Eqs. (18) and (19) and are given by

$$\psi^{(1)}(r,\theta)=\epsilon\Bigg\{(r^2-a^2)\sin\theta\cos\theta+\lambda\left(\frac{b^4}{r'^2}\sin\theta'\cos\theta'-2b^2\sin\theta'\cos\theta'-cr'\sin\theta'\right)-(1-\lambda)(b^2\sin\theta'\cos\theta'+cr'\sin\theta')$$
$$+\lambda\left[-\frac{b^2}{c}\left(2-\frac{b^2}{c^2}\right)R\sin\Theta+\frac{a^2b^2}{c^2}\left(3\frac{b^2}{c^2}-2\right)\sin\Theta\cos\Theta+\frac{a^4b^4}{c^5}\frac{\sin\Theta}{R}+2\frac{a^4b^4}{c^5}\frac{\sin\Theta\cos^2\Theta}{R}+\frac{a^6b^4}{c^6}\frac{\sin\Theta\cos\Theta}{R^2}+cR\sin\Theta\right]$$
$$+(1-\lambda)\left(\left(c-\frac{b^2}{c}\right)\sin\Theta-\frac{a^2}{b^2c^2}\sin\Theta\cos\Theta\right)\Bigg\} \tag{26}$$

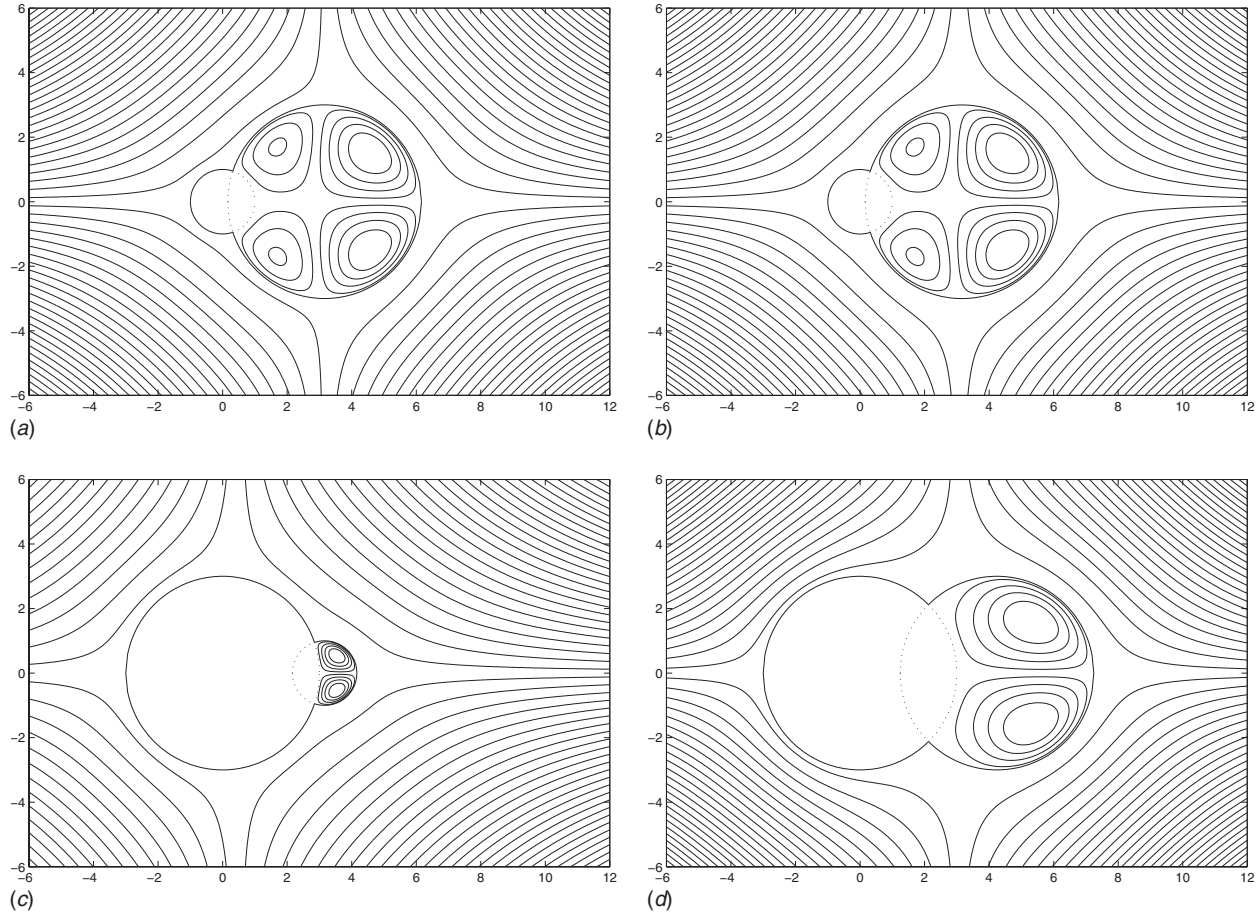

Fig. 4 Streamline patterns for extensional flow (at *O*) past a multiphase droplet for various radii and viscosity ratios. (*a*) $b/a=3$, $\lambda=0.5$; (*b*) $b/a=3$, $\lambda=0.8$; (*c*) $b/a=1/3$, $\lambda=0.5$; (*d*) $b/a=1$, $\lambda=0.8$

for the fluid exterior to the droplet and

$$\psi^{(2)}(r,\theta)=(1-\lambda)\frac{(r'^2-b^2)}{b^2}\left[\left(1-\frac{a^2}{r^2}\right)r'\cos\theta'-(r'^2-b^2)\frac{a^2(r'\cos\theta'+c)}{r^4}+\frac{2a^2r'(r'\cos\theta'+c)(r'+c\cos\theta')}{r^4}\right]r'\sin\theta' \tag{27}$$

for the fluid inside the droplet.

The solution in the continuous phase may be interpreted in terms of the singularities of Stokes flow (i.e., Green's functions). Thus the image system in this phase consists of a Stokes dipole at O, a potential dipole and a Stokes dipole, a potential dipole, a Stokes dipole, a potential octupole, and a Stokes octupole all located inside the droplet, and a uniform flow along the x-direction. Figure 4 shows the streamline patterns for extensional flow with respect to the center at O past Γ for different viscosity and radii ratios. The flow structure in Phase I is symmetrical about the x-axis and this scenario does not appear to change appreciably for various values of these parameters as seen in Figs. 4(a)–4(d). However, in Phase II, the flow field displays different patterns for different radii ratios as shown in Figs. 4(a)–4(d). When the size of the fluid cylinder is three times that of vapor, two pairs of attached eddies symmetrical about, the x-axis appear as shown in Figs. 4(a) and 4(b). The structure of these eddies does not seem to change as the viscosity ratio is varied. The two pairs reduce to two eddies, one above and the other below the x-axis, when the vapor is either three times the size of the fluid cylinder (that is $b/a=1/3$) as shown in Fig. 4(c) or the two have the same radii (that is $b/a=1$) as shown in Fig. 4(d). It appears that the size of the closed eddies increases with increasing radii ratio.

The asymptotic analysis of the stream function in the continuous phase for larger r yields

$$\psi^{(1)}(r,\theta)\sim-\epsilon\frac{b^2}{c}\left(1+\lambda\left(1-\frac{b^2}{c^2}\right)\right)r\sin\theta+O(r^2) \tag{28}$$

and this indicates that there is a subdominant uniform flow along with the basic extensional flow. As in the other two examples, the speed of the uniform flow in the present case depends on the radii of the cylindrical regions, the distance between the centers, and the viscosity ratio. It is clear from Eq. (28) that this uniform flow

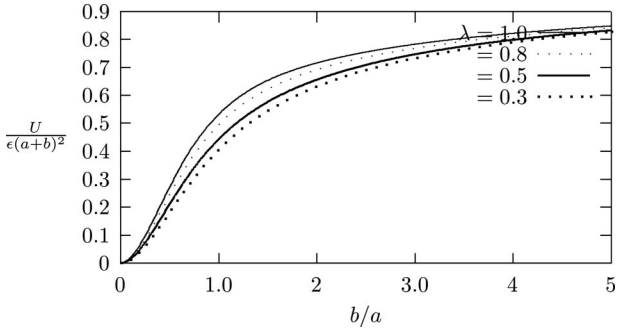

Fig. 5 Uniform flow speed in extensional flow at *O*

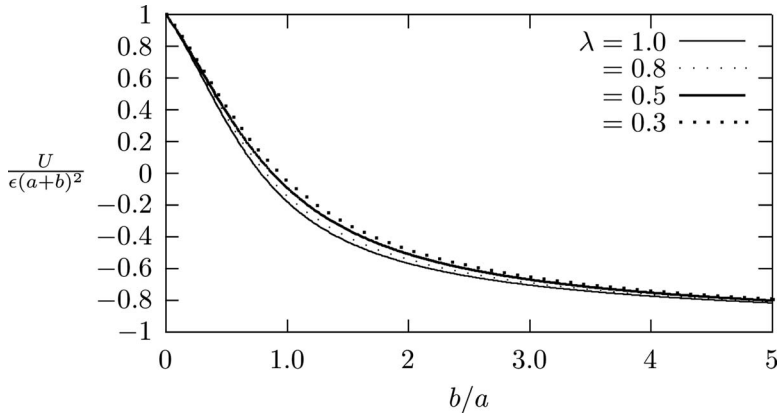

Fig. 6 Uniform flow speed in extensional flow at *D*

vanishes when $b=0$, that is, in the absence of the fluid cylinder c_b. The normalized uniform speed $U/\epsilon(a+b)^2$ is plotted against b/a for different viscosity ratios λ in Fig. 5. It is seen from this figure that the normalized speed increases but little with λ for a fixed radii ratio. It also increase with b/a gradually for a fixed λ and possibly attains a constant value in each case for larger value of the radii ratio.

Extensional Flow at D and the Natural Center for the Drop. The existence of uniform flow is a part of the solution (in all cases) and is due to the asymmetry of the droplet geometry. Though it is subdominant in the examples considered here, it can be used to illustrate the sensitivity of the geometry in nonuniform creeping flows. For the geometry discussed here, it is possible to find the values of the physical parameters for which the uniform flow vanishes (leading to no net force) by moving the origin of the droplet along the x-axis. The origin that makes the net uniform flow zero is the *natural center* of the drop. To illustrate this we compute the stream functions in the two phases for an extensional flow with center at D (Fig. 1). The results of the theoremin Sec. 4.1 are still valid for this case and the computed solutions in the respective phases are as follows:

$$\psi^{(1)}(R,\Theta) = \epsilon\Bigg\{R^2\sin\Theta\cos\Theta - a^2\sin\theta\cos\theta + \frac{a^2}{c}r\sin\theta + \lambda\left(\frac{b^4}{r'^2}\sin\theta'\cos\theta' - 2b^2\sin\theta'\cos\theta' - \frac{b^2}{c}r'\sin\theta'\right)$$
$$-(1-\lambda)(b^2\sin\theta'\cos\theta' + cr'\sin\theta') + \lambda\Bigg[-\frac{b^2}{c}\left(2-\frac{b^2}{c^2}\right)R\sin\Theta + \frac{a^2b^2}{c^2}\left(3\frac{b^2}{c^2}-2\right)\sin\Theta\cos\Theta + \frac{a^4b^4}{c^5}\frac{\sin\Theta}{R}$$
$$+2\frac{a^4b^4}{c^5}\frac{\sin\Theta\cos^2\Theta}{R} + \frac{a^6b^4}{c^6}\frac{\sin\Theta\cos\Theta}{R^2} + \frac{b^2}{c}R\sin\Theta\Bigg] - (1-\lambda)\left(\frac{a^2}{b^2}c^2\sin\Theta\cos\Theta\right)\Bigg\} \tag{29}$$

for the fluid exterior to the droplet, and

$$\psi^{(2)}(R,\Theta) = (1-\lambda)\frac{(r'^2-b^2)}{b^2}\Bigg[\left(1-\frac{a^2}{r^2}\right)r'\cos\theta' - (r'^2 - b^2)\frac{a^2(r'\cos\theta'+c)}{r^4} + \frac{2a^2r'(r'\cos\theta'+c)(r'+c\cos\theta')}{r^4}\Bigg]r'\sin\theta' \tag{30}$$

for the fluid inside the droplet.

The interpretations of the image terms and the flow analysis may be carried out in a similar fashion as explained above. For brevity, we omit these details and provide a discussion of the asymptotic behavior of the flow. For large r, expression (29) yields

$$\psi^{(1)}(R,\Theta) = \epsilon\left[\frac{a^2}{c} - \lambda\left(\frac{b^2}{c} + \frac{b^2}{c}\left(1-\frac{b^2}{c^2}\right)\right) - c(1-\lambda)\right]R\sin\Theta + O(r^2) \tag{31}$$

Here again we see that there is a uniform flow at infinity in the x-direction along with the basic extensional flow. While the speed of this uniform flow depends on the geometrical parameters and the fluid parameters as in the previous cases, the features of this speed are much different from the preceeding examples. To elucidate this, we have plotted the normalized speed $U/\epsilon(a+b)$ (extracted from Eq. (31)) versus b/a for different viscosity ratios in Fig. 6. The comparison of Figs. 5 and 6 shows that the normalized speed in the present case decreases with b/a and λ as well. This behavior is totally different from the normalized speed variation in the extensional flow at O where the speed increased with the radii and viscosity ratios. Furthermore, the speed (of the uniform flow) in the basic extensional flow at D vanishes for the radii ratio b/a close to 1 depending on the viscosity ratio. It is also evident from Eq. (31) that the speed does not vanish if one of the cylinders is absent. This indicates that the natural center of the drop (which

neutralizes the uniform stream) for the extensional flow exists at D for a particular choice of the nondimensional parameters λ and b/a. From Fig. 6 it can be seen that this center does not exist for arbitrary values of the physical parameters, illustrating the sensitiveness of the geometry Γ in $2D$ Stokes flows. Such a natural center for the other flows discussed here (centered shear flow and quadratic flows) may be found in a similar way. These features may play a crucial role in conducting experiments concerning flows involving multiphase 2D droplets.

6 Conclusion

Simple formulas are presented for calculating Stokes flow fields in and around a 2D vapor-liquid compound cylindrical droplet submerged in an arbitrary 2D flow provided that the two cylindrical surfaces intersect orthogonally. Using these analytic formulas, singularity solutions have been found for a variety of primary flows such as centered shear flow, quadratic potential flow, and extensional flows generated at infinity. These singularity form solutions are in ready-to-use form for further calculations. It is shown that the strengths of image singularities (2D Stokes multipoles) depend on dimensionless viscosity ratio and radii. These solutions demonstrate the effectiveness of our method and begin to provide a physical picture of various singularities pertaining to body geometry and flows.

The exact solutions have been used to sketch the streamline patterns in all cases. The streamline plots for centered shear flow show the existence of interior saddle points (hyperbolic points). One might therefore anticipate that the centered shear flow model considered here could exhibit chaos under a time-periodic perturbation. The streamline topologies for quadratic and extensional flows show compartmental divisions representing the flow regions in the continuous phase. Closed eddies are noticed in the dispersed phases for these flows. As shown here, the nondimensional viscosity ratio and the radii ratio of the droplet change the streamline patterns. The far-field analysis leads to a rather surprising conclusion that there is a subdominant uniform flow far away from the droplet in all the flows discussed here. It is shown that the subdominant uniform flow can be eliminated by moving the origin of the droplet along the x-axis. This leads to the existence of the natural center of the drop for a particular choice of the nondimensional parameters. It is noted that if the origin of the primary flow is chosen at a different point inside the 2D compound droplet, other than the natural center, then the features describing the speed of the uniform flow are quite different. This implies that the natural center of the drop is very sensitive to the geometry considered here. The solutions for other complicated 2D flows, including singularity induced flows [6,9,10] in the presence of a multiphase cylindrical droplet, can be found in a similar fashion by the use of our general theorem. In the context of the complex function theory, our solutions in terms of the stream functions provide the imaginary parts of the complex potential for 2D viscous flows. The corresponding solutions in terms of complex potential can also be obtained in the same manner. It should be mentioned that such complex analytic functions will be useful in finding solutions for more complicated geometries via conformal transformation techniques.

Finally, it may be pointed out that the orthogonality condition makes it possible to carry out a detailed analysis of the fluid flows in and around compound droplets. One of the advantages of this assumption is that it allows us to avoid the use of bicylindrical coordinates [26] to construct solutions of these problems, which is very tedious and cumbersome. One would expect that the technique presented here can indeed be applied for the case when the two circular cylinders intersect at a contact angle π/n, n an integer and >2. In such situations (as explained in the Sec. 4.2), the successive reflections will increase with increasing n adding more numbers of terms to the general expressions for the flow fields. However, in the general case of arbitrary contact angles, the problem has to be solved by the use of complex functions in bicylindrical coordinates. It would be certainly interesting to analyze the effect of contact angle on the flow fields and the asymptotic behavior. However, the possibility of solving the problem with arbitrary contact angle in the case of nonuniform flows yet remains to be explored. In electrostatics, the solutions for the electrostatic potentials involving multiphase cylindrical inclusions have connections to the cyclic groups in the abstract algebra [27]. Finding such connections in the viscous flow theory will be of some interest.

Acknowledgment

The author is grateful to one of the reviewers whose criticism led to the present improved version and another reviewer who indicated the natural center notion. He also thanks Professor Al. Boggess (Head) and Dr. N. Sivakumar Department of Mathematics, Texas A&M University, College Station, TX 77843 for their help.

References

[1] Happel, J., and Brenner, H., 1983, *Low Reynolds Number Hydrodynamics*, Matinus Nijhoff, The Hague.

[2] Kim, S., and Karrila, S. J., 1991, *Microhydrodynamics: Principles and Selected Applications*, Butterwort-Heinemann, Boston, MA.

[3] Pozrikidis, C., 1992, *Boundary Integral and Singularity Methods for Linearized Viscous Flow*, Cambridge University Press, Cambridge.

[4] Jana, S. C., Metcalfe, G., and Ottino, J. M., 1994, "Experimental and Computational Studies of Mixing in Complex Stokes Flows: The Vortex Mixing Flow and Multicellular Cavity Flows," J. Fluid Mech., **269**, pp. 199–246.

[5] Meleshko, V. V., and Aref, H., 1996, "A Blinking Rotlet Model for Chaotic Advection," Phys. Fluids, **8**, pp. 3215–3217.

[6] Dorrepaal, J. M., O'Neill, M. E., and Ranger, K. B., 1984, "Two-Dimensional Stokes Flows With Cylinders and Line Singularities," Mathematika, **31**, pp. 65–75.

[7] Ranger, K. B., 1980, "Eddies in Two-Dimensional Stokes Flow," Int. J. Eng. Sci., **18**, pp. 181–190.

[8] Jeffery, G. B., 1922, "The Rotation of two Circular Cylinders in a Viscous Fluid," Proc. R. Soc. London, Ser. A, **101**, p. 169.

[9] Smith, S. H., 1990, "Some Limitations of Two-Dimensional Unbounded Stokes Flow," Phys. Fluids A, **2**, pp. 1724–1730.

[10] Daripa, P., and Palaniappan, D., 2001, "Singularity Induced Exterior and Interior Stokes Flows," Phys. Fluids, **13**, pp. 3134–3154.

[11] Evans, E., and Needham, D., 1988, "Attraction Between Lipid Bilayer Membranes in Concentrated Solutions of Non-Adsorbing Polymers: Comparison of Mean-Field Theory With Measurements of Adhesion Energy," Macromolecules, **21**, pp. 1822–1831.

[12] Evans, E., Klingenberg, D. J., Rawicz, W., and Szoka, F., 1996, "Interactions Between Polymer-Grafted Membranes in Concentrated Solutions of Free Polymer," Langmuir, **12**, pp. 3031–3037.

[13] Johnson, R. E., and Sadhal, S. S., 1985, "Fluid Mechanics of Compound Multiphase Drops and Bubbles," Annu. Rev. Fluid Mech., **17**, pp. 289–320.

[14] Sadhal, S. S., Ayyaswamy, P. S., and Chung, J. N., 1997, *Transport Phenomena With Drops and Bubbles*, Springer-Verlag, New York.

[15] Zimmermann, U., and Vienken, J., 1982, "Electric Field-Induced Cell-to-Cell Fusion," J. Membr. Biol., **67**, pp. 165–182.

[16] Gaver, D. P., and Kute, S. M., 1998, "A Theoretical Model Study of the Influence of Fluid Stresses on a Cell Adhering to a Microchannel Wall," Biophys. J., **75**, pp. 721–733.

[17] Huh, C., and Scriven, L. E., 1971, "Hydrodynamic Model of Steady Movement of a Solid/Liquid/Fluid Contact Line," J. Colloid Interface Sci., **35**, pp. 85–101.

[18] Dussan, V. E. B., and Davis, S. H., 1974, "Motion of a Fluid-Fluid Interface Along a Solid-Surface," J. Fluid Mech., **65**, pp. 71–95.

[19] O'Neill, M. E., Ranger, K. B., and Brenner, H., 1986, "Slip at the Surface of a Translating-Rotating Sphere Bisected by a Free Surface Bounding a Semi-Infinite Viscous Fluid: Removal of the Contact-Line Singularity," Phys. Fluids, **29**(4), pp. 913–924.

[20] Palaniappan, D., and Kim, S., 1997, "Analytic Solutions for Stokes Flow Past a Partially Encapsulated Droplet," Phys. Fluids, **9**(5), pp. 1218–1221.

[21] Aderogba, K., 1976, "The Circulation Produced Within Embedded Liquid Drops," Int. J. Eng. Sci., **14**, pp. 39–48.

[22] Lorentz, H. A., 1896, "A General Theorem Concerning the Motion of a Viscous Fluid and a Few Consequences Derived From It," Verst. kon. Akad. Wet. Ams., **5**, pp. 168–175.

[23] Sen, S. K., 1989, "Circle Theorems for Steady Stokes Flows," ZAMP, **40**, pp. 139–146.
[24] Palaniappan, D., 2004, "Centered Shear Flow Past a Partially Encapsulated Two-Dimensional Droplet," Physica A, **332**, pp. 79–88.
[25] Hackborn, W. W., 1993, "On a Class of Stokes Flows Inside a Corrugated Boundary," Q. Appl. Math., **1**, pp. 329–341.
[26] Radchik, A. V., Paley, A. V., Smith, G. B., and Vagov, A. V., 1994, "Polarization and Resonant Absorption in Intersecting Cylinders and Spheres," J. Appl. Phys., **76**, pp. 4827–4835.
[27] Palaniappan, D., 2005, "Classical Image Treatment of a Geometry Composed of a Circular Conductor Partially Merged in a Dielectric Cylinder and Related Problems in Electrostatics," J. Phys. A, **38**, pp. 6253–6269.

Particle Deposition Onto Rough Surfaces

Giovanni Lo Iacono[1]
e-mail: giovanni.loiacono@bbsrc.ac.uk

Andy M. Reynolds

Rothamsted Research,
Harpenden, Hertfordshire AL5 2JQ, UK

Paul G. Tucker
Whittle Laboratory,
University of Cambridge,
Cambridge CB3 0DY, UK

*Predictions for the number of particles depositing from fully developed turbulence onto a fully roughened k-type surface are obtained from the results of large-eddy simulations for a ribbed-channel flow. Simulation data are found to provide only partial support for the "mass-sink hypothesis," i.e., the notion that all particles entering a mass sink, a volume of fluid extending vertically from the deposition surface, are captured and eventually deposited. The equality of the number of particles entering the mass sink and the number of particles depositing is attained, and a qualitative agreement with the empirical model of Wood (1981, "A Simple Method for the Calculation of Turbulent Deposition to Smooth and Rough Surfaces," J. Aerosol Sci., **12**(3), pp. 275–290) for the height of this mass sink is obtained. However, a significant proportion of particles escapes from the mass sink and the equality of numbers is attained only because many particles deposit onto rib surfaces above the mass sink, without first entering the mass sink.* [DOI: 10.1115/1.2948359]

Keywords: large-eddy simulation, roughness, turbulence deposition, mass sink

1 Introduction

The deposition of particles from turbulent flows onto adjacent flow boundaries is of great interest in many industrial processes. Extensive data on particle deposition onto rough surfaces (see, [1,2] and references therein), have revealed that particle deposition is much greater on roughened surfaces than on smooth surfaces.

The impact of surface roughness upon deposition is, however, far from understood and is usually treated in an ad hoc or semi-empirical manner by invoking the notion of a mass sink; a volume of fluid extending across the entire flow domain in the spanwise and streamwise directions and extending vertically from the deposition surface to a height Σ (mass-sink height). According to the mass-sink hypothesis, all particles transported into mass sink will be captured and deposited. The mass-sink hypothesis was first advocated by Friedlander and Johnstone in 1957 (for an exhaustive review see Ref. [1]) for deposition onto smooth walls. The hypothesis was subsequently applied to rough walls [3].

The aim of the present study is to test the mass-sink hypothesis. Attention is focused on particles in the inertial-moderated regime depositing onto a fully roughened k-type surface (see Refs. [4–7] for an introduction on this classification), consisting of regularly spaced ribs of height h^+ and spacing $w^+=10h^+$ that protrude above the viscous sublayer. Here and throughout, the superscript + denotes quantities rendered nondimensional by the kinematic viscosity ν and the friction velocity u_*. Particles in the inertial-moderated regime can acquire sufficient momentum in the bulk flow to carry them directly through the viscous sublayer. The trajectories of independent, identical particles were simulated by utilizing the results of large-eddy simulations (LESs) to integrate the particle equation of motion under the assumption of one-way coupling [8].

2 Numerical Simulations

2.1 Methodology. In the simplest of the models for the height of the mass sink, the roughened surface is represented by a smooth surface located at a height Δ^+, which depends on the size of the particle and on the geometry of the rough surface. The mass sink Σ^+ is assumed to be equal to this height Δ^+. More elaborate expressions such as $\Sigma^+=\Delta^++S^+$ incorporate the characteristic particle-stopping distance S^+, i.e., the average distance traversed by a particle after being disentangled from the turbulence upon arrival in the near-wall region. Wood [3] suggested that $S^+=0.69\tau_p^+$, where τ_p^+ is the particle aerodynamic response time and $\Delta^+=(d_p^+/2)+\bar{k}^+-e^+$, where d_p^+ is the diameter of the particle and $\bar{k}^+$ and σ_k^+ are the mean and the standard deviation of the heights of the roughness elements. Many alternative expressions for S^+ and Δ^+ have been advocated in literature (see [1] and references therein).

The mass-sink hypothesis has been tested by determining that particular distance Σ^+ from the rough wall at which the number of particles that have reached this distance equals the number of particles that actually deposit. The way the height Σ^+ is estimated is illustrated in Fig. 1.

2.2 Flow Field. The geometry of the ribbed channel is described in Refs. [9,10]; the computational, numerical, and geometric parameters are given in Tables 1 and 2. The geometry and boundary conditions for the LES of the turbulent flow have been chosen to mirror the experiment of Acharya et al. [11]. Numerical details can be found in Ref. [9]. The numerical grid is modest but refinement tests show that it well captures the major second-order statistics for reasons discussed in Ref. [10]. The instantaneous flow exhibits coherent structures similar to those observed in previous works [9,10] and therefore not shown. Simulation data of the streamwise and wall-normal mean velocities and of the Reynolds stresses are comparable with the predictions obtained previously in Refs. [9,10]. Predicted mean flows are also in close agreement with the experiment (Fig. 2).

2.3 Particulate Phase. The trajectories of independent spherical rigid particles of mass m_p are simulated by numerically integrating the equations of motion for particles in a turbulent flow (Refs. [9,12,13], Table 2). The governing forces are drag, gravity, and Saffman lift (whose effect on particle deposition might be significant in a high shear region like the viscous sublayer [12]). Underlying this approach is the assumption that the unresolved subgrid scales of motion are of secondary importance in determining the particle motions. Of greater importance are the resolved scales of motion with typical turbulent time scales greater than the aerodynamic response time of the particle τ_p^+. Particles were released from the midheight of the channel and tracked until they either reached a solid surface whereupon they were assumed to deposit or until they exited the computational domain (Fig. 1).

[1]Corresponding author.

Contributed by the Fluids Engineering Division of ASME for publication in the JOURNAL OF FLUIDS ENGINEERING. Manuscript received January 15, 2007; final manuscript received April 2, 2008; published online June 25, 2008. Assoc. Editor: Ye Zhou.

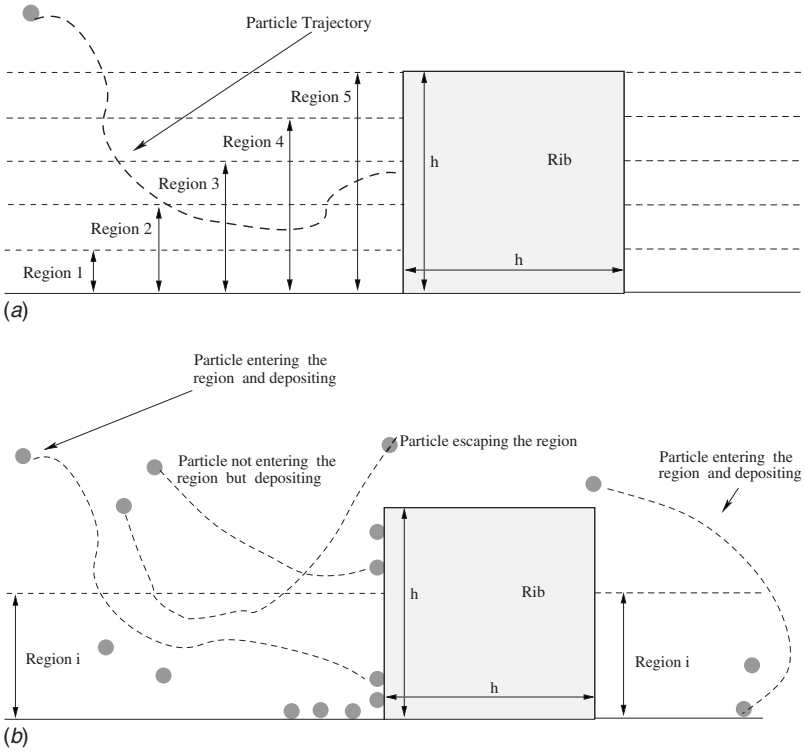

Fig. 1 (*a*) **To estimate the height Σ^+, above the ribbed surface, six different regions limited by the wall itself and by (*x-z*) planes parallel to the wall have been identified. Region 1 coincides with the region when the LES modeled stress tensor is reduced to, it extends from $y^+/h^+=0$ to $y^+/h^+=0.1$, regions 2, 3, 4, 5, and 6 extend from $y^+/h^+=0$ to $y^+/h^+=0.2,0.4,0.6,0.8,1.0$, respectively.** (*b*) **Particles can move away to the central area of the channel; they can deposit onto the walls or onto any face of the rib. At any time *t*, we counted: the number of particles that have entered (but not deposited) a certain region *i*, $N_i^{\text{ent}}(t)$; the number of particles that have escaped the region *i*, N_i^{esc}, the number of particles that have reentered (but not deposited) the region *i*, N_i^R; the number of particles that, being in a region *i*, directly have deposited onto the left face of the rib D_i^L, the right face of the rib D_i^R, and the top face of the rib D^T (of course, those particles can come only from the central region of the channel, above the rib); the number of particles that have deposited on the bottom wall D_b (inevitably, they deposit directly from region 1); the total number of particles that have deposited onto the rough wall $D_i^w=D_i^L+D_i^R+D^T+D_b$; the number of particles that, being outside the region *i*, still have deposited onto the left face of the rib $D_i^{L\ \text{out}}$, the right face of the rib $D_i^{R\ \text{out}}$, the top face of the rib $D^{T\ \text{out}}$, and the total number of particles $D_i^{w\ \text{out}}=D_i^{L\ \text{out}}+D_i^{R\ \text{out}}+D^{T\ \text{out}}$, the total number of particles that have reached the Region *i* regardless of their final condition, i.e., deposited, escaped, reentered, etc. $N_i=N_i^{\text{ent}}(t)+N_i^R+N_i^{\text{esc}}+D_i^w$. Then, from N_i and $D_i^w+D_i^{w\ \text{out}}$ we extrapolated the value of Σ^+ that satisfies $N(\Sigma^+)=D^w(\Sigma^+)+D^{w\ \text{out}}(\Sigma^+)$, i.e., when the total number of particles $N(\Sigma^+)$ that have reached a region of height Σ^+ is equal to the total number of particles that have deposited. This height was defined as mass sink.**

3 Testing the Mass-Sink Hypothesis

Number of particles, N_i and D_i^w, entering and depositing in the six regions, i (see Fig. 1 for the definition of the symbols) was constantly monitored, and equilibrium values of $R_i=D_i^w/N_i(t)$ were determined for particles with $\tau_p^+=29.2$, $d_p^+=0.23$ and $\tau_p^+=610$, $d_p^+=1.04$; in both cases $\rho_p^+/\rho^+=833$ (Figs. 3–7). The fractions $(D_i^{w\ \text{out}}+D_i^w)/N_i$ (7) serve to estimate the height of the mass sink, as illustrated in Fig. 1. The fractions $(D_i^{w\ \text{out}}+D_i^w)/N_i$ can be greater than 1 because it is divided not by the total number of particles that deposit but by the number of particles present in the region. Therefore it includes particles outside the regions $i(D_i^{w\ \text{out}})$, but still depositing on the faces of the rib. This choice is necessary in order to be compatible with the definition of the mass sink. These data were interpolated by a power law curve of the form $N_{\text{dep}}=A+b(y^+/h^+)^c$, where A, b, and c are constants. Both interpolations result in a correlation coefficient $R_{\text{corr}}=0.999$. By fitting these data it can be inferred that this number is equal to unity when $y^+/h^+=0.93$ for $\tau_p^+=610$ and when $y^+/h^+=0.026$ for $\tau_p^+=29.2$. These heights define a mass sink. The predicted heights of the mass sink increase with the particle response time in qualitative agreement with the model present in literature, but the results are different from the predictions $\Sigma^+/h^+=1.16$ and $\Sigma^+/h^+=0.1$ from the model of Wood [3] and other alternative models [1] (and reference therein). This indicates that the height of the mass sink is largely determined by the particle-stopping distance. Despite this, the notion of mass sink should not be taken too literally because an equality of the number of particles entering the mass

Table 1 Parameters used in the Computations

Flow and geometric parameters	Value in physical units: (m),(s)	Value in wall units
Dimension of the square rib h	6.35×10^{-3}	245
Channel width L_y	$0.07=11h$	2698
Streamwise dimension L_x	0.127	4250
Spanwise dimension L_z	0.06	2313
Pitch ratio w	20	
Mean roughness height $\bar{k}$	$\frac{1}{20}h$	12.24
Height standard deviation σ_k	$\sqrt{(19+19^2)/20^3}h$	53.35
Virtual origin e	$5\times10^{-3}h$	1
Roughness function ΔU	16.3	
Reynolds number	7000	
Number of grid points	$121\times112\times33$	
Time step	2.5×10^{-5}	0.6
Particle parameters for $\tau_p^+=29.2$	Value	
Diameter d_p^+	0.23	
Density ratio $\rho_p^+/\rho^+=833$		
Mass-sink distance $(d_p^+/2)+\bar{k}^+ +\sigma_k^+ -e^+$	$64.7=0.26h^+$	
Mass-sink distance $(d_p^+/2)+\bar{k}^+ -e^+$	$11.35=0.05h^+$	
Stopping distance S^+	$20.15=0.08h^+$	
Wood's capture distance Σ^+	$31.05=0.13h^+$	
Particle parameters for $\tau_p^+=610$	Value	
Diameter d_p^+	1.04	
Density ratio $\rho_p^+/\rho^+=833$		
Mass-sink distance $(d_p^+/2)+\bar{k}^+ +\sigma_k^+ -e^+$	$65.07=0.27h^+$	
Mass-sink distance $(d_p^+/2)+\bar{k}^+ -e^+$	$11.72=0.05h^+$	
Stopping distance S^+	$421=1.72h^+$	
Wood's capture distance Σ^+	$432.7=1.77h^+$	

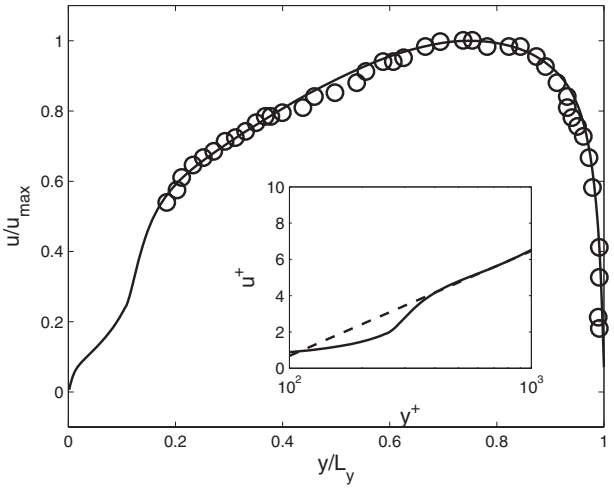

Fig. 2 Averaged streamwise velocity profile along the spanwise (z) and the streamwise (x) direction and in the time interval $t^+-t_0^+=3500$. The velocity and position are normalized, respectively, by the maximum velocity u_{max} and by the channel width L_y. (○) experiment of Hanjalic and Launder [14] (pitch ratio 10), – current LES. The predicted mass flow for $y/L_y \lesssim 0.2$ is necessarily consistent with experiments, despite the absence of measurements for this region. It is found that (not shown here) the velocity exhibits a clear logarithmic profile in the region $y/h \gtrsim 1.5$, where the normal direction is divided by the rib height h [14]. The friction velocity u_* is determined by fitting the current LES according to the same parametrization of Hanjalic and Launder [14], which results in $u_*=0.5950$, $e^+ \sim 1$, $h^+=245$. The inset shows the velocity profile plotted in universal coordinates compared with the modified "law of the wall" for rough surfaces (dashed line) $u^+(y^+)=1/\kappa \log(y^+-e^+)+C-\Delta u^+$. The value of Δu^+ is in agreement with the prediction of Perry et al. [5] that $\Delta u^+=\kappa^{-1}\ln h^+ +2.2=15.3$ (for large w^+) and with other values found in literature (see e.g., Refs. [15,16]). This corresponds to a fully rough regime with equivalent sand grain roughness k_{seq}^+ of the order of $O(3)$ [17].

Table 2 Numerical scheme implemented

Subgrid scale model	Model of Yoshizawa [18] and near the wall ($y^+/h^+<0.1$) length scales derived from Reynolds-average Navier–Stokes (RANS) equations [19].
Boundary conditions treatment	Periodicity in the streamwise and spanwise directions. If a particle leaves the computational domain at one side (in x or z direction), it is reintroduced at the corresponding point on the opposite face of the flow domain. Particles that deposit are not replaced.
Initial conditions	The simulation started from a laminar initial condition developing a natural transition to turbulence due to the disturbance caused by the rib. The LESs were run for a time $t_0^+ \sim 400\tau_f^+$, where $\tau_f^+=h^+/u_{tr}^+$ is the time scale associated with the corner recirculation immediately downwind of the rib and u_{tr}^+ is the mean streamwise flow velocity at the top of the recirculation. 8500 particles were released into the mature LES flow from random locations on the wall-parallel plane (x-z) in the center of the channel (i.e., $y^+/h^+=5.5$). This corresponds to an initial volume particle fraction of order $O(-6)$ and makes appropriate the adoption of a one-way coupling strategy ([8] and references therein). Particle velocities were initialized to the local, instantaneous fluid velocities.
Numerical resolution	A nonuniform containing grid is used. The spacing between consecutive points in the x-, y-, and z-directions ($5 \lesssim \Delta_x^+ \lesssim 70$, $5 \lesssim \Delta_y^+ \lesssim 50$, and $\Delta_z^+ \sim 60$) did not give good spanwise resolution but grid independence studies [10] show that the current grid is sufficient.
Condition for deposition	A particle is assumed to be deposited and remains so at subsequent times, when its center of mass is located at a distance from the wall, less than or equal to the particle-radius.

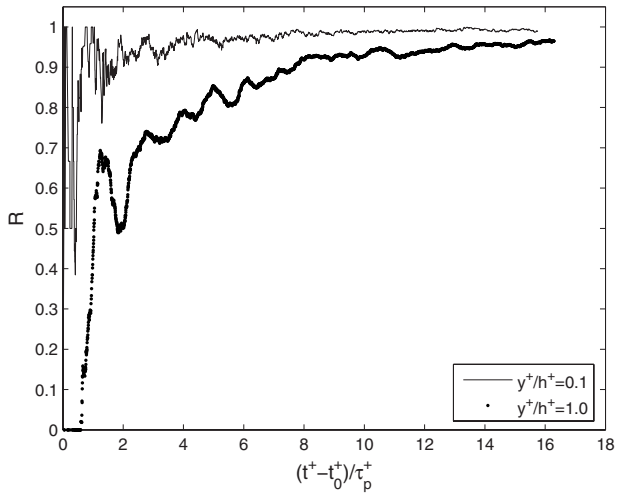

Fig. 3 Ratios $R_i=D_i^w/N_i(t)$ of deposited particles ($\tau_p^+=610$) over particles present in the regions identified by levels $y^+/h^+=0.1$ and $y^+/h^+=1.0$. Similar profiles have been observed for different regions and for $\tau_p^+=29.2$. Particles are released at the horizontal central plane of the channel, then they will enter the six regions shown in Fig. 1 and deposit. An equilibrium phase occurs when the flux of depositing particles is proportional to the flux of particles entering the said region and the trend of R_i is roughly constant. Statistics are extracted upon establishment of constant particle fluxes.

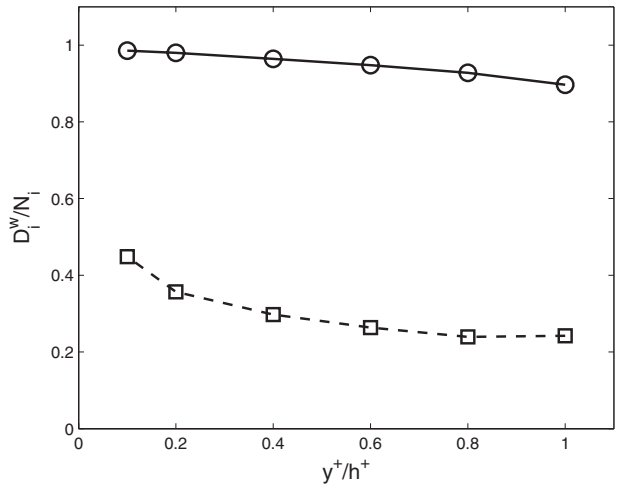

Fig. 4 Fraction of depositing particles within a region. ○ refers to $\tau_p^+=610$. □ refers to $\tau_p^+=29.2$. Same nomenclature as in Fig. 1.

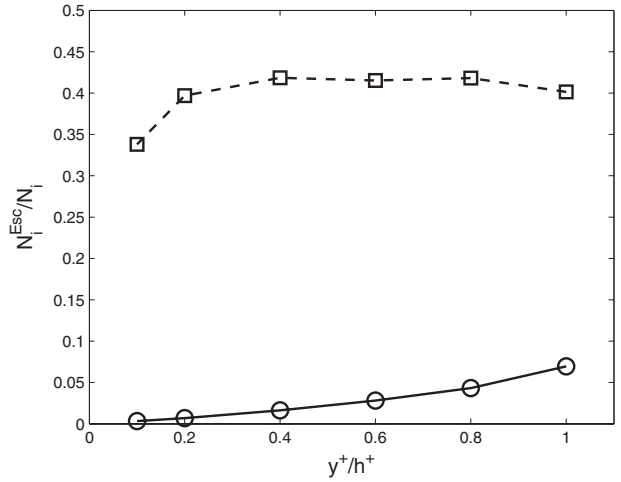

Fig. 5 Fraction of escaping particles from a region. ○ refers to $\tau_p^+=610$. □ refers to $\tau_p^+=29.2$. Same nomenclature as in Fig. 1.

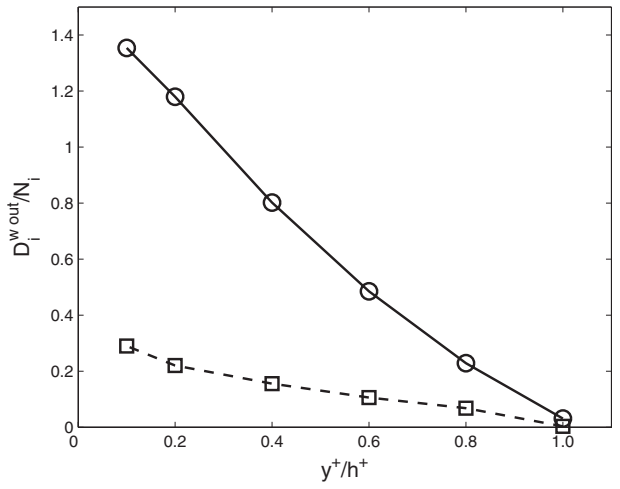

Fig. 6 Fraction of particles depositing on the portion of rib wall outside a region. ○ refers to $\tau_p^+=610$. □ refers to $\tau_p^+=29.2$. Same nomenclature as in Fig. 1.

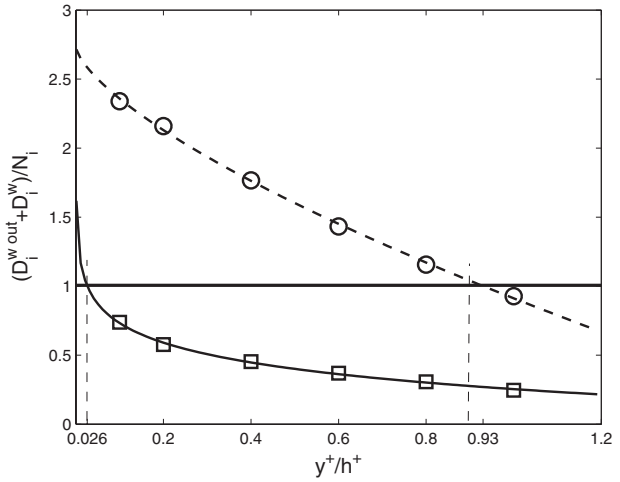

Fig. 7 The total number of particles depositing onto the rough wall. ○ refers to $\tau_p^+=610$. □ refers to $\tau_p^+=29.2$. Same nomenclature as in Fig. 1.

sink and the number of particles depositing does not necessarily arise because all the particles within the mass sink are eventually deposited. It arises because significant numbers of particles are deposited on the surfaces above the height of the mass sink. This supports the employment of the mass-sink hypothesis as a useful guide in engineering practice. This is not a trivial observation because the mass-sink hypothesis was shown not to capture the microphysics of the interaction of the particles with the roughness element.

Acknowledgment

This work was funded by BBSRC through Grant No. 204/D13549. We would like to thank Dr. Yan Liu for helping set up the ribbed-channel LES and IBM for deep computing access.

References

[1] Sippola, M. R., and Nazaroff, W. W., 2002, "Particle Deposition From Turbulent Flow: Review of Published Research and Its Applicability to Ventilation Ducts in Commercial Buildings," Lawrence Berkeley National Laboratory, Technical Report No. LBNL-51432.

[2] Chamberlain, A. C., Garland, J. A., and Wells, A. C., 1984, "Transport of Gases and Particles to Surfaces With Widely Spaced Roughness Element," Boundary-Layer Meteorol., **29**, pp. 343–360.

[3] Wood, N. B., 1981, "A Simple Method for the Calculation of Turbulent Deposition to Smooth and Rough Surfaces," J. Aerosol Sci., **12**(3), pp. 275–290.
[4] Schlichting, H., and Gersten, K., 2000, *Boundary-Layer Theory*, Springer, London.
[5] Perry, A. E., Schofield, W. H., and Joubert, P. N., 1969, "Rough Wall Turbulent Boundary Layers," J. Fluid Mech., **37**(2), pp. 383–413.
[6] Grass, A., 1971, "Structural Features of Turbulent Flow Over Smooth and Rough Boundaries," J. Fluid Mech., **50**, pp. 233–255.
[7] Tani, I., 1987, "Turbulent Boundary Layer Development Over Rough Surfaces," in *Perspectives in Turbulence Studies*, H. U. Meier and P. Bradshaw, eds., Springer, Gottingen, p. 223.
[8] Sommerfeld, M., 2000, "Overview and Fundamentals," in *Theoretical and Experimental Modeling of Particulate Flow* (Lecture Series 2000–2006), J. M. Buchlin, ed., Von Karman Institute for Fluid Dynamics (VKI), Bruxelles, Belgium, pp. 1–62.
[9] Lo Iacono, G., Tucker, P. G., and Reynolds, A. M., 2005, "Predictions for Particle Deposition From LES of Ribbed Channel Flow," Int. J. Heat Fluid Flow, **26**, pp. 557–568.
[10] Liu, Y., Tucker, P. G., and Lo Iacono, G., 2006, "Comparison of Zonal RANS and LES for a Non-Isothermal Ribbed Channel Flow," Int. J. Heat Fluid Flow, **27**(31), pp. 391–401.
[11] Acharya, S., Dutta, S., Myrum, T. A., and Baker, R. S., 1993, "Periodically Developed Flow and Heat Transfer in a Ribbed Duct," Int. J. Heat Mass Transfer, **36**(8), pp. 2069–2082.
[12] McLaughlin, J. B., 1989, "Aerosol Particle Deposition in Numerically Simulated Channel Flow," Phys. Fluids A, **1**(7), pp. 1211–1224.
[13] Lo Iacono, G., 2003, "Numerical Study of Particle Motion in a Turbulent Ribbed Duct Flow," Ph.D. thesis, University of Warwick, Coventry, UK.
[14] Hanjalic, K., and Launder, B. E., 1972, "Fully Developed Asymmetric Flow in a Plane Channel," J. Fluid Mech., **51**(1), pp. 301–335.
[15] Cui, J., Patel, V. C., and Lin, C. L., 2003, "Large-Eddy Simulation of Turbulent Flow in a Channel With Rib Roughness," Int. J. Heat Fluid Flow, **24**(3), pp. 372–388.
[16] Leonardi, S., Tessicini, F., Orlandi, P., and Antonia, R. A., 2004, "Direct and Large Eddy Simulation of a Turbulent Channel Flow With Roughness on One Wall," in *Proceedings of the 15th Australasian Fluid Mechanics Conference*, The University of Sydney.
[17] Cebeci, T., and Bradshaw, P., 1977, *Momentum Transfer in Boundary Layers*, Hemisphere, Washington, DC.
[18] Yoshizawa, A., 1993, "Bridging Between Eddy-Viscosity-Type and Second-Order Turbulence Models Through a Two-Scale Turbulence Theory," Phys. Rev. E, **48**, pp. 273–281.
[19] Tucker, P. G., and Davidson, L., 2004, "Zonal k-l Based Large Eddy Simulations," Comput. Fluids, **33**, pp. 267–287.

Understanding the Boundary Stencil Effects on the Adjacent Field Resolution in Compact Finite Differences

Stephen A. Jordan
Naval Undersea Warfare Center,
Newport, RI 02842
e-mail: jordansa@npt.nuwc.navy.mil

When establishing the spatial resolution character of a composite compact finite differencing template for high-order field solutions, the stencils selected at nonperiodic boundaries are commonly treated independent of the interior scheme. This position quantifies a false influence of the boundary scheme on the resultant interior dispersive and dissipative consequences of the compound template. Of the three ingredients inherent in the composite template, only its numerical accuracy and global stability have been properly treated in a coupled fashion. Herein, we present a companion means for quantifying the resultant spatial resolution properties that lead to improved predictions of the salient problem physics. Compact boundary stencils with free parameters to minimize the field dispersion (or phase error) and dissipation are included in the procedure. Application of the coupled templates for resolving the viscous Burgers wave and two-dimensional acoustic scattering reveal significant differences in the predictive error.
[DOI: 10.1115/1.2948366]

Introduction

Over the past decade, the advanced developments in compact finite differencing for high resolution of complex physics have produced an extensive array of field and boundary schemes. Commonly, this variety appears more often than the traditional explicit schemes. Compact finite differencing owns many attractive properties that are especially well suited for advanced methodologies such as direct numerical simulations (DNSs) and large-eddy simulations (LESs). Unlike the explicit schemes, their stencils can quickly approach spectral-like resolution while simultaneously supplying high-order approximations of difficult boundary conditions. This capability is especially beneficial for efficiently resolving the smaller spatial scales near nonperiodic boundaries. However, before coupling a compact boundary stencil with a similar interior scheme, one should quantify its detrimental effects on the field accuracy, stability, and resolution.

Fourier analysis is the common method for measuring the spatial resolution of the finite differencing approximations. The real and imaginary pairs of the modified wavenumbers quantify the dispersive and dissipative characteristics of the stencil. Without question, Lele [1] enhanced our understanding by applying Fourier treatment to compact finite differencing with one-sided stencils included in his analysis at the nonperiodic boundaries. Carpenter et al. [2] also examined global stability as well as field accuracy of both the fourth- and sixth-order Pade stencils as coupled with a broad mixture of compact definitions at the boundary and first field points (sixth-order only).

We emphasize herein that the spatial resolution and accuracy of differencing schemes are distinctly different characteristics in a sense that two stencils can own equivalent accuracy (as given by their truncation error), but actually resolve the salient physics quite differently. In some instances, one can argue that the wave number resolution holds a more important role in a DNS (or LES) computation than the spatial accuracy. Periodic end conditions formally preserve the attributes of temporal stability as well as spatial accuracy and resolution by studying only the interior stencil from either a local or global perspective. However, the properties of the interior stencil can quickly degrade near nonperiodic boundaries. Certain one-sided stencils for the boundary derivatives (as well as those near boundary points for very high field accuracy) will affect both the accuracy and stability of the adjacent field template. Their own specific properties will propagate far into the adjacent field. Presently, no formal procedure is available for measuring the true spatial resolution error in wave number space when dealing with nonperiodic boundaries.

Thus, the present paper centers on quantifying the influence of the compact boundary stencil on the adjacent interior spatial resolution error. Specifically, we will see a significant degradation of the dispersive and dissipative errors in the coupled template near the boundary as compared to evaluating each stencil separately. These errors are separate and apart from the formal spatial accuracy of the template in a sense that the contributing stencils can own similar truncation errors, but resolve the spatial scales quite differently. One should note that the present procedure culminates the recommended testing (accuracy, stability, and resolution) to gain a thorough understanding of the prevailing properties of their particular composite compact template before beginning the computation.

Compact Finite Differencing

Compact finite differencing is now widely recognized as a viable option towards improved spatial resolution and/or higher accuracy over traditional explicit schemes. Whereas explicit methods gain both resolution and accuracy through Taylor series expansions of neighboring variables, compact differencing carries both the neighboring quantities as well as their respective derivatives. Theoretically, the compact stencils increase the spatial accuracy by two orders over their companion explicit scheme. Quantifying improvement of their spatial resolution error is given by their comparative modified wave numbers.

Central and Upwind Interior Stencils. Central schemes difference the neighboring quantities and their derivatives symmetrically about the point of interest. They can be successfully applied throughout domains having periodic boundary conditions as well as interior nodes that are sufficiently away from nonperiodic boundaries to complete the explicit side of the stencil. A brief illustration of compact differencing is the tridiagonal system for approximating the derivative q' at the discrete ith point up to eighth-order accuracy that appears as

$$aq'_{i+1} + bq'_i + cq'_{i-1} = \beta(q_{i+1} - bq_{i-1}) + \gamma(q_{i+2} - q_{i-2}) + \alpha(q_{i+3} - q_{i-3}) \quad (1)$$

where the variable q must be known at neighboring points $i \pm 1$, $i \pm 2$, and $i \pm 3$ throughout the domain to reach fourth-, sixth-, and eighth-order accuracies, respectively.

Unlike the central schemes, the explicit side of an upwind compact stencil is asymmetric about the ith point of interest. Similar to the explicit upwind forms, their differencing direction promotes numerical stability by switching (if necessary) to the local flow path. Near nonperiodic boundaries, they are often an order lower in formal spatial accuracy than a compact central scheme to accommodate their larger biased stencil. An example of a compact upwind stencil up to seventh-order accuracy appears as

$$aq'_{i+1} + bq'_i + cq'_{i-1} = \eta q_{i+2} + \xi q_{i+1} + \lambda q_i + \alpha q_{i-1} + \gamma q_{i-2} + \beta q_{i-3} \quad (2)$$

Contributed by the Fluids Engineering Division of ASME for publication in the JOURNAL OF FLUIDS ENGINEERING. Manuscript received May 31, 2007; final manuscript received April 5, 2008; published online June 25, 2008. Assoc. Editor: Rajat Mittal.

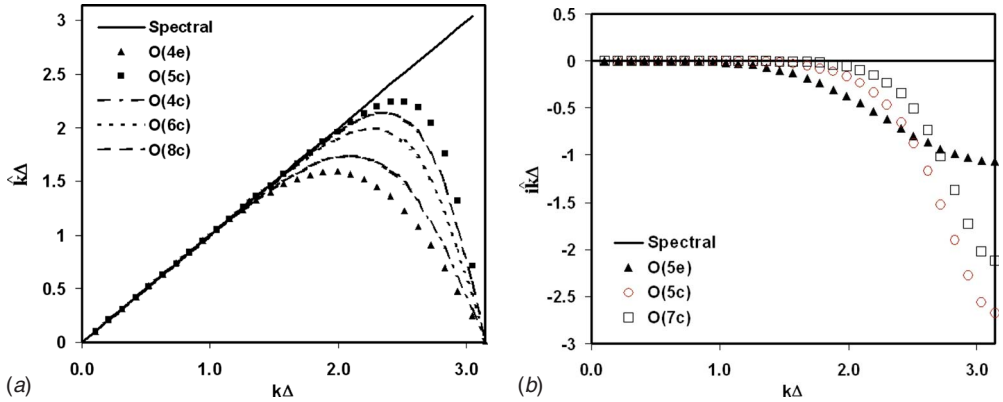

Fig. 1 Spatial resolution errors of the explicit (4e and 5e) and several compact finite difference schemes; 4–8 denotes formal order

Comparisons are shown in Fig. 1 among the dispersion properties of the fourth-order (dispersion only) and fifth-order (dissipation only) explicit schemes against several compact stencils. While the explicit scheme (4e) achieves 90% or better spatial resolution over only about 1/2 of the resolvable scales, the comparative Pade stencil (4c) resolves 59% $[e(\delta_{90}) \leq 0.59]$. When differencing the same number of discrete points as the explicit scheme, the compact stencil increases to sixth order with 70% of the resolvable waves holding 90% or better efficiency. The fifth-order upwind stencil (5c) displays a desirable improvement in dispersive error over higher-order central compact forms. For example, the 8c scheme supplies 90% or better efficiency over 75% of the resolvable waves, which is slightly less than the resolving efficiency of the 5c stencil. This latter stencil provides at least 90% efficiency over 78% of the resolvable waves, which compares to only 54% by the explicit form of the same order. One can readily see that these stencils appear spectral-like as given by their superior resolution efficiencies over a broadband of resolvable wave numbers.

However, a well-understood drawback of upwind differencing is their inherent numerical dissipation. This fact carries into their compact forms as illustrated by the spatial distributions in Fig. 1(*b*) of the imaginary component of the modified wave number. At the higher resolvable scales, the numerical dissipation of the compact upwind stencils far exceeds that imposed by their explicit forms. High levels of numerical dissipation are certainly an undesirable property in a computation because their effect can completely overshadow the lower dispersive error in regions of coarse grid spacing.

Boundary Formulations. Boundary stencils are necessary when approximating derivatives in directions that end with nonperiodic boundaries. The compact variety are always one sided (no fictitious points) and they should be no more than one order lower than the field scheme to preserve the respective formal spatial accuracy. An example of a one-sided compact expression up to fourth-order accuracy is given by

$$aq_2' + bq_1' = \eta q_4 + \alpha q_3 + \gamma q_2 + \beta q_1 \tag{3}$$

where the first point lies on the boundary. However, unlike previous analyses, quantifying the local dispersive and dissipative errors of this stencil is futile because their distributions in wave number space are strongly influenced by the adjacent interior scheme and vice versa.

Lele [1] introduced an idea for minimizing the dispersive and dissipative errors of the compact boundary stencil by extending the right hand side of Eq. (3) further into the field with its formal order unchanged. The new coefficients became free parameters that were subsequently constrained to reach a desired result. Although Lele limited his examples to only two-parameter (second-order) families with each carrying constraints, his procedure is essentially limitless. The fourth-order family holding two free parameters (a, η) appears as

$$aq_2' + bq_1' = \eta q_6 + \xi q_5 + \lambda q_4 + \alpha q_3 + \gamma q_2 + \beta q_1 \tag{4}$$

where the remaining coefficients in terms of the free parameters are defined by

$$\xi = \frac{-3 + a - 60\eta}{12}, \quad \lambda = \frac{8 - 3a + 60\eta}{6}, \quad \alpha = \frac{-6 + 3a - 20\eta}{2}$$
$$\gamma = \frac{24 - 5a + 30\eta}{6}, \quad \beta = -\frac{25 + 3a + 12\eta}{12} \tag{5}$$

This boundary stencil becomes a fifth-order accurate one-parameter family or sixth-order accurate with unique values for all the coefficients. Reduction of Eq. (5) to a third-order accurate two-parameter family $(a, \xi, \eta{=}0)$ defines the respective coefficients as

$$\lambda = \frac{2 - a - 24\xi}{6}, \quad \alpha = \frac{-3 + 2a + 12\xi}{2}, \quad \gamma = \frac{6 - a - 8\xi}{2}$$
$$\beta = \frac{-11 - 2a + 6\xi}{6} \tag{6}$$

where this boundary stencil becomes fourth-order accurate as a one-parameter family and fifth-order accurate with all coefficients defined appropriately. In the next section, we will compare the spatial resolution error of the decoupled and coupled versions of various central and upwind stencils (Eqs. (1) and (2)) as combined with both standard (no free parameters) and multiparameter boundary schemes (Eqs. (3)–(6)).

Coupled (Composite) Templates

The inclusion of two or more dissimilar finite difference stencils of either the explicit or compact variety is defined herein as coupled templates. We will further identify these templates as composites where one of the participating stencils is a boundary scheme, but this structure is not necessarily a limiting factor. Inasmuch as numerical solution of the composite template is implicit, the corresponding spectrum of modified wave numbers at a particular grid point (or cell) is not unique to only its specific stencil. On the contrary, their spectra are locally linked and must be evaluated accordingly, especially when a multiparameter stencil at the boundary is finely tuned to match the resolution character of the interior scheme. We note that this approach deviates from previous analyses that dealt with assessing the dispersive and dissipative errors of composite templates. We will see that the

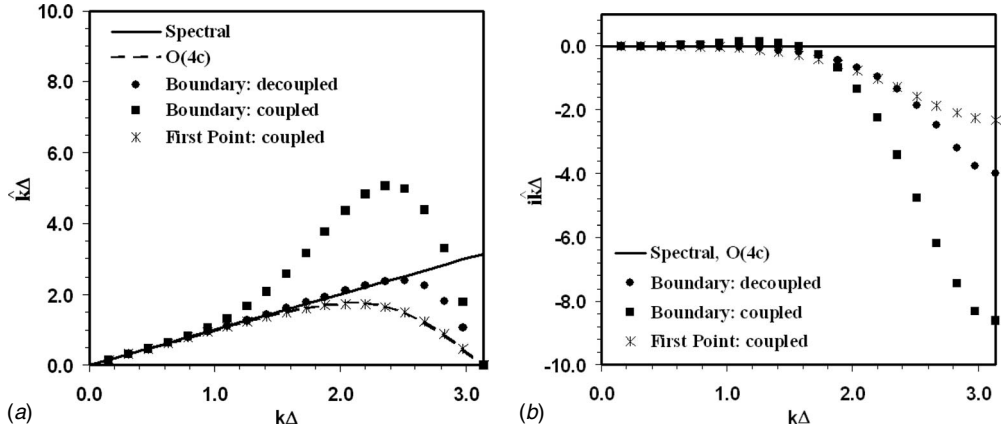

Fig. 2 Real (dispersion) and imaginary (dissipation) distributions of modified wave numbers for composite compact finite difference template (3-4-3) [1]; (3) third-order-accurate on boundary, (4) fourth-order accurate in field

standard approach produces a false understanding of the resolution errors because the compact boundary and interior stencils were not treated as communicative members within the composite.

Modified Wave Number. The fundamental steps for evaluating the modified wave number spectra of a composite template begin with its representation as a linear system of coupled compact finite difference stencils at each boundary and interior nodal points. This system can be illustrated by

$$Mq' = R(q)/\Delta \tag{7}$$

where M is a tridiagonal matrix comprised of the coefficients of the derivative vector (q') and $R(q)$ is a vector of the explicit elements. Substitution of the approximated derivative $q'(x)_{\mathrm{fd}}$ of the basic Fourier wave produces a second linear system that can be defined by

$$i[P(k\Delta)]\{\hat{k}\Delta\} = S(k\Delta) \tag{8}$$

where $P(k\Delta)$ is a $N \times N$ tridiagonal matrix and $S(k\Delta)$ is a N length vector. The variable N denotes the number of nodal points holding a complete modified wave number spectrum over the same resolvable scales $(k\Delta \leq \pi)$.

Solutions of the system in Eq. (8) for template 3-4-3 over wave numbers $0 \leq k\Delta \leq \pi$ produce spectra of the modified wave number, as shown in Fig. 2. This figure also includes a separate profile of $\hat{k}\Delta$ at the boundary as given by the third-order one-sided compact stencil (decoupled). The disparity between companion profiles is clearly not subtle. One obvious difference is the false indication of a small dispersive error when viewing the spectra of only the boundary stencil. This profile suggests that 82% $[e(\delta_{90}) \leq 0.82]$ of the resolvable waves hold at least a 90% resolving efficiency, which is actually only 27% $[e(\delta_{90}) \leq 0.27]$ when properly solved as a coupled composite template. Similarly, the dissipative error is comparatively more than double over the same upper half of resolvable scales. This higher dissipation error influences the adjacent field points as well. Notably, the near boundary points hold a significant degree of dissipation at the higher resolvable scales that would be undetected through separate error analyses of each boundary and interior stencil. At the intermediate scales, the dissipative error becomes slightly positive, which implies potentially unstable solutions.

A three-stencil composite template that also cautions resolution efficiency was developed by Cook and Riley [3] for performing DNS computations of a turbulent reactive plume. The convective derivatives were approximated by a sixth-order Pade-type scheme throughout the flow domain except at the first and second interior points along lines normal to the inlet and exit boundaries—those points were specially treated by optimized fifth-order compact stencils (template 5-5-6-5-5). Comparisons between the resolution errors of the decoupled and coupled versions of their composite template are shown in Fig. 3. Both the dispersive and dissipative errors match the sixth-order Pade-type quite well when analyzing only the decoupled version of their template. However, when the individual stencils are reanalyzed as a linked composite, the resolution errors degrade rapidly over the upper $1/3$ of resolvable wave numbers. Given these distributions, the inlet and exit boundaries in their DNS computations would best be served by fine gridding along the immediate streamwise normal to reconcile uniform spatial resolution throughout the entire turbulent domain.

Multiparameter Templates. A markedly false indication of improved dispersive and dissipative properties at the boundaries comes from fine-tuning the associated free coefficients of a multiparameter stencil to best match the spatial resolution properties of the field scheme. Constraints on the free parameters that tend toward the spatial resolution of the field stencil for all resolvable wave numbers $(\Delta k \leq \pi)$ are chosen. Treatment of the imaginary component can be uniquely fulfilled when compact central differences are chosen to approximate the interior derivatives, but replicating the dispersive error can only converge at discrete wave numbers $(k\Delta)$. To illustrate this condition, we can look at the second-order two-parameter family stencil reported by Lele [1]. The complex form of the modified wave number appears as

$$i\hat{k}\Delta(1 + ae^{ik\Delta}) = \eta e^{3ik\Delta} + \alpha e^{2ik\Delta} + \gamma e^{ik\Delta} + \beta \tag{9a}$$

where the stencil coefficients in terms of the free parameters (a, η) are

$$\alpha = \frac{-1 + a - 6\eta}{2}, \quad \gamma = 2 + 3\eta, \quad \beta = \frac{-3 - a - 2\eta}{2} \tag{9b}$$

After substituting Eq. (9*b*) into Eq. (9*a*), two expressions that hold the real $(\hat{k}_r)$ and imaginary $(\hat{k}_i)$ components of the interior modified wave number in terms of the boundary free parameters arise. These expressions are

$$(-\hat{k}_r \sin k\Delta - \hat{k}_i \cos k\Delta - \sin^2 k\Delta)a = -\hat{k}_i - 1 + 2\cos k\Delta - \cos^2 k\Delta + (2 + 4\cos^3 k\Delta - 6\cos^2 k\Delta)\eta \tag{10a}$$

and

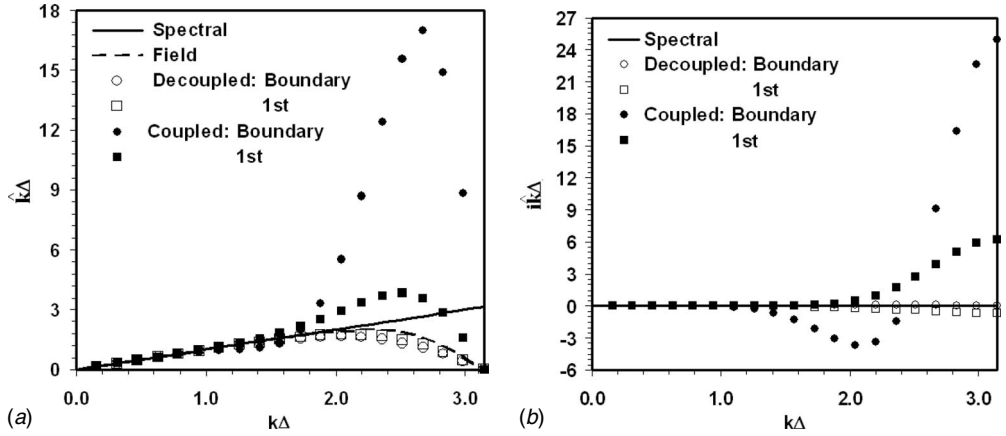

Fig. 3 Real (dispersion) and imaginary (dissipation) distributions of modified wave numbers for composite compact finite difference template (5-5-6-5-5) [3]; (5) fifth-order-accurate on boundary and first interior point, (6) sixth-order Pade-type in remaining field

$$(\hat{k}_r \cos k\Delta - \hat{k}_i \sin k\Delta - \sin 2k\Delta)a = -\hat{k}_r - \sin k\Delta \cos k\Delta + 2 \sin k\Delta + (6 \sin k\Delta - 6 \sin k\Delta \cos k\Delta - 4 \sin^3 k\Delta)\eta \quad (10b)$$

Lele [1] imposed the field constraint $\hat{k}_i\,(k\Delta=\pi)=0$, which gave $\eta=-1/2$. After evaluating the second parameter as $a=4$, an attractive boundary stencil is produced with a dispersive error $e(\delta_{90}) \leq 0.54$ that closely mimics the fourth-order Pade-type scheme $e(\delta_{90}) \leq 0.59$, as illustrated in Fig. 4(*a*). Similarly, the dissipative error of this tuned boundary stencil is nearly negligible for all resolvable wave numbers. However, when the dispersive and dissipative errors of the composite stencil (notation 2^2-4-2^2) are requantified as a truly coupled event (8), the picture changes dramatically as shown in Fig. 4(*b*). At the boundary, a moderate dispersive error ($\delta_r \leq 0.70$) is discernible only over the lower 1/3 of the spectrum $e(\delta_{70}) \leq 0.30$. Beyond $k\Delta \geq \pi/2$, this error quickly rises to several orders of magnitude higher than the decoupled profile. Even the second interior point still indicates considerable dispersion over the upper 3/4 of resolvable scales $e(\delta_{90}) \leq 0.25$. Although not shown, the dissipative error is equally large at the boundary point that becomes negligible once past the second interior nodal point.

A second noteworthy sample of a multiparameter family stencil at the boundary was derived by Carpenter et al. [2]. Their composite template housed a fourth-order Pade-type scheme in the field with an explicit three-parameter family definition at the boundary (template 4^3-4-4^3). While the spatial resolutions of the decoupled and coupled versions are equivalent at the boundary, the impact of the explicit definition still influences the adjacent interior errors. In view of the modified wave number distributions plotted in Fig. 5, this template actually owns a relatively low dispersive error once off the boundary. For example, the resolution efficiency at the first point is 80% or better over 90% of the resolvable wave numbers; $e(\delta_{80}) \leq 9\pi/10$. The less attractive feature of their template is the fact that the dissipative error only becomes negligible once passed the third interior point.

Composite Template Applications

Implementation of the composite templates for numerical solution of the nonlinear Burgers equation and two-dimensional acoustic scattering should supply a suitable means for correlating their resolution properties with the predictive error. Specifically, we desire to locally quantify the detrimental effects of the dispersive and dissipative errors of the boundary compact stencil on the wave amplitudes and phase for various uniform grid spacings. For error assessments of the nonlinear Burgers equations, the computations involve placement of a fictitious (transparent) wall far

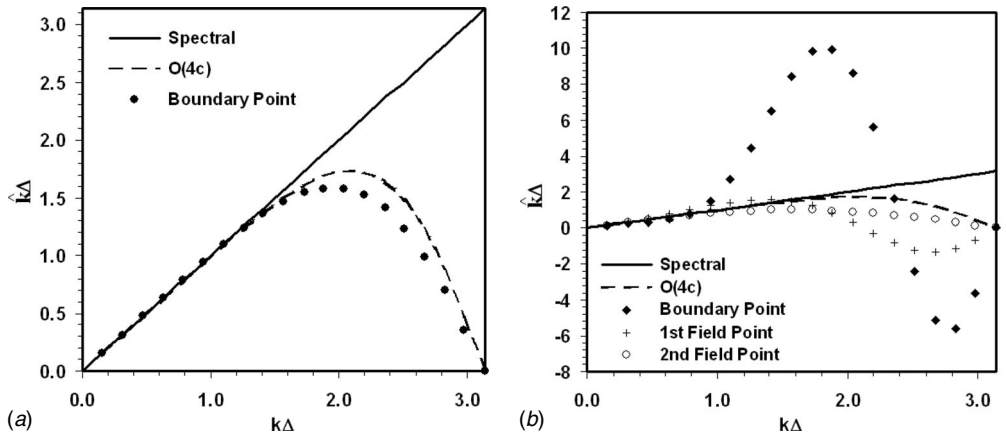

Fig. 4 Dispersive distributions of composite compact finite difference template (2^2-4-2^2) [1]; (2^2) two-parameters ($a=4$, $\eta=-1/2$) second-order-accurate on boundary, (4) fourth-order Pade-type in interior

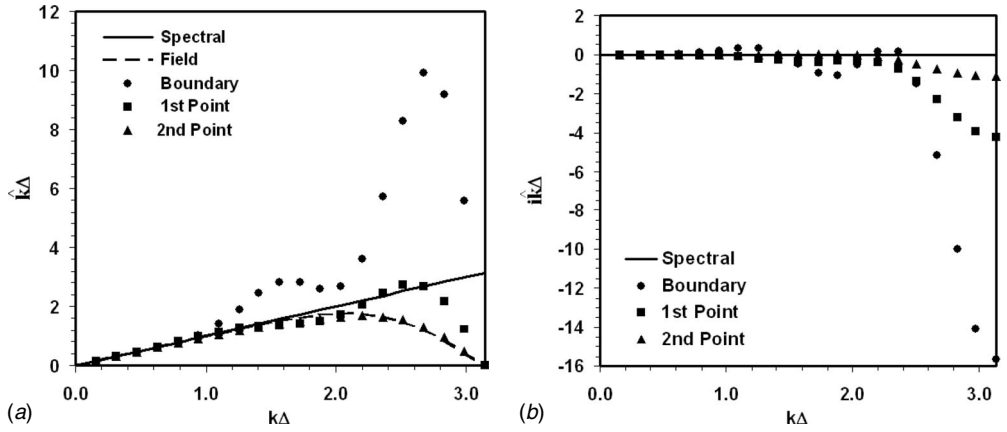

Fig. 5 Real (dispersion) and imaginary (dissipation) distributions of modified wavenumbers for composite compact finite difference template (4^3-4-4^3) [2]; (4^3) explicit fourth-order three-parameter family defined on boundary

downstream from the initial wave position. The wave was time advanced according to the MacCormack method until centered over the wall. At that location, we examined the predictive state of the single wave as compared to the exact solution. This application is also relevant where a composite compact template is used for transferring resolved scales across grid topologies dealing with branch cuts, overlapping grids, discontinuous grids, etc.

Burgers Nonlinear Viscous Equation. The one-dimensional nonlinear Burgers equation has the form

$$u_t + uu_x = \mu u_{xx} \tag{11}$$

where the advective form of the convective derivative is energy nonconservative. Although nonconservative, Fedioun et al. [4] recommended this form for long-time behavior by minimizing the aliasing (and global) errors as produced by highly resolving schemes. The coefficient μ of the second-order term u_{xx} acts as a viscous parameter that aids towards stable solutions. The exact solution for all time is

$$u(x,t) = 1 - \tanh\left(\frac{x'}{2\mu}\right) \tag{12}$$

where $x' = x - x_0 - t$. To isolate the resolving power of the composite template as applied to the convective derivative, the exact form of the viscous term μu_{xx} is used in the computations;

$$\mu u_{xx} = \frac{1}{2\mu}\,\mathrm{sech}^2(v')\tanh(v') \tag{13}$$

where $v' = x'/2\mu$. Inasmuch as a viscous term is present, the wave was advanced using the second-order-accurate Adams–Bashforth scheme for the time derivative u_t. Like Fedioun et al. [4], a small time step (0.001) was chosen to diminish the temporal error contribution of the time derivative approximation to the total error.

Knowing that the advective form of the nonlinear term in Burgers equation does not conserve energy, we desire to explore this loss relative to the resolution efficiency of the composites. Figure 6 shows the relative loss of energy conservation ($|E(t) - E_0|/E_0$) of composite template 3-4-3 over time and reduced grid spacing where the energy at time t is given by $E(t) = \Sigma[u_{\mathrm{fd}}(t)]^2$. Distributions of the respective dispersive and dissipation errors of this template are shown in Fig. 2. Beginning with the exact wave, the time passed to near peak energy loss seems independent of the spatial resolution error. This behavior is more indicative of the small temporal error contribution to the global error via the low time step value chosen to advance the predicted wave. For grid resolutions $k\Delta = 3\pi/4$ and $k\Delta = \pi/2$, large energy losses that correlate well with the respective poor resolution efficiencies of template 3-4-3 are displayed in the figure. However, with reduced grid spacing and concurrently improved resolution efficiency, this loss is suitably minimized such that a fine uniform spacing of $k\Delta = \pi/16$ [$e(\delta_{90}) \leq 0.99$] conserved about 99% of the original wave energy.

Continuing with the 3-4-3 composite template, numerical predictions of the Burger wave as compared to the exact solution are plotted in Fig. 7 at four uniform grid spacings ($k\Delta \sim 3\pi/4$, $\pi/2$, $\pi/4$, and $\pi/8$). These comparisons reside at the fictitious boundary point (100 time units from the initial wave position). We note that the composite template 3-4-3 remained free of oscillations (no filtering) and suitably stable when applied over the coarsest grid, but preserved its formal order with reduced grid spacing only at the interior nodes far removed from the fictitious boundary. Under the coarsest grid ($k\Delta \sim 3\pi/4$), the high dissipative error ($i\hat{k}_i\Delta = -3.43$) of the composite severely dampened the wave peak amplitude ($x' = 0$), but the predictions stayed essentially in phase with the exact wave. Not surprisingly, the template better predicted the peak wave amplitude with reduced grid spacing such that only a 6% error ($E(u) = 0.059$) occurred under the finest grid ($k\Delta \sim \pi/8$) where 98% of the waves are considered *well resolved* [$e(\delta_{90}) \leq 0.98$].

The predictive errors as quantified by the L_2 norm of three standard and three optimized multiparameter composite templates are plotted in Fig. 8(*a*) where $\|L_2\| = \frac{1}{2}[\Sigma|u_e - u_{\mathrm{fd}}|^2]^{1/2}$; u_e and u_{fd} are the exact and predicted discrete velocities of the Burger wave,

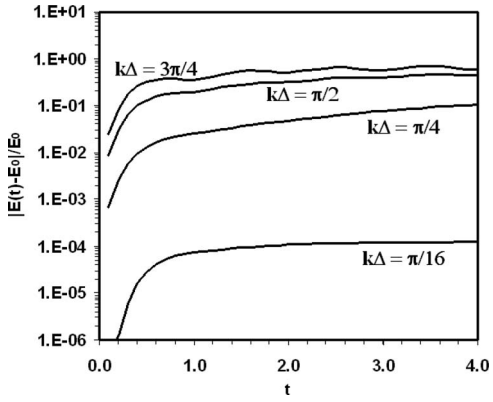

Fig. 6 Energy loss in solutions of Burgers equation using composite template (3-4-3)

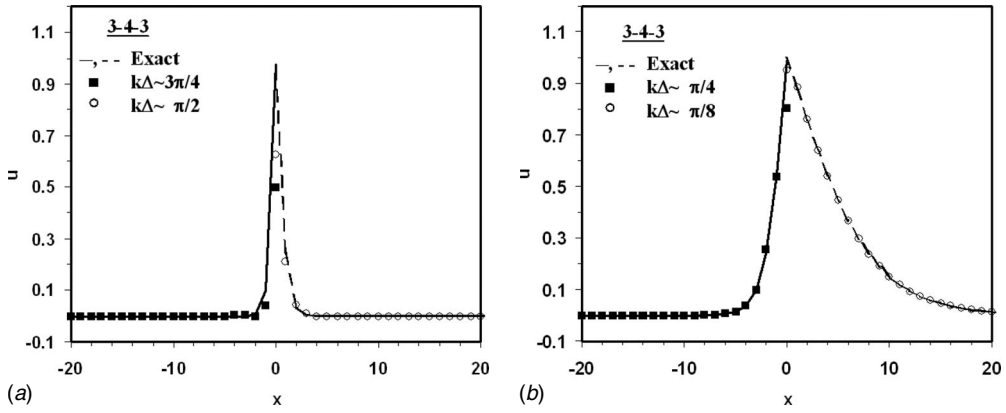

Fig. 7 Solutions of Burgers equation using composite template (3-4-3)

respectively. Each compact template was tested over the same four grid spacings ($k\Delta \sim 3\pi/4$, $\pi/2$, $\pi/4$, and $\pi/16$) with the associated errors calculated using the full wave once centered over the fictitious wall. In view of decoupled resolution errors, predictions by the optimized template 2^2-4-2^2 [1] are directly comparable to the results of composite 3-4-3 (Fig. 2). Similarly, the optimized 5-5-6-5-5 template [4] is an improved version over the standard composite 4-4-6-4-4. We note that evaluation of the L_2 norm from each composite template at time $t=50$ (center interior node) demonstrated proper convergence of Burgers equation with finer grid spacing.

Apart from the optimized composites 2^2-4-2^2 and 5-5-6-5-5, each template closely shares similar reductions of the L_2 norm with none converging on their formal order at the boundary. This behavior is a reflection of the strong influence of their similar boundary resolution errors on the predictive global accuracy. When compared to the other composites, the template 2^2-4-2^2 gave a sizable degradation of the wave amplitude predictions that was caused by its corresponding larger dispersive and dissipative errors. All six templates as tested under the finest grid ($k\Delta \sim \pi/16$) show the lowest predictive errors, which by comparison are barely separable. Again, this result agrees well with their equally shared low dispersive and dissipative errors; i.e., $\delta_r = 97\%$ (3-4-3) versus $\delta_r = 91\%$ (2^2-4-2^2). The most discernible disparity among the predictive errors occurs at the intermediate grid densities. Moreover, these differences also correlate well with their respective spatial resolution errors as well as their formal accuracy at the boundary. Overall, composite 5-5-6-5-5 showed the lowest predictive errors among the six templates with the smallest reductions realized over the finest and coarsest grids. The resolution efficiency of template 5-5-6-5-5 at the boundary remains above 77% for almost half of the resolvable waves; $e(\delta_{77}) \leq \pi/2$. Thus, improved predictions should only be expected at the intermediate grid densities.

No discernible differences were detected by switching the end stencil of the composite template to its explicit counterpart. Evidence of this fact is illustrated in Fig. 8(*b*) where reductions of the L_2 norm are nearly indistinguishable for stencils 3e-4-3e and 4e-4-4e over the four grid densities ($k\Delta \sim 3\pi/4$, $\pi/2$, $\pi/4$, and $\pi/16$). Convergence of the L_2 norm for each composite is similar to the compact fourth-order stencil (4c) with periodic boundary conditions.

Two-Dimensional Acoustic Scattering. The third test problem for illustrating the true spatial resolution character of the composite templates is taken from the Second CAA Workshop [5]. The governing equations in polar coordinates are

$$\frac{\mathrm{d}}{\mathrm{d}t}\begin{bmatrix} u_r \\ u_\theta \\ P \end{bmatrix} + \frac{\mathrm{d}}{\mathrm{d}r}\begin{bmatrix} p \\ 0 \\ u_r \end{bmatrix} + \frac{\mathrm{d}}{r\mathrm{d}\theta}\begin{bmatrix} 0 \\ p \\ u_\theta \end{bmatrix} + \frac{1}{r}\begin{bmatrix} 0 \\ 0 \\ u_r \end{bmatrix} = \begin{bmatrix} 0 \\ 0 \\ 0 \end{bmatrix} \tag{14}$$

where u_r is the radial velocity, u_θ is circumferential velocity, and p is the acoustic pressure. The problem involves inserting a circular cylinder of radius $r=0.5$ at the origin of the cylindrical flow domain $r=10.5$. Only the normal velocity u_r is zero at the cylinder

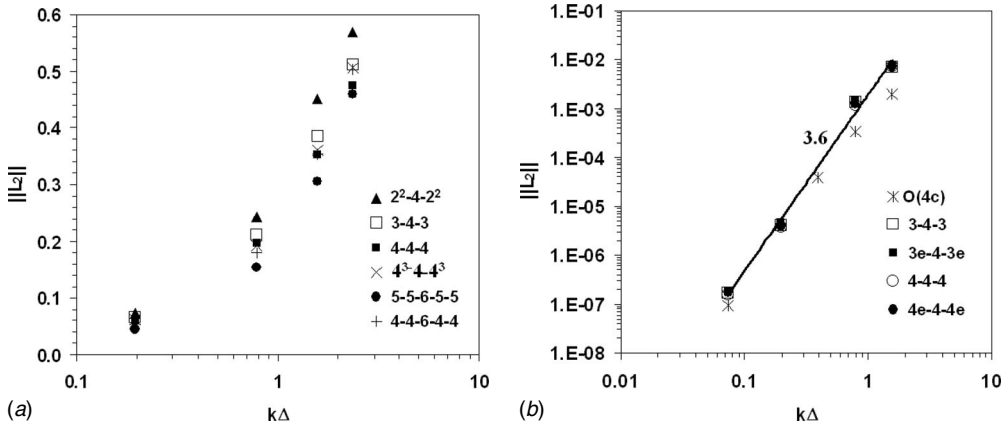

Fig. 8 Predictive errors (L_2 norm) at the fictitious boundary of composite templates as applied to the viscous Burgers equation; $\|L_2\| = [(1/N)\Sigma|u'_e - u'_{fd}|^2]^{1/2}$; optimized composite templates are (2^2-4-2^2) [1], (4^3-4-4^3) [2], and (5-5-6-5-5) [3]

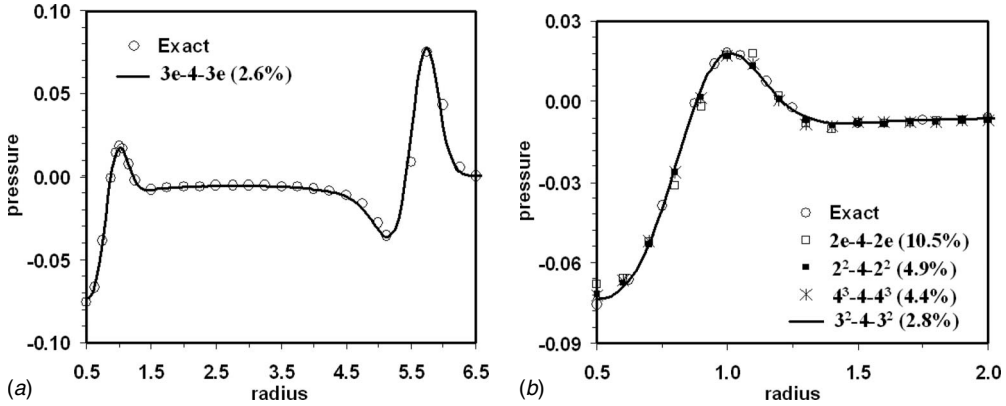

Fig. 9 Radial pressure distribution of acoustic scatter problem (45 deg, $t=4$); optimized composite templates are (2^2-4-2^2) [1] and (4^3-4-4^3) [2]

wall boundary. The circumferential velocity component u_θ and pressure p at the wall were solved using Eq. (4). A pressure source at time $t=0$ is pulsed at the point (4,0 deg) with magnitude

$$p(x,y,0) = \exp\left\{-\ln(2)\left[\frac{(x-4)^2+y^2}{0.04}\right]\right\} \tag{15}$$

The exact solution for the domain acoustic pressures at all times as well as the flow domain exterior boundary condition is given in the CAA Workshop publication [5].

For this unsteady problem, uniform spacing owning 301 circumferential and 201 radial points was used to apply the composite templates. We tested the fourth-order-accurate compact MacCormack-type scheme of Hixon and Turkel [6] (HT); however, their five-point explicit boundary expression was replaced herein with various implicit and explicit definitions. However, coupling a third-order-accurate compact stencil with the HT scheme leads to a singularity along the diagonal of the coefficient matrix $[M]$ in system (7). We can circumvent this difficulty by simply exploring other possibilities such as the optimized templates 2^2-4-2^2 and 4^3-4-4^3 as well as the explicit options 2e-4-2e and 3e-4-3e. Inasmuch as the pressure gradient at the cylinder wall is exactly zero, the discernible differences in the adjacent acoustic pressure predictions is solely a resultant of varying the approximation for the wall radial velocity derivative.

Figure 9 compares the instantaneous pressure predictions by the composite templates to the exact solution along the radial line (r,45 deg) at time $t=4$. While the left figure plots only solutions of the dominant and primary reflected wave by template 3e-4-3e, the right composite focuses on the instantaneous predictions by the four templates specifically near the cylinder wall. The absolute predictive error of the acoustic pressure specifically at the wall boundary is shown in parentheses after each stencil. As previously discussed, template 3e-4-3e underpredicts the principal wave. Outside of template 2^2-4-2^2, predictions of the peak pressure of the primary reflected wave are nearly indistinguishable, which closely match the exact wave. Inside one cylinder radius from the wall boundary, these latter templates also show close agreement but slightly underpredict the drop in near wall acoustic pressure due to the formation of the reflected wave. The present optimized 3^2-4-3^2 and 3e-4-3e templates produced the lowest errors whereas template 2e-4-2e gave the largest error using similar templates.

Final Remarks

One should not expect improved spatial resolution of the boundary and adjacent flow physics by merely switching to a compact finite differencing composite over a simple explicit definition. The associated errors are not noticeably reduced beyond cost-effective first-order or one-sided second-order explicit schemes under moderate grid spacing. Optimized templates are especially susceptible to poor spatial resolution characteristics. The dispersive and dissipative errors of these composite templates must be carefully quantified before exercising their use for resolving the salient problem physics. Working the multiparameter composites show promise, but tuning their free parameters must take place in a coupled fashion to properly match the intended spatial resolution properties of the predominant field stencil. We emphasize that a separate analysis of the coupled resolution errors as well as treatment of the global stability and accuracy is necessary to understand the prevailing numerical character of a composite compact finite differencing template prior to launching the computation.

Acknowledgment

The author gratefully acknowledges the support of the Office of Naval Research (Dr. Ronald D. Joslin, Program Officer), Contract No. N0001406AF00002.

References

[1] Lele, S. K., 1992, "Compact Finite Difference Schemes With Spectral-Like Resolution," J. Comput. Phys., **103**, pp. 16–42.
[2] Carpenter, M. H., Gottlieb, D., and Abarbanel, S., 1993, "The Stability of Numerical Boundary Treatments for Compact High-Order Finite-Difference Schemes," J. Comput. Phys., **108**, pp. 272–295.
[3] Cook, A. W., and Riley, J. J., 1996, "Direct Numerical Simulation of a Turbulent Reactive Plume on a Parallel Computer," J. Comput. Phys., **129**(2), pp. 263–283.
[4] Fedioun, I., Lardjane, N., and Gökalp, I., 2001, "Revisiting Numerical Errors in Direct and Large Eddy Simulations of Turbulence: Physical and Spectral Spaces Analysis," J. Comput. Phys., **174**, pp. 816–851.
[5] Tam, C. K. W., and Hardin, C., 1997, *Second Computational Aeroacoustics (CAA) Workshop on Benchmark Problems*, Hampton, VA, NASA CP-3352.
[6] Hixon, R., and Turkel, E., 1998, "High-Accuracy Compact MacCormack-Type Schemes for Computational Aeroacoustics," Report NASA/CR-1998-208672.

Finite-Amplitude Long-Wave Instability of a Thin Power-Law Liquid Film Flowing Down a Vertical Column in a Magnetic Field

Po-Jen Cheng[1]
Department of Mechanical Engineering,
Far-East University,
Tainan 74448, Taiwan
e-mail: pjcheng@cc.feu.edu.tw

The long-wave perturbation method is employed to investigate the nonlinear hydromagnetic stability of a thin electrically conductive power-law liquid film flowing down a vertical cylinder. In contrast to most previous studies presented in literature, the solution scheme employed in this study is based on a numerical approximation approach rather than an analytical method. The modeling results reveal that the stability of the film flow system is weakened as the radius of the cylinder is reduced. However, the flow stability can be enhanced by increasing the intensity of the magnetic field and the flow index. [DOI: 10.1115/1.2948375]

Keywords: thin film, hydromagnetic stability analysis, power-law fluid

1 Introduction

The hydrodynamic stability of fluid films flowing down a vertical cylindrical surface has attracted particular attention. Krantz and Zollars [1] indicated that the radius of curvature of the cylinder had a significant effect on the stability of the thin-film system. Hung et al. [2] demonstrated the coexistence of supercritical stability in the linearly unstable region and subcritical instability in the linearly stable region. As in Ref. [1], the authors reported that the lateral curvature of the cylinder exerted a destabilizing effect on the stability of the film flow. Analyzing the microstructure of fluid flows has emerged as a major research area in both industrial and academic circles in recent years. Cheng et al. [3] displayed that the micropolar parameters of the fluid play an important role in stabilizing the film flow. Gupta [4] revealed that viscoelastic effects tend to destabilize the film flow. The fluids used in practical engineering applications are commonly classified for analysis purposes as either pseudoplastic ($n<1$) or dilatant ($n>1$) depending on whether they possess shear thinning or shear thickening characteristics, respectively. Ng and Mei [5] investigated the problem of roll waves on a shallow layer of mud modeled as a power-law fluid. Hwang et al. [6] showed that the film system became increasingly unstable as the power-law exponent n decreased. Gorla [7] showed that the rupture time of dilatant fluids flowing down a cylinder is longer than that of Newtonian fluids.

Many researchers have analyzed the stability of electrically conductive fluid films in a magnetic field in recent years. Tsai et al. [8] and Hsieh [9] performed hydromagnetic stability analyses of film flows along vertical and inclined planes and showed that the application of a magnetic field had a stabilizing effect. The current study applies both linear and nonlinear stability analysis theories to investigate the stability of a thin electrically conductive power-law fluid film flowing down a vertical cylinder in an applied magnetic field. The analysis focuses particularly on the respective effects of the Hartmann number, the flow index, and the cylinder radius on the stability of the film flow. Numerical examples are presented to verify the solutions and to demonstrate the effectiveness of the proposed modeling procedure.

2 Mathematical Models

The current problem of a thin electrically conductive power-law fluid film flowing along an infinite vertical cylinder in a transverse magnetic field is studied. The solutions of the flow couple both the Navier–Stokes equations characterizing fluid flow and Maxwell's equations for the magnetic field [8,10]. The magnetic Reynolds number is assumed to be small, and thus, the intensity of the induced magnetic field is negligible compared to that of the applied magnetic field and can therefore be ignored [8]. The unsteady hydromagnetic flow is governed both by the continuity equation and the equation of motion, and the boundary conditions are given in Ref. [11] in which $\tau_{r^*r^*}$, $\tau_{r^*z^*}$, $\tau_{z^*r^*}$, and $\tau_{z^*z^*}$ are the individual stress components of the power-law fluid [12], σ is the electrical conductivity, and B_0^* is the magnetic flux density. For convenience, the following dimensionless quantities can be introduced:

$$z=\frac{\alpha z^*}{h_0^*},\quad r=\frac{r^*}{h_0^*},\quad t=\frac{\alpha u_0^* t^*}{h_0^*},\quad h=\frac{h^*}{h_0^*},\quad \varphi=\frac{\varphi^*}{u_0^* h_0^{*2}},$$

$$p=\frac{p^*-p_a^*}{\rho u_0^{*2}},\quad R=\frac{R^*}{h_0^*}$$

$$\mathrm{Re}_n=\frac{u_0^{*2-n}h_0^{*n}}{\nu_n},\quad S_n=\frac{S_n^*}{(2^{-3n^2+3n+2}\rho_n^{n+2}\nu_n^4 g^{3n-2})^{1/(n+2)}},$$

$$\alpha=\frac{2\pi h_0^*}{\lambda},\quad m=\frac{\sigma B_0^{*2}h_0^{*2}}{\mu_n} \tag{1}$$

where φ^* is the stream function, Re_n is the Reynolds number, R is the dimensionless radius of the cylinder, λ is the perturbed wavelength, ν_n is the kinematic viscosity of the fluid, α is the dimensionless wave number, m is the Hartmann number, h_0^* is the film thickness of the local base flow, and u_0^* is the reference velocity and is defined in Ref. [12]. Thus, the nondimensional governing equations can be given as

$$\frac{\partial p}{\partial r}=\alpha\mathrm{Re}_n^{-1}\left\{n\left[2\left(\frac{\partial}{\partial r}\left(\frac{1}{r}\frac{\partial\varphi}{\partial z}\right)\right)^{n-1}\frac{\partial^2}{\partial r^2}\left(\frac{1}{r}\frac{\partial\varphi}{\partial z}\right)-\left(\frac{\partial}{\partial r}\left(\frac{1}{r}\frac{\partial\varphi}{\partial r}\right)\right)^{n-1}\frac{\partial^2}{\partial r\partial z}\left(\frac{1}{r}\frac{\partial\varphi}{\partial r}\right)\right]+\frac{2}{r}\left[\left(\frac{\partial}{\partial r}\left(\frac{1}{r}\frac{\partial\varphi}{\partial z}\right)\right)^n-\left(\frac{1}{r^2}\frac{\partial\varphi}{\partial z}\right)^n\right]\right\}+O(\alpha^2) \tag{2}$$

$$\frac{1}{r}\frac{\partial}{\partial r}\left\{r\left[\frac{\partial}{\partial r}\left(\frac{1}{r}\frac{\partial\varphi}{\partial r}\right)\right]^n\right\}-(4\Gamma)^{n-1}\frac{m}{r}\frac{\partial\varphi}{\partial r}=(4\Gamma)^n+\alpha\mathrm{Re}_n\left[-\frac{\partial p}{\partial z}+\frac{1}{r}\frac{\partial^2\varphi}{\partial t\partial r}+\frac{1}{r^2}\frac{\partial\varphi}{\partial z}\frac{\partial^2\varphi}{\partial r^2}-\frac{1}{r^3}\frac{\partial\varphi}{\partial z}\frac{\partial\varphi}{\partial r}-\frac{1}{r^2}\frac{\partial\varphi}{\partial r}\frac{\partial^2\varphi}{\partial r\partial z}\right]+O(\alpha^2) \tag{3}$$

The associated boundary conditions are the following: *At the cylinder surface* ($r=R$),

$$\varphi=\frac{\partial\varphi}{\partial r}=\frac{\partial\varphi}{\partial z}=0 \tag{4}$$

[1]Corresponding author.

Contributed by the Fluids Engineering Division of ASME for publication in the JOURNAL OF FLUIDS ENGINEERING. Manuscript received November 12, 2007; final manuscript received April 24, 2008; published online June 26, 2008 Assoc. Editor: Malcolm J. Andrews.

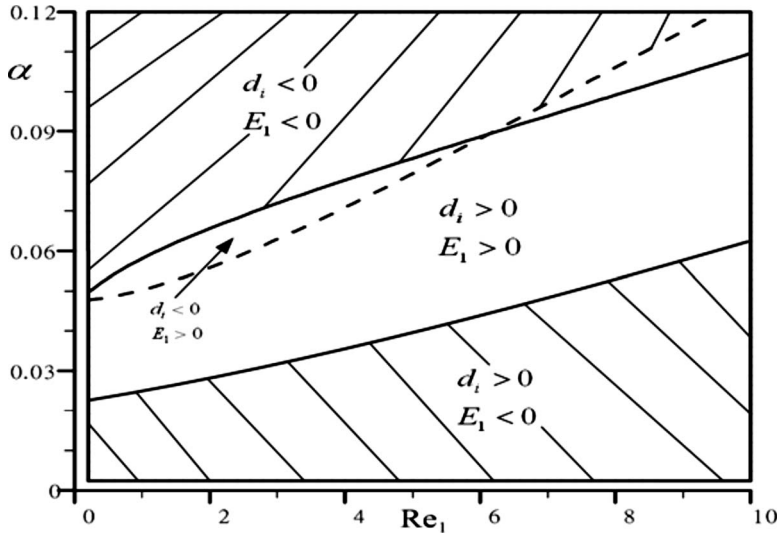

Fig. 1 Neutral stability curves of film flows for $R=20$, $m=0.1$, and $n=0.95$

At the free surface $(r=R+h)$,

$$\frac{\partial}{\partial r}\left(\frac{1}{r}\frac{\partial \varphi}{\partial r}\right) = 0 + O(\alpha^2) \tag{5}$$

$$p = -2S_n \mathrm{Re}_n^{(-3n^2+4n+4)/(n+2)(n-2)} (2\Gamma)^{(3n-2)n/(n+2)} \left(\alpha^2 \frac{\partial^2 h}{\partial z^2} - \frac{1}{r}\right) + \alpha \frac{2}{\mathrm{Re}_n}\left[\left(\frac{\partial}{\partial r}\left(\frac{1}{r}\frac{\partial \varphi}{\partial r}\right)\right)^n \frac{\partial h}{\partial z} + \left(\frac{\partial}{\partial r}\left(\frac{1}{r}\frac{\partial \varphi}{\partial z}\right)\right)^n\right] + O(\alpha^2) \tag{6}$$

$$\frac{\partial h}{\partial t} - \frac{1}{r}\left(\frac{\partial \varphi}{\partial r}\frac{\partial h}{\partial z} + \frac{\partial \varphi}{\partial z}\right) = 0 \tag{7}$$

By employing the long wavelength modes, the dimensionless stream function, φ, and pressure, p, are expanded in terms of some small wave number α as follows:

$$\varphi = \varphi_0 + \alpha\varphi_1 + O(\alpha^2) \tag{8}$$

$$p = p_0 + \alpha p_1 + O(\alpha^2) \tag{9}$$

By substituting these two equations into Eqs. (2)–(7), the governing equations of the thin-film system can be collected and solved on an order-by-order basis. In practice, the nondimensional surface tension, S, has a large value, and thus, the term $\alpha^2 S$ can be treated as a zeroth-order quantity [2,11]. Furthermore, for $r-R \leq h$, the film thickness h is very small, the power series approximation solutions can be obtained up to the order of $(r-R)^5$ at the zeroth and first orders of the stream function. By substituting the solutions of the zeroth- and first-order equations into the dimensionless free surface kinematic equation given in Eq. (7), the following generalized nonlinear kinematic equation can be obtained:

$$h_t + A(h)h_z + B(h)h_{zz} + C(h)h_{zzzz} + D(h)h_z^2 + E(h)h_z h_{zzz} = 0 \tag{10}$$

where $A(h)$, $B(h)$, $C(h)$, $D(h)$, and $E(h)$ are given in the Appendix. I employ linear and nonlinear stability theories to conduct a numerical characterization of thin-film flows traveling down a vertical column. The normal mode approach is first used to compute the linear stability solution for the film flow. The method of multiple scales is then used to obtain the weak nonlinear dynamics of the film flow for stability analysis. The deriving process as well as the derived results have been presented in the previous work of Cheng and Lin [11] in which d_i is the linear growth rate of the amplitudes, E_1 is the coefficient of the Ginzburg–Landau equation, εa_0 is the threshold amplitude, and Nc_r is the nonlinear wave speed.

3 Numerical Examples

In the linear stability analysis, the results indicate that the area of the unstable region $(d_i>0)$ increases as the values of m, n, and R reduce. It can be seen that the amplitude growth rate increases as the values of m, n, and R decrease. In general, the liquid film becomes more stable as the Hartmann number, the flow index, and the cylinder radius increase. The neutral stability curves shown in Fig. 1 corresponding to $d_i=0$ are shifted downward and $E_1=0$ are shifted outward as the value of m increases. In other words, the area of the shaded supercritical instability region decreases, while that of the subcritical stability region $(d_i<0, E_1>0)$ increases at higher values of the Hartmann number. Moreover, it demonstrates that the neutral stability curves of $d_i=0$ and $E_1=0$ are shifted downward as the value of n increases. Therefore, the areas of the shaded subcritical instability region and the subcritical stability region increase, while that of the shaded supercritical instability region decreases at higher values of the flow index. In addition, the results display that the neutral stability curves of $d_i=0$ and $E_1=0$ are shifted upward as the value of R is reduced. In other words, the area of the shaded subcritical instability region increases, while that of the shaded supercritical instability region decreases as the radius of the cylinder increases. Finally, the area of the supercritical stability region $(d_i>0, E_1>0)$ increases, while that of the subcritical stability region decreases as the value of R decreases.

Figure 2 shows that the threshold amplitude reduces as the Hartmann number decreases. Besides, the results display that the value of the threshold amplitude reduces as the flow index and the radius of the cylinder decrease. In such a situation, the film flow becomes inherently more unstable. If the initial finite-amplitude disturbance is less than the threshold amplitude, the system will be conditionally stable. However, if the finite-amplitude disturbance exceeds the threshold amplitude, the system becomes explosively unstable. In the linearly unstable region, the linear amplification rate is positive, while the nonlinear amplification rate is negative. Therefore, the effect of a linear infinitesimal disturbance in the unstable region will cause the amplitude of the disturbed wave to approach a finite equilibrium value rather than an infinite value. Figure 3 demonstrates that the threshold amplitude decreases as the flow index increases. Moreover, it is seen that the threshold amplitude reduces as the Hartmann number and the ra-

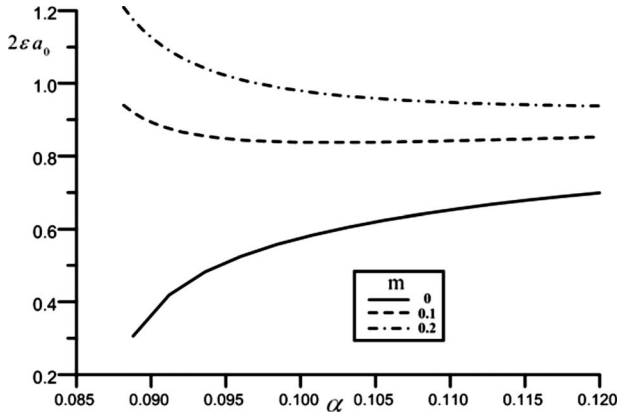

Fig. 2 Threshold amplitude in the subcritical unstable region for three different values of m at $Re_1=5$, $R=20$, and $n=0.95$

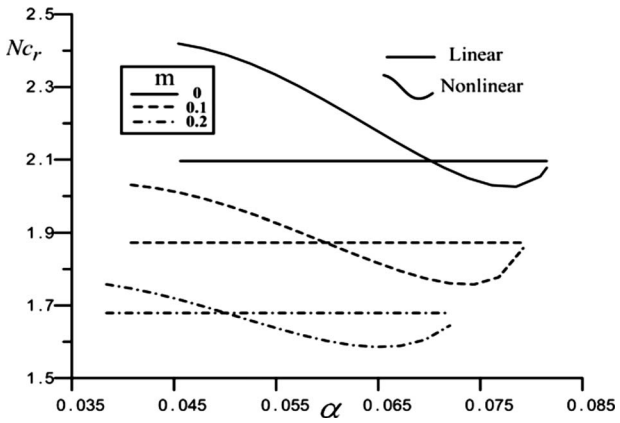

Fig. 4 Nonlinear wave speed in the supercritical stable region for three different values of m at $Re_1=5$, $R=20$, and $n=0.95$

dius of the cylinder increase. In such situations, the flow becomes relatively more stable. The wave speed predicted using linear theory is a constant value for all wave numbers, Reynolds numbers, and cylinder radii. Figure 4 shows that the nonlinear wave speed decreases as the value of m increases. In addition, it can be seen that the nonlinear wave speed increases as the values of n and R decrease.

The degree of stability of the conductive power-law liquid film flow increases as the values of m, n, and R increase. By setting the limiting case of $R\rightarrow\infty$, the problem becomes one of planar flow. Computing the corresponding flow solutions, it is found that the flow field becomes relatively more stable as the Hartmann number increases. This finding is consistent with the results presented in literature [8,9], which showed that the application of a magnetic field had a stabilizing effect. Moreover, by setting $m=0$, the results correspond to those of a power-law film flowing along a vertical wall with no magnetic field. Computing the corresponding results, the solutions are found to be in good agreement with those given by Hwang et al. [6], which displayed that the film system became increasingly unstable as the flow index n decreased.

4 Concluding Remarks

The generalized nonlinear kinematic equations of the free film near the cylindrical surface have been derived and solved numerically in order to explore the stability of the flow field under different values of the Hartmann number (m), the flow index (n), and the cylinder radius (R). The modeling results presented in this study support the following conclusions.

1. According to the linear stability analysis, the degree of stability is enhanced when the flow system is characterized by a lower Reynolds number, a larger Hartmann number, a larger flow index, and a greater cylinder radius.
2. The threshold amplitude εa_0 in the subcritical instability region decreases as the Hartmann number, the flow index, and the cylindrical radius decrease. Both the threshold amplitude and the nonlinear wave speed in the supercritical stability region decrease with increasing values of m, n, and R.
3. The flow field becomes relatively more stable as the values of m, n, and R increase since the microstructure characteristic of the conductive power-law fluid suppresses the convective motion of the flow.
4. The optimum conditions can be found through the use of a system to alter the stability of the film flow by controlling the applied magnetic field.

Acknowledgment

The financial support provided to this study by the National Science Council of Taiwan through Grant No. NSC 95-2221-E-269-027 is gratefully acknowledged.

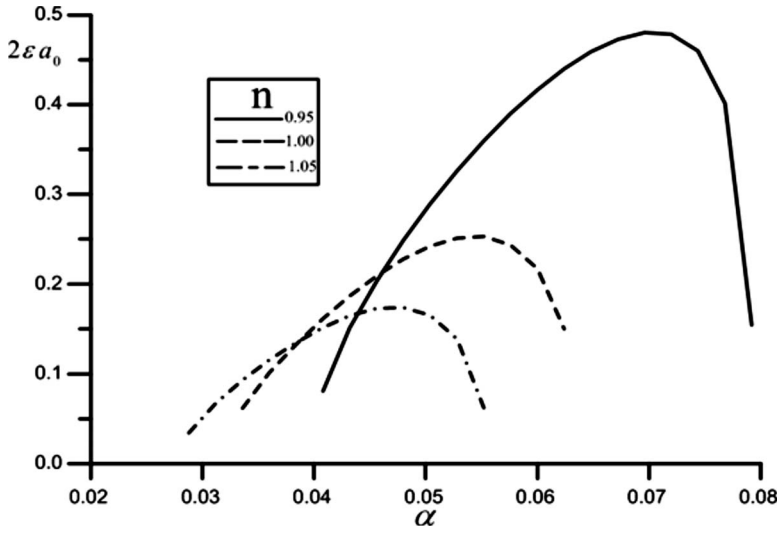

Fig. 3 Threshold amplitude in the supercritical stable region for three different values of n at $Re_1=5$, $R=20$, and $m=0.1$

Appendix

$$A(h) = -4^{n-1}h^2\Gamma^n[160n^2hR^4 - 240n^2R^5 + 2nh^3R^2(-63n + mR^2) + 14h^5(n + mR^2) \times (2n + mR^2) + 10h^2R^3(13n + mR^2) + h^4(91n^2R + 58nmR^3 + 15m^2R^5)]/(15nq\Omega^2) \tag{A1}$$

$$B(h) = \xi h^3\alpha[80nR^3 - 7h^3(n + mR^2) + 2h^2(21nR + 5mR^3)]/(60nq^3\Omega) + 16^n\mathrm{Re}_n h^6R^3\alpha\Gamma^{2n}\{-6664n^3mh^5R^8 + 6080n^4hR^{10} - 3840n^4R^{11} - 96n^3h^3R^8(97n - 19mR^2) + 1120n^3h^2R^9(7n + 2mR^2) + 14h^{11}(n + mR^2)^2(2n + mR^2)(n + 3mR^2) + 8nmh^6R^7(183n^2 + 5m^2R^4) - 8n^2h^4R^7(684n^2 + 677nmR^2 + 15m^2R^4) + 2nmh^9R^4(522n^2 + 188nmR^2 + 62m^2R^4) + 8n^2h^7R^4(141n^2 + 158m^2R^4) + 2nmh^{10}R^3(526n^2 + 575nmR^2 + 222m^2R^4) - 2h^8R^3(-258n^4 + n^3mR^2 - 85n^2m^2R^4 + 95nm^3R^6 + 15m^4R^8) + h^5R[287n^4h^5 + 591n^4h^4R + 60n^4hR^4 + 4n^3R^5(745mh^2 + 219n) + m^2hR^8(59m^2h^4 - 988n^2) - m^2R^9(13m^2h^4 + 12nmh^2 + 1716n^2)]\}/(720n^2q^3\Omega^5) \tag{A2}$$

$$C(h) = \xi\alpha^3h^3[80nR^3 - 7h^3(n + mR^2) - 2h^2R(21n + 5mR^2)]/(15nq\Omega) \tag{A3}$$

$$D(h) = \xi h^2\alpha[80n^2hR^5 - 240n^2R^6 + 7h^6(n + mR^2)(2n + mR^2) + 10nh^2R^4(13n + mR^2) + 8nh^3R^3(10n + 9mR^2) + h^5(49n^2R + 52nmR^3 + 19m^2R^5) + h^4(35n^2R^2 + 66nmR^4 + 15m^2R^6)/(30nq^4\Omega^2) + 16^n\mathrm{Re}_n h^5R^2\alpha\Gamma^{2n}\{-62{,}080n^5hR^{13} + 46{,}080n^5R^{14} + 384n^4h^3R^{11}(289n - 133mR^2) - 70h^{14}(n + mR^2)^2(2n + mR^2)^2(n + 3mR^2) - 640n^4h^2R^{12}(289n + 80mR^2) + 32n^3h^4R^{10}(8536n^2 + 4903nmR^2 + 215m^2R^4) + 8n^3h^5R^9(2551n^2 + 28{,}752nmR^2 + 6157m^2R^4) - 120n^2h^6R^8(795n^3 + 372n^2mR^2 - 323nm^2R^4 + 8m^3R^6) - 2h^{13}R(n + mR^2)(2n + mR^2)(532n^3 + 1411nm^2R^2 + 840nm^2R^4 + 265m^3R^6) - 8n^2h^7R^7(5790n^3 + 18{,}627n^2mR^2 + 5235nm^2R^4 + 331m^3R^6) - 6nh^9R^5(2343n^4 + 2802n^3mR^2 + 2386n^2m^2R^4 + 1074nm^3R^6 - 101m^4R^8) - 8nh^8R^6(2388n^4 + 12{,}441n^3mR^2 + 561nm^3R^6 - 95m^4R^8) - 2h^{10}R^4(5945n^5 + 24{,}546n^4mR^2 + 21{,}834n^3m^2R^4 + 9006n^2m^3R^6 + 609nm^4R^8 - 60m^5R^{10}) - 2h^{11}R^3(596n^5 + 7058n^4mR^2 + 9726n^3m^2R^4 + 4839n^2m^3R^6 + 990nm^4R^8 + 118m^5R^{10}) - 2h^{12}R^2(996n^5 + 19n^4mR^2 + 3264n^3m^2R^4 + 3633n^2m^3R^6 + 1428nm^4R^8 + 122m^5R^{10}) - mh^7R^4[10{,}716n^4R^5 - 4196n^2m^2R^9 - 12n^2hR^4(6493n^2 - 2608nmR^2 + 865m^2R^4) + h^5(4333n^4 + 71m^4R^8) - h^4(4853n^4R + 361m^4R^9)]\}]/(720n^2q^4\Omega^6) \tag{A4}$$

$$E(h) = \xi\alpha^3h^2[240n^2R^5 - 160n^2hR^4 - 2nh^3R^2(mR^2 - 63n) - 14h^5(n + mR^2)(mR^2 + 2n) - 10nh^2R^3(mR^2 + 13n) + h^4(91n^2R + 58nmR^3 + 15m^2R^5)]/(15nq\Omega^2) \tag{A5}$$

where

$$\Omega = 2nR^2 - 2nhR + (2n + mR^2)h^2, \quad \xi = S_n\mathrm{Re}_n^{-2n/n+2}(2\Gamma)^{((3n-2)n)/(2+n)}, \quad q = R + h \tag{A6}$$

References

[1] Krantz, W. B., and Zollars, R. L., 1976, "The Linear Hydrodynamic Stability of Film Flow Down a Vertical Cylinder," AIChE J., **22**, pp. 930–934.

[2] Hung, C. I., Chen, C. K., and Tsai, J. S., 1996, "Weakly Nonlinear Stability Analysis of Condensate Film Flow Down a Vertical Cylinder," Int. J. Heat Mass Transfer, **39**, pp. 2821–2829.

[3] Cheng, P. J., Chen, C. K., and Lai, H. Y., 2001, "Nonlinear Stability Analysis of the Thin Micropolar Liquid Film Flowing Down on a Vertical Cylinder," ASME Trans. J. Fluids Eng., **123**, pp. 411–421.

[4] Gupta, A. S., 1967, "Stability of a Viscoelastic Liquid Film Flowing Down an Inclined Plane," J. Fluid Mech., **28**, pp. 17–28.

[5] Ng, C. O., and Mei, C. C., 1994, "Roll Waves on a Shallow Layer of Mud Modelled as a Power-Law Fluid," J. Fluid Mech., **263**, pp. 151–183.

[6] Hwang, C. C., Chen, J. L., Wang, J. S., and Lin, J. S., 1994, "Linear Stability of Power Law Liquid Film Flows Down an Inclined Plane," J. Phys. D: Appl. Phys., **27**, pp. 2297–2301.

[7] Gorla, R. S. R., 2001, "Rupture of the Thin Power-Law Liquid Film on a Cylinder," Trans. ASME, J. Appl. Mech., **68**, pp. 294–297.

[8] Tsai, J. S., Hung, C. I., and Chen, C. K., 1996, "Nonlinear Hydromagnetic Stability Analysis of Condensation Film Flow Down a Vertical Plate," Acta Mech., **118**, pp. 197–212.

[9] Hsieh, D. Y., 1965, "Stability of Conducting Fluid Flowing Down an Inclined Plane in a Magnetic Field," Phys. Fluids, **8**, pp. 1785–1791.

[10] Kakac, S., Shah, R. K., and Aung, W., 1987, *Handbook of Single-Phase Heat Transfer*, Wiley, New York.

[11] Cheng, P.-J., and Lin, D. T. W., 2007, "Surface Waves on Viscoelastic Magnetic Fluid Film Flow Down a Vertical Column," Int. J. Eng. Sci., **45**, pp. 905–922.

[12] Cheng, P. J., and Liu, K. C., 2006, "Stability Analysis of the Thin Power Law Liquid Film Flowing Down on a Vertical Cylinder," Trans. Can. Soc. Mech. Eng., **30**, pp. 81–96.

NPSHr Optimization of Axial-Flow Pumps

Wen-Guang Li
Department of Fluid Machinery,
Lanzhou University of Technology,
287 Langongping Road,
730050 Lanzhou, P.R.C.
e-mail: liwg40@sina.com

The two-step method for optimizing net positive suction head required (NPSHr) of axial-flow pumps is proposed in this paper. First, the NPSHr at the impeller tip is optimized with impeller diameter based on experimental data of 2D cascades in available wind tunnels. Then, it is optimized again with the velocity moment at the impeller outlet, which is expressed in terms of two parameters. The blade geometry is generated and flow details are clarified by using the radial equilibrium equation, actuator disk theory, and 2D vortex element method in the optimizing process. The NPSHr response surface has been established in terms of these two parameters. The results illustrate that the second optimization allows NPSHr to be reduced by 37.5% compared to the first optimization. Therefore, this two-step method is effective and expects to be applied in the axial-flow pump impeller blade design. The simulations of 3D turbulent flow with various cavitation models and related confirming experiments are going to be done in the axial-flow impellers designed with this method.
[DOI: 10.1115/1.2948368]

Keywords: axial-flow pump, cavitation, net positive suction head required, optimization, impeller, response surface

1 Introduction

As one kind of fluid machine, the axial-flow pump has been applied extensively, and its hydraulic design has been involved in a number of references [1–8]. The primary dimensions of the impeller and other components can be defined with the formulas and plots presented in these references. The net positive suction head required (NPSHr) of axial-flow pump can be calculated with computational fluid dynamics (CFD) available after the geometrical details of the pump have been decided [9,10]. If CFD simulations are performed on each design case of an axial-flow pump, designers will experience far more heavily working load. As a result of this, it is anticipated that NPSHr should be estimated and optimized with a simple method, at first, and then, CFD simulations will be conducted on these optimized design cases for NPSHr to clarify the effects of the geometry on NPSHr and to get optimal geometrical combinations. Axial-flow pumps with optimized (lowest) NPSHr may benefit from its lower installation construction costing and less potential of cavitation damage.

The pressure distributions on the blades of an axial-flow pump have been measured by Morell and Bowerman in 1953 [11]. The hydraulic performance of three axial-flow pump runners was investigated experimentally in great deal, but the results associated with NPSHr were very limited [12]. The cavitation patterns in unshrouded axial-flow pump impellers can be classified into three types: blade surface cavitation, tip clearance cavitation, and tip leakage vortex cavitation [13]. Even though the tip clearance and tip leakage vortex cavitation patterns are important, they just happen under a particular condition, for example, in the impeller with relative large tip clearance [14–17]. If the tip relative clearance (the real clearance is divided by the maximum thickness of the blade at the tip) is kept to be a small value, say, 0.15 [14], or the blade pressure side edge at the tip is around or the blade is skewed forward [17], the tip clearance cavitation and tip leakage vortex cavitation patterns can be suppressed as weakly as possible.

The relation between the suction specific speed of centrifugal or axial-flow pumps and the meridional velocity at the impeller inlet has been debated for the blade surface cavitation; the effect of prerotation and pressure distribution on the blade was illustrated [18]. The relation of NPSHr with pressure coefficient on blade, hub ratio, head and flow rate, and velocity triangle at both inlet and outlet has been expressed in formulas for axial-flow pumps [19]. An optimal geometry, being responsible for a minimum NPSHr, can be found with this relation. However, the pressure coefficient on the blade is borrowed from a single aerofoil (NACA 65 camber and NACA16-009 thickness profile function). Additionally, the hydraulic efficiency and prerotation were not involved. Meanwhile, just the flow in cascade on hub stream surface was analyzed.

In this work, the method for optimizing the NPSHr of axial-flow pumps is presented. NPSHr at the impeller tip is optimized with impeller diameter first. Then, it is optimized once more with the velocity moment at the impeller outlet. The NPSHr is decreased by 37.5% in the second optimization compared to the first one.

2 Methods

The NPSHr of axial-flow pumps depends on the major dimensions of the impeller, blade shape, blade inlet, outlet angles, and so on. In order to let an axial-flow pump have a better cavitation characteristic, all these aspects must be considered carefully. We tend to determine an optimal impeller diameter allowing the impeller to demonstrate a relative low NPSHr at first. Then, the blade inlet and outlet angles are decided based on the optimized moment of absolute velocity of fluid at the impeller outlet by means of the radial equilibrium equation and actuator disk theory. The blade cambers can be constructed by means of these two angles. The blades are formed with these cambers and an airfoil thickness profile with better cavitation feature. Finally, the flow details are captured with the 2D vortex element method by which the better cavitation performance can be confirmed theoretically.

2.1 Effect of Impeller Diameter. The highest relative velocity of liquid can be found at the impeller tip for axial-flow pumps, and cavitation often can be observed at the blade suction side when the tip clearance is below a critical value [1–3]. As a result, the highest NPSHr should occur at the impeller tip, where the NPSHr of axial-flow pumps can be expressed as

$$\mathrm{NPSHr} = \lambda \frac{W_1^2}{2g} + \frac{V_1^2}{2g} \tag{1}$$

where W_1 and V_1 are the relative velocity and absolute velocity of fluid, respectively, λ is the cavitation coefficient, $\lambda = (W_{\max}/W_1)^2 - 1$, and $W_{\max}$ is the maximum relative velocity on impeller blade surface.

It should be noticed that λ just depends on the ratio $W_{\max}/W_1$; consequently, $W_{\max}/W_1$ is the critical variable to estimate NPSHr. Since cascade geometry is unavailable at the initial period of design of axial-flow pumps, it is impossible to attain an exact $W_{\max}/W_1$ through flow analysis; instead, it should be estimated by using existing experimental data for cascades. $W_{\max}/W_1$ plots were given by Lieblein [20] based on the experimental data of two-dimensional cascades with airfoil series of NACA65(A_{10}) and C4 in wind tunnels. The empirical formula of $W_{\max}/W_1$ is read as

Contributed by the Fluids Engineering Division of ASME for publication in the JOURNAL OF FLUIDS ENGINEERING. Manuscript received August 20, 2007; final manuscript received April 3, 2008; published online July 22, 2008. Assoc. Editor: Chunill Hah.

$$\frac{W_{\max}}{W_1} = 1.12 + 0.61\frac{\sin^2\beta_1}{\sigma_t}(\mathrm{ctg}\beta_1 - \mathrm{ctg}\beta_2) \tag{2}$$

where β_1 and β_2 are the inlet and outlet angles of flow, and σ_t is the cascade solidity at the impeller tip. Based on the velocity triangles at the inlet and outlet of the impeller tip, and note the constant meridional velocity at the impeller inlet and outlet, $V_{m1} = V_{m2}$, we have

$$\frac{W_{\max}}{W_1} = 1.12 + 0.61\frac{\sin^2\beta_1}{\sigma_t}\frac{(V_{u2} - V_{u1})u}{V_{m1}u} \tag{3}$$

where V_{u1} and V_{u2} are the circumferential components of absolute velocity at the inlet and outlet, respectively. u is the impeller tip speed. By means of Euler's equation of turbomachinery and the relation $W_1^2 = (u - V_{u1})^2 + V_{m1}^2$, Eq. (3) is rewritten as

$$\frac{W_{\max}}{W_1} = 1.12 + 0.61\frac{V_{m1}}{[(u - V_{u1})^2 + V_{m1}^2]u}\frac{gH_{\mathrm{th}}}{\sigma_t} \tag{4}$$

where the theoretical head of the impeller $H_{\mathrm{th}} = H/\eta_h$, and η_h is the pump hydraulic efficiency.

The absolute velocity two components V_{m1} and V_{u1}, impeller tip speed u (when the impeller rotational speed is constant, it is equivalent to the impeller diameter), and theoretical head H_{th} (flow dynamic load on blade) as well as cascade solidity σ_t at the impeller tip have influence on the $W_{\max}/W_1$ and NPSHr in turn. If these parameters are known, the NPSHr can be predicted immediately.

The well-known empirical formula for the meridional velocity at impeller inlet is written as [21]

$$V_{m1} = (0.06 - 0.08)\sqrt[3]{Qn^2} \tag{5}$$

where Q is the design flow rate of a pump (m^3/s), and n is the pump rotating speed (rpm). When V_{m1} is chosen, the impeller diameter is

$$D = \sqrt{\frac{4Q}{\pi(1 - \nu)V_{m1}}} \tag{6}$$

where ν is the hub ratio of impeller, $\nu = D/d$, and d is the hub diameter.

The tangential component V_{u1} of the absolute velocity of liquid is associated with the moment of absolute velocity in front of the impeller. The well-known empirical formula for semispiral casings can be used to estimate the velocity moment at the impeller inlet [21],

$$K_1 = (0.065 - 0.08)\sqrt[3]{Q^2n} \tag{7}$$

where K_1 the velocity-moment coefficient at inlet is $K_1 = V_{u1}D/2$. After K_1 is specified, we can get V_{u1}, via $V_{u1} = 2K_1/D$. A suitable value of K_1 should yield an absolute prewhirl angle of less than 30 deg.

Since NPSHr has been linked to impeller diameter D through Eqs. (1) and (4)–(7) already, an optimal D being responsible for an impeller having lower NPSHr can be decided.

2.2 Effect of Velocity Moment at Outlet. The radial equilibrium equation and actuator disk theory are applied to establish blade inlet and outlet angle at several cylindrical stream surfaces, then a blade camber is constructed by using a third-order polynomial; consequently, a blade section is formed by superimposing the airfoil thickness profile chosen on the camber generated. The flow details on the blade surface are given by using the 2D vortex element method [8]. The corresponding NPSHr can be predicted. Finally, a 3D blade is generated by stacking the blade section on each stream surface together.

In the application of radial equilibrium equation for establishing the blade outlet angle, the velocity moment at the impeller outlet must be specified initially. We believe that this moment is associated with NPSHr. The velocity moment at the impeller outlet is expressed in terms of a dimensionless parameter ξ.

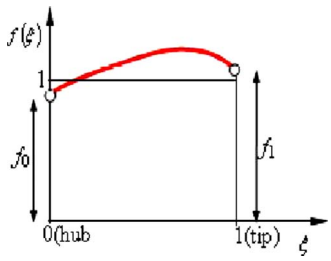

Fig. 1 Velocity-moment shape function in terms of dimensionless parameter ξ

$$V_{u2}R = Kf(\xi) \tag{8}$$

and

$$\int_0^1 f(\xi)d\xi = 1 \tag{9}$$

where $\xi = (2R - d)/(D - d)$, and R is a radius at the impeller exit. The simplest type of $f(\xi)$ is known as the parabolic shape function of ξ. In this case, the coefficients in $f(\xi)$ are controlled by two parameters, f_0 and f_1 (Fig. 1).

Obviously, the velocity moment can be controlled by using these two parameters. The constant K in Eq. (8) may be determined by the averaged Euler equation of turbomachinery in the following manner:

$$K = \frac{gQH_{\mathrm{th}} + \int_{d/2}^{D/2} 2\pi u K_1 V_{m1} dR}{\int_{d/2}^{D/2} 2\pi u f(\xi) V_{m2} dR} \tag{10}$$

After f_0 and f_1 are specified, the $V_{u2}R$ is available at once.

Since the radial equilibrium equation is responsible for the meridional flow field infinitely far from rather than nearby an impeller, the actuator disk theory must be employed to clarify the meridional flow field near the impeller. The combination of both presents the meridional flow field desired, then the right relative flow angle at the inlet and outlet can be determined. After these angles are modified with the optimal fluid angle of attack and fluid deviation angle, the blade angle at the inlet and outlet, and stagger angle can be established. Because of the actuator disk theory and the optimal fluid angle of attack as well as the deviation angle being dependent on blade geometry, the blade angle determining process is iterative essentially. Once the computation converges, the blade camber can be generated; in turn, the blade sections are constructed. Consequently, the flow details are analyzed by using the 2D vortex element method, and NPSHr is predicted.

In this way, we can establish the NPSHr response surface in terms of f_0 and f_1. Based on the surface, an optimal $V_{u2}R$ and blade geometry being expected to give a relative low NPShr can be attained.

2.3 Effect of Blade Thickness Profile. The thickness profiles of airfoil NACA-0012 and NACA-66-010 are likely applicable to generate a blade section of axial-flow pumps (Fig. 2). It can be observed that the peak thickness is located at 50% of chord for NACA-66-010 instead of 30% for NACA-0012. Peak thickness position that moves backward helps decrease hydrodynamic loading around blade leading edge and put the blade under less risk of cavitation. Consequently, the profile of NACA66-010 is desired to possess a low NPSHr. Thus, this profile is applied in this work.

3 Results

We have planed to develop a double-suction axial-flow pump with the specifications: $Q = 600\ \mathrm{m}^3/\mathrm{h}$, $H = 3$ m, $n = 1450$ rpm at

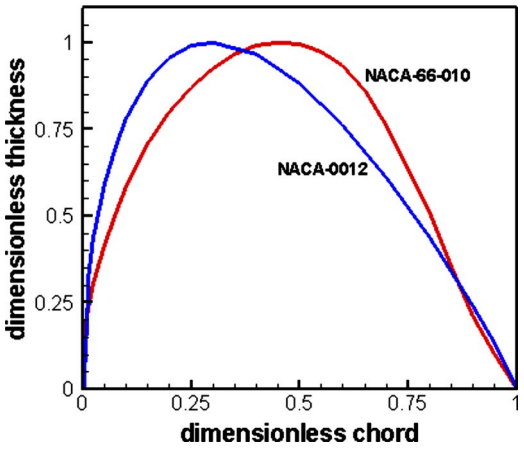

Fig. 2 Dimensionless thickness against the dimensionless chord for the two types of airfoil

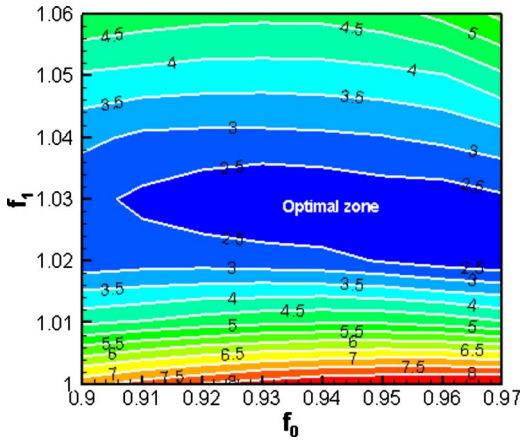

Fig. 4 Response surface of NPSHr as a function of the parameters f_0 and f_1

the design point with a specific speed of $n_s=3.65n\sqrt{Q/2}/H^{3/4}=670$ rpm m^3/s m (in China) or $N_s=n\sqrt{Q/2}/H^{3/4}=9566$ rpm GPM ft (in USA). We select $\eta_h=0.85$; $\sigma_t=0.85$, $K_1=0$ m^2/s, 0.1 m^2/s, 0.15 m^2/s, 0.2 m^2/s, and $\nu=0.53$ to investigate their effects on the impeller diameter and NPSHr.

Figure 3 demonstrates NPSHr versus impeller diameter D when $K_1=0$ m^2/s, 0.1 m^2/s, 0.2 m^2/s, $\eta_h=0.85$, $\sigma_t=0.85$, and $\nu=0.53$. It can be seen that there exists the diameter, which enables an impeller to have minimum NPSHr for the defined velocity moment at inlet. The position of minimum NPSHr seems to be independent of K_1. The optimal diameter is 197 mm and the corresponding NPSHr is 4.0 m as $K_1=0.151$ m^2/s.

Figure 4 presents the response surface of NPShr in terms of f_0 and f_1. It can be observed that the parameter f_1 has more significant effect on NPSHr compared to f_0. Moreover, a valley with low NPSHr can be found. For f_1, to approach unity can result in a rapid increase in NPSHr. In the optimal zone, NPSHr is less than 2.5 m, and at least 37.5% reduction is achieved. If $f_0=0.94$, $f_1=1.03$, we get the lowest NPSHr of 2.01 m.

Figure 5 illustrates the pressure coefficient C_p on the blade surface at hub, midspan, and tip stream surfaces. Because the peak coefficient occurs on the blade pressure side rather than on the blade suction side, the angle of attack is positive, which is the case we desire. What we are concerned with is that the blade at the hub experiences more heavily hydrodynamic loading than at the midspan and tip. Such a large loading will be responsible for the flow stall.

A blade 3D shape optimized has been shown in Fig. 6. The pressure coefficient contour on the blade surface also has been illustrated. The minimum pressure coefficient can be found on the blade suction side at the hub. The blade stagger at the hub seems to be large. Thus, the blade geometry at the hub should be amended later.

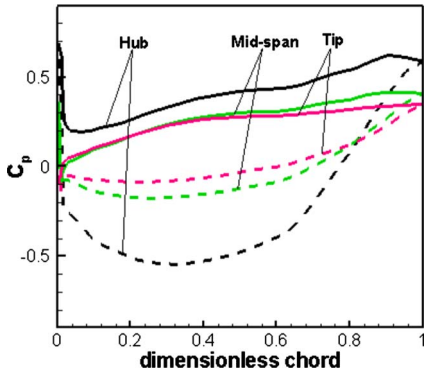

Fig. 5 Pressure coefficient distribution on the blade surfaces at hub, mid-span and tip stream-surfaces. The solid line is for blade pressure side, and the dashed for blade suction side.

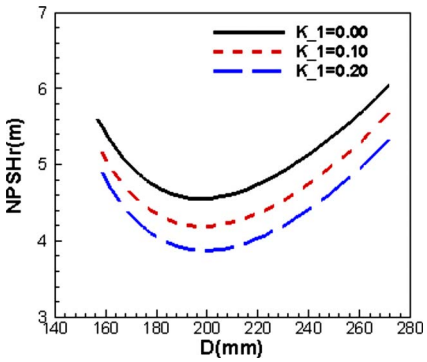

Fig. 3 NPSHr versus the impeller diameter when $K_1=0$ m^2/s, 0.1 m^2/s, 0.2 m^2/s, $\eta_h=0.85$, $\sigma_t=0.85$, and $\nu=0.53$

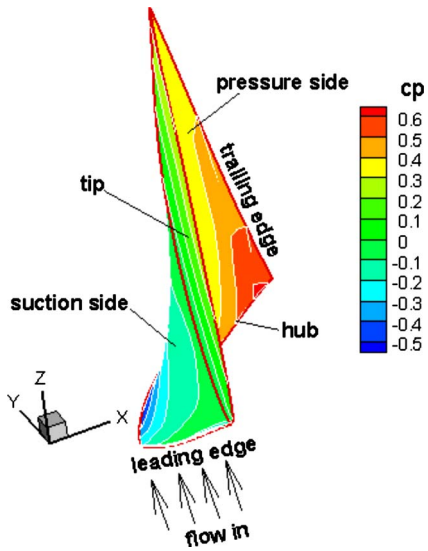

Fig. 6 Blade 3D shape optimized and the pressure coefficient contour on blade surface

It should be noticed that the flow is highly complex in a real axial-flow pump, especially at the blade tip and hub. The flow in 3D cascade of axial-flow pumps significantly differs from that of our 2D case. The simulations of 3D turbulent flow with cavitation in axial-flow pumps expect to be done soon and the related experimental work also is being considered.

4 Conclusion

An optimization method for determining the NPSHr of axial-flow pumps with a low specific speed of 9566 has been proposed in this work, and a series of parameter studies has been carried out. It has been demonstrated that this two-step method proposed is really effective and it expects to be applied in the axial flow pump blade design. Based on these results, two conclusions may be made: (1) NPSHr is related to the impeller diameter by the relations (1) and (4), and the diameter allowing a pump to have lower NPShr can be decided; (2) NPSHr can be reduced further by means of an optimized velocity-moment distribution at the impeller outlet based on the radial equilibrium equation and actuator disk theory as well as 2D vortex element approach. The optimal zones of the two parameters, f_0 and f_1, which determine the velocity-moment distribution at impeller exit, are found to be 0.91–0.97 and 1.025–1.035, respectively.

Acknowledgment

This work was supported fully by the Administrative Department of Science and Technology, Gansu Province, China, under the Grant No. 62206. The Department was acknowledged indeed.

References

[1] Wislicenus, G. F., 1947, *Fluid Mechanics of Turbomachinery*, McGraw-Hill, New York.

[2] Stepanoff, A. J., 1948, *Centrifugal and Axial Flow Pumps*, John Wiley & Sons, New York, pp. 143–165.

[3] Lazarkiewicz, S., and Troskolanski, A. T., 1965, *Impellers Pumps*, Pergamon, Oxford, pp. 218–250.

[4] Govida Rao, N. S., 1965, "Studies on Certain Aspects of the Design of Axial and Mixed Flow Impellers," *Proceedings of the Symposium on Pump Design, Testing and Operation*, National Engineering Laboratory, East Kilbride, Glasgow, UK, April 12–14, Paper No. C1-2.

[5] Hay, N., and Metcalfe, R., 1978, "A Simple Method for the Selection of Axial Fan Blade Profiles," Proc. Inst. Mech. Eng., **192**, pp. 269–275.

[6] Zaher, M. A., and Ipenz, M., 2000, "Preliminary Determination of Basic Dimensions for an Axial Flow Pump," Proc. Inst. Mech. Eng., Part E, J. Process Mech. Eng., **214**(3), pp. 173–183.

[7] Turton, R. K., 1994, *Rotodynamic Pump Design*, Cambridge University Press, Cambridge, pp. 124–138.

[8] Lewis, R. I., 1996, *Turbomachinery Performance Analysis*, Arnold, London, pp. 82–142.

[9] Fukaya, M., Okamura, T., Tamura, Y., and Matsumoto, Y., 2003, "Prediction of Cavitation Performance of Axial Flow Pump by Using Numerical Cavitating Flow Simulation with Bubble Flow Model," *Proceedings of the 5th International Symposium on Cavitation (CAV2003)*, Osaka, Japan, Nov. 1–4, Paper No. Cav03-OS-6-012.

[10] Bouziad, Y. A., Farhat, M., Guennoun, F., Kueny, J. L., and Miyagawa, K., 2003, "Physical Modelling and Simulation of Leading Edge Cavitation-Application to an Industrial Inducer," *Proceedings of the 5th International Symposium on Cavitation (CAV2003)*, Osaka, Japan, Nov. 1–4, Paper No. Cav03-OS-6-014.

[11] Morell, D. A., and Bowerman, R. D., 1953, "Pressure Distributions on the Blade of Axial-Flow Propeller Pump," Trans. ASME, **75**, pp. 1007–1013.

[12] Miller, M. J., Crouse, J. E., and Sandercock, D. M., 1967, "Summary of Experimental Investigation of Three Axial-Flow Pump Rotor Tested in Water," ASME J. Eng. Power, **92**, pp. 589–599.

[13] Murayama, M., Yoshida, Y., and Tsujimoto, Y., 2006, "Unsteady Tip Leakage Vortex Cavitation Originating From the Tip Clearance of an Oscillating Hydrofoil," ASME J. Fluids Eng., **128**, pp. 421–429.

[14] Mitchell, A. B., 1961, "An Experimental Investigation of Cavitation Inception in the Rotor Blade Tip Region of an Axial Flow Pump," ARC CP-527.

[15] Straka, W. A., and Farrell, K. J., 1992, "The Effect of Spatial Wandering on Experimental Laser Velocimeter Measurements of the End-Wall Vortices in an Axial-Flow Pump," Exp. Fluids, **13**, pp. 163–170.

[16] Farrell, K. J., and Billet, M. L., 1994, "A Correlation of Leakage Vortex Cavitation in Axial-Flow Pumps," ASME J. Fluids Eng., **116**, pp. 551–557.

[17] Laborde, R., Chantrel, P., and Mory, M., 1997, "Tip Clearance and Tip Vortex Cavitation in an Axial Flow Pump," ASME J. Fluids Eng., **119**, pp. 680–685.

[18] Wislicemus, G. F., 1956, "Critical Considerations on Cavitation Limits of Centrifugal and Axial-Flow Pumps," Trans. ASME, **78**, pp. 1707–1714.

[19] Bowerman, R. D., 1956, "The Design of Axial Flow Pumps," Trans. ASME, **78**, pp. 1723–1734.

[20] Lieblein, S., 1959, "Loss and Stall Analysis of Compressor Cascades," ASME J. Basic Eng., **81**(3), pp. 387–397.

[21] Guan, X. F., 1987, *Rotodynamic Pump Principal and Design*, Mechanical Industry Press, Beijing, in Chinese, Chaps. 4 and 6.

Procedure for Estimation and Reporting of Uncertainty Due to Discretization in CFD Applications

*Since 1990, the Fluids Engineering Division of ASME has pursued activities concerning the detection, estimation and control of numerical uncertainty and/or error in computational fluid dynamics (CFD) studies. The first quality-control measures in this area were issued in 1986 (1986, "Editorial Policy Statement on Control of Numerical Accuracy," ASME J. Fluids Eng., **108**, p. 2) and revised in 1993 (1993, "Journal of Fluids Engineering Editorial Policy Statement on the Control of Numerical Accuracy," ASME J. Fluids Eng., **115**, pp. 339–340). Given the continued increase in CFD related publications, and the many significant advancements in computational techniques and computer technology, it has become necessary to revisit the issue and formulate a more detailed policy to further improve the quality of publications in this area. This brief note provides specific guidelines for prospective authors for calculation and reporting of discretization error estimates in CFD simulations where experimental data may or may not be available for comparison. The underlying perspective is that CFD-related studies will eventually aim to predict the outcome of a physical event for which experimental data is not available. It should be emphasized that the requirements outlined in this note do not preclude those already published in the previous two policy statements. It is also important to keep in mind that the procedure recommended in this note cannot possibly encompass all possible scenarios or applications.* [DOI: 10.1115/1.2960953]

Preliminaries

The *computer code* used for an application must be fully referenced, and previous code *verification studies* must be briefly described or cited. The word "verification" is used in this note in its broadest sense, meaning that the computer code is capable of solving a system of coupled differential or integral equations with a properly posed set of initial and/or boundary conditions correctly, and reproduces the exact solution to these equations when sufficiently fine grid resolution (both in time and space) is employed. The *formal order of accuracy* in time and space for each equation solved should be also stated clearly, with proper references where this information is accessible to the readers. Before any discretization error estimation is calculated, it must be shown that *iterative convergence* is achieved with at least three (preferably four) orders of magnitude decrease in the normalized residuals for each equation solved. (This commonly used criterion does not always ensure adequate convergence; see Appendix) For time-dependent problems, iterative convergence at every time step should be checked, and sample convergence trends should be documented for selected, critically important, variables. A possible method for assessment of iteration errors is outlined in the Appendix.

It should also be recognized that uncertainty in inlet flow boundary conditions could be a significant contributor to the overall uncertainty. Here we recommend that the degree of sensitivity of the presented solution to small perturbations in the inlet conditions be studied and reported.

The recommended method for discretization error estimation is the Richardson extrapolation (RE) method. Since its first elegant application by its originator [1,2], this method has been studied by many authors. Its intricacies, shortcomings, and generalization have been widely investigated. A short list of references given in the bibliography [3–12,15] is selected for the direct relevance of these references to the subject and for brevity. The limitations of the RE method are well known. The local RE values of the predicted variables may not exhibit a smooth monotonic dependence on grid resolution, and in a time-dependent calculation, this nonsmooth response will also be a function of time and space. Nonetheless, it is currently the most reliable method available for the prediction of numerical uncertainty. Prospective authors can find many examples in the above references. As new and more reliable methods emerge, the present policy statement will be reassessed and modified as needed.

The Grid Convergence Method (GCI) method (and is based on RE) described herein is an acceptable and a recommended method that has been evaluated over several hundred CFD cases [19,14,2,10,7]. If authors choose to use it, the method per se will not be challenged in the paper review process. If authors choose to use another method, the adequacy of their method will be judged in the review process. This policy is not meant to discourage further development of new methods. in fact, JFE encourages the development and statistically significant evaluation of alternative methods of estimation of error and uncertainty. Rather, this policy is meant to facilitate CFD publication by providing practitioners with a method that is straightforward to apply, is fairly well justified and accepted, and will avoid possible review bottlenecks, especially when the CFD paper is an application paper rather than one concerned with new CFD methodology.

Recommended Procedure for Estimation of Discretization Error

Step 1. Define a representative cell, mesh, or grid size h. For example, for three-dimensional calculations,

$$h = \left[\frac{1}{N} \sum_{i=1}^{N} (\Delta V_i) \right]^{1/3} \tag{1}$$

For two dimensions,

$$h = \left[\frac{1}{N} \sum_{i=1}^{N} (\Delta A_i) \right]^{1/2} \tag{2}$$

where ΔV_i is the volume, ΔA_i is the area of the ith cell, and N is the total number of cells used for the computations. Equations (1) and (2) are to be used when integral quantities, e.g., drag coefficient, are considered. For field variables, the local cell size can be used. Clearly, if an observed global variable is used, it is then appropriate to use also an average "global" cell size. The area should be interpreted strictly according to the mesh being used, i.e., the mesh is either 2D (consisting of areas) or 3D (consisting of volumes) irrespective of the problem being solved.

Step 2. Select three significantly different sets of grids and run simulations to determine the values of key variables important to the objective of the simulation study, for example, a variable ϕ critical to the conclusions being reported. It is desirable that the grid refinement factor $r = h_{\text{coarse}}/h_{\text{fine}}$ be greater than 1.3. This value of 1.3 is based on experience and not on formal derivation. The grid

Table 1 Sample calculations of discretization error

	ϕ=dimensionless reattachment length (with monotonic convergence)	ϕ=axial velocity at $x/H=8$, $y=0.0526$ ($p<1$)	ϕ=axial velocity at $x/H=8$, $y=0.0526$ (with oscillatory convergence)
N_1, N_2, N_3	18,000, 8000, 4500	18,000, 4500, 980	18,000, 4500, 980
r_{21}	1.5	2.0	2.0
r_{32}	1.333	2.143	2.143
ϕ_1	6.063	10.7880	6.0042
ϕ_2	5.972	10.7250	5.9624
ϕ_3	5.863	10.6050	6.0909
p	1.53	0.75	1.51
ϕ_{ext}^{21}	6.1685	10.8801	6.0269
e_a^{21}	1.5%	0.6%	0.7%
e_{ext}^{21}	1.7%	0.9%	0.4%
GCI_{fine}^{21}	2.2%	1.1%	0.5%

refinement should, however, be done systematically, that is, the refinement itself should be structured even if the grid is unstructured. Use of geometrically similar cells is preferable.

Step 3. Let $h_1<h_2<h_3$ and $r_{21}=h_2/h_1$, $r_{32}=h_3/h_2$, and calculate the apparent order p of the method using the expression

$$p = \frac{1}{\ln(r_{21})}|\ln|\varepsilon_{32}/\varepsilon_{21}| + q(p)| \tag{3a}$$

$$q(p) = \ln\left(\frac{r_{21}^p - s}{r_{32}^p - s}\right) \tag{3b}$$

$$s = 1 \cdot \text{sgn}(\varepsilon_{32}/\varepsilon_{21}) \tag{3c}$$

where $\varepsilon_{32}=\phi_3-\phi_2$, $\varepsilon_{21}=\phi_2-\phi_1$, and ϕ_k denotes the solution on the kth grid. Note that $q(p)=0$ for $r=$const. Equation (3) can be solved using fixed-point iteration, with the initial guess equal to the first term. The absolute value in Eq. (3*a*) is necessary to ensure extrapolation toward $h=0$ (Celik and Karatekin [4]). Negative values of $\varepsilon_{32}/\varepsilon_{21}<0$ are an indication of oscillatory convergence. If possible, the percentage occurrence of oscillatory convergence should also be reported. The agreement of the observed apparent order with the formal order of the scheme used can be taken as a good indication of the grids being in the asymptotic range; the converse should not necessarily be taken as a sign of unsatisfactory calculations. It should be noted that if either $\varepsilon_{32}=\phi_3-\phi_2$ or $\varepsilon_{21}=\phi_2-\phi_1$ is "very close" to zero, the above procedure does not work. This might be an indication of oscillatory convergence or, in rare situations, it may indicate that the "exact" solution has been attained. In such cases, if possible, calculations with additional grid refinement should be performed; if not, the results may be reported as such.

Step 4. Calculate the extrapolated values from

$$\phi_{\text{ext}}^{21} = (r_{21}^p\phi_1 - \phi_2)/(r_{21}^p - 1) \tag{4}$$

similarly, calculate ϕ_{ext}^{32}.

Step 5. Calculate and report the following error estimates, along with the apparent order p.

In approximate relative error,

$$e_a^{21} = \left|\frac{\phi_1 - \phi_2}{\phi_1}\right| \tag{5}$$

In extrapolated relative error,

$$e_{\text{ext}}^{21} = \left|\frac{\phi_{\text{ext}}^{12} - \phi_1}{\phi_{\text{ext}}^{12}}\right| \tag{6}$$

In the fine-grid convergence index,

$$\text{GCI}_{\text{fine}}^{21} = \frac{1.25e_a^{21}}{r_{21}^p - 1} \tag{7}$$

Table 1 illustrates this calculation procedure for three selected grids. The data used are taken from Ref. [4], where the turbulent two-dimensional flow over a backward facing step was simulated on nonuniform structured grids with total number of cells N_1, N_2, and N_3. Hence, according to Table 1, the numerical uncertainty in the fine-grid solution for the reattachment length should be reported as 2.2%. Note that this does not account for modeling errors.

Discretization Error Bars

When computed profiles of a certain variable are presented, it is recommended that numerical uncertainty be indicated by error bars on the profile, analogous to the experimental uncertainty. It is further recommended that this be done using the GCI in conjunction with an average value of $p=p_{\text{ave}}$ as a measure of the global order of accuracy. This is illustrated in Figs. 1 and 2.

Figure 1 (data taken from Ref. [4]) presents an axial velocity profile along the y-axis at an axial location of $x/H=8.0$ for a *turbulent*

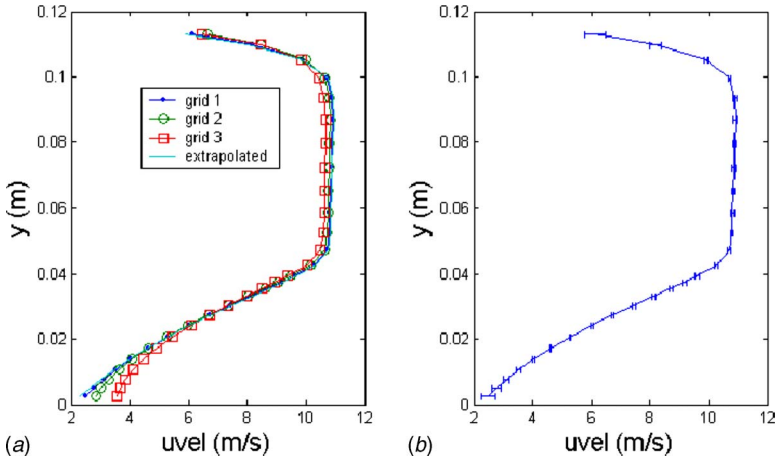

Fig. 1 (*a*) Axial velocity profiles for a two-dimensional turbulent backward-facing-step flow calculation [16]; (*b*) Fine-grid solution, with discretization error bars computed using Eq. (7).

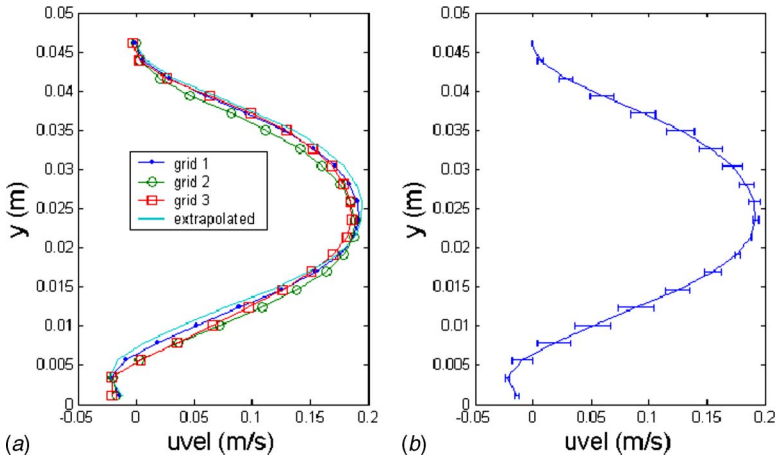

Fig. 2 (*a*) Axial velocity profiles for a two-dimensional laminar backward-facing-step flow calculation [16]; (*b*) Fine-grid solution, with discretization error bars computed using Eq. (7)

two-dimensional backward-facing-step flow. The three sets of grids had 980, 4500, and 18000 cells, respectively. The local order of accuracy p calculated from Eq. (3) ranges from 0.012 to 8.47, with a global average p_{ave} of 1.49, which is a good indication of the hybrid method applied for that calculation. Oscillatory convergence occurs at 20% of the 22 points. This averaged apparent order of accuracy is used to assess the GCI index values in Eq. (7) for individual grids, which is plotted in the form of error bars, as shown in Fig. 1(*b*). The maximum discretization uncertainty is 10%, which corresponds to ± 0.35 m/s.

Figure 2 (data taken from Ref. [16]) presents an axial velocity profile along the y-axis at the station $x/H=8.0$ for a *laminar* two-dimensional backward-facing-step flow. The Reynolds number based on step height is 230. The sets of grids used were 20×20, 40×40, and 80×80, respectively. The local order of accuracy p ranges from 0.1 to 3.7, with an average value of $p_{\text{ave}}=1.38$. In this figure, 80% out of 22 points exhibited oscillatory convergence. Discretization error bars are shown in Fig. 2(*b*), along with the fine-grid solution. The maximum percentage discretization error was about 100%. This high value is relative to a velocity near zero and corresponds to a maximum uncertainty in velocity of about ± 0.012 m/s.

In the not unusual cases of noisy grid convergence, the least-squares version of GCI should be considered [13,14,17].

Appendix: A Possible Method for Estimating Iteration Error

Following Ferziger [18,19], the iteration error can be estimated by

$$\varepsilon^{n}_{\text{iter},i} \cong \frac{(\phi_i^{n+1} - \phi_i^{n})}{\lambda_i - 1} \tag{A1}$$

where n is the iteration number and λ_1 is the principal eigenvalue of the solution matrix of the linear system, which can be approximated from

$$\lambda_i \cong \frac{\|\phi_i^{n+1} - \phi_i^n\|}{\|\phi_i^n - \phi_i^{n-1}\|} \tag{A2}$$

The uncertainty δ_{iter} in iteration convergence can then be estimated as

$$\delta_{\text{iter}} \cong \frac{\|\varepsilon_{\text{iter},i}^n\|}{\lambda_{\text{ave}} - 1} \tag{A3}$$

where $\| \ \|$ is any appropriate norm, e.g., L_∞ norm. Here, λ_{ave} is the average value of λ_i over a reasonable number of iterations. If $\lambda_{\text{ave}} \approx 1.0$, the difference between two consecutive iterations would not be a good indicator of iteration error. In order to build conservatism into these estimates, it is recommended that a limiter of $|\lambda| < 2$ be applied in calculating λ_{ave}.

It is recommended that the iteration convergence error calculated as suggested above (or in some other rational way) should be at least one order of magnitude smaller than the discretization error estimates for each calculation (for alternative methods see, e.g., Refs. [20,21]).

Ismail B. Celik
Urmila Ghia
Patrick J. Roache
Christopher J. Freitas
Hugh Coleman
Peter E. Raad

References

[1] Richardson, L. F., 1910, "The Approximate Arithmetical Solution by Finite Differences of Physical Problems Involving Differential Equations, With an Application to the Stresses in a Masonary Dam," Philos. Trans. R. Soc. London, Ser. A, **210**, pp. 307–357.
[2] Richardson, L. F., and Gaunt, J. A., 1927, "The Deferred Approach to the Limit," Philos. Trans. R. Soc. London, Ser. A, **226**, pp. 299–361.
[3] Celik, I., Chen, C. J., Roache, P. J., and Scheurer, G., Editors. (1993), "Quantification of Uncertainty in Computational Fluid Dynamics," ASME Fluids Engineering Division Summer Meeting, Washington, DC, Jun. 20–24, ASME Publ. No. FED-Vol. 158.
[4] Celik, I., and Karatekin, O., 1997, "Numerical Experiments on Application of Richardson Extrapolation With Nonuniform Grids," ASME J. Fluids Eng., **119**, pp. 584–590.
[5] Eca, L., and Hoekstra, M., 2002, "An Evaluation of Verification Procedures for CFD Applications," *24th Symposium on Naval Hydrodynamics*, Fukuoka, Japan, Jul. 8–13.
[6] Freitas, C. J., 1993, "Journal of Fluids Engineering Editorial Policy Statement on the Control of Numerical Accuracy," ASME J. Fluids Eng., **115**, pp. 339–340.
[7] Roache, P. J., 1993, "A Method for Uniform Reporting of Grid Refinement Studies," *Proceedings of Quantification of Uncertainty in Computation Fluid Dynamics*, Edited by Celik, et al., ASME Fluids Engineering Division Spring Meeting, Washington, D.C., June 23–24, ASME Publ. No. FED-Vol. 158.
[8] Roache, P. J., 1998, "Verification and Validation in Computational Science and Engineering," Hermosa Publishers, Albuquerque, NM.
[9] Stern, F., Wilson, R. V., Coleman, H. W., and Paterson, E. G., 2001, "Comprehensive Approach to Verification and Validation of CFD Simulations—Part 1: Methodology and Procedures," ASME J. Fluids Eng., **123**, pp. 793–802.
[10] Broadhead, B. L., Rearden, B. T., Hopper, C. M., Wagschal, J. J., and Parks, C. V., 2004, "Sensitivity- and Uncertainty-Based Criticality Safety Validation Techniques," Nucl. Sci. Eng., **146**, pp. 340–366.
[11] DeVolder, B., Glimm, J., Grove, J. W., Kang, Y., Lee, Y., Pao, K., Sharp, D. H., and Ye, K., 2002, "Uncertainty Quantification for Multiscale Simulations," ASME J. Fluids Eng., **124**(1), pp. 29–41.
[12] Oberkampf, W. L., Trucano, T. G., and Hirsch, C., 2003, "Verification, Validation, and Predictive Capability in Computational Engineering and Physics," Sandia Report No. SAND2003-3769.
[13] Eça, L., Hoekstra, M., and Roache, P. J., 2005, "Verification of Calculations: An Overview of the Lisbon Workshop," *AIAA Computational Fluid Dynamics Conference*, Toronto, Canada, Jun., AIAA Paper No. 4728.
[14] Eça, L., Hoekstra, M., and Roache, P. J., 2007, "Verification of Calculations: an Overview of the 2nd Lisbon Workshop," *Second Workshop on CFD Uncertainty Analysis, AIAA Computational Fluid Dynamics Conference*, Miami, FL, Jun., AIAA Paper No. 2007-4089.
[15] Roache, P. J., Ghia, K. N., and White, F. M., 1986, "Editorial Policy Statement on Control of Numerical Accuracy," ASME J. Fluids Eng., **108**, p. 2.
[16] Celik, I., and Badeau, A., Jr., 2003, "Verification and Validation of DREAM Code," Mechanical and Aerospace Engineering Department, Report No. MAE_IC03/TR103.
[17] Roache, P. J., 2003, "Conservatism of the GCI in Finite Volume Computations on Steady State Fluid Flow and Heat Transfer," ASME J. Fluids Eng., **125**(4), pp. 731–732.
[18] Ferziger, J. H., 1989, "Estimation and Reduction of Numerical Error," *ASME Winter Annual Meeting*, San Fransisco, CA, Dec.
[19] Ferziger, J. H., and Peric, M., 1996, "Further Discussion of Numerical Errors in CFD," Int. J. Numer. Methods Fluids, **23**, pp. 1263–1274.
[20] Eça, L., and Hoekstra, M., 2006, "On the Influence of the Iterative Error in the Numerical Uncertainty of Ship Viscous Flow Calculations," *26th Symposium on Naval Hydrodynamics*, Rome, Italy, Sept. 17–22.
[21] Stern, F., Wilson, R., and Shao, J., 2006, "Quantitative V&V of CFD Simulations and Certification of CFD Codes," Int. J. Numer. Methods Fluids, **50**, pp. 1335–1355.